Modeling and Experimental Study of Methane Catalytic Cracking as A Hydrogen Production Technology

by

Ashraf Mukhtar Lotfi Amin

A thesis
presented to the University of Waterloo
in fulfillment of the
thesis requirement for the degree of
Doctor of Philosophy
in
Chemical Engineering

Waterloo, Ontario, Canada, 2011

AUTHOR'S DECLARATION

I hereby declare that I am the sole author of this thesis. This is a true copy of the thesis, including any required final revisions, as accepted by my examiners.

I understand that my thesis may be made electronically available to the public.

Abstract

Production of hydrogen is primarily achieved via catalytic steam reforming, partial oxidation, and auto-thermal reforming of natural gas. Although these processes are mature technologies, they are somewhat complex and CO is formed as a by-product, therefore requiring a separation process if a pure or hydrogen-rich stream is needed. As an alternative method, supported metal catalysts can be used to catalytically decompose hydrocarbons to produce hydrogen. The process is known as catalytic cracking of hydrocarbons. Methane, the hydrocarbon containing the highest percentage of hydrogen, can be used in such a process to produce a hydrogen-rich stream. The decomposition of methane occurs on the surface of the active metal to produce hydrogen and filamentous carbon. As a result, only hydrogen is produced as a gaseous product, which eliminates the need of further separation processes to separate CO_2 or CO. Nickel is commonly used in research as a catalyst for methane cracking in the 500-700°C temperature range. As a sequence of the process, carbon is deposited on the catalyst in the form of carbon filaments but part of the carbon is deposited as encapsulating carbon which causes catalyst deactivation.

To conduct methane catalytic cracking in a continuous manner, regeneration of the deactivated catalyst is required and circulation of the catalysts between cracking and regeneration cycles must be achieved. Different reactor designs have been successfully used in cyclic operation, such as a set of parallel fixed-bed reactors alternating between cracking and regeneration, but catalyst agglomeration due to carbon deposition may lead to blockage of the reactor and elevated pressure drop through the fixed bed. Also poor heat transfer in the fixed bed may lead to elevated temperature during the regeneration step when carbon is burned in air, which may cause catalyst sintering. A fluidized bed reactor appears as a viable option for methane catalytic cracking, since it would permit cyclic operation by moving the catalyst between a cracker and a regenerator. In addition, there is the possibility of using fine catalyst particles, which improves catalyst effectiveness. A fluidized bed reactor also overcomes fixed bed plugging problems due to carbon deposition and the poor mass and heat transfer experienced in the fixed bed. A fluidized bed process for methane catalytic cracking, known as the “HYPRO” process, was patented back in 1966, but its higher operating cost prevented it from competing favorably with conventional steam reforming. However, many improvements could be made, such as optimizing the catalyst and the overall operating conditions. A critical step to study

the feasibility of the process is to model the fluidized bed cracking reactor. The model will help in predicting the effect of various parameters (e.g. methane flow rate, concentration, pressure, reaction kinetics, hydrodynamics) on the overall system performance.

In this project, a three-phase bubbling fluidized bed model for catalytic cracking of methane was developed to predict the performance of methane catalytic cracking in a fluidized bed using 10%Ni/γAl_2O_3 and 10%Ni/αAl_2O_3 catalysts, and to optimize the operating conditions and the sizing of the reactor. To develop such a model, experimental and modeling steps were required. The experimental steps provided the model with all the required data including kinetic, physical, and chemical data. Some experiments, in particular experiments in a lab-scale fluidized bed were used to validate the model.

The experimental work consisted of three different stages. The first stage includes a kinetic study of methane cracking carried out in a thermo balance using 10%Ni/γAl_2O_3 (porous) and 10%Ni/αAl_2O_3 (nonporous) catalysts to develop a reaction rate, and to study the effect of alumina structure on the reaction. The rate of reaction is a function of temperature and partial pressures of methane and hydrogen. The temperature range used in the kinetic study is 500-650ºC. Different partial pressures of methane in the inlet gas were used, either as a mixture with hydrogen or as a mixture with nitrogen as an inert gas. Methane partial pressure was varied in a mixture with nitrogen to study the effect of varying P_{CH4} using the ratios 90/10, 70/30, and 50/50 CH_4/N_2. P_{CH4}/P_{H2} ratio was varied: 95/5, 90/10, 85/15, and 80/20. The flow rate was varied between 72-240 ml/min to investigate the presence of external diffusion limitations. The particle diameter effect was varied between 300-1000 μm to investigate the presence of internal diffusion limitations. The results showed that the nonporous catalyst performed better than the porous catalyst in terms of cracking during the first cycle. And the developed model showed excellent fitting for the experimental data and the estimated kinetic parameters agree with that reported in literature. The activation energy of methane cracking is estimated at 88 and 75 kJ/mol for the porous and non-porous catalysts, respectively.

Due to catalyst deactivation, the rate of the reaction at any time was divided into two quantities: the initial rate and the activity coefficient, which is a function of time, temperature, and methane and hydrogen partial pressures. The data required to formulate the initial rate expression were collected at the beginning of the reaction, when the rate reaches a maximum. At this stage there

is no effect of carbon deposition on the rate. By assigning the maximum reaction rate at the onset of reaction to a time value of zero, then the rate at subsequent times will be a fraction of the maximum rate, and the activity is determined as the ratio of the rate (at time t) to the initial reaction rate. The experiments in the thermo balance were continued until no weight change is observed, which indicates no further reaction is occurring and/or complete catalyst deactivation.

The second experimental stage included the investigation of the effect of regeneration using air on the catalyst activity. Regeneration at 550ºC gave a reasonable regeneration rate. Then, methane cracking/regeneration cycles were performed in the thermo balance using air as a regeneration gas at 550ºC, for 10%Ni/γAl_2O_3 and 10%Ni/αAl_2O_3. The performance of the porous catalyst became better than the nonporous beyond the first cycle. The porous catalyst kept its activity for 24 cracking/regeneration cycles, while the non-porous catalyst lost half of its activity by the second cracking cycle and almost all of its activity after six cycles. Formation of $NiAl_2O_4$ and sintering caused the nonporous catalyst activity loss. The results obtained from the cracking/regeneration cycles were used to extend the reaction rate developed from the first stage to predict catalyst performance at different cracking cycles. The kinetic model agreed well with the experimental data including initial rate and activity decay at different cycles.

After modeling the experimental results from the thermo balance in a kinetic model for methane cracking, the kinetic model was used to develop the fluidized bed model. Finally, the last experimental stage of the work was carried out in a lab-scale fluidized bed using Ni/γAl_2O_3, Ni/αAl_2O_3, and Ni/SiO_2. The objective of the fluidized bed experiments is to check the validity of the proposed methane catalytic cracking model by comparing the experimental data with model predictions. The data is used to tune the model for better predictive ability. Also silica was included as a support to study the effect of the support type on methane cracking performance. A two level factorial experimental design was developed and applied for each catalyst individually. Three factors were used in the experimental design: temperature (550-650ºC), P_{CH4}/P_{N2} (0.8/0.2-0.5/0.5 atm/atm), and particle diameter (108-275 μm). The effect of flow rate was investigated by using different flow rates: the flow rate corresponding to U_{mf} (the minimum fluidizing velocity) and the flow rate corresponding to 1.5 U_{mf}. Cracking/regeneration cycles were performed for each catalyst to assess the catalyst ability to be used in a continuous methane cracking process. Fixed bed experiments were carried out to check the effect of the reactor variation on catalyst performance.

In the fluidized bed experiments, methane conversion decreased in the following order: 10%Ni/SiO_2> 10%Ni/αAl_2O_3> 10%Ni/γAl_2O_3. From a factorial experimental design, the temperature was the dominating factor for the rate of hydrogen production, and the particle diameter was the dominating factor for total carbon deposited. Increasing the temperature and the particle size from 108 to 275 μm had a positive effect on methane conversion. Increasing the flow rate and P_{CH4} caused a drop in methane conversion. A higher conversion and faster deactivation with methane were observed in the fixed bed. The pressure build up inside the fixed bed stopped the reaction. During cracking/regeneration cycles in the fluidized bed, 10%Ni/SiO_2 was thermally stable but the mechanical attrition in the fluidized bed crushed the catalyst into smaller particles, although the catalyst maintained its activity. 10%Ni/αAl_2O_3 and 10%Ni/γAl_2O_3 were thermally unstable, due to sintering of the active sites after the first cycle leading to decreased methane conversion.

Finally, a bubbling fluidized bed model is developed. The model prediction showed good agreement with the experimental data from the fluidized bed study. The model was used to estimate the impact of different process parameters including reactor dimensions and process conditions e.g. temperature and catalyst circulation rate. The model can help in optimizing methane catalytic cracking process in a fluidized bed reactor.

Acknowledgements

I would like to express my sincere gratitude and appreciation to my supervisors, Professor Eric Croiset and Professor Bill Epling, who showed a great confidence in me and provided me with a great support from the preliminary to the concluding level, valuable ideas, guidance, and helpful advices. I really feel fortunate to learn from such great professors. I would like to thank the members of the chemical reaction group, Professor Bob Hudgins and Professor Peter L. Silveston, for their valuable advices throughout the project. I would like extend my appreciation and thanks to my supervisory committee members for their valuable comments:

Professor Jafar Soltan (University of Saskatchewan, Department of Chemical Engineering)

Professor Cécile Devaud (University of Waterloo, Department of Mechanical Engineering)

Professor Xianshe Feng (University of Waterloo, Department of Chemical Engineering)

Professor Ting Tsui (University of Waterloo, Department of Chemical Engineering)

Professor Aiping Yu, thanks a lot for your valuable help during my research. Professor Ting Tsui, thanks a lot for your help with the SEM imagining instrument. The Department of Chemical Engineering staff, in particular Lorna Kelly, Pat Anderson, Liz Bevan, Rose Guderian and Ingrid Sherrer, were all very helpful. Thank you for your time and patience. I would also like to thank Ralph Dickhout, the Department's Analytical Technician, for helping me with many technical issues especially the ICP analyzer. I would like to extend my thanks to Bert Habicher, the Department's Mechanical Systems Designer, for his great support and for helping me in the thermo balance and fluidized bed setup. I would like to thank Ravindra Singh, Rick Hecktus, Dennis Herman, and Ron Neill for their technical support throughout the duration of my research.

Colleagues and friends in the chemical reaction engineering group, Zuhair, Amran, Dr. Mook, Dr. Meshari, Osama, Aftab, Ali, Dr. Xuxian Hou (Peter), and Dr. Jinyong Luo (John) and many more; thanks a lot for your help, cheer up, and moral support. Co-op students, Jodi, Jostin, Sue Kim, Maxime-Alexandre Ferko, and Harminbar, I really appreciate your valuable assistance in

running the experiments. My friends in the department of chemical engineering and all CEGSA members, I enjoyed working with you in the CEGSA and 5 years of the best in my life.

My supervisors, instructors, and friends in Egypt in, ElMinia University, Cairo University, and the Department of Chemical Engineering in the national research centre, in Particular Professors Hammam El-Abd, Omar El-Farouk, Sanaa Abdel-Halim, Guzine El Diwani and Kamil El-Khatib; Thanks a lot for your support and great confidence in me. I would like to thank in particular the Ministry of Higher Education and Scientific Research for their sponsorship during my study and the Natural Sciences and Engineering Research Council of Canada for financial support. Also to all my friends in Egypt, particularly, Aymen Elqady, thanks a lot for your encouragement.

Finally, I would like to acknowledge my wife Rabab, my children Ahmed and Ream, my parents, my brother Ahmed, my sisters, Amani, Aiat, and Aalaa, and all my family, thanks a lot for your support, patience and sacrifice.

Dedication

To my beloved Parents,

To my beloved wife ….Rabab,

and my lovely children ….Ahmed…Ream,

To my brother and sisters

Table of Contents

List of Figures

List of Tables

Nomenclature

Nomenclature (Chapter 4):

a : Activity coefficient

A: Arrhenius constant

b: Order of hydrogen adsorption effect on a, atm^{-b}

$C_{C_{Ni,f}}$: Concentration of Carbon dissolved in nickel on the nickel/gas interface, mol_C/m^3_{Ni}

$C_{C_{Ni,r}}$: Concentration of Carbon dissolved in nickel on the nickel/Support interface, mol_C/m^3_{Ni}

$C_{C_{fil.}}$: Carbon deposited as carbon filaments

E: Activation energy, J/mol

h: Order of methane adsorption effect on activity, atm

I: Vacant site

k : Specific rate constant for methane cracking, $mmol_{CH4}/g_{Ni}/min/atm$

K_1 , K_2 , K_3 , K_4 , K_5 : The equilibrium constantans for step 1 though step 5.

K_C: The reciprocal of the equilibrium constant for step 7

K_{CH4}: The adsorption constant for methane, atm^{-1}

K_H: The reciprocal of the equilibrium constant for step 6,

K_{H2}: The adsorption constant of hydrogen, $atm^{3/2}$

K_P: Equilibrium constant for methane cracking, atm.

k_d : Specific rate constant for encapsulating carbon formation (deactivation)

$\mathrm{kd}_{\mathrm{H_2}}$: Specific rate constant for hydrogen adsorption effect on a

$\mathrm{kd}_{\mathrm{CH_4}}$: Specific rate constant for methane adsorption effect on a

n : Order of deactivation

P_{CH4}, P_{H2}: Methane and hydrogen partial pressures, atm.

$r_{\mathrm{exp.}}$: Methane cracking rate from experimental work.

$r_{calc.}$: Methane cracking rate calculated from the developed model.

RTD: Residence time distribution

t : Time, min

$X.I$: Active site occupied by intermediate X

θ_X : Fractional coverage of active sites with intermediate x

α : The fraction of active sites not deactivated

ΔH: Heat of adsorption J/mol

Nomenclature (Chapter 6):

A_R: Reactor sectional area, m
C_n: Outlet concentration of gas leaving stage n, mol/l
C_0: Initial gas concentration of reactant, mol/l
D_{AB}: Diffusion coefficient in m^2/s
D_B: Bed diameter, m

d_{bm}: The limiting size of bubble expected as very deep bed, m
d_{b0}: The initial bubble size formed near the bottom of the bed, m
d_P: Average particle diameter based on screen analysis, m
dz : Stage height, m
f_{CW}: Ratio of cloud-wake volume to bubble volume
g: Acceleration of gravity, 9.8 m^2/s
k_{bc}: Rate of gas diffusion from bubble to cloud-wake phase, s^{-1}
k_{ce}: Rate of gas diffusion from cloud-wake to emulsion phase, s^{-1}
L_b : Bed height at bubbling conditions, m
L_m : Bed height at fixed bed conditions, m
L_{mb} : Bed height at min. bubbling conditions, m
L_{mf} : Bed height at min. fluidization conditions, m
l_{or} : The spacing between adjacent holes, m
n : Total number of stages
n_d : The number of orifices per unit area, No/m^2
P_{CH4} : Methane partial pressure, atm
u_b: Velocity of gas in bubble phase, m/s
u_{bm}: Minimum bubbling velocity, m/s
u_{br}: bubble rise velocity with respect to emulsion phase, m/s
u_e: Velocity of gas in emulsion phase, m/s
U_{mf}: Minimum fluidization velocity, m/s
U_0: Inlet velocity of fluidization gas, m/s
$U_{s,down}$: The down flow velocity of emulsion solids, m/s
V_{or} : Volumetric flow rate through a single orifice
V: The volume of the fluidized bed, m^3
Z: Height above gas distributor

Greek letters:
ε_{mf} : Void fraction in a bed at minimum fluidizing condition

ε_m : Void fraction in a bed at fixed bed condition

ε_{mb} : Void fraction in a bed at minimum bubbling condition

ε_b : Volume fraction of bubbles in the bed

ϕ_S : Sphericity of catalyst particles, dimensionless factor

μ : Gas viscosity, kg/m.s

ψ : Shape factor

ρ_g, ρ_S : Gas density of gas and solid respectively, kg/m^3

η_d : No. of perforations

γ : The kinematic viscosity, m^2/s

γ_c, γ_e : Solid fraction in cloud-wake and emulsion phases respectively

Subscripts:

b: bubble phase

cw: Cloud-wake phase

e: emulsion phase

n: number of stage

Chapter 1
Introduction and Motivation

Hydrogen is mostly produced from fossil fuels, which are expected to continue to be a major hydrogen source in the medium to long term [1-3]. Presently, hydrogen is used as a chemical rather than a fuel in commercial applications, but if hydrogen is going to replace existing fuels, appropriate methods for large-scale production of CO-free hydrogen must be developed. The steadily growing interest in proton-exchange membrane (PEM) fuel cells as an alternative to internal combustion engines is forecasted to dramatically increase CO-free hydrogen demand [4, 5].

Now, production of hydrogen is primarily achieved via catalytic steam reforming, and partial oxidation of natural gas. Although these processes are mature technologies, they are somewhat complex and CO is formed as a by-product, which needs subsequent removal, because the Pt-based electrocatalyst used in a PEM fuel cell is sensitive to CO. More specifically, the CO concentration in hydrogen streams used as a fuel for PEM fuel cells must be lower than 20 ppm in order to prevent significant deactivation of the electrocatalyst [6], therefore requiring a complicated CO separation processes to achieve the required purity.

Supported metal catalysts can be used to catalytically decompose hydrocarbons to produce hydrogen as an alternative method to the traditional steam reforming technique. The process is known as catalytic cracking of hydrocarbons. Methane, the hydrocarbon containing the highest percentage of hydrogen, can be used to produce a hydrogen-rich stream. The decomposition of methane occurs on the surface of the active metal to produce hydrogen and filamentous carbon [7, 8].

As a result, only hydrogen is produced as a gaseous product, which eliminates the need of further separation processes to separate CO_2 or CO [6]. Furthermore, unlike the steam reforming process, catalytic cracking of methane does not include water gas shift and preferential oxidation of CO, which considerably simplifies the process and may reduce the hydrogen production cost. From process design calculations, methane catalytic cracking can be economically viable if the produced filamentous carbon is economically utilized [2, 3, 9].

The methane catalytic cracking process needs a highly active catalyst at moderate temperatures (500-600°C) to make this process economically viable. Since the kinetics of non-catalytic methane

cracking are too slow at temperatures lower than 1000ºC, a catalytic process is needed. Nickel has been demonstrated as a very active element for hydrocarbon cracking especially for the most stable hydrocarbon, methane, in the temperature range of 500-700ºC [2, 10, 11]. Cobalt and iron can also be used for methane cracking, but their carbon/active site capacities are much lower than nickel, with the additional problem of higher cost and toxicity for cobalt [12].

Metal catalysts are usually deposited on supports such as SiO_2 or Al_2O_3 and the performance of metal catalysts depends largely on the combination of, or interaction between, metal and support. This is attributed to the change of the structure or electronic state of metal species due to the interaction with the supports [13]. In addition to hydrogen, carbon is the other product of reaction during methane cracking. Ideally, this carbon participates in carbon filament growth. Unfortunately, carbon also deposits as encapsulating carbon which deactivates the catalyst. A regeneration step is thus necessary to regenerate the catalyst.

The major challenge in hydrogen production using catalytic cracking of methane is the regeneration of the spent catalyst; especially if methane cracking is to be used to produce hydrogen in a continuous process [1, 14]. Thus, catalyst regeneration is important for the recovery of the catalyst activity and the improvement of the overall process economics. The filamentous carbon formation mechanism, where the active nickel atom is found to be on the tip of filament [14, 15], maintains the catalytic activity of the supported catalyst for a long period; however, the catalyst will deactivate due to the formation of encapsulating carbon that blocks reactant access to nickel. For conducting methane cracking in a continuous process, circulation of the spent catalyst from the cracking step to a regeneration step is necessary.

A fluidized bed reactor appears as the most viable option for the methane catalytic cracking process [16]. Fluidized bed reactors have wide applications in many fields including chemical, metallurgical and petroleum industries. A fluidized bed system has the advantage of allowing continuous addition or removal of solids as the reaction proceeds. In a fluidized bed reactor, the bed of catalyst particles behaves as a continuously stirred tank reactor, which improves both heat and mass transfer [17]. Improving heat and mass transfer in the fluidized-bed reactor prevents radial and axial temperature gradients. The fluidized bed provides better utilization of the catalyst particles (no internal diffusion limitations) due to the ability of using small catalyst particles while maintaining small pressure drop.

Patented at 1966, the "HYPRO" process is the first industrial process for producing hydrogen by catalytic cracking of light hydrocarbons and natural gas using a fluidized bed [18]. The capital cost for the "HYPRO" process was somewhat lower than that of the steam reforming of methane. But the high operating and maintenance costs of the fluidized bed increased the price of the hydrogen produced from the "HYPRO" process compared to the conventional steam reforming and decreased the competitive attractiveness of the "HYPRO" process [7]. Nevertheless, the economics of the "HYPRO" process can be improved significantly by optimizing the overall operating conditions and by developing better catalysts. Developing a model for methane cracking is essential to study the feasibility of the process and the effect of any change in the operating conditions. By modelling methane catalytic cracking, the effect of various parameters (e.g. methane flow rate, concentration, pressure, residence time, reaction kinetics, hydrodynamics) on the overall system performance can be investigated.

The aims of this project were 1) to develop and characterize a suitable nickel-based catalyst and 2) to develop a model for thermal catalytic decomposition of methane in a fluidized bed. The proposed model can predict the performance of the methane catalytic cracking fluidized bed, and can help in optimizing the operating conditions and the sizing of the reactor. To develop such a model, experimental and modeling steps were required. The experimental steps were designed to provide the model with all required data including kinetics, physical and chemical data (e.g. particle size, density, activity). Some experiments, in particular the lab-scale fluidized bed experiments, were also used to validate some aspects of the model.

A kinetic study was conducted using a thermo balance to collect the data required for the model, using nickel supported on two different alumina supports (porous and nonporous). A comparison between the two catalysts was performed to study the effect of alumina structure on the catalyst performance. A series of cracking/regeneration cycles experiments were carried out on each catalyst to check the catalysts' ability to catalyze methane cracking in successive cracking/reaction cycles.

Reaction rate and activity terms were developed to predict the catalyst performance at different activity levels and in different cracking cycles. Experiments in an actual fluidized bed were also conducted to verify the model predictions and to extract measurements for some model parameters. The proposed model was implemented into MATLAB to predict the fluidized bed performance.

Specifically, the main steps of this project were:

- Prepare various nickel-based catalysts. The different catalysts differed depending on the support (alumina or silica, porous or non-porous).

- Conduct a kinetic study using a thermo balance to determine the reaction rate equations in terms of the partial pressures of reactant (methane) and gaseous product (hydrogen).

- Evaluate the deactivation rate as a function of catalyst time on stream.

- Carry out a regeneration study to evaluate the regeneration method for a spent catalyst.

- Develop mathematical models for the kinetics of methane cracking, including deactivation.

- Develop a fluidized bed mathematical model for methane catalytic cracking and catalyst regeneration.

- Carry out a set of experiments using a laboratory-scale fluidized bed reactor to evaluate the model prediction.

- Use the experimental data from the fluidized bed experiments to tune and verify the fluidized bed model (e.g. flow rate, concentration, bed diameter, and temperature).

The thesis is divided into seven chapters. The first chapter represents the introduction and motivation for this work. The second chapter is a comprehensive literature review for methane catalytic cracking for hydrogen production. This chapter has been published as a review paper in the International Journal of Hydrogen Energy (review paper). The third chapter presents an experimental parametric study on a thermo-balance to characterize methane cracking using nickel supported on porous or nonporous alumina.

The fourth chapter includes the development of the kinetic model and the activity term (to represent deactivation) for methane cracking. The fifth chapter describes and discusses the experimental

work in the lab-scale fluidized bed. The sixth chapter describes the fluidized bed model and shows a comparison between the model prediction and the experimental data in the fluidized bed. Finally, the seventh chapter includes the conclusions for the whole project and recommendations for further work.

Chapter 2
Literature Review*

2.1 Introduction and Overview

The majority of current energy needs is supplied by combustion of non-renewable energy sources, namely fossil fuels, and is associated with the release of large quantities of greenhouse gases (GHG), especially carbon dioxide (CO_2), and other harmful emissions to the atmosphere. The gradual depletion of these fossil fuel reserves, and efforts to combat pollution and greenhouse gas emissions, have generated considerable interest in using alternative sources of energy. Hydrogen gas may one day replace fossil fuels for various applications such as in automobiles and power stations [1]. However, hydrogen nowadays is mostly produced via fossil fuel reforming and fossil fuels are expected to remain a major hydrogen source in the long term [2]. Presently, hydrogen finds application as a chemical compound rather than a fuel in commercial operations, but if hydrogen is used to replace existing fuels, appropriate methods for large-scale production must be developed.

Hydrogen is the simplest element and the most plentiful gas in the universe. Yet, hydrogen never occurs by itself in nature; it is found combined with other elements such as oxygen and carbon, i.e. water or hydrocarbons, so these substances must be decomposed/reformed to get H_2 [3]. To release hydrogen, heat can be applied to hydrocarbons and water to break down the molecules (thermo-chemical), and electric charging (electrolysis) or a photolytic process can be used to decompose water. Some separation processes combine heat and electricity (steam electrolysis). Bacteria and algae can also be used to produce H_2 from biomass.

Currently, the main process for producing hydrogen is steam reforming of natural gas [1]. Steam reforming is a multiple stage process. The first stage is the highly endothermic catalytic reforming of methane ($\Delta H°_{298}$ = 206 kJ/mol CH_4) conducted at high temperature (800–900°C), while the second stage is the catalytic water gas shift (WGS) reaction, occurring in two steps: the first stage is conducted at (400–500°C) to reduce the carbon monoxide (CO) concentration to 2-5%, and the second stage is conducted at (177–257°C) to reduce CO to 1%. The third stage is the separation of the H_2–CO_2 mixture using pressure-swing adsorption (PSA) [4-6].

* Reprinted from [103] with permission from the International Journal of Hydrogen Energy

This process needs other auxiliary steps, such as a desulphurization unit and a steam generation section. In addition to steam reforming, partial oxidation is also used to generate hydrogen from fossil fuels [7], but the produced hydrogen is still mixed with CO and CO_2, which again needs a complicated separation process as in the steam reforming case.

Increasing demand for CO-free hydrogen has increased interest in the direct catalytic cracking of natural gas [8-9], described by Equation 2.1. The two reaction products are hydrogen and carbon, the latter being essentially in the form of filamentous carbon or carbon nanotubes [10].

$$CH_4 \leftrightarrow C_s + 2H_2 \qquad \Delta H°_{25°C} = 74.8 \text{ kJ/mol} \qquad (2.1)$$

As a result of methane cracking, only hydrogen is produced as a gaseous product in a mixture with unreacted methane. Separation of methane and hydrogen can be achieved easily by absorption or membrane separation to produce a stream of 99% by volume hydrogen, which is much simpler than the need for further complicated separation processes that deal with CO_2 or CO [2,7]. This would be particularly important in the case of proton-exchange membrane (PEM) fuel cell applications, since the Pt-based electrocatalyst is poisoned by CO [11]. More specifically, the CO concentration in hydrogen streams used as fuel for PEM fuel cells must be lower than 20 ppm in order to prevent significant deactivation [5]. The carbon nanotubes produced as a solid product are a commercially valuable material; they are useful in many applications, especially in adsorption processes and catalysis or to store as an option for reducing carbon emissions [2,12].

Unlike the steam reforming process, the catalytic decomposition of methane (CDM) does not include water gas shift and preferential oxidation of CO, which considerably simplifies the process and may reduce the hydrogen production costs [2,13]. The energy required for methane catalytic cracking is nearly one half that required for steam reforming per mole of methane decomposed (for steam reforming $\Delta H°_{298}$ = +253.2 kJ/mol, for methane cracking $\Delta H°_{298}$ = +74.8 kJ/mol) [2,9,14-15]. Per mole of hydrogen produced, the energy requirement is 37.4 kJ/mol H_2 in methane catalytic cracking compared to 63.3 kJ/mol H_2 in the steam reforming process [15]. In addition to the lower energy demand for methane catalytic cracking compared to steam reforming, there is no need for additional energy for steam generation or gas treatment. The heat

requirement for catalytic cracking can be covered by burning ~15-20% of the hydrogen produced, which further reduces CO_2 emissions [16].

Thermal methane cracking is not feasible at moderate temperatures. To achieve a reasonable yield, a temperature higher than 1200°C is required [3,17]. Supported metal catalysts can be used to catalytically decompose hydrocarbons to produce hydrogen at more moderate temperatures. Nickel is particularly active for hydrocarbon cracking, especially for methane [18]. Cobalt and iron can also be used to catalyze methane cracking but their carbon/active site capacities are much lower than that of nickel, with additional problems in the case of cobalt, which are associated with its higher cost and toxicity [19]. Metal catalysts are usually deposited on supports such as SiO_2 or Al_2O_3 and the performance of the catalyst depends to some extent on the combination of metal and support [20].

Early methane cracking was done in fire-brick furnaces at 1500ºC to produce soot [2]. In 1966, the HYPRO process was introduced and was the first commercial process for the catalytic cracking of methane and gaseous hydrocarbons for hydrogen production [21]. The HYPRO process was based on a circulating fluidized bed, operating at temperatures up to 980°C and at atmospheric pressure. The carbon produced during the cracking step was burned in a regenerator to supply the process energy requirements and to regenerate the catalyst [2]. The HYPRO process could convert a dry gas mixture of methane and light hydrocarbons to 90% hydrogen with 10% unconverted methane, using a 7% Ni/Al_2O_3 catalyst. The capital cost of this process was lower than the steam reforming process [2,21]. However, the operating cost of the process was high, partially due to the circulation of catalyst between the two fluidized beds, which required a certain pressure drop be maintained between the different reactors [22]. More recent economic studies of the methane cracking process indicate that the viability of the process depends in a large part on the selling price of the filamentous carbon [23].

The major challenge in a continuous process for hydrogen production using methane catalytic cracking is the regeneration of the spent catalyst [24], which is also critical in the overall economics of the process. During filamentous carbon formation in methane catalytic cracking the active nickel atom is found on the tip of the filament [18,25], as shown in Figure 2.1. Being located on the tip, the catalytic activity of the supported catalyst can be maintained for an extended period of time. However, the catalyst deactivates due to the formation of encapsulating

carbon that ultimately blocks access to the nickel. Steam gasification or air oxidation can be used to regenerate the deactivated catalyst [26].

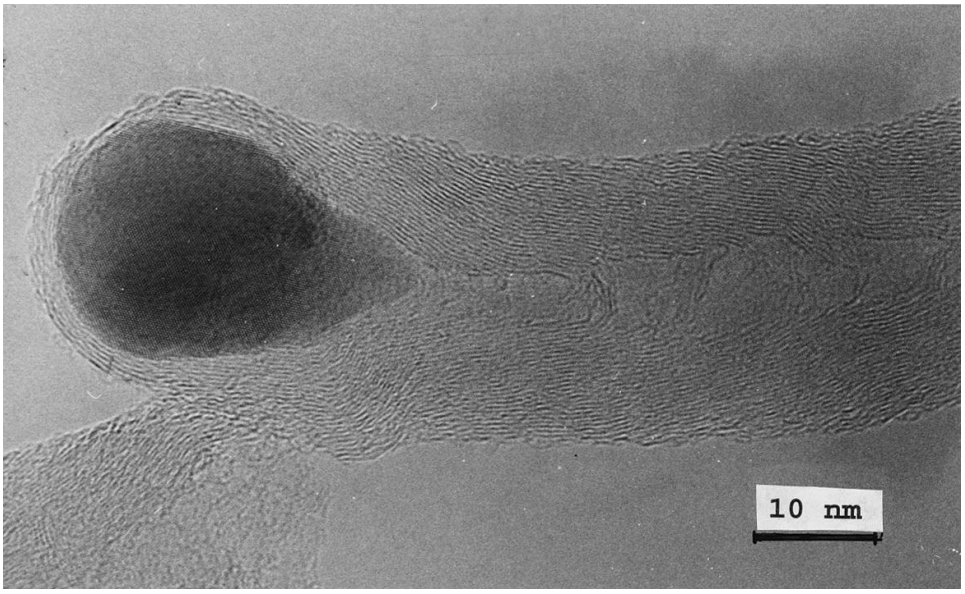

Figure 2.1- Metal particle on the tip of a carbon filament (Reprinted from [18], with permission from Elsevier)

Different reactors for continuous methane cracking have been proposed, such as a set of parallel fixed-bed reactors alternating between different conditions or a fluidized bed/regenerator combination [27]. In either system, the ability of the catalyst to accumulate significant amounts of filamentous carbon prior to its deactivation allows for substantial catalyst time-on-stream or residence times in the reactor or reaction zone. For fluidized bed systems, regeneration of the catalyst requires continuous catalyst circulation between the cracker and regenerator sections. Another advantage, coincident with this continuous operation, is that a fluidized bed system allows continuous addition or removal of solids as the reaction proceeds. Furthermore, in a fluidized bed reactor the bed of catalyst particles behaves as a continuously stirred tank reactor, which improves heat and mass transfer [27], preventing radial and axial temperature gradients and providing better utilization of the catalyst particles, due to the high external mass transfer rates. Also, small catalyst particles can be used while maintaining small pressure drop.

This review will discuss different aspects related to methane catalytic cracking, subdivided into three parts; the first part discusses the fundamentals of the thermodynamics, catalyst development, carbon filaments formation, and catalyst deactivation associated with methane catalytic cracking. The second part includes different methods used for catalyst

regeneration, and reaction mechanism and reaction rate models. The last part discusses the engineering of the process, focusing on application of fluidized bed reactors, and scale up from laboratory to industrial scale.

2.2 Thermodynamics of Methane Cracking

The equilibrium constant for the methane catalytic cracking reaction is usually expressed only in terms of the partial pressures of CH_4 and H_2 [28-30], and assumes that the activity of carbon on the catalyst is unity, as shown in Equation 2.2:

$$K_P = \left(p_{H_2}^2\right)_{eq} / \left(p_{CH_4}\right)_{eq} \tag{2.2}$$

However, carbon has been shown to affect equilibrium and its activity seems to be inhomogeneous over nickel. This is due to the super-saturation required for carbon filament formation, which further requires different carbon activities at the gas/metal and metal/support interfaces [31-33]. The equilibrium constant for the overall reaction, assuming carbon forming a solution in the active metal (e.g. Ni), $K_{CH4/H2}^{sol}$, is related to the partial pressure of methane and hydrogen as follows [33]:

$$K_{CH4/H2}^{sol} = \frac{\left(p_{H_2}^2\right)_{eq} c_{CH4/H2}^{sol}}{\left(p_{CH_4}\right)_{eq}} \tag{2.3}$$

Where $c_{CH4/H2}^{sol}$ is the solubility of carbon in the active metal (e.g. Ni) in contact with the hydrogen/methane mixture (units of mol C/volume of active metal particle).

Equilibrium methane conversion, as well as the number of moles of CH_4, H_2 and C (for an initial 100 moles of CH_4) as a function of temperature is shown in Figure 2.2. Equilibrium conversion increases with increasing temperature, starting from ~30% conversion at 500ºC to almost complete conversion at 1000ºC.

The value of the equilibrium constant can be predicted from Gibbs free energy equations and temperature dependent equations are available in the literature, all of which consider carbon as graphite [13-34]. For example, Villacampa et al. [13] proposed the following correlation for the Gibbs free energy:

$$\Delta G°(J/mol) = 89658.88 - 102.27T - 0.00428T^2 - 2499358.99/T \quad (2.4)$$

Ginsburg et al. [34] developed another equation for calculating the Gibbs free energy for methane cracking:

$$\Delta G°(J/mol) = 58886.7 + 270.55T + 0.0311T^2 - 3*10^{-6}T^3 + 291405.7/T - 54.598T\ln(T) \quad (2.5)$$

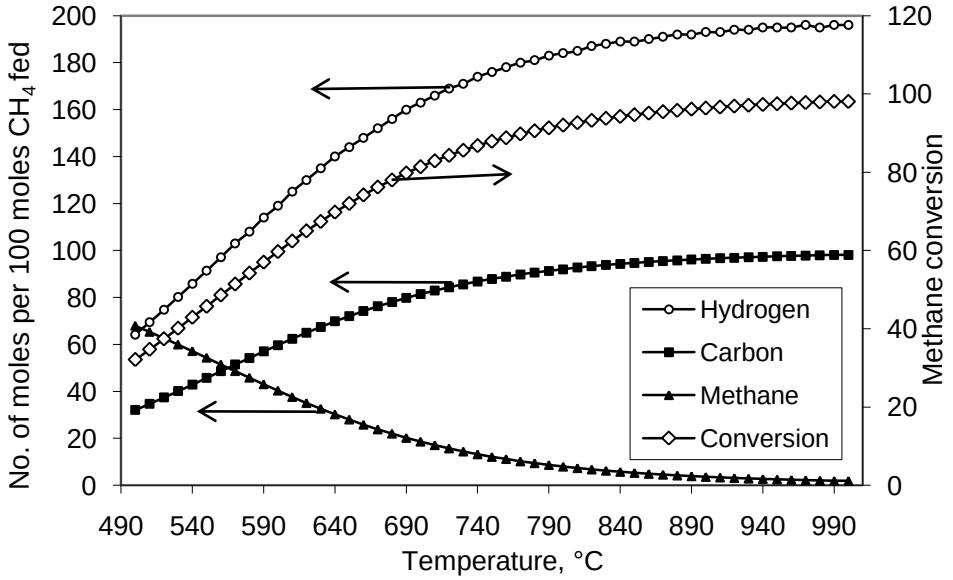

Figure 2.2 - Equilibrium composition and conversion as a function of temperature. The figure shows the equilibrium number of moles based on an initial 100 moles of CH_4.

Both Equations 2.4 and 2.5 lead to a zero $\Delta G°$ at 547°C, indicating that, thermodynamically, methane decomposes to form carbon and hydrogen at temperatures above 547ºC. However, methane cracking has been reported in the literature at temperatures as low as 500°C [24]. This shows that calculating the Gibbs free energy using graphite may not be adequate. Indeed, the carbon nanotubes produced during methane cracking have chemical and thermodynamic properties different from those of graphite [25].

Rostrup-Nielsen [28] studied the deposition of carbon on various nickel catalysts during methane cracking and found a deviation from the equilibrium data when assuming that carbon is deposited as graphite. They attributed the deviation, between the experimental data and the equilibrium calculation taking into consideration graphite, to the surface disorder of the formed

carbon structure and the higher surface energy of the carbon filaments. The authors proposed an equation to calculate the difference in the Gibbs free energy, ΔG_C, between $\Delta G°$ (Gibbs free energy for methane cracking calculated by assuming that carbon produced is deposited as graphite, from Equations 2.4 or 2.5) and $\Delta G_{Observed}$ (actual Gibbs free energy for methane cracking):

$$\Delta G_C = \Delta G_{Observed} - \Delta G^{\circ} \tag{2.6}$$

$$\Delta G_C = -RT \ln\left(\frac{K_{P-observed}}{K_{P-Graphite}}\right) \tag{2.7}$$

Rostrup-Nielsen [28] found that the value of ΔG_C decreased with increasing temperature and nickel loading. For 25% Ni/MgO, ΔG_C dropped from 1.88 kcal/mol at 400ºC to 0.8 kcal/mol at 600ºC. At 500ºC, ΔG_C increased from 0.56 kcal/mol for 25% Ni to 2.17 kcal/mol for 14% Ni.

De Bokx et al. [35] also studied the thermodynamics of methane cracking and found a deviation between the calculated data and the equilibrium data assuming graphite formation for nickel and iron catalysts. Even by taking into account the structural disorders and the contribution of the surface energy of the high surface area filaments [28]; the deviation between the actual data and the data calculated based on graphite formation is still considerable [35]. Also, Snoeck et al. [25] have differentiated between the enthalpy and the entropy change calculation based on the experimental results and those calculated using graphite and nickel carbide as a final product. They noticed that even the morphology of the carbon filaments produced from methane cracking is different from graphite and nickel carbide.

Yang and Chen [32] performed solubility measurements of carbon in nickel in contact with a mixture of methane and hydrogen and confirmed that the solubility of carbon in nickel at the support side of the nickel particle was determined by the thermodynamic properties of carbon filaments and that the solubility of carbon at the gas/metal interface is determined by the properties of the gas phase components (i.e. CH_4 and H_2) and the Henry's law constant of the solution of carbon in nickel. They also reported that the carbon content at saturation was 35% higher than that of a mixture in equilibrium with graphite.

Since the chemical potential of carbon is not constant throughout the nickel particle [33], the carbon activity cannot be constant and thus cannot be equal to 1. So, instead of using K_P to represent the equilibrium conditions for the reaction (e.g. like in Equation 2.2 where the carbon activity was assumed equal to 1), a coking threshold, K_M^*, has been defined and determined by measuring the reaction quotient, $K_M = p_{H_2}^2 / p_{CH_4}$, where neither carbon deposition nor gasification occurs, in other words when the overall rate of methane cracking is zero [25]. Therefore, when $K_M > K_M^*$ no cracking will take place. Since K_M^* is measured at zero carbon deposition/gasification, it can be assumed that, at this particular condition, the carbon chemical potential and the solubility of carbon in nickel are uniform throughout the nickel particle. If the carbon deposited was only graphitic carbon, K_M^* would be equal to the K_p described above. Snoeck et al. [25] came up with mathematical formulas to predict the value of K_M^* at different methane partial pressures and temperatures based on experimental observations (see Equations 2.8-2.12). For comparison, they also gave the expressions for the equilibrium constants in the case of graphite (Equation 2.11) and nickel carbide (Equation 2.12).

At $P_{CH_4} = 1.5\,\text{bar}$ $K_M^* = \exp(116.1/R).\exp(-100765/R/T)$ (2.8)

At $P_{CH_4} = 5\,\text{bar}$ $K_M^* = \exp(156.1/R).\exp(-134230/R/T)$ (2.9)

At $P_{CH_4} = 10\,\text{bar}$ $K_M^* = \exp(164.7/R).\exp(-141900/R/T)$ (2.10)

Graphite $K_M^{gr} = \exp(104.8/R).\exp(-84400/R/T)$ (2.11)

Nickel carbide $K_M^{Ni_3C} = \exp(121.3/R).\exp(-124600/R/T)$ (2.12)

Figure 2.3 shows the experimental values for K_M^* at different methane partial pressures and temperatures, as well as the values of K_M^* for graphite and nickel carbide at different temperatures. This figure shows a remarkable difference of K_M^* between graphite and nickel carbide but also shows that the values of K_M^* for graphite and the experimental values at 1.5 bar are very close.

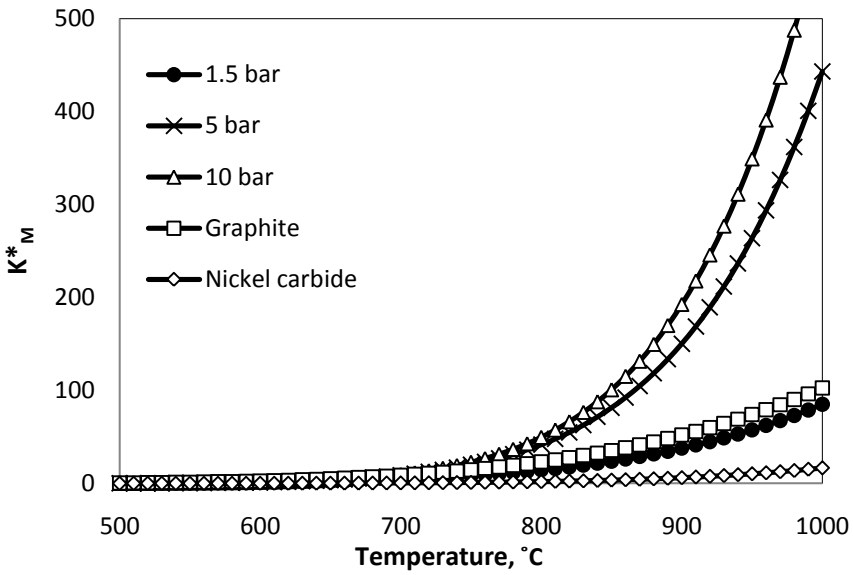

Figure 2.3 - K_M^* versus temperature at different methane partial pressures and K_M^* for graphite and nickel carbide. Based on Equations 2.8-2.12 [25].

Snoeck et al. [25] postulated that for $K_M < K_M^*$, either encapsulating carbon species or carbon filaments are produced. Zhang and Smith [36] determined another threshold value, K_M^f, at which only carbon filaments are formed. They proposed a criterion for stable cracking activity, based on the value of K_M relative to the two thresholds, K_M^* and K_M^f. If K_M^f is between K_M and K_M^* ($K_M < K_M^f < K_M^*$) the cracking activity will be unstable due to the formation of encapsulating carbon. However, if K_M is between K_M^f and K_M^* ($K_M^f < K_M < K_M^*$), cracking activity will be stable.

2.3 Catalysts for Catalytic Methane Cracking

Most studies considered nickel, iron or activated carbon with a few papers reporting other active metals, such as cobalt. The support has also been shown to have an effect on the cracking conversion/deactivation. Therefore, this section will be divided into two parts: active phase and support.

2.3.1 Active phase

This section discusses different catalysts used for methane catalytic cracking and the different factors affecting catalyst activity. The catalyst function is to reduce the activation energy required for methane decomposition, leading to lower operating temperatures. Non-catalytic methane cracking is very slow for practical application at temperatures below 1000°C, while catalytic cracking of methane can be conducted at temperatures as low as 500°C [19]. For example, for a highly active catalyst such as Ni/γ-Al_2O_3, optimal performance has been reported in the 500–550°C temperature range [37].

Iron group metals are known to have the highest activity for hydrocarbon cracking. In the case of methane, which has the highest stability in comparison to other hydrocarbons [9], nickel has been described as the most active catalyst for methane cracking among the iron group metals. Cobalt could potentially be used as a catalyst for methane cracking, but it is less active, has toxicity issues, and higher cost compared to nickel. Iron has also been studied as a catalyst for methane catalytic cracking but it showed lower activity compared to nickel [19]. Direct comparison shows that the methane cracking catalytic activity for the iron group metals is: Ni > Co > Fe [38].

Operating conditions, such as temperature, electronic state and dispersion, affect nickel's stability and activity for methane cracking [20,39]. Optimum operation has been observed in the 500–552°C temperature range [19], and in a separate study, a maximum in methane conversion was observed at 552°C [35]. The maximum conversion being attained at 552°C is due to equilibrium being achieved between the carbon deposited on the nickel and the surface migration and diffusion of carbon through nickel. At temperatures higher than 552°C, carbon is formed at a rate higher than bulk diffusion and surface migration causing an excess of carbon to deposit as encapsulating carbon [19,37]. At temperatures below 500°C, carbon is formed at a rate lower than the carbon solubility in nickel, thus reducing the driving force for carbon diffusion in the metal. The consequence is that less carbon is formed before the catalyst deactivates [37].

Nickel-based catalyst performance is not just a function of reactor operating conditions; it is also a function of nickel electronic state and dispersion. For example, Echegoyen et al. [20] studied the role of copper on nickel dispersion by adding 3% copper nitrate to a nickel/alumina catalyst during catalyst preparation; the results showed an enhanced hydrogen yield and better catalyst stability when copper was used as a promoter. Also Figueiredo et al [26] studied a La_2O_3-

doped Ni–Cu Raney-type catalyst. The catalyst showed better stability compared to a La_2O_3-doped Ni Raney-type catalyst. Figueiredo et al [26] attributed the improved stability to an electronic promotion effect. The improved performance with copper addition was attributed to the strong influence of copper on the dispersion of the nickel by inhibiting the formation of nickel aluminate, which increased the metallic nickel phase available for reaction and the nickel surface area subject to reaction. Gac et al. [40] reported that addition of magnesia to a methane cracking catalyst increased the initial cracking rate. The authors attributed the initial rate increase to the formation of smaller nickel crystals and stronger adsorption sites when magnesium was present.

The catalyst activity is not a linear function of the nickel amount in the catalyst/support matrix. Venugopal et al. [41] conducted an experimental study in a fixed bed reactor using a Ni/SiO_2 catalyst with nickel loadings in the 5 to 90% range. The results revealed that increasing nickel loading has a positive effect on methane conversion and catalyst stability until 30% is reached, and there a maximum in conversion was achieved. Increasing the nickel percentage beyond 30% resulted in poorer methane conversion and catalyst stability, as shown in Figure 2.4.

Due to fast deactivation observed with nickel-based catalysts at higher temperature (~600°C) [42], different catalysts have been tested either as a mixture with nickel, like copper and iron [20-42], or separately, for example iron [43], copper [44], and activated carbon [2,27,45]. Chesnokov and Chichkan [42] developed a 70%Ni-10%Cu-10%Fe/Al_2O_3 catalyst for methane cracking, where the addition of iron increased the optimal operating temperature range from 600-675°C for $Ni/Cu/Al_2O_3$ to 700-750°C while maintaining good catalyst stability. Jang and Cha [43] used an iron supported on alumina catalyst. The performance of the iron catalyst was greatly affected by the reaction temperature; at temperatures below 750°C, the catalyst rapidly deactivated, but at higher temperatures, the catalyst retained a reasonably stable activity for at least 100 minutes. At 1000°C, Jang and Cha [43], using a fluidized bed, reported an increase in activity over time with an iron catalyst; over 100 minutes the methane conversion continuously increased, reaching 90%, but no data were presented past 100 minutes. Ammendola et al. [44] have used a copper supported on alumina catalyst for methane cracking and were able to achieve, in a fluidized bed, 90% methane conversion for 90 minutes, but for very diluted methane conditions (i.e. 5%). Iron oxide has been studied as an alternative, but the results showed no appreciable conversion below 800°C [2].

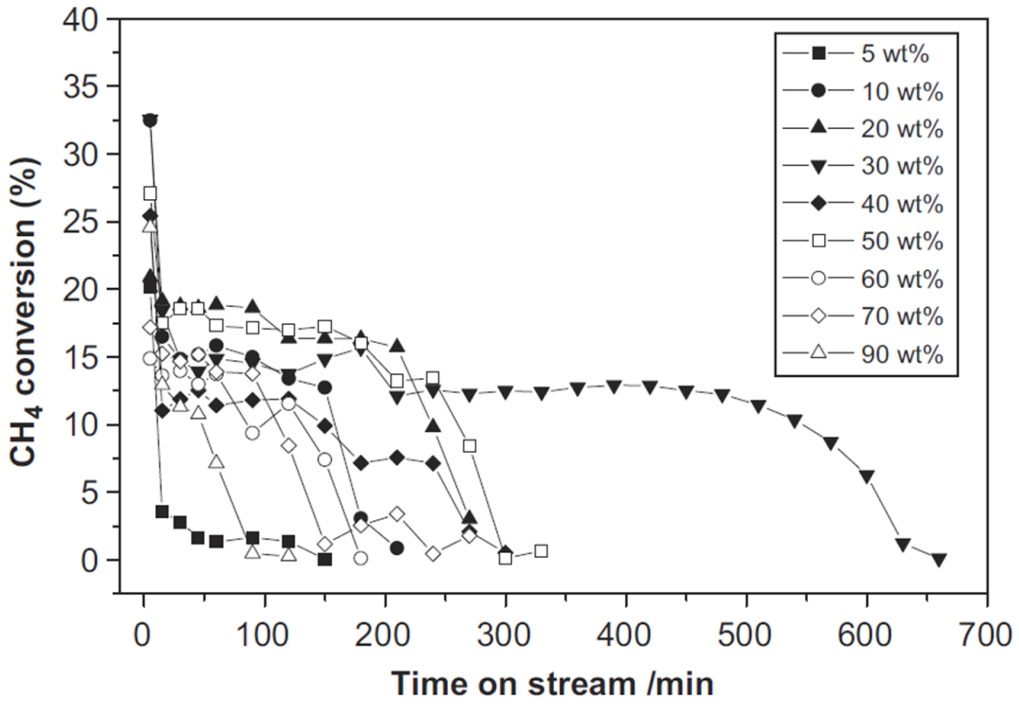

Figure 2.4 - Methane conversion over various Ni/SiO_2 catalysts at 600°C (Reprinted from [41], with permission from the International Journal of Hydrogen Energy)

Activated carbon has also been tested as a catalyst for methane cracking in fluidized and fixed bed reactors. In both reactors, activated carbon showed similar behaviour, with an initially high catalytic activity, but then rapid deactivation due to carbon deposition. The deposited carbon was shown to block access to active sites [2,27]. Suelves et al. [45] used carbon black and activated carbon as catalysts for methane catalytic cracking and reported better performance with carbon black, while the activated carbon suffered from rapid deactivation. The authors found that pore distribution and the surface chemistry played an important role in the instantaneous rate and catalyst life time before deactivation.

The catalyst pre-treatment method is another important factor for performance, primarily affecting the percentage of the metallic catalyst that will be active during the reaction. After the catalyst is prepared using impregnation, co-precipitation or any other preparation techniques, the catalyst needs to be activated (nickel metal is the oxidation state required) prior to reaction. The pre-treatment includes calcination and reduction. The calcination step helps in removing any residual precursor species and to change the precursor material to metal oxide. The reduction step is required after calcination to transform metal oxide to the active metal phase. The temperature

and the duration of the calcination and reduction steps influence how much catalyst is activated. Calcination or reduction above the optimum temperature also affects the catalyst texture and may cause sintering, whereas using temperatures lower than the optimum temperature may not activate the catalyst completely. For methane catalytic cracking, Echegoyen et al. [20] studied the effect of calcination temperature on nickel activity during reaction and found that 600°C resulted in the highest yield for the catalyst tested. Li et al. [46] reported that nickel supported on γ-alumina was reduced easily between 500-920ºC, but the lower the reduction temperature, the better the ultimate catalyst activity [10].

2.3.2 Support material

Methane conversion is a function of the catalyst matrix, i.e. including the active material and the support [40-41]. Echegoyen et al. [20] found that minimal interaction between the active component and the support is important for increased conversion. The support material also directly affects methane conversion by affecting the surface area of metal subjected to the reaction and the metal's electronic state. For example, the effect of magnesia and silica as supports for nickel were compared [19]. The authors attributed the lower methane conversion using magnesia to the formation of a solid solution between Ni and magnesium, while the higher methane conversion achieved using silica is attributed to the instability of nickel silicates, which may form, and their tendency to decompose at higher temperatures during the reduction step. In another study, Ermakova and Ermakov [9] compared Ni/SiO_2 and Fe/SiO_2 using different catalyst preparation methods and operating conditions. For nickel, the maximum yield (384 g C/g Ni) was achieved when the catalyst was silicate free; if 1.5-2 % of the nickel was transformed into nickel silicate the yield dropped to 40 g C/g Ni. For Fe, the addition of silica resulted in inhibition or promotion of methane conversion depending on the amount of silicate in the catalyst formed during the pretreatment. Takenaka et al. [47] used X-ray diffraction to characterize nickel on different supports (SiO_2, TiO_2, graphite, Al_2O_3, MgO and $SiO_2 \cdot MgO$). All catalysts were calcined in air at 600°C for 5 hours, and reduced with hydrogen at 550°C for 1 hour. They found that, for equivalent surface area, the lower the interaction between nickel and the support, the higher the methane conversion. Finally, under their test conditions, they showed that silica and titania supports resulted in the highest methane conversions, as shown in Figure 2.5.

The support structure and textural properties (e.g. porosity) also affect methane conversion. Ermakova et al. [19] studied the catalytic performance of nickel promoted with

different supports, including silica, magnesia, alumina, and zirconium oxide. The results indicated that the catalytic activity and lifetime of the catalyst depend significantly on the pore structure of the catalyst; they reported that nickel promoted with silica (i.e. with silica as a promoter, not support) that has wide pores gave the highest methane conversion and longest lifetime.

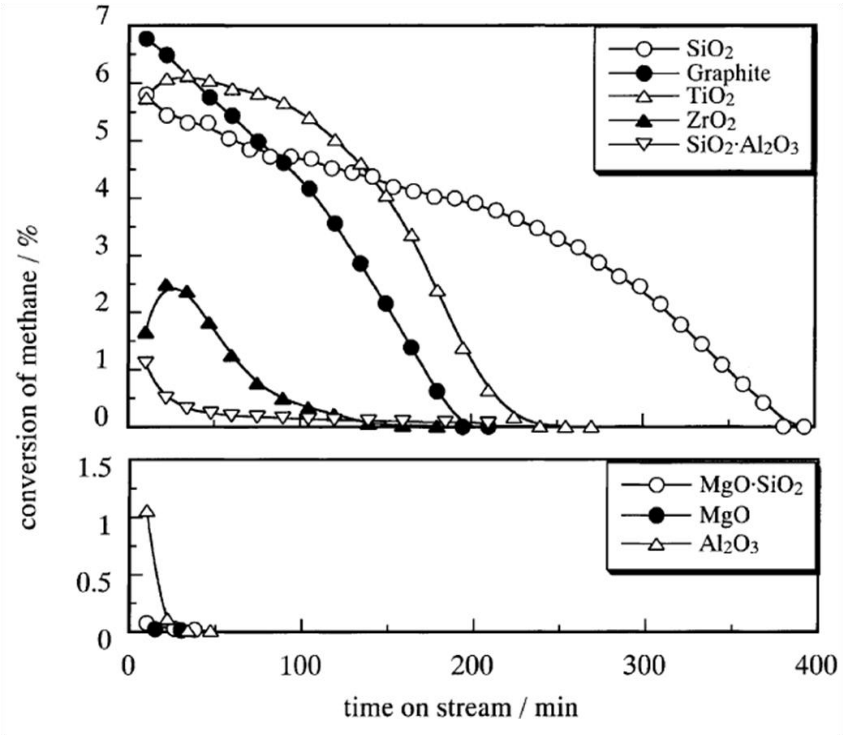

Figure 2.5 - Methane conversion over Ni catalysts supported on different supports at 500ºC (Reprinted from [47], with permission from Elsevier)

The support structure may also affect the outlet gas composition and the morphology of the deposited carbon. For example, higher oxygen capacity supports like ceria, are not favorable unless the catalyst is prepared in such a way that the surface oxygen is immobilized to prevent it from reacting with deposited carbon, and forming carbon monoxide [48].

2.4 Description of Carbon Filament Formation and Growth

2.4.1 Overview of the process for carbon formation

There are three types of coke that form during methane cracking on supported metal catalysts, namely polymeric, filamentous, and graphitic carbon. Polymeric coke is produced during thermal decomposition of hydrocarbons, while the filamentous and graphitic carbons are formed during catalytic cracking of hydrocarbons [34,49]; the classification here is related to the

reaction conditions [49]. Coke can also be characterized based on its reactivity with hydrogen, water, and oxygen [49]. The formation of coke on nickel is a multistage process. The process starts with methane adsorption followed by several dehydrogenation reactions and ends with coke formation, as shown in Figure 2.6. After methane is adsorbed on the fresh nickel catalyst and the hydrogen is released, the remaining deposited carbon dissolves in nickel forming a layer of uniform concentration solution of carbon in nickel at the gas side; the carbon concentration is equivalent to the gas-phase solubility of carbon in nickel. Then carbon diffuses through the nickel particle to the support side until the carbon solution of nickel is supersaturated with respect to the filamentous carbon; at that time, nucleation of filamentous carbon begins [32-33,50-51]. With carbon filament growth, encapsulating carbon forms, which slows the cracking rate and ultimately deactivates the catalyst.

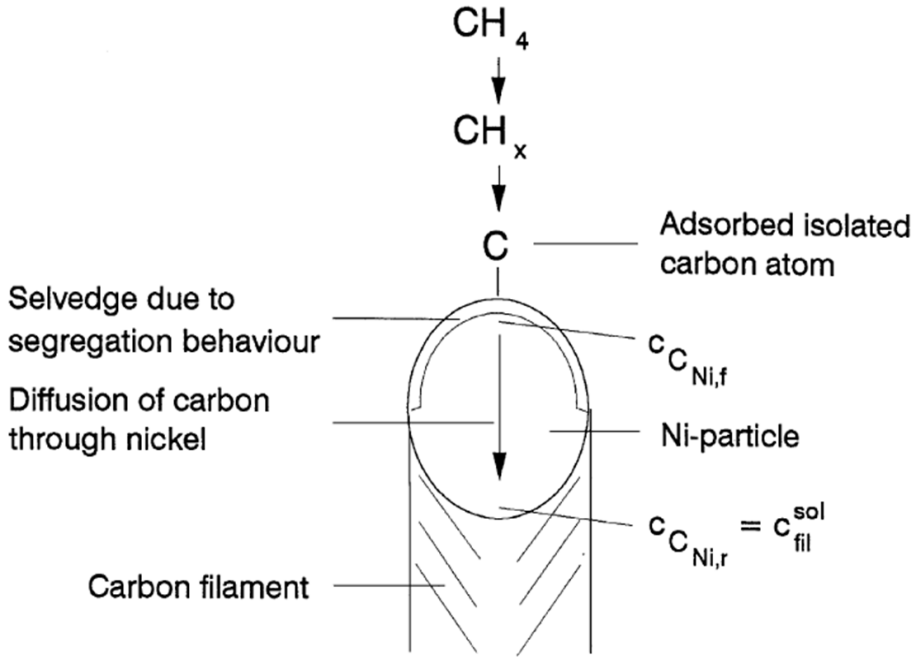

Figure 2.6 - Schematic of the classical mechanism of carbon filament formation (Reprinted from [25], with permission from Elsevier)

The driving force for filament formation is the temperature gradient [32,51] and/or the concentration gradient due to the difference in solubility of carbon at the gas/metal interface and that at the metal/support interface [29,31,52]. It can be seen from Figure 2.6 that at the gas/metal interface, carbon is in the form of a solute dissolved in nickel as a solvent, forming an unstable intermediate of surface nickel-carbide or "selvedge", which is super-saturated with carbon at high

temperature and the carbon concentration and temperature are decreasing in the direction of metal/support interface.

2.4.2 Nucleation

Since most studies were conducted with nickel as the active metal, the nucleation discussion presented will be primarily relevant to nickel, although most of the processes describe here could be also applied to other metals.

The first stage of filament growth is nucleation. During this stage nickel possesses liquid properties and the nucleation is due to 1) high carbon coverage on the Ni surface, 2) subsequent high concentration of carbon dissolved in the nickel particle and 3) carbon segregation behaviour.

The surface coverage of carbon at the gas side is increased to high levels and, as a result, the net rate of surface reactions is reduced, even though the gas mixture may have a composition that thermodynamically favours carbon formation. Then, the carbon dissolves in the nickel particle, diffuses through it, and precipitates at the metal/support interface [51-52]. According to Kock et al. [52], a key step prior to nucleation is the formation of nickel carbide. They proposed the following nucleation mechanism in the case of methane cracking over a 50 wt% Ni/SiO_2 catalyst:

1. Carburization to form nickel carbide
2. Carbide decomposition
3. Nucleation of graphite
4. Precipitation of graphite layer at the nickel/support interface
5. Detachment of the nickel particle from the support.

The detachment is responsible for the appearance of the carbon filament. Solid or hollow filaments of various diameters are formed depending on operating conditions, in particular the temperature [33]. At low temperatures, diffusion through the metal particle is slower than the nucleation/precipitation rates and thus nucleation occurs more uniformly at the metal/support interface. As a consequence, the detachment step leads to a non-hollow solid filament. In addition the nickel particle retains most of its original shape. On the other hand, at higher temperatures, distortion of the nickel particle has been observed [33, 53-54] when the nucleation rate becomes

greater than the diffusion rate. In this case, nucleation/precipitation occurs close to the metal/gas interface, thus creating a hollow filament. The hollow feature is due to the uplifting of the particle where no precipitation occurred. At these particular locations, because nickel/support binding forces must be overcome, a deformation of the particle occurs forming a "pear"-shaped particle [33]. Schematics of the detachment with formation of solid and hollow carbon filaments, along with particle deformation, are shown in Figures 2.7a and 2.7b, respectively [33]. Other shapes have also been proposed, such as a conical shape [53].

Boellaard et al. [53] investigated the microstructure of the carbon filaments and mentioned that the coke layers resemble fish-bone-like structures, which were also discussed by Gac et al. [40], and proposed a filament growth mechanism where carbon species are excreted from the metal particle perpendicular to the metal/filament interface and deposited upon one another in a conical form, as shown in Figure 2.8a. However, this mechanism assumed that the perimeter of the cone increases and eventually leads to the filament bursting, which is not consistent with the assumption that the diameter of the filament remains constant over very long distances. In order to overcome this problem they added the concept of slippage in another mechanism they proposed, where the excreted coke layers push metal particles upward along the direction of the filament axis, so that the filament diameter remains constant as shown in Figure 2.8b.

Temperature also has an effect on the filament diameter, where for temperatures between 500 and 650°C for a Ni/Al_2O_3 catalyst, the filament diameter decreases with increasing temperature [24], as shown in Figure 2.9. It was postulated that the change in nucleation rate and particle deformation at various temperatures may be responsible for the differences in diameter observed.

Catalyst characteristics (i.e. preparation method, metal loading, and calcination and reduction temperatures), as well as gas composition control the maximum number of filaments that can be formed and consequently the maximum amount of carbon that can be formed during the nucleation step [13]. For example, increasing the methane concentration accelerates the nucleation rate and the number of filaments formed since the partial pressure of methane determines the degree of super saturation required for nucleation to begin [13,33]. The degree of super saturation required for nucleation is exceeded only when the activity of carbon in the gas

phase exceeds unity and the activity of carbon, a_C, can be calculated using the following equation [32]:

$$a_C = K_P * \frac{p_{H_2}^2}{p_{CH_4}} \tag{2.13}$$

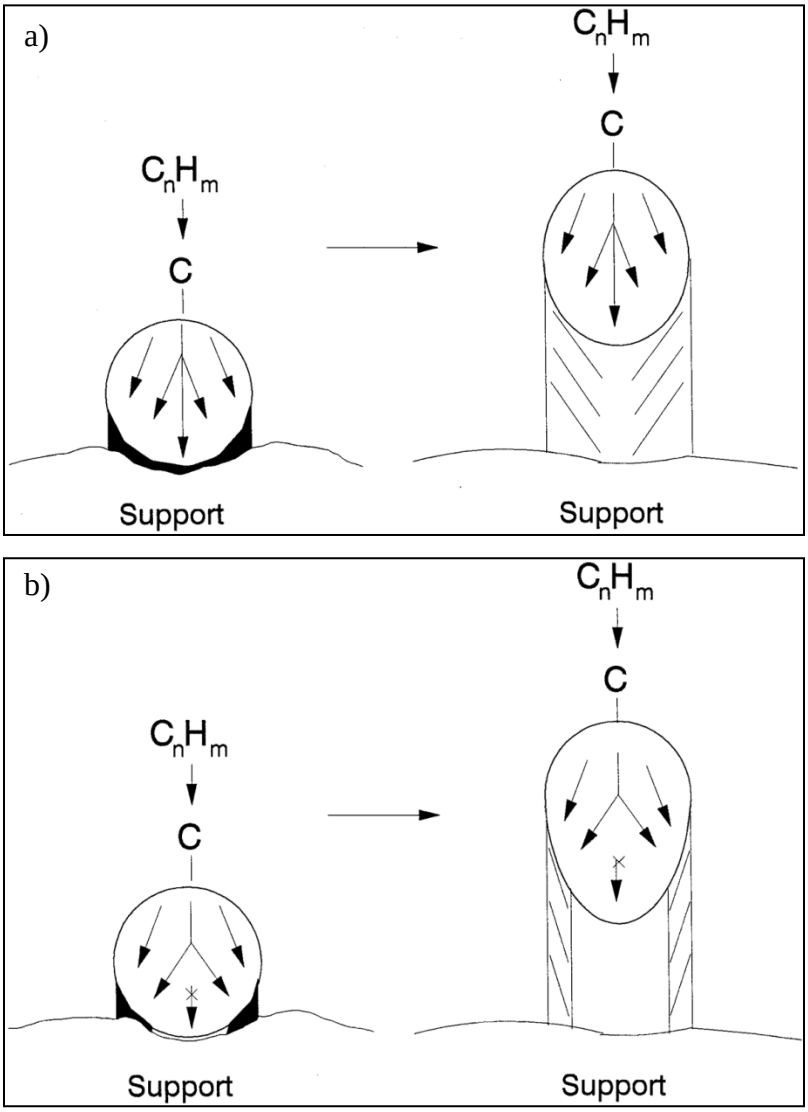

Figure 2.7 - Particle detachment and formation of a) solid filament and b) hollow filament. Note the particle deformation in b) (Reprinted from [33], with permission from Elsevier)

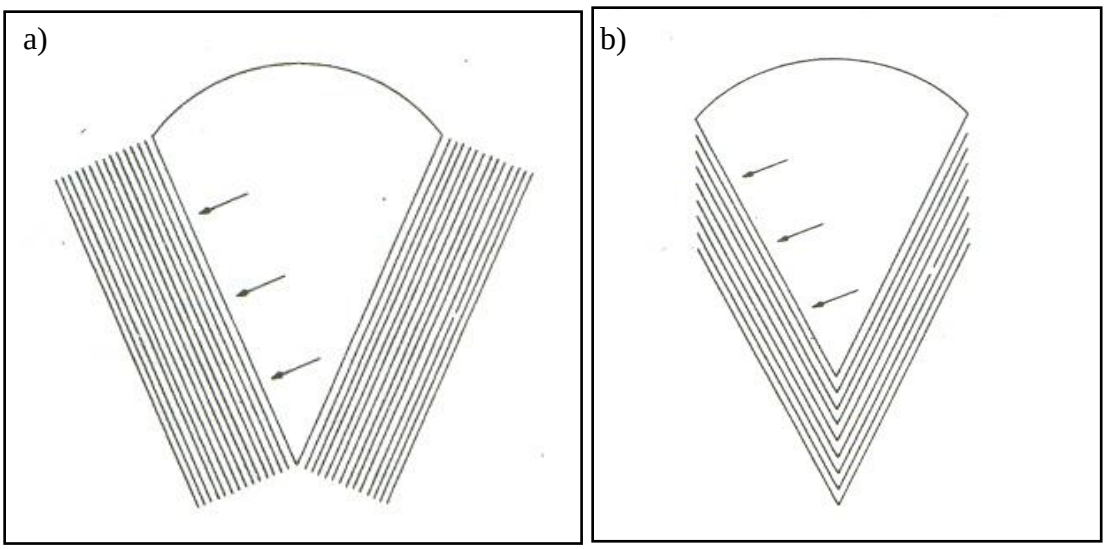

Figure 2.8 - Cross sections of conical graphite layers excreted in a direction perpendicular to the metal/filament interface; a) without slippage, b) with slippage (Reprinted from [53], with permission from Elsevier)

Experimental observations have shown that the nucleation of filamentous carbon is more difficult when there is a lower partial pressure of methane. This is due to slower nucleation and longer periods over which the rate of carbon formation increases, resulting in a smaller number of carbon filaments formed [32].

Also, Villacampa et al. [13] showed that as the catalyst reduction temperature increases more nickel sintering occurs and fewer filaments are formed. Yet, because of the lower interaction between the nickel and support at higher reduction temperature, the nucleation rate still increases with the reduction temperature, which indicates the presence of an optimal reduction temperature.

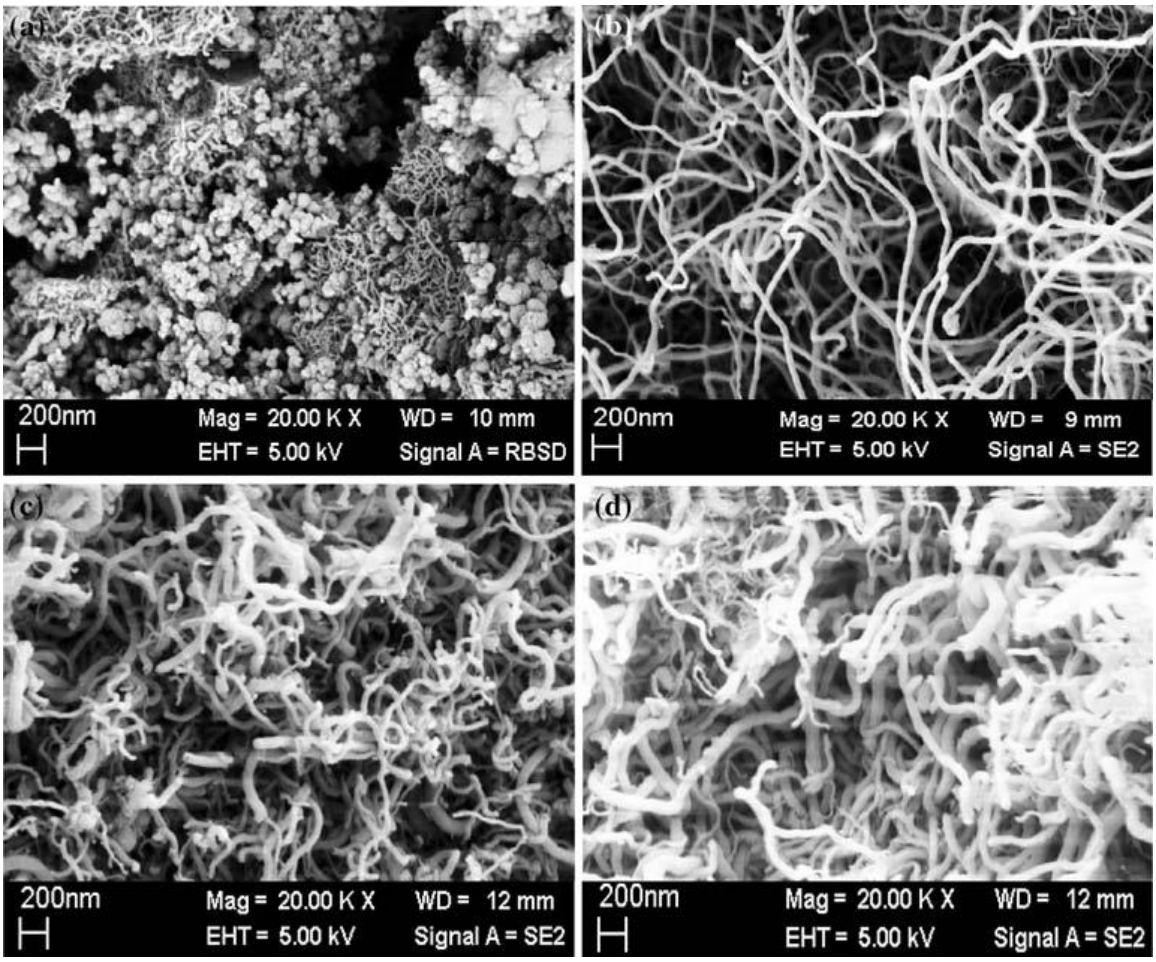

Figure 2.9 - SEM micrographs of a 5 wt% Ni/α-Al_2O_3 catalyst after (a) 14 h reaction at 650°C, (b) 13 h reaction at 600°C, (c) 8 h reaction at 550°C and (d) 16 h reaction at 500°C (Reprinted from [24], with permission from Springer).

2.4.3 Filament growth

After the nucleation period, the Ni particle detaches from the support surface, now being supported by the carbon filament, and the concentration of the carbon at the metal/filament interface drops to the saturation concentration of filamentous carbon, leading to a different carbon concentration gradient in the nickel particle, and thus a different rate of carbon diffusion [33]. A thermal phenomenon has been reported immediately following nucleation: after detachment, the nickel is on the tip of the insulating carbon filament and the support no longer acts as a heat sink [40,51]. As a consequence, the particle temperature during filament growth increases somewhat, thus also contributing to an increase in carbon growth rate [51].

A constant filament growth rate is reached when the maximum number of filaments is nucleated. During the constant growth rate stage, a uniform temperature on the nickel particle prevails due to the balance between the heat losses and the heat gains from the surrounding environment, and the number of filaments remains constant [55].

2.4.4 Catalyst deactivation or tailing stage

Due to the presence of excess carbon on the gas side of the nickel surface, some carbon deposits on the nickel surface form encapsulating carbon, which is responsible for catalyst deactivation. As the encapsulating carbon deposits on nickel, a gradual decrease in available nickel surface area for methane cracking occurs. In addition, this gradual decrease in active surface area results in less heat input to the metal particle, which decreases the rate of carbon diffusion through the nickel particles by reducing the carbon solubility. This, in turn, slows down the removal of carbon at the gas side which further increases the rate of encapsulating carbon deposition [51]. Because of these cause-and-effect phenomena, the active nickel particles ultimately become completely encapsulated by carbon and filament growth ceases.

2.4.5 Proposed mechanisms for carbon filament growth

Although most authors agree on the main stages for carbon filament growth, different mechanisms have been proposed for carbon filament formation, with different assumptions concerning the composition and nature of the selvedge and the driving force for carbon movement. In the following paragraphs, the different mechanisms of carbon filament formation are discussed in their chronological order of appearance in the literature.

Assuming temperature as the driving force for carbon filament formation, Baker et al. [51] developed a three-step model to explain filament formation. In the first step, hydrocarbons adsorb and decompose on certain faces of the metal particle. The second step involves dissolution of some of the carbon species into the bulk and diffusion through the metal particle from the hotter leading face (exposed to the gas) to the cooler rear face (facing the support), where carbon is precipitated from the solution to form carbon filaments. Finally, in the third stage, the growth rate declines due to the formation of encapsulating carbon.

McCarty et al. [50] assumed that an intermediate product, called selvedge, is formed at the gas/metal interface due to the segregation behaviour of carbon in nickel. The segregation behaviour takes place due to the carbon concentration gradient between the surface and bulk over a number of atomic layers. Then, filamentous carbon is formed as a product of hydrocarbon dissociative chemisorption on the metal surface. The dissociative chemisorption produces carbon atoms on the catalyst particle face, which then diffuse towards the opposite face where the carbon atoms crystallize in the form of a continuous graphite-like structure. Based on their evidence they concluded that this rate of carbon deposition is governed by isothermal carbon diffusion through the metal particle.

Kock et al. [52] discussed carbon thermodynamic properties as a function of carbon origin. They proposed that the carbon at the metal/filament interface has a higher solubility in the catalyst than the carbon deposited at the metal/support interface; and the difference in solubility is the driving force for carbon transport.

Alstrup [29] defined the selvedge as surface carbide. This assumption of carbide presence was also used by Schouten et al. [56] who assumed that the carbon atoms entering the selvedge create surface carbide species. But Snoeck et al. [33] reported that assuming nickel carbide as an intermediate product is impractical because nickel carbide decomposes at 350°C and the presence of sub-stoichiometric carbide could not be determined with certainty during steady-state carbon filament formation.

Instead, Snoeck et al. [33] developed a model for carbon filament formation that was based on the solubility of carbon in nickel depending on the extent of the driving force in the gas phase towards carbon formation (i.e. higher partial pressure of methane and/or lower partial pressure of hydrogen). The higher the driving force toward carbon formation, the higher the amount of dissolved carbon in nickel. Snoeck et al. [33] found that at a fixed temperature in the nickel particle, the solubility at the gas/metal interface and solubility at metal/filament interface may differ by a factor of 200.

Aiello et al. [57] used a mechanism similar to the previously mentioned ones, but assumed that the rate determining step is carbon diffusion through nickel and that catalyst deactivation results from the space limitation for carbon filament growth. They assumed that deactivation takes place when the carbon filaments come into contact with each other.

Shah et al. [58] studied the catalytic decomposition of pure methane using nano-scale binary Fe-M (M = Pd, Mo, or Ni) catalysts supported on alumina. SEM and TEM techniques were used to characterize carbon. A substantial amount (> 90%) of the carbon produced during catalytic decomposition of methane, between 700°C to 800°C, was in the form of potentially useful multi-walled carbon nano-tubes, but the carbon formed above 900°C was amorphous with a small percentage of carbon flakes and carbon fibres [40]. Shah et al. [58] confirmed with the help of XAFS and Mössbauer spectroscopy that the catalyst particle remained in its metallic state, even after it had been lifted off the alumina support, and was covered by encapsulating carbon. No carbide species were observed. Shah et al. [58] noted that the change in surface structure did not actually deactivate the catalyst; instead the catalyst was gradually encapsulated by the free carbon thereby isolating the catalyst from methane.

Toebes et al. [59] studied carbon deposition by decomposition of carbon containing gases (CH_4, CO/H_2 or C_2H_4/H_2) using Ni/SiO_2 or unsupported nickel as a catalyst. They assumed a delicate balance between dissociation of the carbon-containing gases and carbon diffusion through the catalyst particle, and a balance between carbon diffusion through the catalyst particle and rate of nucleation and formation of graphitic layers. As in most of the other studies, the authors proposed that the carbon filament is formed by carbon diffusion through nickel from the gas side to the support side. The diffusing carbon is deposited at the nickel/support interface and leads to carbon filament formation. The authors support the mechanism that describes the segregation behaviour of carbon in nickel, creating a selvedge with a high concentration at the nickel surface on the gas side. They again suggested there is a gradient in carbon concentration with a high level at the surface and less in the bulk. Furthermore, the segregated carbon atoms at the surface compete with the gas phase atoms (methane and hydrogen) for active sites. They also indicated, as mentioned above with other studies, the carbon diffusion driving force is the difference between dissolved carbon in the nickel at the gas side of the particle and solubility of carbon at the support side of the particle.

In terms of carbon species activities, not isolated to filaments in this case, different types of carbon are produced during hydrocarbon dissociation, each with its own properties and reactivity [34]. Trimm [60] mentioned in his review of coking during steam reforming that two kinds of carbon are produced when hydrocarbons dissociate, namely an α-type carbon (Cα) and a β-type carbon (Cβ). The Cα is more reactive than Cβ and can be easily gasified using oxygen.

When an excess amount of Cα is present, Cα transforms to Cβ. Although the fate of Cβ has not been completely elucidated, it is thought that some of the Cβ may not diffuse through the nickel but instead, remain on the catalyst surface, slowly building up and eventually encapsulating the catalyst leading to complete deactivation. Guo et al. [49] used temperature-programmed reaction techniques and Raman spectroscopy to characterize carbon deposited on 5% $Ni/MgAl_2O_4$ during methane cracking. They found three forms of carbon on the catalyst surface during methane catalytic cracking, α-type carbon (Cα) and β-type carbon (Cβ), and γ- type carbon (Cγ). Using Raman spectroscopy, they found that Cγ is graphite-like, and assigned it as that responsible for catalyst deactivation. During carbon gasification experiments, they reported that Cγ showed a resistance to gasification using oxygen or hydrogen. However, Cγ showed an unexpectedly high gasification rate with carbon dioxide, which they attributed to the formation of carbonate, bidentate and formate species on $MgAl_2O_4$. Other authors (e.g. [11,34]) identified five different types of carbon that may form during hydrocarbon dissociation, which can be distinguished based on their crystalline properties and reactivity, and are listed as:

1. Cα: Adsorbed atomic carbon (dispersed, surface carbide), formed between 200-400ºC.
2. Cβ: Polymeric filaments (amorphous), formed between 250-500ºC.
3. Cv: Carbon filaments (amorphous), formed between 300-700ºC.
4. Cγ: Nickel carbide (bulk), formed between 150-250ºC.
5. Cc: Graphitic film (crystal), formed at temperatures greater than 600ºC.

2.5 Catalyst Deactivation

2.5.1 Coking as the main deactivation process in methane catalytic cracking

Ni-based catalysts are highly active and selective for hydrocarbon cracking. They are characterized by a high capacity for carbon adsorption [49], but the adsorbed carbon also causes deactivation. There have been multiple studies focused on the deactivation mechanisms with the ultimate goal targeting lengthening the catalyst life. These studies have evaluated parameters affecting deactivation, the period of stable catalyst performance, and when the catalyst needs to be replaced. Poisoning, fouling or coking (carbon deposition), sintering and mechanical degradation are the common forms of catalyst deactivation [11].

The main deactivation mechanism during methane catalytic cracking is coking, which can be defined as the physical deposition of carbonaceous species from the reacting species onto the catalytic surface [11,61-62], which may result in loss of catalytic activity as a result of blocking of catalyst sites and/or pores [11, 63]. When large amounts of carbon deposit, coking may also result in disintegration of catalyst particles and reactor plugging [11]. The coke/carbon formed during hydrocarbon processing is usually classified according to reaction type, catalyst type, and reaction conditions [63]. Deactivation due to coke forming reactions on metals (e.g. methanation, Fischer–Tropsch synthesis, and steam-reforming) occurs due to the difference between the carbon formation and carbon gasification rates [63]. Coking may affect catalyst activity in several ways; in some cases all the effects combine [11,34]. The carbon can:

1- adsorb strongly on the active phase surrounding and blocking access to the active phase surface;
2- encapsulate the active metal particle;
3- plug the micro and mesopores, denying access to the active phase inside the pores;
4- accumulate as strong carbon filaments leading to catalyst pellet disintegration; and
5- in extreme cases, physically block the reactor.

The deposited carbonaceous materials may vary in chemical structure from hydrogen-deficient, aromatic-type polymers, to graphitic carbon. In extreme cases the catalyst surface is covered with layers of coke deposit, thereby decreasing the accessibility to surface sites. Although coking is not desirable in most hydrocarbon processing reactions, in some catalytic cracking processes, for example the catalytic cracking of methane for hydrogen production, coking is a direct product. More coke deposited on the catalyst means better hydrogen production occurred, since the reaction products are hydrogen and coke.

Some researchers attribute deactivation to reasons other than the carbon layer formed around the active sites. For example, Ishihara et al. [64] observed that a 10% Ni/SiO_2 catalyst was still active after a large amount of carbon deposited on the surface, up to a 200-carbon atom/nickel atom ratio. They concluded that active site blocking is not necessarily the reason for deactivation. Using scanning electron microscope (SEM) and transmission electron microscopy

(TEM) to characterize the spent catalyst, they found that carbon was deposited as filaments with the nickel particle on the tip, as described above. They concluded that deactivation occurred due to space limitation, when the formed filaments began to interfere with each other inside or outside the catalyst pellet, inhibiting the deposition of more carbon atoms in filamentous form. Aiello et al. [57] reported the same conclusion when they studied methane cracking using Ni/SiO_2; after deposition of thousands of carbon atoms on nickel, the catalyst was deactivated due to space limitations imposed by reactor space.

2.5.2 Coking deactivation mechanism

Methane decomposes at the gas/metal interface, producing carbon which dissolves and diffuses through and around the catalyst particle to the metal/support interface, detaching the catalyst particle from the support, forming a filament with the catalyst particle on the filament's tip [39-40,57,64]. Diffusing carbon deposits as filamentous carbon [39], and the deposition rate is controlled by heat transfer through carbon [9] or the concentration gradient of carbon through the nickel particle [29]. Carbon diffusion through the metal particle has been proposed as the rate-controlling step, and deactivation is a result of space limitation in the reactor [57,64] and/or is a result of a solubility limitation of carbon in nickel when the dissolved carbon reaches its saturation concentration, which leads to encapsulating carbon formation [24,33,40,58]. As a result of carbon deposition on nickel, the catalyst activity changes as the reaction proceeds.

So, during coking-based deactivation, carbon is deposited on the active site at the active site/gas interface forming a layer called encapsulating carbon, which blocks reactant access [36]. Encapsulating carbon causes catalyst deactivation either by blocking the catalyst pores or by complete encapsulation. Encapsulating carbon formation has been found to be inversely proportional to methane partial pressure, while increasing hydrogen partial pressure has a negative impact on the encapsulating carbon formation rate [13,26]. Also, increasing temperature increased encapsulating carbon formation [44]. The form of the encapsulating carbon is also dependent on the temperature. At temperatures < 500°C, encapsulating carbon is deposited as a polymeric film. While at temperatures > 450°C, deposition of whisker-like carbon is more likely to take place. But at higher temperatures > 600°C, pyrolitic coke forms as the encapsulating carbon layer [34,63].

Takenaka et al. [47] studied the structural changes of nickel during methane cracking over Ni/SiO_2. The XANES/EXAFS spectra of the pure nickel were measured, and compared to the spectra of the supported nickel to measure the changes in nickel structure during methane cracking. XRD was also used to determine the chemical forms of nickel. The results showed that nickel kept its metallic state until the ratio of the carbon deposited over nickel was, C/Ni, > 900, as shown in Figure 2.10. The results also indicated that the methane cracking rate was not affected as long as nickel remained in its metallic form. After the C/Ni ratio exceeded 900, XANES/EXAFS spectra showed some discrepancy between the catalyst and nickel foil readings, whereas the catalyst spectrum before reaction resembled that of Ni foil. In addition, the methane cracking rate started to decrease for C/Ni ratios above 900. The XANES spectrum for the supported nickel was then closer to that for nickel treated with CO, and indicated complete deactivation. XRD studies of the deactivated catalyst showed that nickel was present in two forms; metallic and carbide. The authors concluded that the carbide form is responsible for catalyst deactivation via formation of an inactive component with nickel. The authors also studied the detected carbide form, and the results indicated that the physical properties of the detected carbide are different from that of Ni_3C.

2.5.3 Factors affecting catalyst deactivation

The catalyst deactivation rate is of course affected by operating conditions. The operating conditions reported in the literature as having the most effect on the deactivation rate are methane flow rate (or more specifically the gas hourly space velocity, GHSV), reaction temperature [19,65], methane partial pressure, and hydrogen partial pressure [13]. Suelves et al. [65] reported that the higher the temperature and methane flow rate, the shorter the catalyst life; so, temperature and methane flow rate are directly related to the catalyst deactivation rate. Villacampa et al. [13] found that the deactivation rate is inversely proportional to hydrogen partial pressure. We can summarize the effect of different factors on the reaction rate and deactivation rate as follows: any parameter that can increase the reaction rate also increases the deactivation rate. Ermakova et al. [19] studied the effect of temperature on deactivation. Their conclusions agreed with that of Suelves et al. [65]. An example of the effect of temperature [19] on deactivation rate is shown in Figure 2.11.

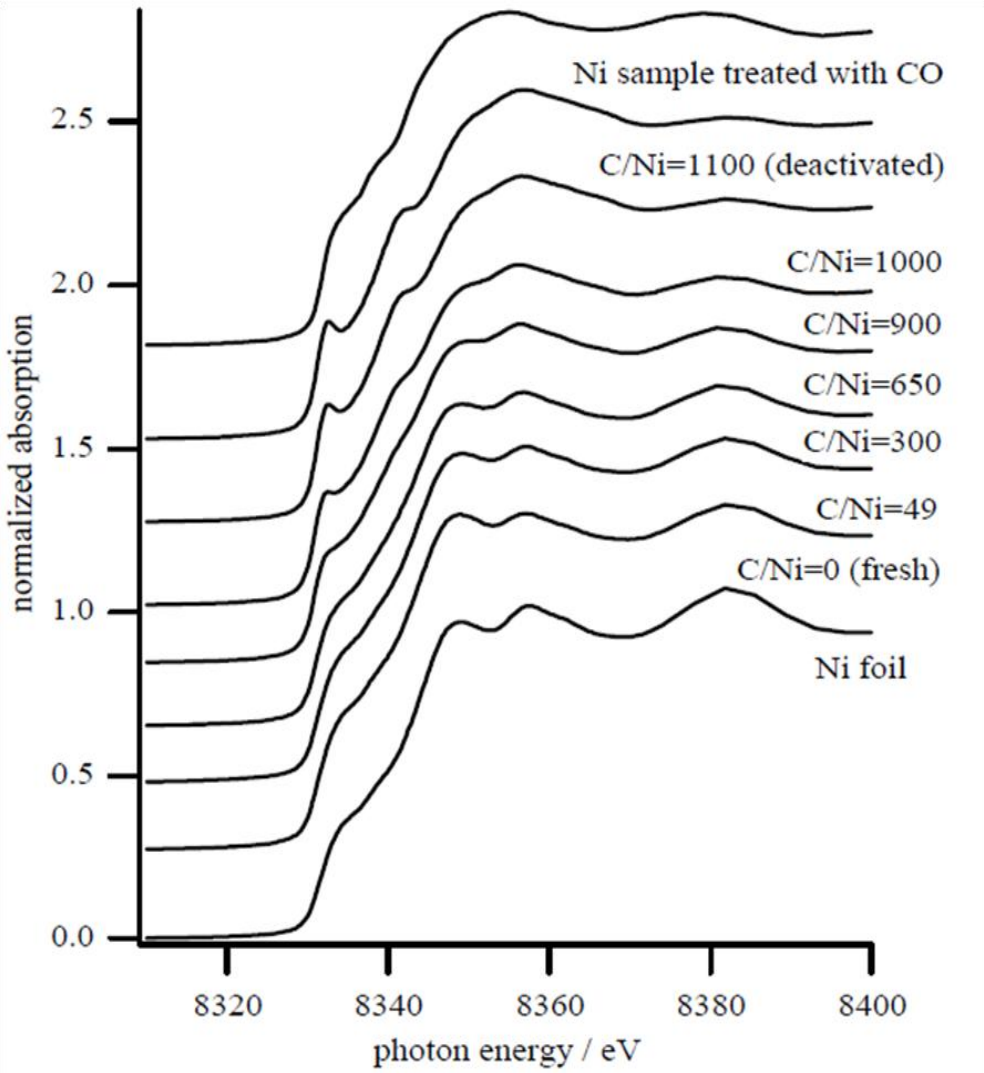

Figure 2.10 - Ni K-edge XANES/EXAFS spectra of Ni/SiO_2 catalysts with and without deposited carbon, Ni foil, and the foil treated with CO (Reprinted from [14], with permission from the International Union of Crystallography (http://journals.iucr.org/)

Suelves et al. [65] studied the methane flow rate and temperature effects on deactivation using a fixed bed reactor and a 65% Ni supported on silica and alumina catalyst, with 2 and 0.3 g of catalyst used to vary the space velocity. Using 100% methane and at 700°C, Suelves et al. [65] found that with a space-time of 1.15 s, catalytic activity did not decay after 16 h on stream, with a carbon yield of 55.6% (as a percent of the total methane passed through the reactor) and 6.3 g of carbon/g of catalyst. While at a space-time of 0.23 s, the catalyst completely deactivated after 90 min with almost half the amount of carbon deposited, about 6.7% yield. Then the authors used the 1.15 space time but at 550°C to study the effect of temperature. The results showed that at 550ºC,

the catalyst held its activity for 16 hrs at a yield of 43.8% and a total amount of 14.3 g of carbon/g of catalyst. In their conclusions, they reported that increasing the flow rate and/or the reaction temperature decreased catalyst life time.

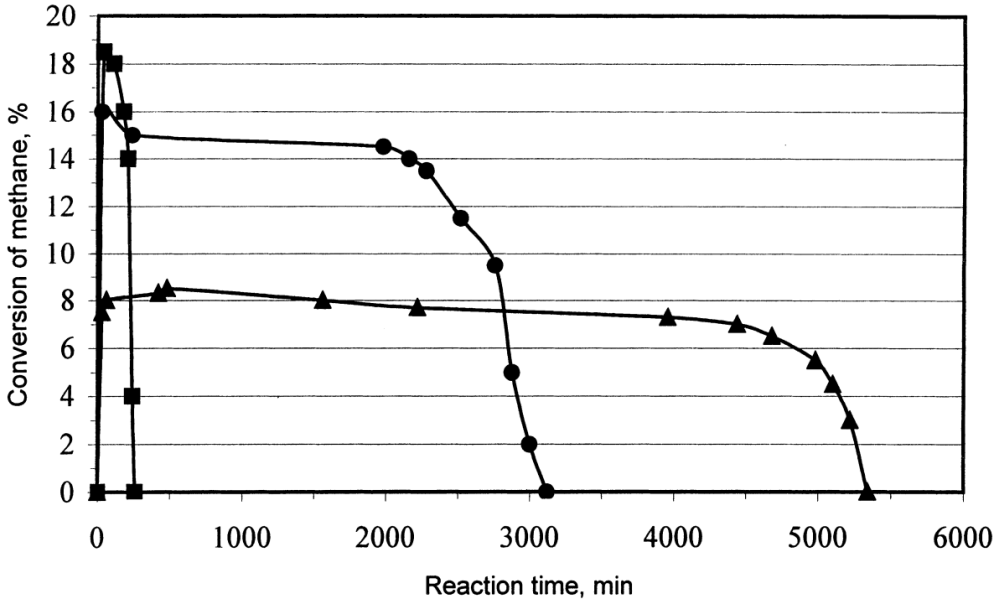

Figure 2.11 - Methane conversion vs. time, at 600 ºC (squares), 550 ºC (circles), and 500 ºC (triangles) (Reprinted from [19], with permission from Elsevier)

The third factor affecting catalyst deactivation is the hydrogen partial pressure, which was studied by Villacampa et al. [13]. They used different mixtures of CH_4 and H_2 to study the influence of hydrogen on the kinetics of methane catalytic cracking. They observed that the presence of a small amount of hydrogen actually increased the total amount of carbon deposited, although the methane cracking rate was lower, compared to the hydrogen-free feed, as shown in Figure 2.12.

Toebes et al. [59] attributed the effect of hydrogen partial pressure to a reduction in the encapsulating carbon formation rate. Because hydrogen is a reaction product, and may adsorb on, or interact with, the active sites, it can prevent methane from adsorbing, which reduces both the cracking rate and the deactivation rate.

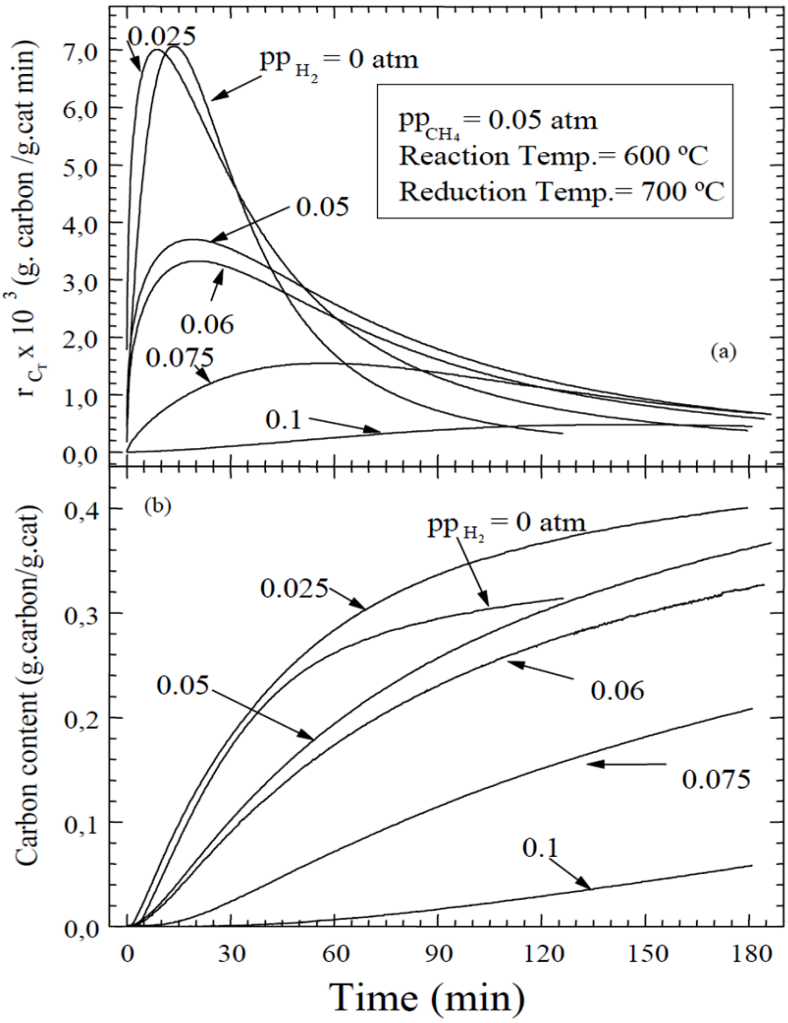

Figure 2.12 - Influence of hydrogen partial pressure on (a) carbon formation rate and (b) carbon content deposited on the catalyst (Reprinted from [13], with permission from Elsevier)

Villacampa et al. [13] studied the effect of methane partial pressure on catalyst deactivation and carbon deposition rate. Increasing P_{CH4} increased cracking and deactivation rates, and slightly reduced the total carbon deposited on the catalyst. The deactivation rate is higher with increasing P_{CH4} due to the increase in encapsulating carbon formation.

2.6 Catalyst Regeneration

The major challenge for a continuous hydrogen production process using catalytic cracking of methane is regeneration of the deactivated catalyst. Two different catalyst regeneration methods are commonly proposed in the literature: steam regeneration and air

regeneration, and to a lesser extent CO_2. In steam regeneration, steam reacts with carbon producing hydrogen with a mixture of carbon monoxide and carbon dioxide. In air regeneration, oxygen reacts with the deposited carbon to burn it; a mixture of carbon oxides is produced depending of the amount of excess air used. In carbon dioxide regeneration, deposited carbon reacts with CO_2 forming CO, producing a mixture of carbon oxides. Each method has its advantages and disadvantages, and the choice of the optimum method depends on the overall process economics. Three factors are essential before choosing the regeneration method; the energy needs for the process, the catalyst circulation time, and the effect on catalyst performance.

From an energy point of view, a method that will produce energy to cover part of the methane cracking energy demand is better (e.g. air regeneration). On the other hand, additional hydrogen is produced during steam regeneration, approximately 2 and 3.4 moles of hydrogen per mole of methane that was introduced during the cracking portion of the cycle for air oxidation and steam gasification, respectively [37,57]; but steam regeneration is endothermic while air regeneration is exothermic, as shown in Equations 2.14 and 2.15 [5]:

$$C + O_2 \leftrightarrow CO_2 \qquad \Delta H_{1073} = 174.5 \text{ kJ/mol} \qquad (2.14)$$

$$C + H_2O \leftrightarrow CO + H_2 \qquad \Delta H_{1073} = 135.9 \text{ kJ/mol} \qquad (2.15)$$

Regarding the regeneration time, the faster regeneration process is obviously better so higher catalyst circulation rates can be achieved and the air regeneration process is faster than steam regeneration. Regarding the effect on catalyst texture however, in air regeneration, local hot spots may form, affecting some active sites by converting them to an oxide form, which would then require a reduction step before using the catalyst again for methane cracking [37]. Also, and probably more serious, the localized high temperature areas may cause sintering, decreasing the exposed nickel surface area [57]. On the other hand, in steam regeneration, the catalyst bed temperature can be kept more uniform, thereby avoiding sintering [37,57]. Furthermore, Muradov et al. [66] mentioned that treatment with steam may result in an increase in catalyst surface area for activated carbon. Muradov et al. [66] used activated carbon as a catalyst for methane cracking at 850ºC, and after 1 hr the catalyst partially deactivated and the surface area of the activated carbon dropped from 670 m^2/g to 324 m^2/g. After treatment of the activated carbon with steam at 950ºC for 0.5 h, the surface area increased to 617 m^2/g.

2.6.1 Air regeneration

Zhang and Amiridis [37] used a 16.4% Ni/SiO_2 catalyst for methane cracking and air oxidation to regenerate the spent catalyst at 550ºC. The catalyst was quickly and fully regenerated using air oxidation but the high temperature generated during the oxidation process resulted in disintegration of the sample to a fine powder. This was also reported by Rahman [67]. Furthermore, XRD analysis showed that Ni oxide had formed, requiring reduction of the catalyst before further use for methane cracking.

Villacampa et al. [13] used a 3% oxygen stream to fully regenerate a 30% Ni/Al_2O_3 catalyst. They reported that the catalyst lost its activity after the first regeneration experiment, as shown in Figure 2.13. Rahman et al. [24] found very similar results. Villacampa et al. [13] attributed the loss of activity after regeneration with air to active site sintering due to the high temperature generated during oxidation of the deposited carbon. Rahman [67], on the other hand, attributed the activity loss to the fact that the catalyst was completely disintegrated after the first regeneration, as seen in Figure 2.14, where it is apparent that the catalyst became like fine powder. It was speculated that this may be due to the growth of carbon filaments inside the porous catalyst during the previous cracking portion of the cycle.

Otsuka et al. [5] used oxygen to regenerate the carbon deposited on $Pd\text{-}Ni/SiO_2$, Ni/TiO_2, and Ni/Al_2O_3, and reported that all the used catalysts regained their activity after regeneration, for 5 cracking/regeneration cycles. Carbon deposited on the catalyst was oxidized at 480ºC for those tests, but for complete elimination of the deposited carbon, a temperature higher than 500ºC was needed. They also ran catalyst activity tests at 550ºC for all the used catalysts for several cracking/regeneration cycles. For Ni/SiO_2, the catalyst lost its activity over several cycles due to sintering of the catalyst. For Ni/TiO_2, Ni/Al_2O_3, and $Pd–Ni(1:3)/SiO_2$, the catalysts showed good stability over the cycles.

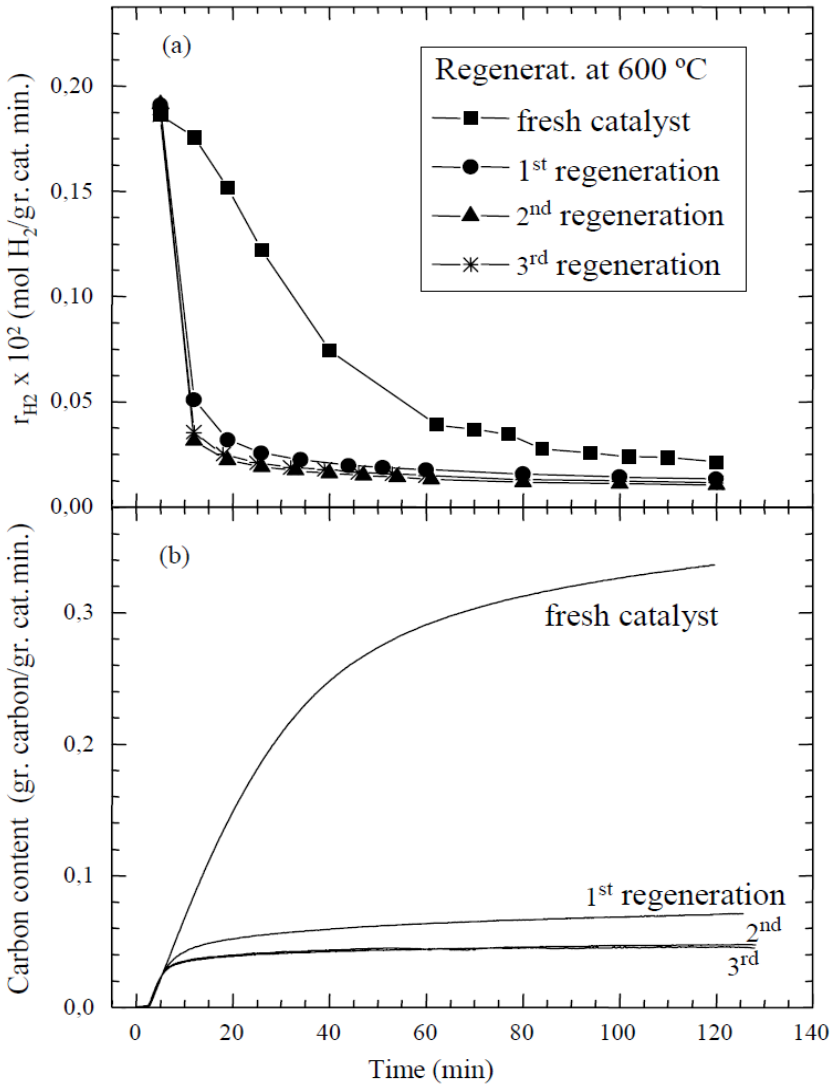

Figure 2.13 - Influence of regeneration cycles on the evolution of (a) hydrogen production rate and (b) on carbon content using 30% Ni/Al_2O_3 and the cracking temperature was 600ºC (Reprinted from [13], with permission from Elsevier)

a)  b) 

Figure 2.14 - a) Fresh catalyst before calcination, and b) after complete regeneration in air [67]

As an alternative to complete regeneration, the concept of partial regeneration was introduced [24,68]. In partial regeneration, only part of the deposited carbon is removed. Koc et al. [68] partially regenerated a 15%Ni/γ-Al_2O_3 catalyst at 500ºC using air and found that the partially regenerated catalyst, after gasifying 90% of the coke, regained excellent activity, similar to that during the previous cycle, for up to 4 cycles.

Besides sintering and disintegration, deterioration in performance after complete regeneration was also attributed to the change in orientation of nickel atoms from Ni (110) to Ni (111) and Ni (100) [65]. Ni (110) is a highly active face for carbon formation while Ni (100) has much lower activity, and Ni (111) shows no activity at all [69].

2.6.2 Steam regeneration

For steam regeneration of the spent catalyst, the process can be described as steam reforming with two stages. In the first stage only pure hydrogen is produced, while in the second stage hydrogen contaminated with carbon monoxide and carbon dioxide is produced [37].

Zhang and Amiridis [37] used steam gasification to regenerate a deactivated 16.4% Ni/SiO_2 catalyst at 550ºC. The catalyst regained its activity and the XRD pattern showed that the nickel kept its metallic form after regeneration was complete, but also indicated the presence of small pockets of carbon. TEM was used to investigate the nature of the remaining carbon. The data indicated that the remaining carbon was filamentous, but had thinner walls and the authors concluded from this that the external walls of the originally solid filaments were more resistant to steam gasification. Zhang and Amiridis [37] suggested running an air oxidation cycle with successive cycles of steam gasification to remove the steam gasification resistant carbon.

Aiello et al. [57] regenerated a deactivated 15% Ni/SiO_2 at 650ºC using steam, and regained initial activity. The results revealed no appreciable loss in catalytic activity after 10 successive cycles, as shown in Figure 2.15. XRD analysis indicated no increase in carbon remaining on the catalyst after successive regenerations and no structural changes in the nickel particles as the catalyst was cycled between cracking and steam regeneration, as shown in Figure 2.16. Aiello et al. [57] found only trace amounts of nickel oxide on the regenerated samples. SEM micrographs indicated that carbon was removed during steam regeneration, but again small pockets of carbon remained, which resisted steam regeneration.

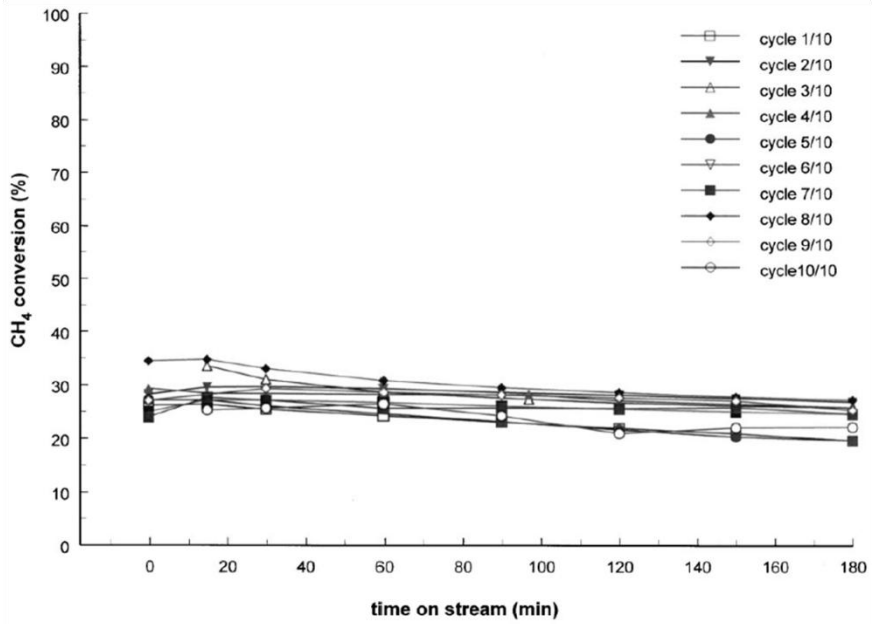

Figure 2.15 - Methane conversion obtained during successive cracking cycles (Reprinted from [57], with permission from Elsevier)

Choudhary et al. [70] studied methane cracking using nickel supported on different metal oxides and zeolites. Cracking and regeneration were conducted at 500ºC using two parallel fixed beds operated in a cyclic mode and alternating the feed from methane to steam. The total amount of carbon deposited on the catalyst was 0.82 g of carbon per gram of catalyst after cracking while the total carbon remaining on the catalyst after regeneration was 0.044 g of carbon per gram of catalyst, so around 95% of the deposited carbon was removed by steam gasification.

Muradov et al. [66] used activated carbon as a catalyst for methane cracking in a fluidized bed. They used steam to regenerate the deactivated catalyst at 950ºC for 0.5 h. By conducting methane cracking/steam gasification cycles, Muradov et al. [66] found that the catalyst could regain its activity completely after regeneration with steam.

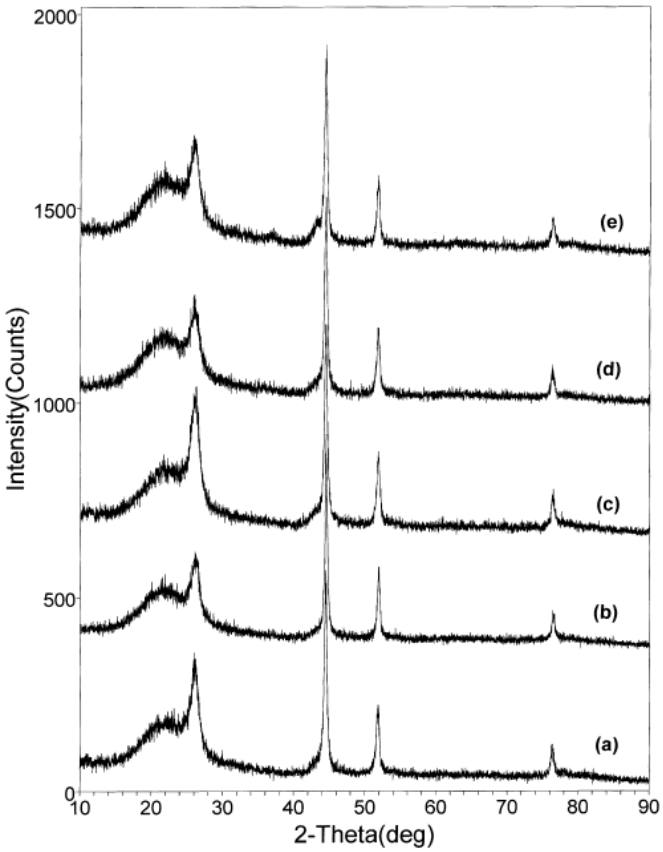

Figure 2.16 - XRD patterns of the Ni/SiO_2 catalyst after (a) 1, (b) 2, (c) 3, (d) 5, and (e) 10 successive cracking/regeneration cycles (Reprinted from [57], with permission from Elsevier)

2.6.3 CO_2 regeneration

Although steam regeneration and air regeneration are widely mentioned in the literature as regenerating methods, CO_2 regeneration has also been evaluated [71], with the reaction shown in the following equation [5]:

$$C + CO_2 \leftrightarrow 2CO \qquad \Delta H°_{800°C} = 174.5 kJ/mol \qquad (2.16)$$

Takenaka et al. [72] studied methane cracking over nickel supported on SiO_2, TiO_2, and Al_2O_3 at 550ºC and subsequent regeneration of the catalyst using CO_2 at 650ºC. They observed the production of CO during regeneration, and found that 95% of the carbon deposited on the catalyst was converted to CO. After conducting a number of cracking/regeneration cycles for each catalyst, the results showed that for Ni/SiO_2 the catalytic activity decreased significantly

after the fifth cycle to reach almost half of the initial activity. For example, 10% Ni/SiO_2 showed an initial activity of 2000 (H_2/Ni). In the fifth cycle the ratio of H_2/Ni decreased to 1000. The authors attributed the activity loss to sintering. In the case of Ni/TiO_2 and Ni/Al_2O_3, the catalysts kept their stability over the six cycles that were conducted.

Pinilla et al. [71] used CO_2 to regenerate a deactivated carbon catalyst but the high temperature required to effectively eliminate all of the residual carbon affected the textural parameters of the catalyst. After the third regeneration/reaction cycle, they concluded that most of the mass of the catalyst originates from carbon formed during cracking, as the activated carbon that comprised the original catalyst completely gasified. Abbas and Wan [73] also used CO_2 to regenerate activated carbon. They conducted methane cracking at 850 and 950°C. The regeneration experiments were conducted at 900, 950 and 1000°C. The results showed that the combination of 950°C as a cracking temperature and 1000°C as the regeneration temperature maintained the catalytic activity of the activated carbon, with no remarkable loss of activity for 6 cracking/regeneration cycles.

2.7 Reaction Rate Equations and Reaction Mechanisms

In this section, different kinetic models that have been proposed in the literature for methane catalytic cracking are reviewed. The models range from those based on a detailed reaction mechanism to a global rate expression, from those that cover just the stable catalytic activity region to models that describe the whole reaction process including deactivation, and from models that calculate methane cracking rates to models that give the total amount of carbon deposited. Overall, the rate equations for methane cracking available in the literature can be divided into three main categories; detailed mechanistic rates, interpolated mathematical equations, and finally a global rate equation.

2.7.1 Detailed mechanism rate equations

In 1965, Grabke [74] studied methane cracking over γ-iron in the 800-1040ºC temperature range. Grabke developed the first rate equation for methane catalytic dissociation in the form of a reversible reaction rate. Grabke proposed that the forward reaction is proportional to $P_{CH4}P_{H2}^{1/2}$ while the reverse reaction is proportional to $P_{H2}^{3/2}$ and the concentration of carbon deposited on the catalyst at low concentrations. In his conclusions, Grabke [74] proposed that the methane cracking reaction is a multi-step reaction. Grabke suggested that methane undergoes a

series of dehydrogenation reactions and concluded that the rate controlling step of methane cracking is the formation of the methyl group from methane.

Five years later, Grabke [75] continued his research on methane cracking; also using iron again, but here supported on γ-alumina as the catalyst and developed a detailed mechanism of the reaction. Grabke [75] suggested a reaction mechanism that later became the basis for all methane cracking mechanisms found in the literature. Grabke concluded that after methane adsorption on the catalyst, the methyl group passes through a series of dehydrogenation steps, until it ends up as dissolved carbon. Despite the fact that all the reaction mechanisms proposed in the literature since stem from the same designed by Grabke [74-75], there have been slight differences proposed, either in the methane dissociation steps or by adding more steps to the Grabke mechanism.

Grabke [75] assumed that the adsorption of methane on the catalyst is non-dissociative, as shown in Table 2.1, which has been used as the first step for methane cracking mechanism by many researchers [25,76-78]. Although the non-dissociative adsorption of methane is more often used, dissociative methane adsorption has also been proposed [79-80], as shown in Table 2.2.

Table 2.1- Mechanism of methane cracking starting with non-dissociative methane adsorption

$CH_4 + I$ (Vacant site) $= CH_4$(ad)	(1)
CH_4(ad) = CH_3 (ad) + H (ad)	(2)
CH_3(ad) = CH_2 (ad) + H (ad)	(3)
CH_2(ad) = CH (ad) + H (ad)	(4)
CH (ad) = C (ad) +H (ad)	(5)
C(ad) = C (dissolved)	(6)
2H (ad) = H_2 +2I	(7)

Table 2.2- Mechanism of methane cracking starting with dissociative methane adsorption

$CH_4 + I$ (Vacant site) = CH_3 (ad) + H (ad)	(1)
CH_3(ad) = CH_2 (ad) + H (ad)	(2)
CH_2(ad) = CH (ad) + H (ad)	(3)
CH (ad) = C (ad) +H (ad)	(4)
C(ad) = C (dissolved)	(5)
2H (ad) = H_2 + 2I	(6)

In Grabke's suggested mechanism, Grabke [75] didn't explain how the deposited carbon will form carbon filaments. Grabke proposed carbon adsorption on the active site and dissolution in the active site, which may explain the deactivation behaviour, but the mechanism doesn't reflect the complete process of forming carbon filaments. The adsorbed carbon is an intermediate compound that later forms either carbon filaments or encapsulating carbon as shown in Table 2.3. So, two additional reaction steps were needed to represent the diffusion of adsorbed carbon through and around nickel to form carbon filaments [25,79] and a third step was needed to account for encapsulating carbon formation [80-81].

Table 2.3- Carbon diffusion and encapsulating carbon formation

Diffusion in Ni phase	
C(dissolved) = C(nickel rear)	(1)
Precipitation from Ni phase	
C(nickel rear) = C(Carbon filaments)	(2)
Formation of encapsulating carbon	
C(ad) = C (encapsulating)	(3)

In the following section each model will be discussed. A comparative summary between the different detailed mechanism rate models is illustrated in Table 2.4.

2.7.1.1 Models assuming non-dissociative adsorption of methane (Table 2.1)

Grabke [75] model

Assuming that step 3 in Table 2.1 is the rate limiting step, Grabke [75] studied the kinetics of carbon deposition on a γ-Fe surface exposed to CH_4 and H_2 gas mixtures. Grabke [75] used two iron foils placed inside aluminum tubes in the same furnace; one foil was subjected to a mixture of CH_4 and H_2 for carburization (increasing the carbon content of the iron foil using a mixture of CH_4 and H_2) and hydrogen for decarburization (decreasing the carbon content of the iron foil using hydrogen). The other iron foil was kept in a hydrogen atmosphere as a reference. The electrical resistance of the reacting foil was recorded to study the change in the composition relevant to the reference sample. The reaction rate of the limiting step was taken as the rate of

carburization while the rate of decarburization was used as the reverse reaction rate. As a result, the reaction rate is equal to the carburization rate minus the decarburization rate. As mentioned above, the rate of the forward reaction was found proportional to $P_{CH_4} / P_{H_2}^{1/2}$ and the reverse reaction rate was proportional to $P_{H_2}^{3/2}$. The methane cracking rate equation (Equation 2.17) can be expressed as a dependence on the partial pressures of methane and hydrogen as follows:

$$-\frac{dC_{CH_4}}{dt} = kP_{CH4} / P_{H2}^{1/2} - k' P_{H2}^{3/2} a_C \qquad (2.17)$$

where k and k' are the forward and reverse specific reaction constants for the rate limiting step and a_C is the carbon chemical activity.

The results showed that the rate of the forward reaction was independent of the carbon atoms dissolved on the iron foil surface. The backward reaction was found to be linearly dependent on the carbon concentration for low carbon concentrations. The experimental data agreed well with the results predicted from Equation 2.17.

Bernardo et al. [82] model

Bernardo et al. [82] used a 1% copper/10% nickel alloy supported over silica catalyst to study methane catalytic cracking and steam reforming. A mixture of methane and hydrogen was used and the rate of carbon deposition over the catalyst was calculated. The proposed rate equation, assuming step 1 in Table 2.1 as the rate limiting step, can be written as follows:

$$-\frac{dC_{CH_4}}{dt} = (kP_{CH4} - k' P_{H2}^2) / P_{H2}^{\alpha}[C] \qquad (2.18)$$

where k and k' are again the forward and reverse specific reaction rate constants for the rate limiting step.

Table 2.4- Comparison of different detailed mechanism rate models

Model	Rate limiting step	Catalyst used	Temperature range, °C	Reactor type
Models assuming non-dissociative adsorption of methane (Table 2.1)				
Grabke [75]	$CH_3(ad) = CH_2 (ad) + H (ad)$	γFe	1000-1150	Tube
Bernardo et al. [82]	CH_4 + I (Vacant site) = $CH_4(ad)$	Cu-Ni/SiO_2	525-675	Microbalance
Demicheli et al. [76]	CH_4 + I (Vacant site) = $CH_4(ad)$	Ni/Al_2O_3 -CaO	565-665	Microbalance
Snoeck et al. [25]	$CH_4(ad) = CH_3 (ad) + H (ad)$	commercial nickel catalyst	500-550	Microbalance
Kuvshinov et al. [77]	CH_4 + I (Vacant site) = $CH_4(ad)$	highly loaded nickel catalyst	530-590	Fluidized bed
Models assuming dissociative adsorption of methane (Table 2.2)				
Alstrup and Tavares [79]	1- CH4 + I (Vacant site) = CH3 (ad) + H (ad) 2- CH3(ad) = CH2 (ad) + H (ad)	Ni/SiO_2	450-550	Microbalance
Zavarukhin and Kuvshinov [78]	CH_4 + I (Vacant site) = CH_3 (ad) + H (ad)	90 wt.% Ni-Al_2O_3	490-590	Fluidized bed
Hazra et al. [80]	All steps in Tables 2.2 and 2.3 are taken into consideration	5% Ni/γ-Al_2O_3	500	Microbalance
Borghei et al. [83]	CH_4 + I (Vacant site) = CH_3 (ad) + H (ad)	Ni-Cu/MgO	550-650	Fixed bed

The equation as written above is a modified form of the rate equation developed by Grabke [75]. Two essential differences are observed between the two. In Bernardo et al.'s [82] equation, the rate is independent of carbon activity and an inhibiting effect by hydrogen is taken into account, in the denominator of Equation 2.18, with experimental data demonstrating inhibition by hydrogen as shown in Figure 2.17. Bernardo et al. [82] found that for the Cu-Ni alloy, the value of alpha that best fits Equation 2.18 to the experimental data was 0.3. The rate equation predicted the experimental data well at lower hydrogen pressures, but at higher hydrogen pressures, a discrepancy between the predicted and experimental rate was observed due to high carbon gasification rates.

Demicheli et al. [76] model

Demicheli et al. [76] studied carbon formation from CH_4-H_2-N_2 mixtures using Ni/Al_2O_3-CaO in the 565-665ºC temperature range. The authors implemented a separable kinetics technique for developing a rate equation to predict carbon deposition. The authors used two dependent variables to calculate the reaction rate: the first is the rate of carbon deposition without deactivation (r*) and the second is an activity factor (a). The actual rate of carbon deposition at any time (r) is equal to the product of (r*) and (a). (r*) can be defined as the maximum carbon deposition rate at time (t) while (a) is the activity coefficient which accounts for the reduction in the maximum rate of carbon deposition due to active sites being blocked. The model was able to accurately predict the rate and the deactivation regime for the catalyst under study.

Using the reaction mechanism shown in Table 2.1, and assuming methane adsorption as the rate limiting step (step 1 in Table 2.1), Demicheli et al. [76] developed the following equations to calculate the maximum rate for carbon deposition and the catalyst activity:

$$r^* = k(P_{CH_4} - \frac{P_{H_2}}{K_p}) / (1 + K_H P_{H_2}^{0.5})^n \quad (2.19)$$

For activity:

$$a = \exp(-k_d P_{CH_4} \tau / P_{H_2}) \quad (2.20)$$

$$\tau = t - t^* \quad (2.21)$$

so that the total rate at time t:

$$r = r^*.a \quad (2.22)$$

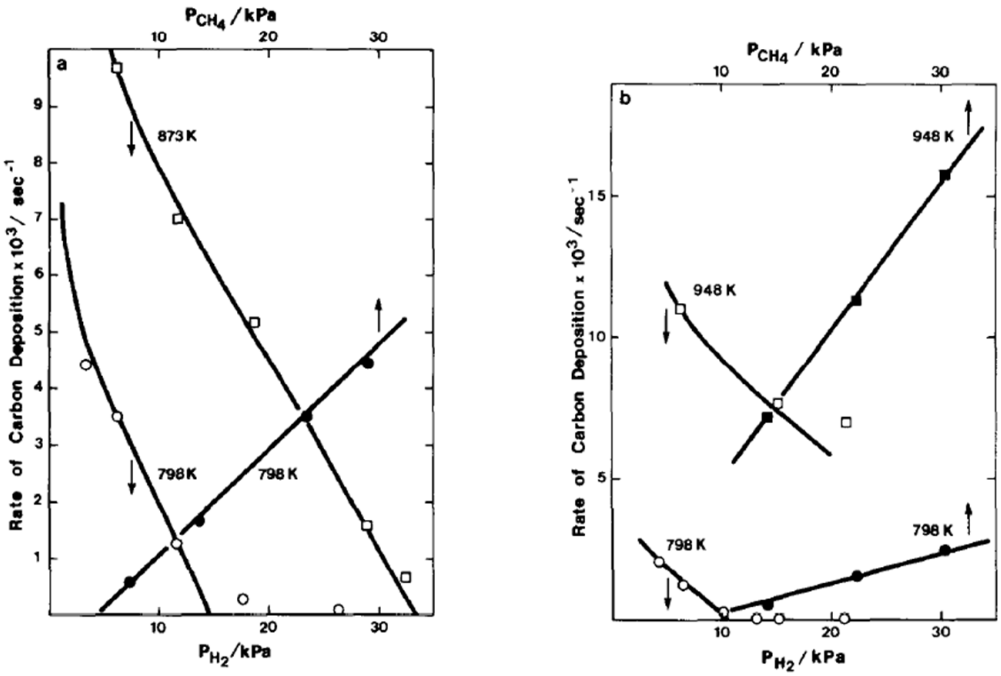

Figure 2.17 - The rate of carbon deposition on Cu-Ni/SiO_2, with a) 1% Cu and b) 10% Cu (Reprinted from [82], with permission from Elsevier).

where:

$k = 2.83*10^{8} \exp(-97000/(RT))$ and is the specific rate constant for the rate of carbon deposition (g /g_{cat} h kPa) [77];

K_p : equilibrium constant for methane cracking (kPa) [77];

$K_H = 9.883*10^{-9} \exp(108300/(RT))$ and is the equilibrium constant for hydrogen adsorption ($kPa^{-0.5}$) [77];

k_d is the specific rate constant for the deactivation rate (h^{-1});

t^* is the time at which carbon deposition rate reaches a maximum (h); and

n is the number of active sites participating in the rate limiting step, best fit at n=7 [77].

Snoeck et al. [25] model

Snoeck et al. [25] developed a model for the formation of filamentous carbon via methane cracking over a commercial nickel catalyst. The experimental work supporting this model was done in an electro-balance in the 500-550°C temperature range and a pressure

between 1.5-10 bar. This model assumes that methane is first adsorbed, followed by a series of dehydrogenation reactions leaving carbon adsorbed on nickel. This carbon will eventually form the carbon filament, as shown in Tables 2.1 and 2.3. The release of the first hydrogen atom from the adsorbed methane is assumed to be the rate-determining step, step 2 in Table 2.1. The reaction steps could be arranged based on the physical process taking place: surface reactions, dissolution/segregation at the gas/nickel side, diffusion of carbon through nickel, and precipitation/dissolution of carbon as filaments at the nickel/support side. The possible surface reaction mechanisms they described for methane cracking on a nickel surface are shown in Figure 2.18.

By assuming the surface concentrations of adsorbed H, CH, and CH_2 are negligible, the following rate equation was derived assuming all reaction steps are reversible at high carbon concentration and a small concentration gradient around the active site:

$$r = \frac{k_m^+ K_{CH_4}.(P_{CH_4} - \frac{1}{K_M^*}.P_{H_2}^2)}{\left(1 + \frac{1}{K_r^{"}}.P_{H_2}^{3/2} + K_{CH_4}.P_{CH_4}\right)^2} \qquad (2.23)$$

where:

$k_m^+ = 25040\exp(-58893/(RT))$ and is the specific rate constant for the rate limiting step, mol/g_{cat}.h;

$k_{CH_4} = 0.21\exp(-567/(RT))$ and is the equilibrium constant for methane adsorption, J/mol;

K_M^* is the experimental threshold constant; and

$K_r^{"} = 5.18*10^7 \exp(-133210/(RT))$

The model results showed that the surface concentrations of adsorbed methane and hydrogen are correlated to the partial pressures of methane and hydrogen. While for the carbon surface concentration, the results showed that it is not dependent on hydrogen and/or methane partial pressures. The model gave excellent prediction of the carbon formation rate at 500ºC, as shown in Figure 2.19.

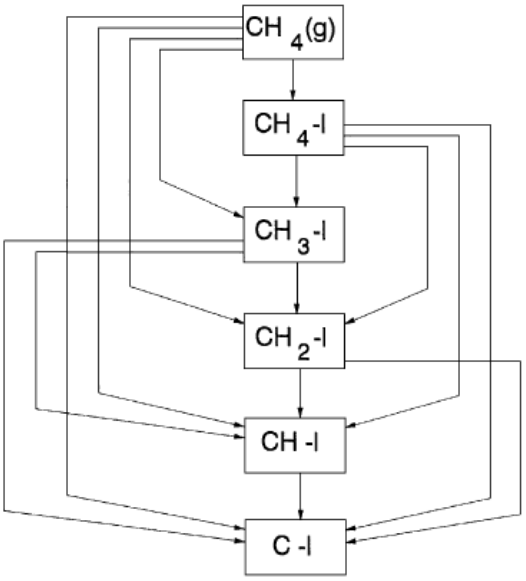

Figure 2.18 - Possible methane cracking reaction pathways (Reprinted from [25], with permission from Elsevier)

Kuvshinov et al. [77] model

Kuvshinov et al. [77] developed a model predicting carbon deposition as a result of methane catalytic cracking. To develop their model, they studied the effect of varying CH_4-H_2 and temperature on a highly loaded nickel catalyst in a flow vibro-fluidized bed catalyst micro-reactor. This model calculates the maximum carbon deposition while taking into account catalyst deactivation. Kuvshinov et al. [77] used the maximum carbon deposition rate developed by Demicheli et al. [76], and then developed an equation that predicts the maximum amount of carbon deposition until the catalyst is completely deactivated.

The rate of carbon formation ($g/g_{cat}.h$) can be calculated from the following equation:

$$r = \left[-\frac{n+1}{2} k^* r^{*1/n+2} (C^2 - C_{\max}^2) + r^{*1+1/n} \right]^{n/(n+1)} \tag{2.24}$$

The maximum amount of carbon deposited (g/g_{cat}) until the catalyst is deactivated is:

$$C_{\max b} = \left[-\frac{2}{k^* (n+1) r^{*1/n+2}} + C_{\max}^2 \right]^{1/2} \tag{2.25}$$

where:

r^* is the rate of carbon formation ($g/g_{cat}.h$), as calculated from Equation 2.19 (Demicheli et al. [76] model);

C_{max} is the specific weight of carbon formed during time t where the rate of formation is maximum (g/g_{cat});

n is the number of active sites participated in the limiting step, best fit at n=7;

C is the specific weight of carbon formed on the catalyst (g/gcat); and

$k^* = 2.73*10^{-13}\exp(99270/(RT))$, which is the deactivation rate constant in $(g_{cat})^3$. h/g^3.

In their conclusions, Kuvshinov et al. [77] found that the methane catalytic cracking mechanism can be interpreted using the Langmuir–Hinshelwood approach. The controlling step is the dissociative adsorption of methane. Catalyst deactivation was proportional to the amount of carbon deposited on the catalyst.

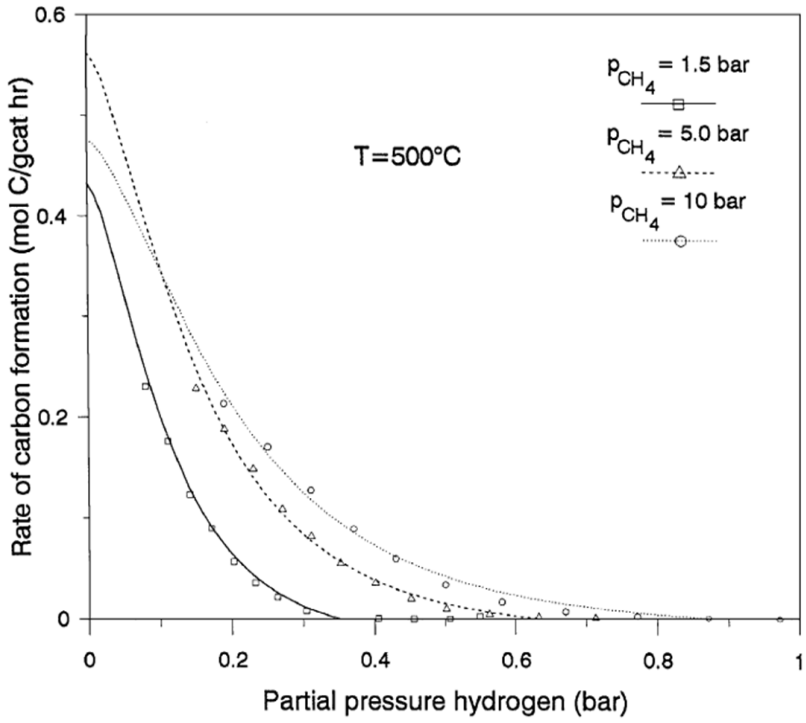

Figure 2.19 - Model prediction and experimental results of the carbon formation rate at 500ºC using a commercial nickel catalyst (Reprinted from [25], with permission from Elsevier)

2.7.1.2 Models assuming dissociative adsorption of methane (Table 2.2)

Alstrup and Tavares [79] model

Starting with the Grabke [75] mechanism, Alstrup and Tavares [79] developed a model for methane catalytic cracking to calculate the carbon deposition rate. In their experimental study, they used a Ni/SiO_2 catalyst and a mixture of CH_4 and H_2 as the reactant gas. Using molecular beam studies of methane interacting with Ni(111), Alstrup and Tavares modified the Grabke model to start with direct methane dissociative chemisorption as shown in Table 2.2.

Using a Langmuir-type model (the occupation of a site is independent of other sites being occupied), Alstrup and Tavares developed the model assuming that: 1) all the reaction mechanism steps are in equilibrium except steps 1-4 in Table 2.2, 2) the surface species are competing for the surface sites, and 3) a constant carbon coverage on the catalyst surface.

The authors derived four rate equations; each equation representing the rate of carbon deposition assuming that one of the steps described by 1-4 in Table 2.2 is the rate limiting step. By comparing the experimental results with the predicted results for each case, Alstrup and Tavares concluded that assuming steps 3 or 4 as the rate limiting step didn't truly predict the experimental data. While assuming steps 1 or 2 as the limiting steps, the predicted values agreed well with the experimental data, as shown in Figure 2.20. Then they modified their model assumptions: steps 1 and 2 are not in equilibrium and the rates for both steps are equal and the two rates also equal the overall rate.

Considering step (1) as the rate-limiting step, they developed the following rate equation:

$$r_1 = k_1(P_{CH_4} I^2 - \frac{I_{CH_3} I_H}{K_1}) \qquad (2.26)$$

Considering step (2) as the rate-limiting step, they developed the following rate equation:

$$r_2 = k_2(I_{CH_3} I_v - \frac{I_{CH_2} I_H}{K_2}) \qquad (2.27)$$

Where K_1 and K_2 are the equilibrium constants for reaction steps (1) to (2) and k_1 and k_2 are the forward rate constants for reaction steps (1) and (2), respectively. I is the concentration of vacant sites. The site balance for the vacant sites could be expressed as:

$$I = 1 - I_H - I_{CH} - I_{CH_2} - I_{CH_3} - I_C \quad (2.28)$$

where, I_x is the concentrations of sites occupied by species x.

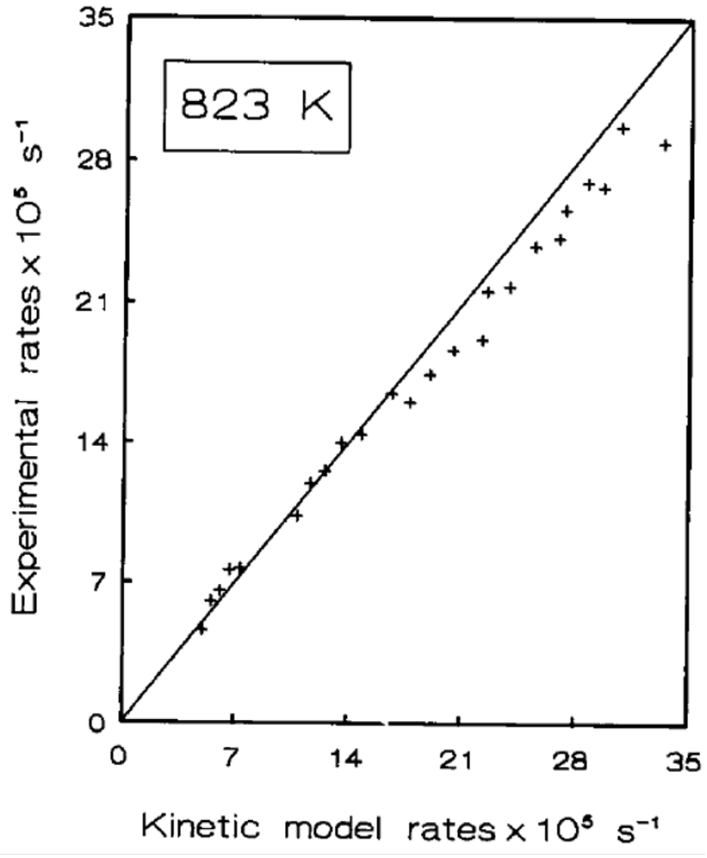

Figure 2.20 - Predicted and experimental rate of carbon deposition (Reprinted from [79], with permission from Elsevier).

Zavarukhin and Kuvshinov [78] model

Zavarukhin and Kuvshinov [78] developed a mathematical model for the formation of carbon from methane catalytic cracking using different mixtures of CH_4-H_2 and a 90 wt.% Ni-Al_2O_3 catalyst. Zavarukhin and Kuvshinov [78] used the reaction mechanism shown in Table 2.2. The hydrogen volume in the mixture was varied between 0-40%, and the temperature was varied between 490-590ºC in a fluidized catalyst bed micro-reactor. The rate limiting step was assumed to be the release of the first hydrogen atom, as shown in step 1 of Table 2.2.

The maximum rate for carbon formation, g/h.g_{cat}, can be calculated from the following equation:

$$r_{\max} = k(P_{CH_4} - \frac{P_{H_2}^2}{K_p}) / (1 + K_H P_{H_2}^{0.5})^2 \quad (2.29)$$

The change in total carbon deposited and rate of deposition can be calculated by integrating the following equations:

$$\frac{dc}{dt} = r_{\max} a \quad (2.30)$$

$$\frac{da}{dt} = -k_a r_{\max}^2 ca \quad (2.31)$$

where:

C is the specific weight of carbon deposited on the catalyst (g/gcat);

$k = \exp\left(20.492 - \frac{104{,}200}{RT}\right)$ and is the specific rate constant for the rate of carbon deposition (kPa);

$K_p = 5.088 * 10^5 \exp\left(-\frac{91{,}200}{RT}\right)$ and is the equilibrium constant for methane cracking (kPa);

$K_H = \exp\left(\frac{163{,}200}{RT} - 22.426\right)$ and is the equilibrium constant for hydrogen adsorption ($kPa^{-0.5}$);

k_d is the specific rate constant for the deactivation rate (h^{-1});

$k_a = \exp\left(\frac{135{,}600}{RT} - 32.077\right)$ and is the deactivation rate constant $(g_{cat})^3$. h/g^3; and

a is the activity coefficient, $a = r / r_{\max}$.

Zavarukhin and Kuvshinov [78] applied their model equations to predict the specific carbon content on the catalyst at 823°C. The discrepancy between the calculated and experimental data didn't exceed 10%, as shown in Figure 2.21.

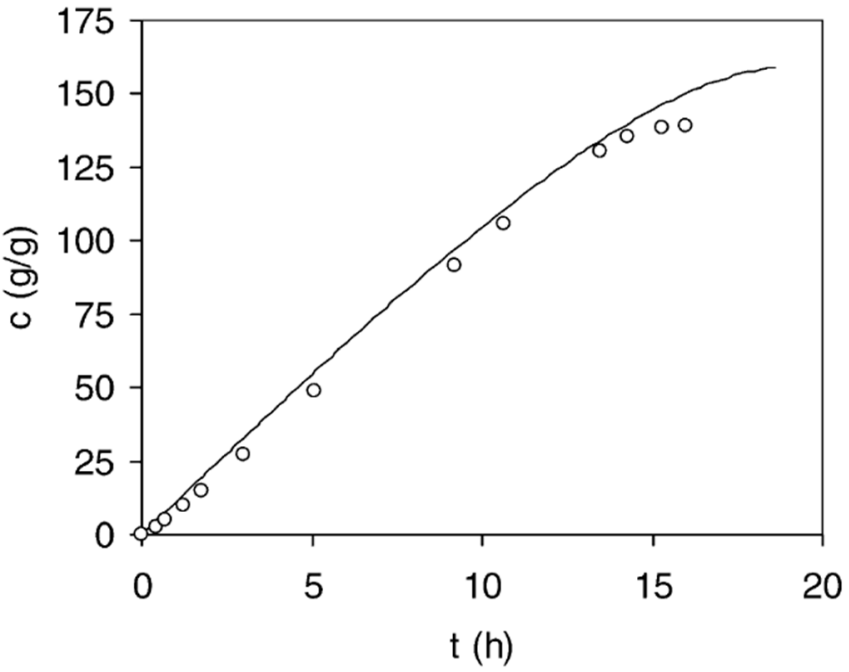

Figure 2.21 - Experimental (points) and calculated (line) carbon deposition amounts as a function of time at 550ºC (Reprinted from [78], with permission from Elsevier)

Hazra et al. [80] model

Hazra et al. [80] performed an experimental study using a thermo-balance at 500°C at 1-10 bar and a 5% Ni/γ-Al_2O_3 catalyst. The authors assumed that the cracking rate is controlled by the deposition of carbon and the formation of carbon whiskers. They assumed that deactivation takes place due to the formation of encapsulating carbon. The 9-step mechanism shown in Tables 2.2 and 2.3 were used. Using the Langmuir–Hinshelwood mechanism, they developed a reaction rate equation based on non-separable kinetics. The model is a series of differential equations that measures the concentration of the reaction intermediates starting with the partial pressures of CH_4 and H_2. By solving the differential equations without assuming any rate limiting step, the model can predict the reaction rate and the change in catalyst weight from the onset of the reaction to complete deactivation of the catalyst as a function of time, as shown in Figure 2.22. The deactivation predicted in the model occurs via a decrease in the number of active sites available for the reaction due to encapsulating carbon deposition. Hazra et al. [80] also reported that increasing the total pressure may increase the catalytic activity of the catalyst over time. They attributed this pressure increase effect to the increase in hydrogen partial pressure, which may decrease the rate of carbon formation and catalyst deactivation at the same time.

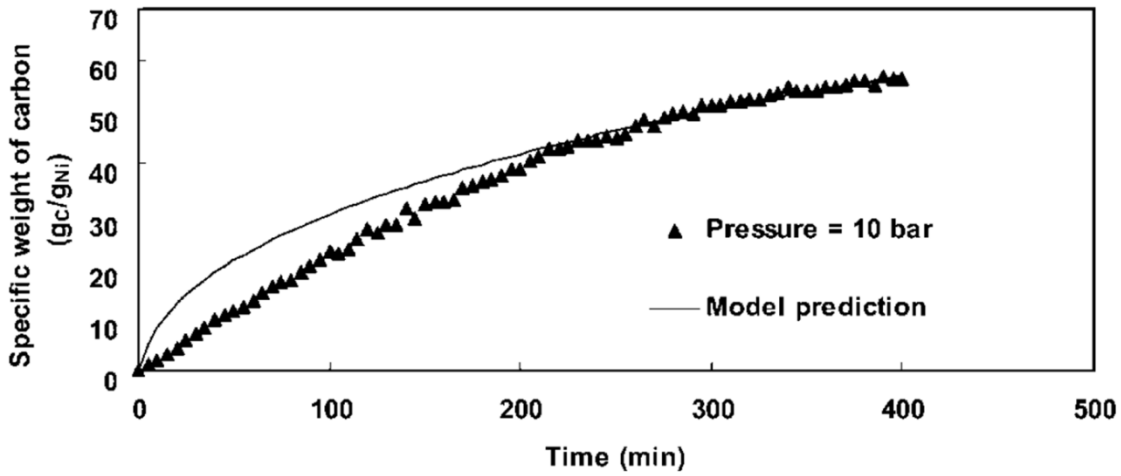

Figure 2.22 - Experimental and calculated change in specific carbon weight at 500ºC (Reprinted from [80], with permission from John Wiley & Sons)

Borghei et al. [83] model

Borghei et al. [83] developed a kinetic model for methane cracking over Ni-Cu/MgO in the temperature range 550-650°C using a CH_4-H_2 mixture at atmospheric pressure. The rate limiting step is the dissociative adsorption of methane, step 1 in Table 2.2. They developed the following equation for calculating the maximum methane decomposition rate, in mol/gcat.h, assuming the surface concentrations of the reaction intermediates are negligible:

$$r^* = \frac{k^+ P_{CH4} - \frac{k^-}{k_r} P_{H2}^2}{\left(1 + \frac{k^-}{k_r} P_{H2}^{3/2}\right)^2} \tag{2.32}$$

They defined an activity term, a, as a function of time, which can be calculated from the following equation:

$$a = \frac{1}{[1+(d-1)r_d t]^{1/(d-1)}} \tag{2.33}$$

so that the overall reaction rate is:

$$r = r^*.a \tag{2.34}$$

where:

$k^+ = 597.98 * (51234.6/\mathrm{RT})$ and is the rate constant of the forward reaction of the rate limiting step, mol/gcat/h/atm;

$k^- = 17 * (9217.5/\mathrm{RT})$ and is the rate constant of the reverse reaction of the rate limiting step, mol/gcat/h/atm$^{1/2}$;

$k_r = 0.607 * (8045.6/\mathrm{RT})$, atm$^{3/2}$;

d is the order of deactivation, and the optimum value is 2.11;

k_d is the specific constant of deactivation; and

r_d is a function of temperature, and methane and hydrogen partial pressures;

The deactivation of the catalyst was found to be a second order reaction. The deactivation is a function of time, temperature, and partial pressures of methane and hydrogen. The model showed excellent agreement with the experimental data.

2.7.2 Mathematically fit rate equations

This group of models predicts the total carbon deposited on the catalyst, but doesn't take into account the different reaction mechanisms that have been proposed for methane cracking. Caton et al. [10] and Villacampa et al. [13] divided the reaction term from the onset of reaction to catalyst deactivation into two physical stages: 1) nucleation and 2) filament growth, which takes into account the catalyst deactivation stage. An equation was developed for each stage to calculate the carbon deposited. Then by adding the two amounts together, the total amount of carbon formed can be calculated from which the total carbon formation rate can be predicted. The proposed equations have been fit mathematically (regression analysis) using different parameters. The parameters were correlated to different reaction conditions, which are listed in Tables 2.5 and 2.6.

For both models, four variables must be defined before discussing any details:

C_{Cm}: the total number of carbon filaments that can be formed in the nucleation stage at certain conditions;

C_{CN}: total amount of carbon deposited during the nucleation stage, mg;

C_{CW}: total amount of carbon deposited during the carbon filament stage, mg; and

C_C : the total content of carbon, mg.

Where,

$$C_C = C_{CN} + C_{CW} \quad (2.35)$$

Table 2.5- The effect of reaction temperature on the kinetic parameters discussed in reference [10] ([10], with permission from Elsevier)

$T_{reac.}$, °C	C_{Cm} (g.c/g.cat.)	$\psi_{C1}*10^2$ (g.c/g.cat. min.)	ψ_{C2} (g.c/g.cat.min.)	rc_W (g.c/g.cat.min.)
550	0.18256	5.019	0.2592	7.2
600	0.22010	6.214	0.37254	5.7
625	0.21368	7.224	0.47159	3.1
650	0.14463	13.139	1.57469	4

Table 2.6- The effect of reduction temperature on the kinetic parameters in reference [10] ([10], with permission from Elsevier)

$T_{red.}$, °C	C_{Cm} (g.c/g.cat.)	$\psi_{C1}*10^2$ (g.c/g.cat. min.)	ψ_{C2} (g.c/g.cat.min.)	rc_W (g.c/g.cat.min.)
600	0.39801	0.02872	0.16627	4.2
700	0.23620	0.06434	0.32012	6.4
800	0.18625	0.11645	0.55713	6.6

Caton et al. [10] model

This model was developed based on an experimental study that was conducted using a Ni/Al_2O_3 catalyst and a thermo-balance, in the 600-800ºC temperature range. Several parameters were studied experimentally to determine their effect on the reaction rate, including hydrogen partial pressure, methane partial pressure, reaction temperature, and pre-reduction temperature. Deactivation was assumed to be due to encapsulation of Ni with coke and/or space limitations. The driving force for coking was assumed to be the difference in chemical potential between the gas phase and the carbon filaments. A maximum number of carbon filaments can be formed during the nucleation step according to the reaction conditions, C_{Cm}, which consequently

determines the maximum amount of coke that can be deposited, C_C. Based on the previous assumptions, Caton et al. [10] developed the following equations.

The rate of carbon formation during the nucleation stage can be expressed as:

$$r_{CN} = \frac{dC_{CN}}{dt} = \psi_{C1}(C_{Cm} - C_C)^2 + \psi_{C2} C_C (C_{Cm} - C_C) \tag{2.36}$$

The rate of filament growth during the final steady-state period is:

$$rc_W = dC_{CW} / dt \tag{2.37}$$

By integrating Equations 2.36 and 2.37 and replacing the terms in Equation 2.35, the total carbon deposited is:

$$C_C = C_{Cm} \frac{\psi_{C1}(1 - \exp(-\psi_{C2} C_{Cm} t))}{\left(\psi_{C1} + (\psi_{C2} - \psi_{C1})\exp(-\psi_{C2} C_{Cm} t)\right)^2} + r_{CW} t \tag{2.38}$$

And the overall rate of carbon formation will be:

$$rc = \left[\frac{\psi_{C1}(\psi_{C2} C_{Cm})^2 (1 - \exp(-\psi_{C2} C_{Cm} t))}{\left(\psi_{C1} + (\psi_{C2} - \psi_{C1})\exp(-\psi_{C2} C_{Cm} t)\right)^2} \right] + r_{CW} \tag{2.39}$$

$C_{Cm}, \psi_{C1}, \psi_{C2}$ (which are fitting parameters), and rc_W were correlated using nonlinear regression, and their values at different reaction and reduction temperatures are listed in Tables 2.5 and 2.6 [10].

Villacampa et al. [13] model:

This model was used to predict the total carbon deposited from the start of the cracking reaction until complete catalyst deactivation. A comprehensive experimental study was conducted using a 30% Ni/Al_2O_3 catalyst in a thermo-balance. The study parameters were reaction and reduction temperatures and feed composition. This model follows the same trends proposed by Caton et al. [10] and it uses the same equations that were discussed in the Caton et al. [10] model. However, Villacampa et al. [13] conducted a more detailed experimental study to better understand the effect of operating conditions on the deposited carbon and the rate of deposition,

to help achieve a better correlation for the model parameters ($C_{Cm}, \psi_{C1}, \psi_{C2}$, and rc_w). The comparison between the model prediction and the experimental results is shown in Figure 2.23; the figure shows excellent agreement between the experimental and model results.

Villacampa et al. [13] reported data for the effect of CH_4 and H_2 partial pressures, reaction temperature, reduction temperature, and reaction generation cycles on the kinetic parameters ($C_{Cm}, \psi_{C1}, \psi_{C2}$, and rc_W). Based on these data, the following equations were developed to predict the kinetic parameters in the 550 - 650°C temperature range:

$$C_{Cm} = 0.239T - 8.433T^2 + 9.913E-7T^3 - 3.88E-10T^4 \quad (2.40)$$

$$\psi_{C1} = -25.587T + 0.089T^2 - 1.033E-4T^3 - 3.989E-8T^4 \quad (2.41)$$

$$\psi_{C2} = -5.427T + 0.0188T^2 - 2.186E-5T^3 + 8.435E-9T^4 \quad (2.42)$$

$$rC_w = -27.9116T + 0.0962T^2 - 1.104E-4T^3 + 4.216E-8T^4 \quad (2.43)$$

where T is the temperature in Kelvin units.

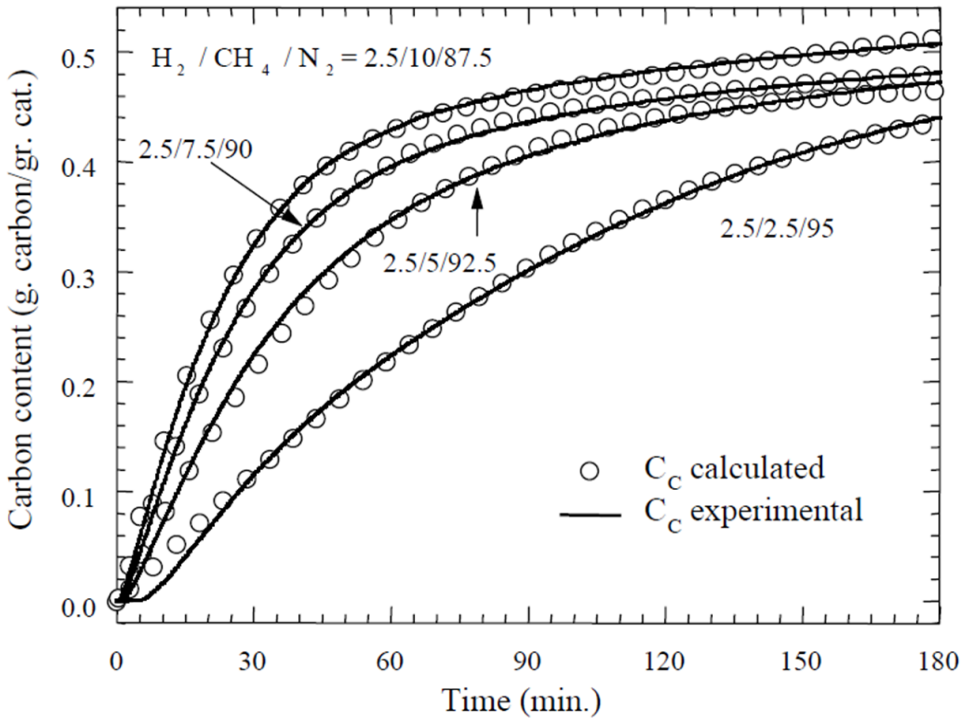

Figure 2.23 - Experimental and predicted data for different reacting mixtures at 600ºC **(**Reprinted from [13], with permission from Elsevier)

The value of ψ_{C2} was assigned to zero for the regenerated catalyst, because the catalyst was completely sintered during the regeneration period. Therefore, they developed Equation 2.39 [10] for calculating the total carbon deposited to become in the following form:

$$C_C = C_{Cm} \frac{\psi_{C1} C_{Cm} t}{1 + \psi_{C1} C_{Cm} t} + r_{Cw} t \qquad (2.44)$$

2.7.3 Global rate equation models

Fukada et al. [30] rate equation

The model developed by Fukada et al. [30] was used to study the overall cracking rate of methane in a fixed bed reactor using a nickel/silica catalyst. The model was developed to predict the cracking rate until the catalyst completely deactivated. The authors found that the rate can be expressed using a single reaction rate equation that is first order in methane. The overall first order reaction rate constant, $k_{decomp.}$, was expressed as:

$$k_{decomp} = 3.09 * 10 \exp(-29.5[kJ/mol]/R_g T) \qquad s^{-1} \qquad (2.45)$$

Muradov et al. [66] rate equation

The model developed by Muradov et al. [66] was used to study the methane cracking rate over activated carbon and carbon black. They found that the apparent reaction order is 0.5 in methane for both activated carbon and carbon black, as shown in the following equation:

$$-r_{CH_4} = k * P_{CH_4}^{0.5} \qquad (2.46)$$

The apparent activation energy measured was 160-201 kJ/mol for activated carbon and 205-236 kJ/mol for carbon black, in the temperature range of 600-900°C.

2.8 Fluidized Bed Reactor Applications for Methane Catalytic Cracking

Fluidized bed reactors have a wide range of applications in the chemical, metallurgical and petroleum industries. A fluidized bed reactor is particularly suitable for methane catalytic cracking since it enables continuous addition or withdrawal of solid particles. The catalyst can be circulated between the cracking reactor and the regenerator based on the deactivation rate and the

energy requirement of the unit, since the catalyst is the heat source for the cracking reactor. Therefore the ratio of the total solid catalyst amount to the total gas amount must be high enough to prevent a temperature drop through the fluidized bed [2,84]. Fluidized bed reactors offer many advantages for solid-catalyzed reactions over fixed-bed reactors. Those advantages are: ease of temperature control, ease of maintaining a constant temperature in the bed due to vigorous mixing provided by fluidization, enhanced heat and mass transfer, and low cost of catalyst handling [15,66,71]. Fluidized bed reactors are considered the most promising reactor for the large-scale catalytic cracking of natural gas to produce hydrogen-rich gas [84].

2.8.1 Process economics

Thermal energy calculations indicate that the energy requirement per mole of hydrogen produced from methane catalytic cracking (37.4 kJ/mol H_2) is considerably less than that required for producing one mole of hydrogen from the steam reforming process (63.3 kJ/mol H_2) [2,15]. In addition, the hydrogen produced from methane catalytic cracking does not contain any CO or CO_2, which eliminates further downstream separation processes. While the ratio of hydrogen produced per mole of methane fed is lower in methane catalytic cracking due to the absence of steam, overall economic studies have shown that a fluidized bed catalytic cracking unit has cost advantages over steam reforming units [5-6,85]. The fluidized bed catalytic cracking unit should contain two fluidized bed reactors; one for cracking and one for regenerating the catalyst. However, studies have also shown that the operating cost for the two fluidized bed reactors for cracking and regeneration and the solids-circulation system are higher than the operating cost for the conventional steam reforming unit [22].

In 1987 U.S. dollars, Steinberg and Cheng [85] compared different methods for hydrogen production at an industrial scale of 10^8 SCF/D of hydrogen gas at 300-600 psig. They concluded that methane thermal cracking is the most economical method for hydrogen production. For an energy amount of 10^6 Btu (~3.7 kmol of H_2), they found that hydrogen produced from methane cracking will cost U.S. $5.1. In Table 2.7, the cost of hydrogen production for each method is given in terms of the net hydrogen production cost for 10^3 SCF, the credit gained from by-products, and finally the net cost for producing 10^6 Btu after including the cost of different operations required for processing hydrogen after production, like separation and enriching. All the prices are in U.S. $ and the processes are arranged in terms of the net cost of 10^6 Btu.

Table 2.7 – Comparison of hydrogen production costs for different processes ([85], with permission from the International Journal of Hydrogen Energy)

Process	Total hydrogen production cost in U.S.$ for 10^3 SCF	By-product	By product credit (U.S.$)	Net cost for 10^6 Btu (U.S.$)
Methane cracking	2.29	Carbon	0.65	5.1
Hydrocarb process	5.82	Carbon	4.04	5.52
Steam reforming	2.06	Steam	0.16	5.9
Coal gasification with electricity chemical shift (Westinghouse)	4.51	Steam	1.8	8.4
Partial oxidation	3.12	Sulphur	0.03	9.6
Steam iron	4.75	Power	1.14	11.21
High temperature steam electrolysis	5.06	Oxygen	0.84	13.12
Texaco gasification	4.35	Sulphur	0.08	13.26
Coal gasification with high temperature electrolysis	4.43	None	0	13.76
K-T gasification	5.12	sulphur	0.02	15.84
Water electrolysis	6.57	Oxygen	0.83	17.83

Muradov [7] performed an economic study of methane catalytic cracking in a fluidized bed catalytic reactor and a fluidized bed heater for catalyst regeneration. The final gaseous product of the industrial unit under study was assumed > 99% by using a gas separation unit. The analysis was done at three levels of production, based on unit size in MMscfd (Million Metric Standard Cubic Feet per Day), namely: small (6 MMscfd), medium (20 MMscfd) and large (60 MMscfd). The carbon selling price was assumed U.S. $300/ton. Muradov [7] developed a relationship between the market value of hydrogen and natural gas for the three plant sizes, as shown in Figure 2.24. The authors also compared methane catalytic cracking and methane steam reforming based on the large plant size (60 MMscfd). The study involved two cases for methane steam reforming, with and without CO_2 sequestration. The carbon price was assumed to range between U.S. $160-460/ton. The results showed that methane catalytic cracking in a fluidized bed is more economic than steam reforming with CO_2 sequestration and is comparable with steam

reforming without CO_2 sequestration. If future environmental regulations impose CO_2 sequestration, then methane catalytic cracking will be the better option even without adding the carbon selling credits.

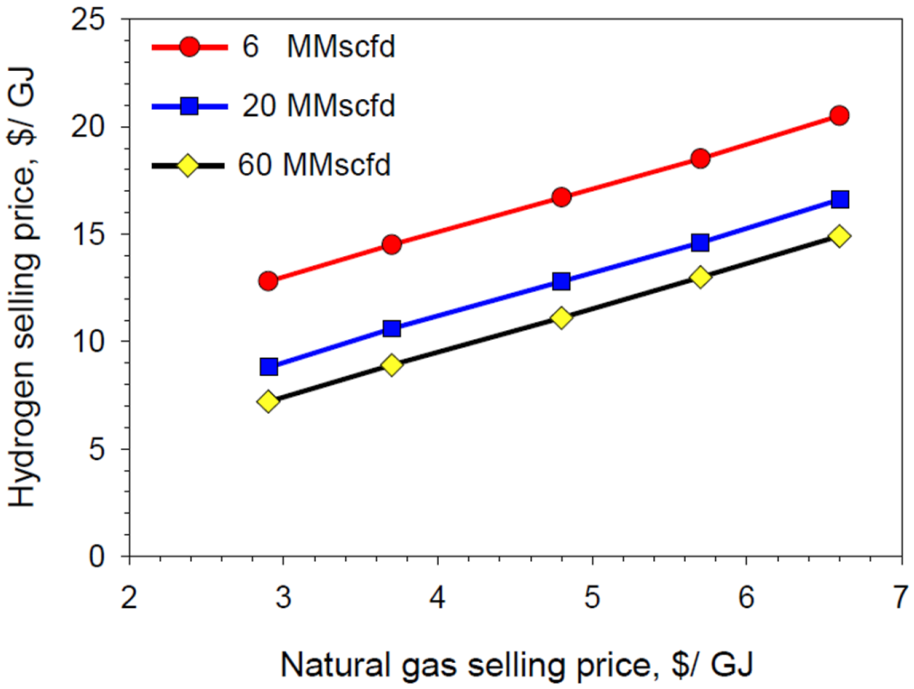

Figure 2.24 - The relationship between hydrogen and natural gas selling prices (Reprinted from [7], with permission from the National Renewable Energy Laboratory for the U.S. Department of Energy)

A common conclusion in the reported literature economic analyses of methane catalytic cracking [17-18,57,65] is that the carbon-selling price is the key aspect to make the process economically attractive. However, the carbon-selling price is a function of the properties of the deposited carbon [65]. The properties of carbon produced depend on the operating conditions and the type of catalyst used [15,65]. The key is therefore to devise a process that maximizes the quality of the carbon and to find an optimum balance between selling the carbon produced and gasifying it for catalyst regeneration. Carbon can be used as a commodity product or sequestered (or stored) for future uses [84]. For example, carbon can be used as a substitute for carbon black, fibres, graphite, electrodes in the aluminum industry, composites, and carbon fillers, in tires and plastics, or can be used as a catalyst support [5,16]. Also, filamentous carbon is used as an additive in polymers and electronic components. Carbon may also be burned in air (Equation 2.14) and/or in CO_2 (Equation 2.16) to supply heat to the cracking reactor or gasified with H_2O (Equation 2.15) to produce additional hydrogen.

Separation of the product carbon filaments is a promising way for producing high quality carbon nano-tubes. Separation of the carbon filament from the support is much less of an issue [59] than the removal of the metal (e.g. by acid treatment), the latter still being an important challenge [65]. One way to improve the marketing of the filamentous carbon is to increase the amount of carbon deposited on the catalyst, which will reduce the metal concentration to acceptable marketing limits [65]. For example, nickel may be considered an impurity for some applications but considered an "additive" for others, such as using this carbon as a support for a nickel catalyst or using it for hydrogen storage applications.

2.8.2 Studies involving fluidized beds and methane catalytic cracking

Universal Oil Products developed the Hypro process for cracking natural gas to produce high-purity hydrogen [21]. The Hypro process was conducted in a fluidized bed reactor containing 7% Ni/Al_2O_3. The fluidized bed cracker was connected to a fluidized bed regenerator [22]. Deactivated catalyst was regenerated by burning the deposited carbon in air using the regenerator and the catalyst circulation from the regenerator to the cracker was used to supply heat to the reaction [21]. A maximum production rate was achieved at ambient pressure and a cracking reactor temperature of 870°C [22]. Increasing the total pressure had a strong detrimental effect on the reaction rate. For example, at 870°C, the hydrogen in the effluent was reduced from 97.6% at 1 atm to 75.8% at 17 atm.

Weizhong et al. [86] modified a two-stage fluidized bed reactor to study methane catalytic cracking using a $Ni/Cu/Al_2O_3$ catalyst. The temperature in each stage was controlled separately. The temperature at the upper section was varied between 500-850ºC, while the lower section temperature was fixed at 500ºC. The high temperature stage was used to ensure high methane conversion, while the lower temperature stage was used to boost the effective carbon diffusion through the metal to form filamentous carbon. Weizhong et al. [86] conducted the same set of experiments with two other reactors and compared them to this two-temperature stage fluidized bed reactor; a packed bed reactor and a single-stage fluidized bed reactor with uniform temperature. Results indicated that the catalyst life and the conversion of methane increased significantly in the two-stage fluidized bed reactor compared to the other configuration. The catalyst life was significantly prolonged in the two-stage temperature reactor since the mismatch between carbon production rate and carbon diffusion rate at high temperature was advantageously

used. The carbon was produced at a higher rate in the high temperature stage and still diffused through nickel in the lower temperature stage.

Carbon black and activated carbon were used extensively in different studies for catalyzing the methane cracking reaction in a fluidized bed. Lee et al. [27] used different types of activated carbon to catalyze methane cracking. They studied several parameters including reaction temperature, gas velocity, and particle size. The catalyst showed good activity at the beginning but rapidly deactivated due to channel blocking by carbon deposition.

Muradov et al. [66] used a circulating fluidized bed reactor for methane cracking experiments, using carbon black and activated carbon catalysts. The catalyst flowed continuously between the cracker and regenerator as shown in Figure 2.25. Under the test conditions, in the cracker, both catalysts experienced an initial rapid drop in activity followed by slow deactivation, with the carbon black taking longer to deactivate. In terms of regeneration, the authors compared steam and carbon dioxide as regeneration agents. The activated carbon regained its activity completely after regeneration using steam, but the carbon black did not.

Dunker et al. [15] also used a carbon black catalyst for the methane cracking reaction in a fluidized bed reactor at temperatures between 810–980ºC. The results showed a rapid decrease in reaction rate in the first 50 minutes followed by a period of 1000 minutes where the rate remained stable, before slowly decreasing again. Dunker et al. [15] attributed the loss of activity to the reduced catalytic activity of the carbon produced compared to the initial carbon used and the filling of the micro pores and internal cavities in the catalyst by deposited carbon.

Jang and Cha [43] used Fe/Al_2O_3 catalyst for methane cracking in a fluidized bed at 700ºC. They studied several operating parameters and their effect on the hydrogen yield. The hydrogen yield increased when increasing the reaction temperature and decreased when increasing the methane flow rate. They also reported an interesting result concerning catalyst activity; the catalyst activity could be maintained via attrition of the deposited carbon.

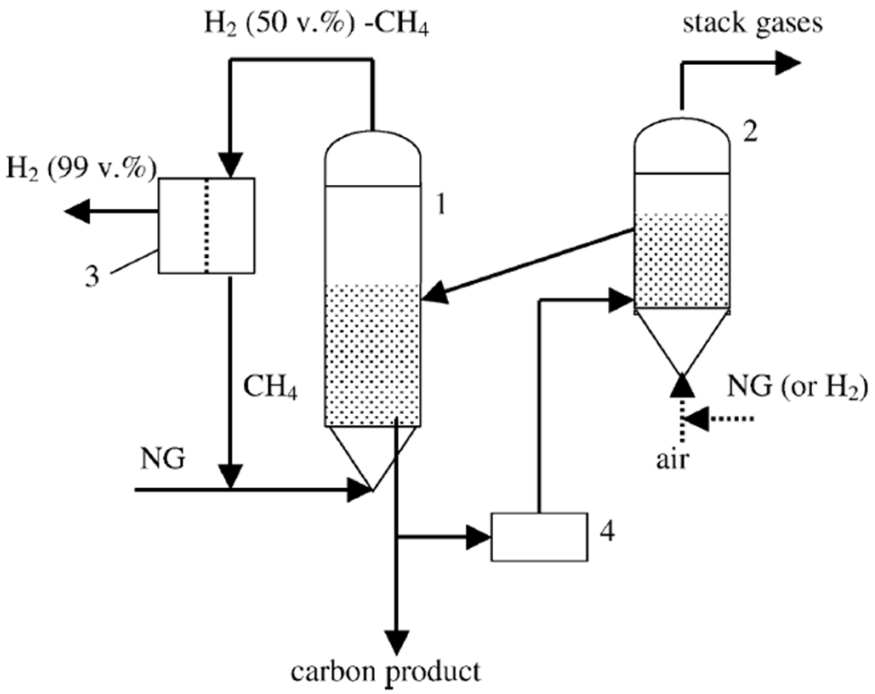

Figure 2.25 - Hydrogen production by the thermo catalytic decomposition of natural gas: 1—fluidized bed reactor, 2—heater, 3—gas separation unit, 4—grinder (Reprinted from [16], with permission from the International Journal of Hydrogen Energy)

Shah et al. [87] fabricated a 0.5% Mo/4.5% Fe/Al_2O_3 catalyst and used it for methane catalytic cracking in a fluidized bed between 650-700ºC. They used an intermittent mode of operation in a fluidized bed at high methane flow rates and a fixed bed at low methane flow rates. They concluded that the continuous fixed bed mode with low methane flow rate was more effective than the intermittent fluidized bed. Shah et al. [87] reported that the bench scale reactor they used in the experimental work had no heat or mass limitations which explained the better performance in the fixed bed compared to the fluidized bed, with a higher contact time also achieved in the fixed bed.

Ammendola et al. [44] studied methane catalytic cracking in a fluidized bed between 700–850ºC using a Cu/Al_2O_3 catalyst. They studied the effect of methane inlet concentration, reaction temperature, and the contact time by monitoring the total amount of carbon deposited on the catalyst and the deactivation time. The results showed that increasing the methane inlet concentration increased the total amount of carbon deposited until the methane concentration reached 20%, with any further increase in inlet methane concentration negatively affecting the

amount of carbon deposited. The deactivation time decreased with increasing methane concentration. Increasing the reaction temperature had a negative effect on the amount of carbon deposited and deactivation time. Increasing the contact time increased the amount of carbon deposited, but did not show any effect on the deactivation time.

Pinilla et al. [88] studied methane decomposition in a fluidized bed using a $Ni/Cu/Al_2O_3$ catalyst between 650-800°C. Different factors were studied including catalyst particle size, reaction temperature, and the space velocity and its ratio to the minimum fluidizing velocity. They found that increasing reaction temperature, space velocity, and the ratio of space velocity to minimum fluidizing velocity increased the reaction rate and deactivation rate at the same time. So, optimum conditions should be selected based on the balance between hydrogen production and catalyst deactivation. Between 650-700°C, high hydrogen production and catalyst deactivation rates were observed, and the carbon was deposited in the form of carbon nanotubes. At temperatures higher than 700°C, the carbon was deposited as encapsulating carbon. High hydrogen production and lower agglomeration were observed when the catalyst particle diameters were about 150 μm. To maximize hydrogen production and process economics, the effects of operating conditions must be well studied and quantified. In the following sections, the effects of operating parameters on methane cracking are discussed.

Reaction temperature

The stable operating temperature range for methane cracking using nickel is narrow, between 500 and ~550°C, with a maximum yield observed at 552°C [19]. Increasing the reaction temperature increases the initial reaction rate, but deactivation becomes faster at higher reaction temperatures due to rapid carbon deposition, which blocks the active sites [27].

Gas velocity

The gas velocity is a key parameter in fluidized bed operation. The fluidization quality or the gas–solid contacting pattern is strongly dependent on gas velocity. Usually the superficial velocity in the fluidized bed is expressed in terms of a multiple of the minimum fluidizing velocity [27]. If the gas flow rate is higher than that corresponding to the minimum fluidizing velocity, bubbles can form, which reduces the contact between the gases and catalyst. A lower gas velocity reduces the throughput of the reactor and will not induce fluidization, thus eliminating the positive effects of fluidized bed reactors [27].

Lee et al. [27] studied the behaviour of activated carbon for methane cracking in a fluidized bed at 850ºC. At lower gas velocities, methane conversion was higher than that at higher gas velocities, as shown in Figure 2.26.

Several equations are available to predict the minimum fluidizing velocity, U_{mf}. Geldart [89] proposed the following equations to calculate U_{mf} (in m/s):

for particles larger than 100 μm

$$U_{mf} = \frac{\mu}{\rho_g d}\left[(1135.7 + 0.0408 * Ar)^{1/2} - 33.7\right] \tag{2.47}$$

for particles smaller than 100 μm

$$U_{mf} = \frac{{d_p}^{1.8}\left(\rho_s - \rho_g\right)^{0.934} g^{0.934}}{1111\mu^{0.87}\rho_g^{0.066}} \tag{2.48}$$

where:

Ar is the Archimedes number, and is defined as:

$$Ar = \frac{{d_p}^3 \rho_g \left(\rho_s - \rho_g\right) g}{\mu^2} \tag{2.49}$$

d_P is the particle diameter (m);

ρ_s is the particle density (kg/m^3);

ρ_g is the density of methane (kg/m^3);

g is the gravity acceleration factor (m/s^2); and

μ is the gas viscosity (kg/m.s).

There are empirical equations that have been used for predicting the minimum fluidizing velocity for methane cracking. Muradov [16] used the following equation from [90] to calculate the minimum flow rate necessary for fluidizing the catalyst particles using methane:

$$G = \frac{0.005 d_P^2 {\varepsilon_m}^3 (\rho_s - \rho_g) \rho_g g}{\psi^2 (1 - \varepsilon_m)\mu} \tag{2.50}$$

where G is the mass flow rate necessary to initiate fluidization (g/cm).

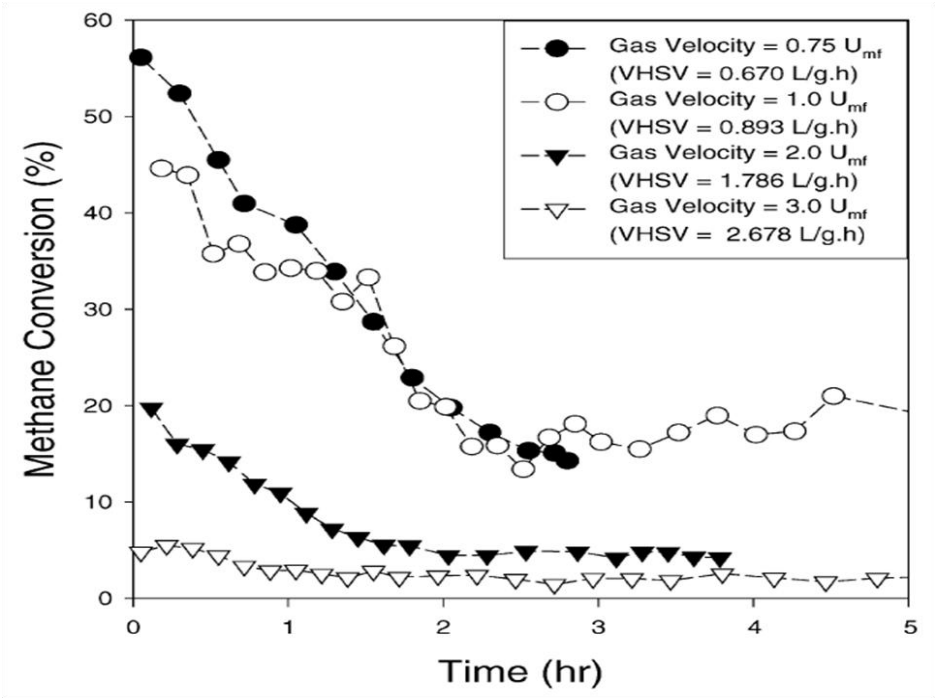

Figure 2.26 - Methane conversion as a function of gas velocity using activated carbon at 850ºC (Reprinted from [27], with permission from Elsevier)

Dunker et al. [15] used the following equation from [91] to calculate the minimum fluidizing velocity in cm/s:

$$U_{mf} = \frac{\varepsilon_{mf}^{3} d_P^2 (\rho_s - \rho_g) g}{180(1-\varepsilon_m)\mu} \tag{2.51}$$

where:

d_P is the particle diameter (cm);

ε_{mf} is the void fraction at minimum fluidization conditions;

ρ_s is the particle density (g/cm^3);

ρ_g is the density of methane (g/cm^3);

g is the gravity acceleration factor (cm/s^2);

ψ is the catalyst shape factor, 1 for spherical particles; and

μ is the gas viscosity (g/cm.s).

The temperature and pressure in the fluidized bed affect the minimum fluidizing velocity [89]. Yang [92] reported that the effect of temperature and pressure on the minimum fluidizing velocity is dependent on the particle size. The pressure showed nearly no effect on the minimum fluidizing velocity for a fine powder (less than 100 micron, Geldart A particles) but the minimum fluidizing velocity decreases with increasing pressure for coarser particles [89,92]. As predicted from Equations 2.47-2.49, the U_{mf} decreases with increasing temperature [89,92], and experimental evidence has shown that increasing temperature caused a reduction in the minimum fluidizing velocity for the fine powder. But, for coarse powders, experimental work shows that U_{mf} increases with increasing temperature [89].

With increasing temperature, different characteristics of the bed may vary, including bed expansion, gas density, gas viscosity, and bed void fraction [89, 93]. On the other hand, Geldart [89] also discussed the fluidized particles being subjected to density changes and sintering. It is important to also consider the effect of carbon deposition when the minimum fluidizing velocity is calculated [94], since carbon deposition changes particle density and increases the sintering and agglomeration between the particles (as observed from preliminary experiments in our laboratory). So, using Equations 2.47-2.51 to predict the minimum fluidizing velocity for the modified particles (after carbon deposition) may result in prediction error since the correlations in Equations 2.47-2.51, or the correlations available in the literature that have been derived from Ergun's equation (e.g. [61,95-96]), are sensitive to the value of the void fraction at minimum fluidization conditions. But the void fraction at higher temperatures is difficult to predict due to the agglomeration, sintering, and cohesion as a result of carbon deposition and high temperature [89,96-97]. To overcome the complication raised from experiments at high temperatures and to accurately predict U_{mf} under real conditions, two common approaches have been proposed in the literature for U_{mf} at high temperature.

1- Empirical equations for predicting U_{mf} at high temperature

Plenty of equations are available to predict U_{mf} at high temperature, but a common observation is that each equation is only applicable for a certain material under certain conditions (e.g. [97]). Generalized equations have been proposed for different materials under wider operating conditions but the predictive abilities are not always accurate. Sangeetha et al. [93] developed a generalized equation for U_{mf} that has an error >50% in some cases. With carbon

deposition, using empirical correlations will be difficult unless it was developed for a similar experimental setup.

2- Experimental investigation of U_{mf} at high temperature

In this approach, which was proposed by Pinilla et al. [94] based on the approach developed by Pattipati and Wen [97], the minimum fluidizing velocity is determined under reaction conditions (by using catalyst particles that undergo methane catalytic cracking with carbon deposited on them). The authors propose using an inert gas, like nitrogen, and plotting the pressure drop across a bed of carbonaceous material, made by using the fresh catalyst in methane cracking, against the fluidizing gas velocity, as shown in Figure 2.27. In Figure 2.27, an offset in the pressure transducer reading led to measure a pressure drop at zero velocity. Then, the velocity calculated experimentally for nitrogen is multiplied by a factor to account for the effect of using methane. Pinilla et al. [94] determined this factor to be 1.4.

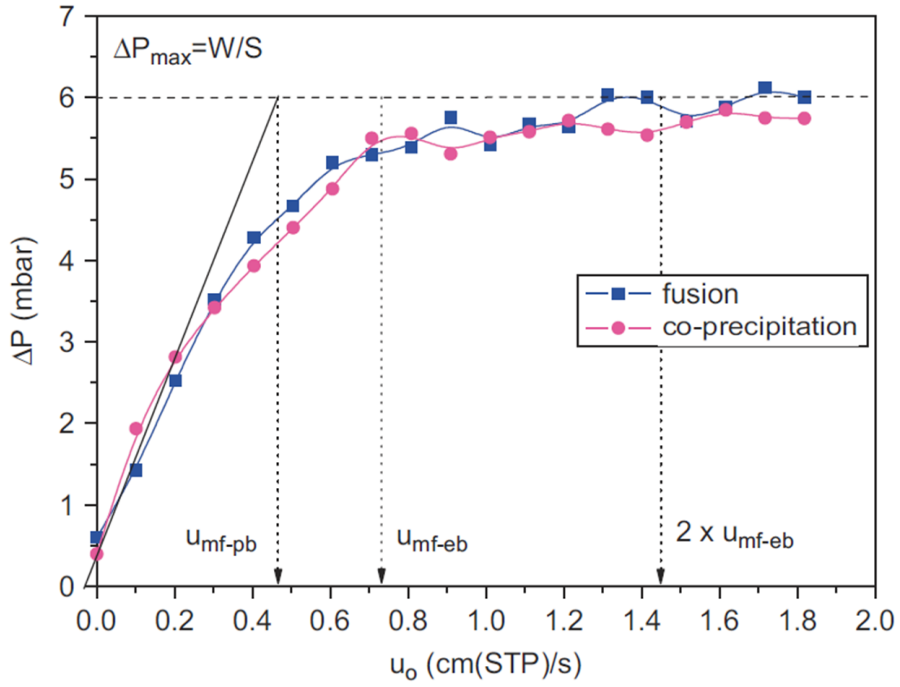

Figure 2.27 - U_{mf} and pressure drop, using nitrogen at 700°C (Reprinted from [94], with permission from the International Journal of Hydrogen Energy)

U_{mf-pb} : the minimum fluidizing velocity at the onset of fluidization calculated for the particle.

U_{mf-eb} : the minimum fluidizing velocity at complete fluidization calculated for the bed.

This approach takes into account the change in the fluid dynamic properties when the particles increase in diameter and decrease in density due to the deposition of filamentous carbon and due to agglomeration and changing void fraction at minimum fluidization conditions [92,94]. The maximum theoretical pressure drop was calculated from the following equation:

$$\Delta P_{max} = W / S \tag{2.52}$$

Where, W is the mass of carbon product, in kg, and S is the cross sectional area in m^2.

For circulating fluidized beds, another velocity value that is important for scale up is the terminal falling velocity. The terminal falling velocity of a particle, U_t, is its falling velocity through a fluid [96,98]. To reduce the catalyst carry over, the operating velocity should be kept between U_{mf} and U_t. Muradov et al. [66], evaluated U_t during methane cracking, and calculated the terminal falling velocity using a method developed by Gibilaro et al. [98]. Kunii and Levenspiel [96] mentioned the following equation to calculate U_t in cm/s:

$$U_t = U_t^* \left[\frac{\mu(\rho_s - \rho_g)g}{\rho_g^2} \right]^{1/3} \tag{2.53}$$

For spherical particles:

$$U_t^* = \left[\frac{18}{(dp^*)^2} + \frac{0.591}{(dp^*)^{0.5}} \right]^{-1} \tag{2.54}$$

For particles with shape factor ψ_s between 0.5-1:

$$U_t^* = \left[\frac{18}{(dp^*)^2} + \frac{2.335 - 1.744\psi_s}{(dp^*)^{0.5}} \right]^{-1} \tag{2.55}$$

$$dp^* = dp \left[\frac{\rho_g(\rho_s - \rho_g)g}{\mu^2} \right]^{1/3} \tag{2.56}$$

where:

d_P is the particle diameter;

ρ_s is the particle density;

ρ_g is the density of methane;

μ is the gas viscosity; and

g is the gravity acceleration factor.

Particle size

In fluidization, usually Geldart A (30-100 µm) type particles are used, since it is well known that Geldart A type particles lead to smooth fluidization, give better contact between the gas and catalyst, and achieve higher catalyst effectiveness factors [27,84]. Lee et al. [27] studied the effect of the catalyst particle size on the quality of methane cracking using activated carbon at 850ºC. The results revealed that the smaller the particle size, the higher the methane conversion due to the higher surface area. But the effect of the particle size diminished after time-on-stream, as shown in Figure 2.28. The authors found that, under their operating conditions, the best fluidization quality and contact efficiency was achieved with a particle size of 108 µm.

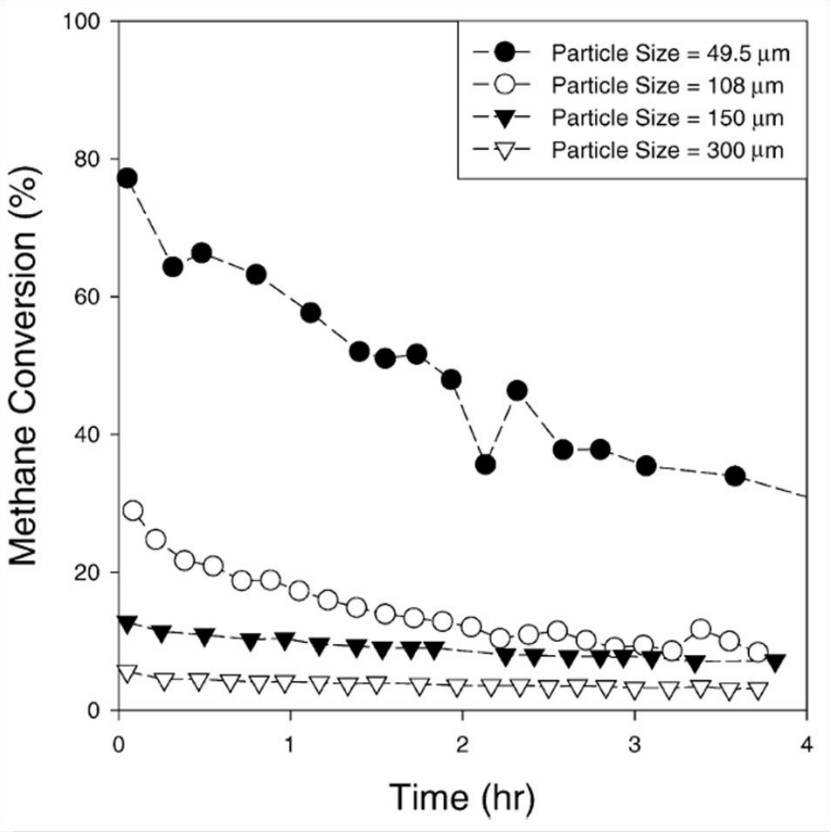

Figure 2.28 - Effect of activated carbon particle size and time-on-stream on methane cracking at 850ºC (Reprinted from [27], with permission from Elsevier)

2.8.3 Fluidized bed modeling

Accurate models are required to predict the process response to a change in any operating parameters. This is also true for methane catalytic cracking in a fluidized bed, to improve the

hydrogen output and hence the process economics. Before discussing the fluidized bed model developed by Muradov et al. [66], some general features of fluidized bed models available in literature, modelling patterns and the associated physical conditions for each model pattern are discussed.

Fluidized bed models are widely available in the literature; but before using any model to simulate the performance of the system under study, the model should be reviewed to find the one that best matches operating conditions. Any fluidized bed model has at least one of the following limitations [99]:

- model predictions are not consistent with the experimental results;
- model is valid for a narrow range of conditions;
- at least one of the model parameters is not readily obtainable, curve fitting for the experimental data is required to get these parameters; and
- solving the model equations is difficult.

In general, to model a fluidized bed reactor properly two sub-models must be developed to simulate the physical and chemical phenomena taking place in the fluidized bed reactor simultaneously. The physical phenomena correspond to the changes in the bed hydrodynamics, i.e., properties of the bubble and emulsion phase, whereas the chemical phenomena correspond to the chemical changes occurring in each phase [100].

Different patterns of fluidized bed models

The fluidized bed models in the literature are usually classified based on the flow type regime inside the fluidized bed. The flow regime changes with increasing gas velocity [96]. As the gas velocity increases, the flow regime changes between the bubbling regime, the slugging regime (occurs only in reactors with small diameters), the turbulent regime, fast fluidization, and pneumatic transport as shown in Figure 2.29. The two common types of fluidized bed models are the bubbling fluidized bed and the turbulent fluidized bed.

Bubbling fluidized bed

There are also two different categories of models widely used in the literature to simulate the bubbling fluidized bed. They are the two-phase and three-phase bubbling fluidized bed models. The three-phase models were developed assuming the presence of three phases in the fluidized bed [96], namely, the bubble phase, the wake-cloud phase, and the dense phase as shown in Figure 2.30. The two-phase models do not include the wake-cloud phase, assuming that the wake-cloud and bubbling phases are lumped into one phase.

Turbulent fluidized bed

Turbulent fluidized bed models are divided into single-phase or two-phase models. Single-phase models are represented by a plug flow reactor, most often the axially dispersed plug flow, while two-phase models are represented as continuously stirred tank models [66].

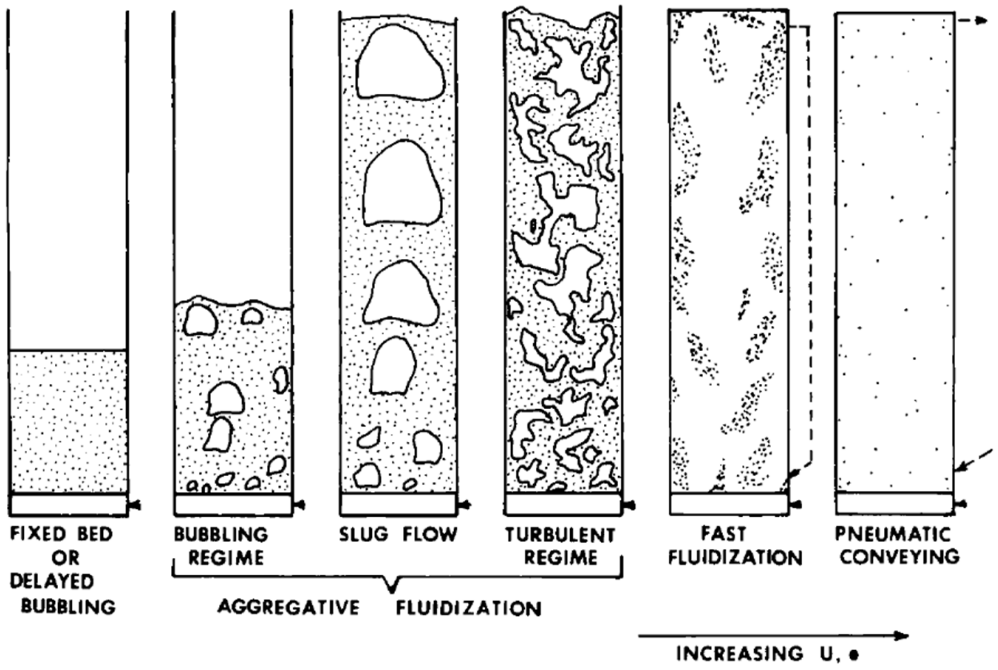

Figure 2.29 - Flow patterns in a fluidized bed (Reprinted from [101], with permission from John Wiley & Sons)

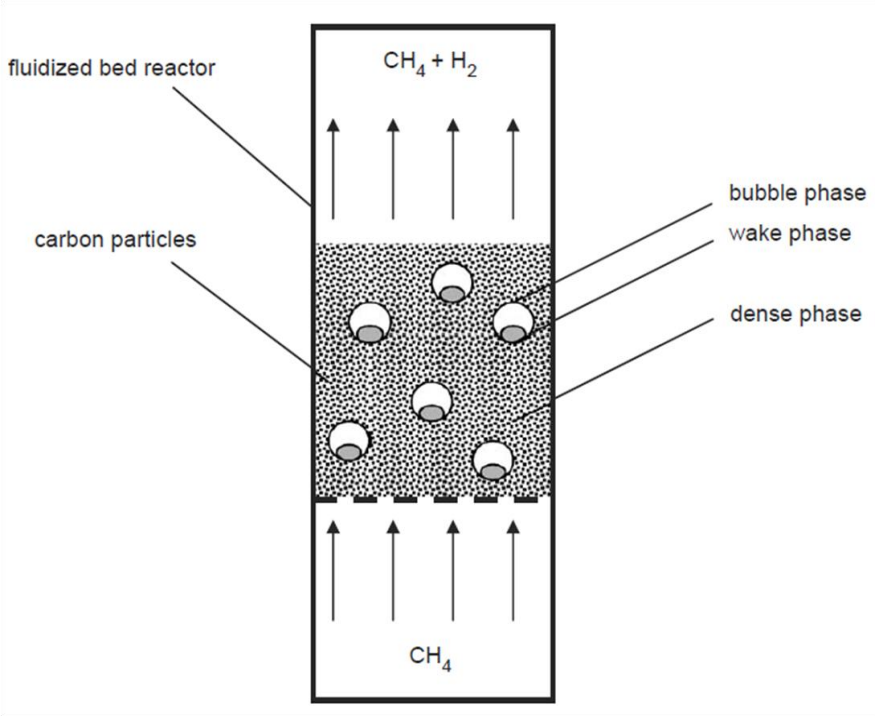

Figure 2.30 - Schematic of a bubbling fluidized bed of carbon particles (Reprinted from [66], with permission from the International Journal of Hydrogen Energy)

In some cases, the turbulent fluidized bed and the bubbling fluidized bed models are used to simulate the same case based on the physics inside the fluidized bed; for example, Gungor and Eskin [102] used a turbulent two-phase model for the bottom zone of the reactor and a three-phase bubbling bed model for the upper zone.

Muradov et al. [66] model

This model was developed to simulate and scale up methane cracking in a cracking-regeneration fluidized bed system using a carbon catalyst circulating continuously between the cracker and the regenerator. Muradov et al. [66] developed two models for the system under study; one model was developed to simulate methane cracking in a bubbling fluidized bed and the other was developed to simulate methane cracking in a turbulent fluidized bed. The two models captured most of the physics and chemistry inside the fluidized bed. The rate of methane cracking is calculated using Equation 2.46.

Carbon circulation rate

The carbon flow rate in this study was calculated assuming a methane conversion of 38%; the maximum conversion obtained during experiments using activated carbon in a lab-scale reactor. The carbon flow rate was calculated based on the heat requirement of the reactor, not on the deactivation rate of the catalyst.

$$\text{Carbon flow rate} = -\frac{Energy\ required}{C_{pc}(T_{in,C} - T_{bed})} \tag{2.57}$$

$$\text{Energy Required} = -m_m x \Delta H + m_m C_{pm}(T_{bed} - T_{in.m}) \tag{2.58}$$

where:

C_{pc} is the carbon specific heat, J/mol/K;

m_m is the molar flow rate of methane, mol/s;

C_{pm} is the methane specific heat, J/mol/K;

x is the methane conversion; and

$T_{bed}, T_{in.m}, T_{in,C}$ are the fluidized bed, methane inlet, and carbon inlet temperatures respectively, in Kelvin.

The residence time was calculated as follows:
residence time of methane = reactor volume /methane flow rate and
residence time of carbon = bed mass/carbon circulation rate.

Muradov et al. [66] solved the previous equations with the mass conversation equations. The model predictions were comparable to the experimental results. For large scale production, the dimensions of the cracker and regenerator fluidized beds that were predicted are comparable with those of industrial fluid catalytic cracking reactors used in the petroleum refining industry.

2.9 Current Trends, Future Research

Currently, methane cracking is not used industrially since it is not yet economically competitive with well developed methane steam reforming. But with the currently increasing demand for CO-free hydrogen, a continuous process for methane cracking is becoming more attractive. High methane conversion and utilization of the produced carbon filaments are essential

factors for process economics. A continuous process of methane catalytic cracking is likely needed to compete commercially, but rapid catalyst deactivation is a key deterrent. A circulating fluidized bed arrangement that has separate cracking and regeneration units represents a potential solution. The catalyst would move between the two units for not only regeneration but also for heat transfer. Also, developing methods for separating carbon filaments from the catalyst or investigating new applications for the un-separated carbon filaments will further the economic potential. To help with the economics, an active catalyst that can achieve high conversions, and remain stable is therefore critical. Based on the challenges that impede methane cracking from competing with other hydrogen production methods, some potential future research and development directions are discussed here.

A durable catalyst for fluidized bed applications needs to be developed. Different characteristics are required. The catalyst needs to:

- provide high conversion;
- have excellent thermal and chemical stability;
- have high carbon capacity;
- last a long time (until complete deactivation);
- withstand attrition; and
- be light weight.

Along these lines, a suitable catalyst support, which as noted, plays a major role in catalyst stability and strength, needs to be developed. It should withstand the damaging mechanical effect of carbon filaments and the high friction imposed in the fluidized bed.

Optimum operating conditions need to be realized. Process variables like methane/hydrogen ratio, temperature, flow rate, and pressure need to be further studied to determine optimum operating conditions. Similarly, methane cracking kinetics, including deactivation, need to be confidently determined, which will help in the development of an accurate process model. Modelling can be used to narrow the research range, in terms of significant parameters. Furthermore, with the difficulties associated with experimental work in fluidized beds, modelling is a less costly method to optimize operating conditions and to investigate the best way to improve the process economics. Also, and a critical aspect for the

economics, new methods for carbon filament separation and improving the quality of the carbon deposited during methane cracking need to be developed.

2.10 Conclusions

Methane catalytic cracking is a promising process to produce carbon monoxide-free hydrogen. Different catalysts can be used for methane cracking, including nickel, copper, iron, activated carbon, and carbon black. Carbon filaments are produced as a result of the reaction product carbon diffusing through the metal catalyst particle, and then the diffusing carbon is deposited in a filament form on the nickel/support interface. The driving force for carbon diffusion is the temperature gradient or concentration gradient around the catalyst particle. Catalyst deactivation has been discussed in detail. Encapsulating carbon and/or reactor space limitations are the primary deactivation causes. Different regeneration methods have been evaluated. Regeneration with steam or air is widely used in the literature, and carbon dioxide has also been tested for catalyst regeneration. Regeneration with steam and partial regeneration using air are effective in regaining the initial catalyst activity. The reaction kinetics have been discussed, and two different mechanisms are commonly used in the literature. The two mechanisms start with either dissociative or non-dissociative adsorption of methane, then the two mechanisms assume that the methyl group goes through a series of dehydrogenation steps until carbon is produced as a deposit on the catalyst. The reaction models in the literature have been categorized into models based on a detailed mechanism, models based on mathematical fitting of experimental data, and global rate models. Unfortunately, there is no consensus on the reactant reaction orders.

Acknowledgements

The authors wish to thank the Natural Sciences and Engineering Research Council of Canada and the Department of Chemical Engineering in the National Research Centre of Egypt for financial support.

Chapter 3
Methane Cracking Using Ni Supported on Porous and Nonporous Alumina Catalysts

---

Overview

Porous and nonporous alumina catalysts were used as nickel supports to catalyze methane cracking. Different operating parameters were studied in the thermo-balance, including methane and hydrogen partial pressures, temperature, flow rate, and particle diameter. During CH_4 cracking, carbon builds up on the catalyst surface and therefore the catalyst requires periodic regeneration. Cycling tests were performed, using air during the regeneration phase to burn off the carbon. The results showed that the nonporous catalyst performed better than the porous catalyst in terms of cracking during the first cycle. After regeneration, the performance of the porous catalyst became considerably better than the nonporous. The porous catalyst kept its activity for 24 cracking/regeneration cycles, while the non-porous catalyst lost half of its activity by the second cracking cycle and almost all of its activity after six cycles. Formation of $NiAl_2O_4$ and Ni sintering caused the nonporous catalyst activity loss. Full regeneration of the catalysts by oxidizing the deposited carbon was achieved at 550°C, while oxidation was very slow at 500°C. Three different types of carbon were detected by the change of the carbon gasification rate.

3.1 Introduction

Hydrogen is the most abundant element in the universe, but is not naturally available in its pure form. H_2 is widely used in industrial applications and is a promising fuel in the automotive sector, especially if PEM fuel cells penetrate this market. The annual global hydrogen consumption in 2006 was about 50 million tons, including industrial applications and merchant use [1-3]. The average annual increase in hydrogen demand was 4% from 1997 to 2006 in general, and 9.5% for carbon monoxide free hydrogen from 1997 to 2002, and by 10% from 2003 to 2006 [1]. Currently, hydrogen is mostly produced from hydrocarbon sources, and mainly from methane, which has the highest hydrogen/carbon ratio of all hydrocarbons [4]. Steam reforming is widely used for producing hydrogen, but the CO produced is poisonous for many hydrogen-based catalytic applications [5-7]. Alternatively, methane catalytic cracking can produce a 90% concentrated stream of CO-free hydrogen, mixed with residual methane [8]. In addition to producing CO-free hydrogen, methane catalytic cracking produces a significant amount of carbon filaments, which have wide industrial applications, or which alternatively could be burned to provide the heat necessary for the cracking process [9].

Nickel is widely used as a catalyst for methane cracking due to its high activity [10, 11]. But a persistent problem associated with methane cracking is the rapid catalyst deactivation [12]. Carbon produced from methane cracking is deposited on the catalyst either as a carbon filament or as encapsulating carbon, and the latter form together with catalyst sintering are believed to be the primary catalyst deactivation mechanisms [11, 13].

In methane cracking, the catalyst support plays an important role. A desirable support is one which does not significantly interact with the metal particles, provides good catalyst distribution, and minimizes sintering [4]. For example, previous research has shown that less interaction between the catalyst and the support results in increased catalyst carbon capacity (the maximum amount of carbon that can deposit on the catalyst before deactivation) [14, 15]. Ermakova et al. [14] reported that nickel supported on highly porous silica had the highest activity and slower overall deactivation compared to nickel catalysts supported on silica (with smaller pores),

alumina, magnesia, and zirconia. Takenaka et al. [6] studied the catalytic performance of Ni supported on different supports with different pore structures and specific surface areas, such as SiO_2, TiO_2, Al_2O_3, graphite, MgO, and SiO_2.MgO. The results indicated that again the support pore structure affects the catalytic activity and lifetime. In their study, Ni supported on silica with no pore structure showed the best catalytic activity and the longer lifetime. Although over one cracking cycle, silica support shows higher activity than alumina support, some studies indicated that over several cracking/regeneration cycles the alumina support is more stable than the silica one [16, 17]. Several studies on alumina support also show that the cracking activity using alumina support actually increases after the first cycle [16, 18].

In the present study, the activities of Ni supported on porous and non-porous alumina were compared. The effect of pore structure was not studied for alumina and this is the reason why alumina was chosen here. Experiments included varying the temperature, methane and hydrogen partial pressures, flow rates, and particle diameter. In order to use the catalyst in a continuous process, the catalyst must maintain its performance over a large number of cracking/regeneration cycles, realizing that deactivation is non-preventable during the cracking phase. Therefore, changes in catalyst performance over successive cracking/regeneration cycles were also studied. Different methods have been proposed in the literature to regenerate the catalyst deactivated during the cracking phase, including: 1) air oxidation to achieve either partial regeneration [18, 19] or full regeneration [17, 19], 2) steam oxidation [20, 21], and 3) and carbon dioxide oxidation [22]. In this study, the catalyst was regenerated using the air oxidation since it is easier to implement in an actual industrial plant and air oxidation is an exothermic reaction which may reduce the energy demand for methane cracking.

3.2 Experimental Work

The catalyst was prepared by wet impregnation of alumina using an aqueous solution of $Ni(NO_3)_2 \cdot 6H_2O$ (99.99%, Alfa Aesar). Two different supports were used: 1) a porous γ-alumina support [99.97% metal basis, 3 micron APS powder, Alfa Aesar] and 2) a non-porous α-alumina support [99.99% metal basis, 0.9-2.2 micron APS powder, Alfa Aesar]. The catalyst preparation method included drying the support

overnight at 150°C, preparing a solution of the nickel nitrate hexa-hydrate in de-ionized water, then adding the alumina to the solution. The nickel and alumina amounts chosen to obtain a 10wt% Ni loading for all experiments. For the porous support catalyst, the slurry was then stirred in a beaker over a hot plate at 80°C for 3 hrs. For the non-porous catalyst, a rotary spinning evaporator in an oil bath was used, with the oil bath temperature kept at 100°C. A different method for the non-porous catalyst was needed because poor Ni dispersion over the support was observed when using the same method as that employed for the porous catalyst. The samples were finally dried at 120°C overnight [23]. The nickel amounts were checked using a Prodigy/Prism high dispersion ICP, manufactured by Teledyne-Leeman. The catalysts were calcined in air at 600°C inside the thermal gravimetric analyzer (TGA) for 30 minutes. The reduction step was then also carried out in the TGA, at the reaction temperature, for 30 minutes using a 10 vol.% H_2 and 90 vol.% N_2 mixture [19] , with a flow rate of 120 ml/min. The BET specific surface areas of the supports were 68.3 and 14.3 m^2/g for the porous and non-porous supports, respectively.

The TGA used was a Cahn TG 151 manufactured by Thermo Cahn. The TGA was used to measure catalyst weight, since for CH_4 cracking, an increase in weight occurs with carbon deposition on the catalyst, with the carbon originating from each CH_4 molecule cracked. Thus the weight directly corresponds to the amount of CH_4 cracked. The instrument set-up is shown in Figure 3.1. The TGA can hold pressures up to 70 bar, and can operate at temperatures up to 1100°C. A quartz, flat bottom sample holder was used. All experiments were conducted with 10 mg of the fresh catalyst, with this small amount, the catalyst particles in the sample holder are not in contact with each other, thus eliminating any interference between the particles and any packed bed effects. The inlet gas flow rate was also varied in order to investigate the effect of flow rate and to select a flow rate with minimal noise influencing the results.

Scanning electron microscopy (SEM) and transmission electron microscopy (TEM) were used to study catalyst morphology. The SEM images were taken using a LEO FESEM 1530 manufactured by Carl Zeiss. The TEM images were taken using a FEI-Philips CM300 microscope, manufactured by FEI, operating at a 200 kV accelerating voltage. BET experiments were conducted using a Micromeritics Gemini III 2375 surface area analyzer. The nickel dispersion was measured using a Hiden

Catlab Microreactor with a QIC-20 mass spectrometer. A 5% H_2 in He mixture was used, with chemisorption measurements obtained at 25°C after the sample had been pre-treated at 550ºC using a 10% H_2 in N_2 mixture, then cooled in pure He to 25ºC. X-ray diffraction (XRD) measurements were also obtained, using a D8 FOCUS XRD system, manufactured by Bruker AXS. CuKα radiation was used, with a 40 KV potential and a 40 mA current. The 2θ angles measured were 30 to 80° using an angle step of 0.05° and a count time of 1 s.

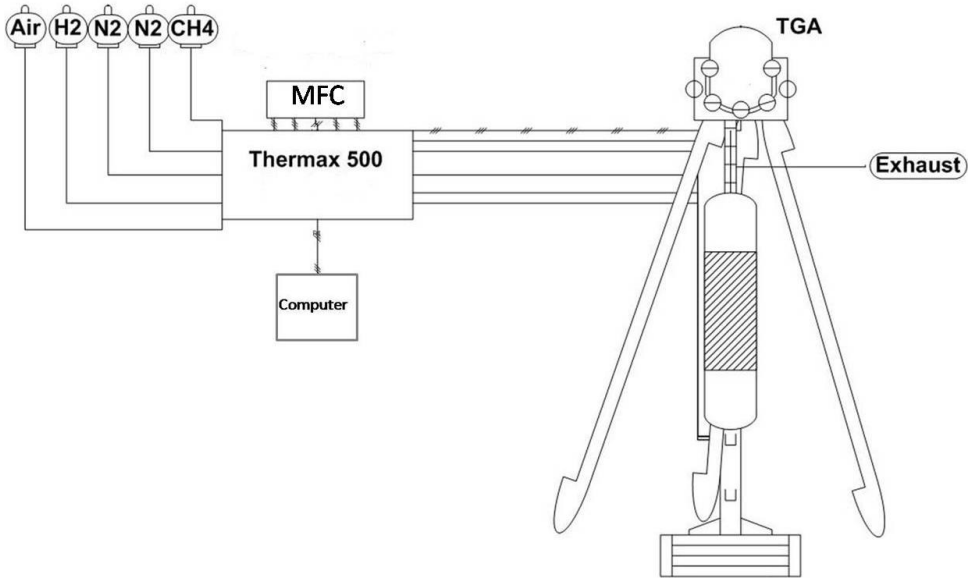

Figure 3.1 – Schematic of the thermal gravimetric analyzer (TGA)

3.3 Results and discussion

An example of the normalized weight gain over time obtained from the TGA is shown in Figure 3.2 for the porous support tested at 550ºC, with a flow rate of 120 ml/min in 100% methane and at 1 atm. We define here the paper, the carbon capacity is defined as the maximum normalized amount of carbon deposited after complete catalyst deactivation (unit of g_C/g_{Ni}). The carbon formation rate discussed throughout the paper is defined as the ratio of 99% of the carbon capacity over the time required to reach 99% of the carbon capacity, as shown in Figure 3.2. The carbon formation rate is a global parameter that complements the carbon capacity that takes into account the time required to deactivate. For comparison purposes the results for both carbon capacity and carbon formation rate are discussed, since using only one of them may lead to misleading conclusions. Since a higher carbon capacity may deposit in a longer period.

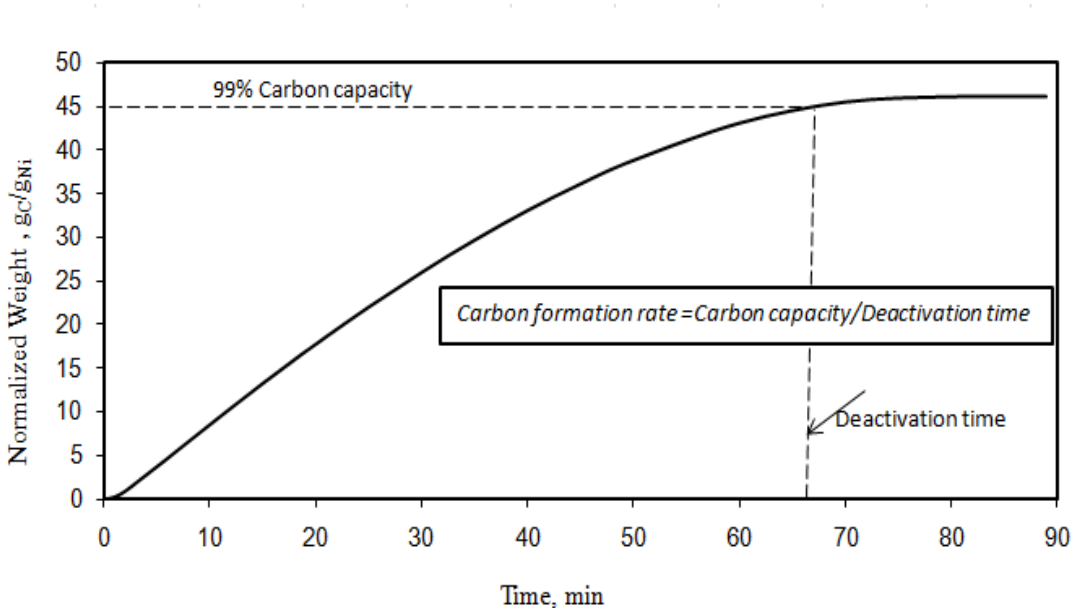

Figure 3.2 – Normalized weight change for the porous catalyst in g_C/g_{Ni} at 550ºC, 120 ml/min, 100% methane, and 1 atm.

3.3.1 Effect of Particle diameter

The effect of catalyst particle diameter on carbon capacity and carbon formation rate for the porous and non-porous catalysts is shown in Figure 3.3. The results show that for the porous catalyst, the errors on the measurement were small and the trend indicated a slight decrease in carbon capacity when increasing the particle diameter (by about 10% from 300 to 1000 μm particles). This can be explained by the slight increase in specific area when decreasing the particle diameter as indicated in Table 3.1. The carbon formation rate for the porous catalyst also decreased when increasing the particle diameter from 300 to 725 μm, but no changes in carbon formation rate were observed between 725 and 1000 μm.

For the non-porous catalyst both the carbon capacity and carbon formation rate are independent of the particle diameter, at least in the range 300-1000μm. For the non-porous catalyst, the BET specific area increases only by 2 m^2/g when changing the particle diameter from 300 to 1000 μm, hence the non effect of particle diameter observed experimentally.

Table 3.1 – BET specific surface area for porous and non-porous catalyst at different particle sizes.

Particle diameter	Porous	Non-porous
300 μm	70 m^2/g	18 m^2/g
725 μm	67 m^2/g	18 m^2/g
1000 μm	59 m^2/g	16 m^2/g

Comparison between the porous and non-porous catalyst shows that the carbon capacity is significantly higher for the non porous one (~76 g_C/g_{Ni} for non-porous catalyst and ~45 g_C/g_{Ni} for the porous one). This may be attributed to the presence of nickel particles in the non-porous catalyst close to the external catalyst surface, resulting in less interference between the filaments and thus increased carbon capacity [24]. Nonetheless, the carbon formation rates are similar between the porous and non-porous catalysts. In the rest of this paper, all experiments reported were carried out with 725 μm particle size.

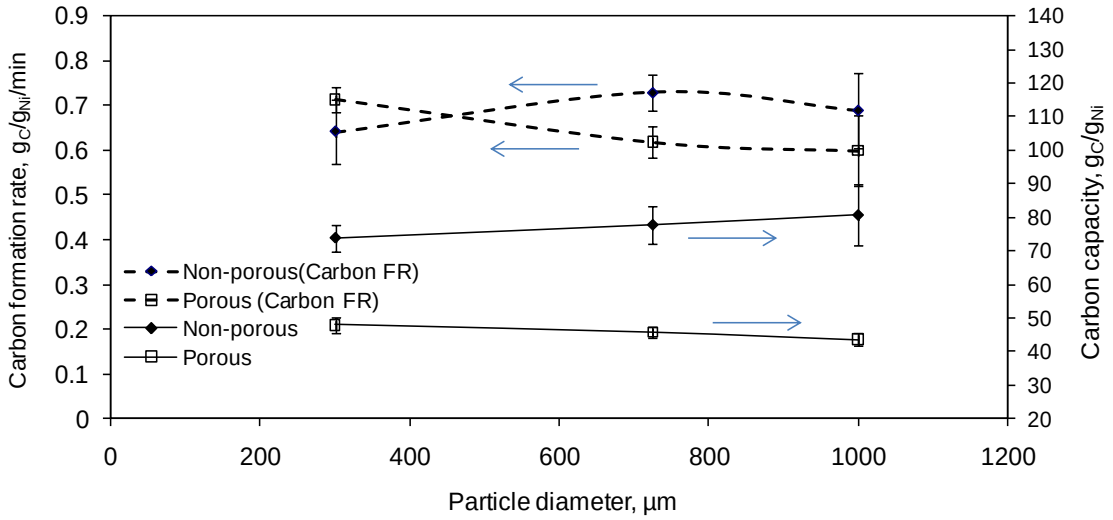

Figure 3.3 – Effect of particle diameter on carbon formation rate and on carbon capacity at 550ºC, 120 ml/min, 100% methane, and 1 atm.

3.3.2 Effect of gas flow rate and temperature

Figure 3.4 illustrates the effect of temperature and gas flow rate on carbon capacity and carbon formation rate for the porous catalyst. The trends were very similar for non-porous

catalyst (not shown here) with only few differences such as higher carbon capacity as seen in the previous section.

Effect of gas flow rate:

The gas flow rate mentioned here is the flow rate of the reacting gas flowing around the catalyst holder inside the TGA. The superficial velocities around the catalyst are thus much lower than the gas velocity in the TGA chamber. The recommended flow rate by the TGA manufacturer is 120 ml/min. The purpose of the experiments at different flow rates was to determine whether the flow rate has any effect on the cracking reaction and to assess whether the TGA recommended flow rate was adequate to study methane cracking.

The effect of flow rate on carbon capacity for the porous catalyst is seen in Figure 3.4a. At 500 and 550°C, increasing the flow rate from 120 to 240 ml/min has little effect on the carbon capacity. However, at higher temperatures (600 and 650°C) similar changes in flow rates lead to a decrease in carbon capacity. Superposing the normalized weight curves obtained at 650°C for 120 and 240 ml/min (see Figure 3.5) indicates that for the 5 first minutes the flow rate did not have any effect on the reaction. It is only after the first 5 minutes that the catalyst at 240 ml/min started deactivating faster than at 120 ml/min. A similar observation was made at 600°C except that the behaviour of the curves started to deviate from each other after approximately 15 minutes.

The cracking rate is the result of a fine balance between the filament growth rate, the encapsulating carbon rate (which leads to deactivation) and eventually transport limitation. The gas flow rate should not have an impact on the kinetics of the reaction (whether it is filament growth or carbon encapsulation) and should affect only mass and/or heat transfer. Since the flow rate affects the overall cracking reaction only from a certain time on stream, it may be due to the growing influence of transport limitation that started to occur once the particles reached a certain size. This assumption is reinforced by the fact that this phenomenon was observed at higher temperatures where a kinetic controlled regime is less likely to take place, and by the fact the superficial velocity around the particle in the sample holder is certainly small. In this case, as the impact of transport limitation increases at 120 ml/min (compared to at 240 ml/min), not only does the cracking rate decreases, but also the carbon encapsulating rate, thus allowing more carbon to deposit. At low gas flow rate (e.g. 72 ml/min) the uncertainty in the measurement is much higher and no conclusion could be drawn.

For temperatures of 550°C and below, using the TGA recommended gas flow rate of 120 ml/min is fine. Above 550°C, at 120 ml/min one has to expect the carbon capacity to be dependent on the flow rate. However, when considering the global carbon formation rate, Figure 3.4b shows no difference between 120 and 240 ml/min, even at 600 and 650°C. For the experiments in the rest of this chapter, assume the gas flow rate to be the recommended 120 ml/min to keep the weight measurement noise to a minimum.

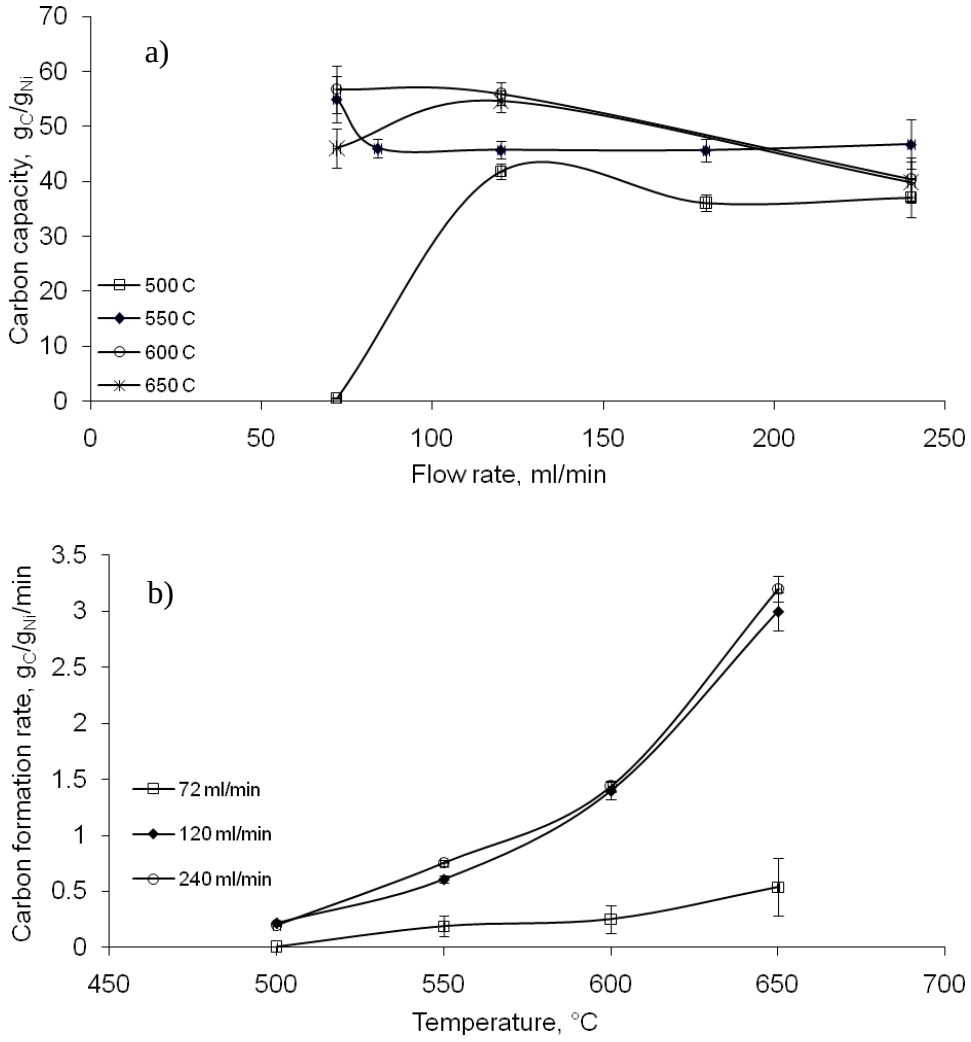

Figure 3.4 –Effect of flow rate and temperature for the porous catalyst on a) carbon capacity and b) carbon formation rate. Conditions: 725 µm particle diameter, 100% methane.

Effect of temperature:

Ignoring the lowest flow rate (72 ml/min), at a given flow rate, the carbon capacity is the same at 600 and 650°C. The minimum carbon capacity was observed, for all gas flow rates, at 500°C, although the difference becomes smaller as the flow rate increases (especially with experiments at 600 and 650°C). At the highest flow rate (240 ml/min), the carbon capacity is higher at 550°C than at all other temperatures. The case of 240 ml/min is particularly interesting here as transport effects are minimized, as explained in the previous section.

A maximum carbon capacity at 550°C can be explained based on conclusions of Ermakova et al. [14]: at temperatures less than 550°C, the surface carbon concentration is small and does not achieve the degree of super saturation necessary for the nucleation of carbon filaments, so that more carbon is deposited as encapsulating carbon, resulting in catalyst deactivation. On the other hand, at temperatures higher than 550°C, surface carbon formation is fast, relative to the diffusion of carbon through the particle to form filaments, so that carbon accumulates on the catalyst surface resulting in a more rapid catalyst deactivation and therefore reduced carbon capacity before deactivation. As explained in the previous section the lower carbon capacity at 550°C compared to 600 and 650°C, is likely due to transport limitation that appeared during the course of the reaction.

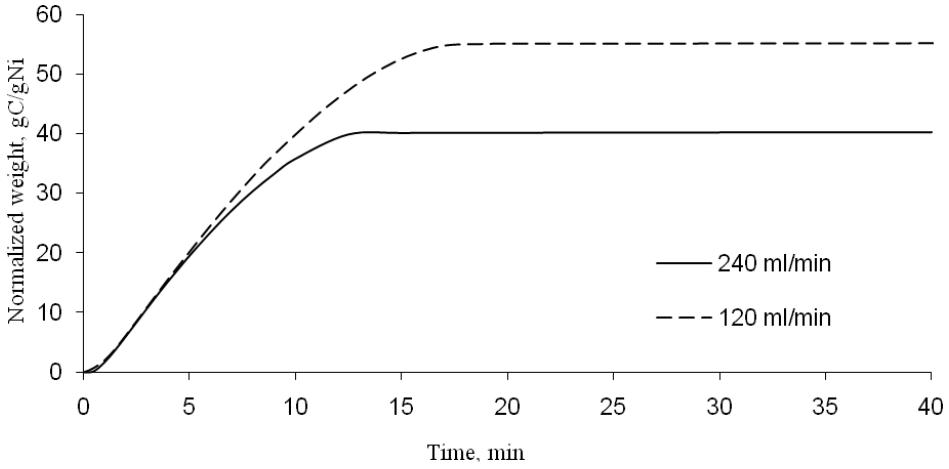

Figure 3.5 – Normalized weight vs. time at 650°C for two gas flow rates: 120 and 240 ml/min. Methane cracking in 100% methane.

3.3.3 Effect of methane partial pressure

The effect of methane partial pressure was studied by varying the methane amount from 50 to 100%, balanced with nitrogen at atmospheric pressure. The carbon capacity of the catalyst and the carbon formation rate are shown in Figures 3.6a and 3.6b, respectively, for the porous catalyst. For the non-porous catalyst (not shown here) similar trends were observed.

For Figure 3.6a, it is seen that for P_{CH4} between 0.5 and 0.9 atm, the carbon capacity did not change much for all temperatures considered. Only slight increases in carbon capacity could be observed. However, except at 550°C, the carbon capacity increased markedly between 0.9 and 1.0 atm (25 to 45% increase depending on the temperature). Another interesting observation is that for P_{CH4} less than 1.0 atm, there is an optimum temperature where the carbon capacity is maximized and this temperature appears to be close to 550°C. A similar explanation as the one brought forward in the previous section based on Ermakova's result [14], could be invoked here to explain the particular role of 550°C. Only at P_{CH4} of 1 atm, do we have a monotonous increase in carbon capacity when increasing the temperature from 500 to 650°C.

Figure 3.6b shows the carbon formation rate for the non-porous support at different methane partial pressures. The data in Figure 3.6b indicate that the carbon formation rate is primarily dependent on temperature with, as expected, increasing rate as the temperature increases. As for the effect of P_{CH4}, it is very much dependent on temperature. The increase in carbon formation rate when increasing P_{CH4} is more and more pronounced as the temperature increases. In fact, at 550ºC and below, the carbon formation remains almost unchanged when changing P_{CH4}.

3.3.4 Effect of hydrogen partial pressure

The effect of hydrogen partial pressure was investigated by varying the inlet hydrogen partial pressure from 0.05 to 0.2 atm., mixed with methane at atmospheric pressure. The experiments were conducted in the TGA with only 10 mg of catalyst, so that the reaction product did not affect the bulk reacting mixture concentration. Therefore, any hydrogen produced during the reaction did not affect the reacting mixture composition. Figures 3.7a and 3.7b show the results for the hydrogen partial pressure effect for the porous catalyst at 550 and 650°C, respectively. The carbon capacity and carbon formation rate are not compared here because of the

large variations in the time needed for complete catalyst deactivation at different hydrogen partial pressures. For example, under some conditions, the samples were not deactivated, even after more than 1000 minutes on stream, as shown in Figure 3.7a for 15% H_2. It was therefore not possible to determine the carbon capacity and the carbon formation rate for experiments with higher H_2 content at 550°C.

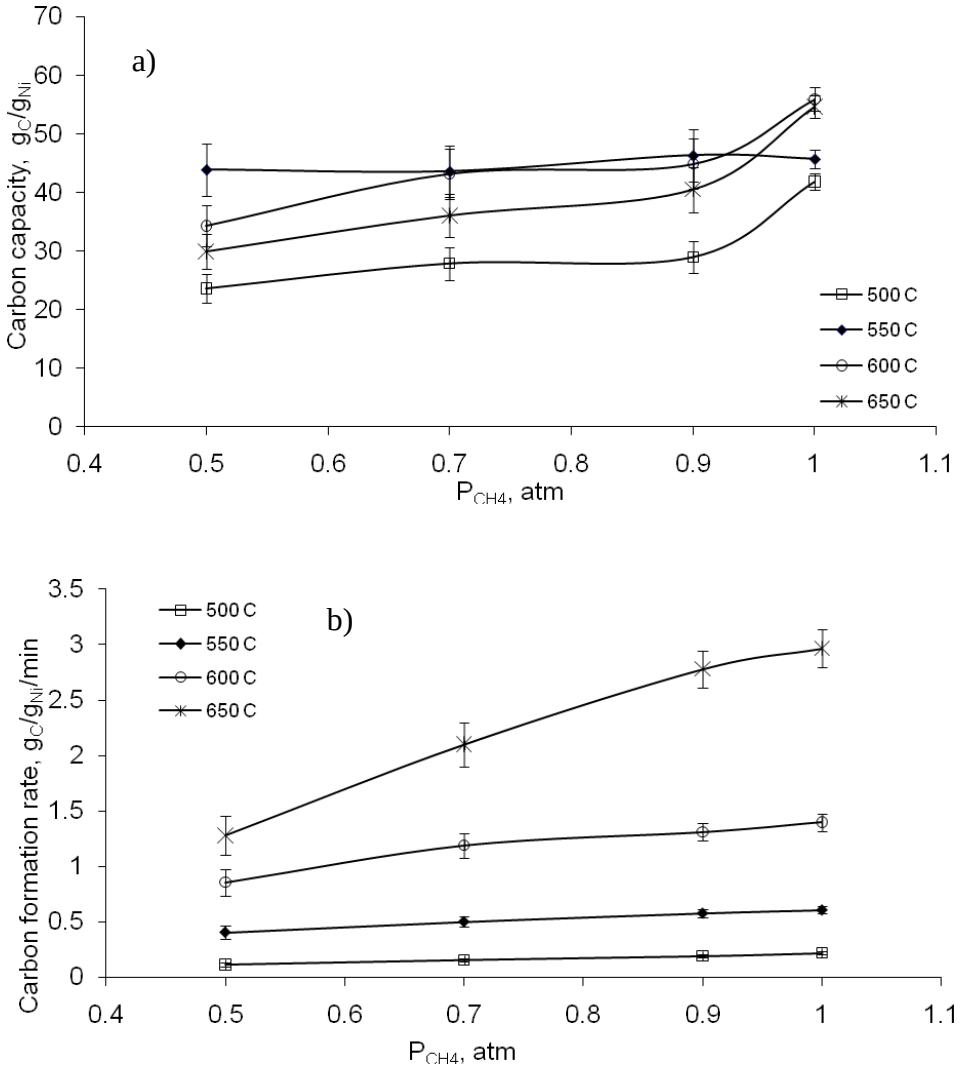

Figure 3.6 – Effect of methane partial pressure for the porous catalyst on a) carbon capacity and b) carbon formation rate. Conditions: 725 µm particle diameter, 120 ml/min, balance nitrogen.

The trends observed in Figure 3.7a at 550°C for the porous catalyst, were similar to those observed for the porous catalyst at 500ºC and for the non-porous catalyst at 500 and 550ºC. Increasing hydrogen in the inlet gas leads to a decrease in the reaction rate, and the time required for deactivation increases due to the slower rates. The drop in reaction rate was particularly

notable when increasing P_{H2} from 0.10 to 0.15 atm. The carbon capacity for the porous catalyst increased from 45 to 70 g_C/g_{Ni} by increasing the hydrogen partial pressure from 0 to 0.05-0.1 atm. However, increasing hydrogen partial pressure to 0.15 atm. resulted in a rapid drop in carbon deposition rate and an associated increase in deactivation time. An additional increase in hydrogen partial pressure to 0.2 atm resulted in almost no carbon deposition (less than 1 gC/gNi as seen in the insert in Figure 3.7a), which indicates nearly no catalyst activity. The effect of P_{H2} can be interpreted from both a carbon deposition rate point of view and a deactivation rate point of view. The carbon decomposition rate can be estimated from the initial slopes observed in the normalized weight gain curves. From Figure 3.7a, it is clear that the initial rate decreased as P_{H2} increased and this can be attributed to the fact that H_2 is a reaction product that competes with CH_4 for the active sites. A consequence of this competition for active sites is that the concentration of carbon on the surface is lowered; thereby decreasing both the cracking and carbon encapsulating formation rates [20], thus reducing the deactivation rate and then increasing the carbon capacity. In addition, it is also possible that H_2 reacts with encapsulated carbon to gasify it back into methane.

The effect of P_{H2} at 0.2 atm was further investigated to determine whether the reactant composition had an effect on the very initial period when filamentous carbon formation is initiated (nucleation period). The experiment began with 100% methane for 10 minutes and then the reaction gas was changed to 80/20 CH_4/H_2. The results are shown in Figure 3.8. After switching to 80/20 CH_4/H_2, the reaction rate decreased significantly compared to that for pure methane. Although significantly slower, the reaction still continued to proceed, unlike what was observed when starting with just the 80/20 CH_4/H_2 mixture. This suggests that the composition of the reaction mixture affects the nucleation period. It also suggests that the gas composition during the nucleation period impacts the reaction rate even after the end of the nucleation period.

Data obtained using the porous catalyst at 650ºC are shown in Figure 3.7b. Similar trends were observed for the porous catalyst at 600ºC and for the non-porous catalyst at 600 and 650ºC. At 650°C, the final normalized weight (i.e. carbon capacity) is similar no matter the partial pressure of H_2 used (around 50 g_C/g_{Ni}). This is very different from what was observed at 550°C. The explanation used to explain the effect of P_{H2} at 550°C still holds, in particular the effect of P_{H2} on the initial deposition rate: from Figure 3.7b the initial slopes still decreased as P_{H2} increased. However, as the higher temperature of 650°C, less H_2 is adsorbed on the surface and thus P_{H2} as

less of an effect on competing for sites on the surface. The deactivation rate is then less influenced by P_{H2}, as seen by small variations in carbon capacity in Figure 3.7b.

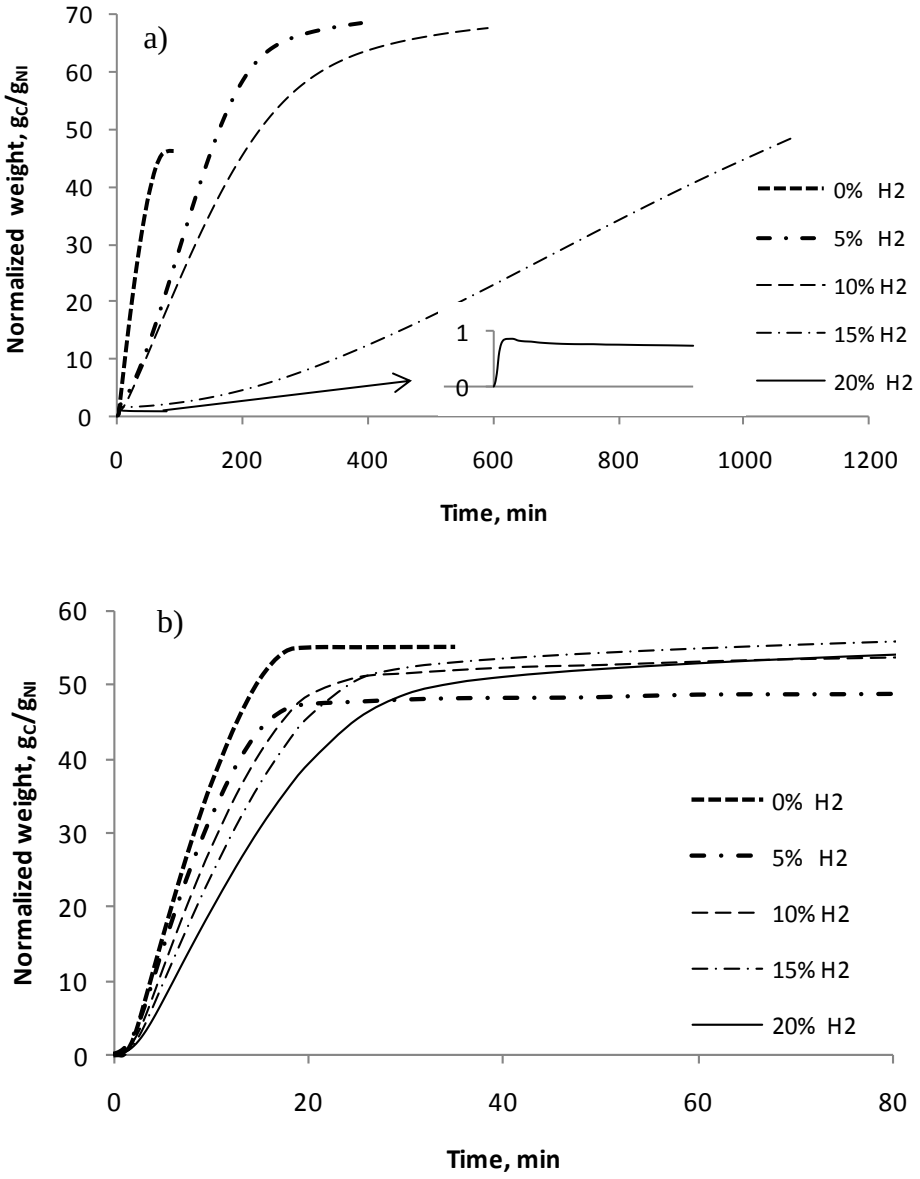

Figure 3.7 – Effect of hydrogen partial pressure on the normalized weight gain as a function of time for the porous catalyst at a) 550°C, and b) 650°C. Conditions: 725 µm particle diameter, 120 ml/min, balance methane.

3.3.5 Catalyst regeneration

As shown previously, the catalyst deactivates during the cracking reaction due to carbon build-up. Periodic regeneration is therefore necessary. Both the porous and non-porous catalysts

were further studied to assess their ability to be used in a cracking/regeneration cyclic mode of operation, for example in a fluidized bed or in a battery of fixed bed reactors. Before conducting the cracking/regeneration cycles, full regeneration of the deactivated catalyst using air oxidation was examined at 500 and 550ºC, as this temperature range was proposed by Guo et al. [13] after studying carbon deposited on 5% Ni/γAl_2O_3 using Raman spectroscopy. Figure 3.9 shows the results obtained during regeneration in air of the porous and non-porous catalysts at 500 and 550ºC. Prior to regeneration, the cracking step was carried out at 550°C under 100% methane.

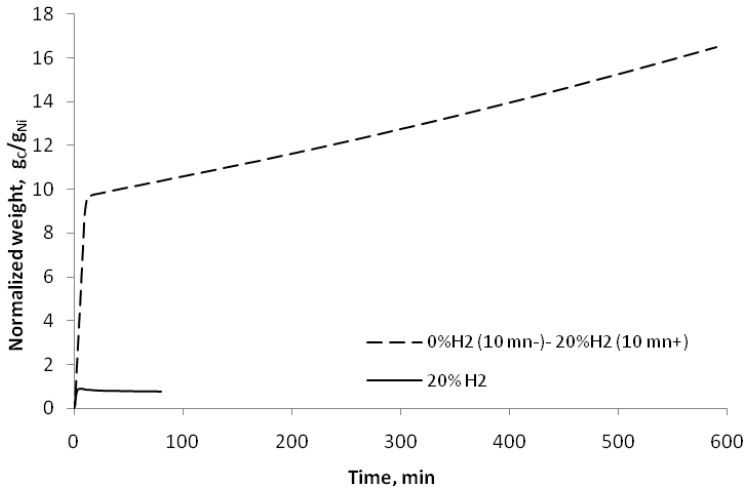

Figure 3.8 – Effect of initial conditions on the normalized weight gain for the porous support using 725 µm particle diameter, 120 ml/min, at 550°C, and balance methane.

During regeneration at 500ºC, the weight of the non-porous catalyst decreased slowly, losing only half of the carbon deposited after two hours. For the porous catalyst, the weight of the catalyst also decreased slowly, with a weight reduction of only around 10% (5 g_C/g_{Ni}) after one hour. Since regeneration at 500ºC was inefficient, and nowhere near completion, higher temperatures were needed to increase the oxidation rate. Regeneration at 550ºC was significantly faster for both catalysts. The porous catalyst was completely regenerated in about 40 minutes, while it took less than 1 hour to fully regenerate the non-porous catalyst. By comparing the curves at 500 and 550°C in Figure 3.9, it is apparent that the rate of regeneration of the non-porous catalyst was faster than that of the porous catalyst at both 500 and 550ºC. This is due to the location of the carbon on the external surface for the non-porous catalyst, which is more easily accessible and generating more localized heat.

Based on these results, 550°C was chosen as the temperature for successive cracking/regeneration cycles. The cracking cycle was conducted until the catalyst was completely deactivated, in other words until the weight change curve levelled off. Also, the regeneration cycle was continued until the weight loss stopped changing. Figure 3.10 shows the curve of the normalized weight gain during cracking versus time for different cycles in the case of porous and non-porous catalysts. Figure 3.11 shows the changes over cycles in carbon formation rate and carbon capacity. Six cycles were enough for the non-porous catalyst to lose its activity, while the porous catalyst remained active even after 24 cycles. At the beginning of the 25th cycle, the porous catalyst still showed the same activity as during the 24th cycle, and at this point the experiment was terminated. The maximum number of successful successive cracking/regeneration cycles reported in literature is 10 cycles [5].

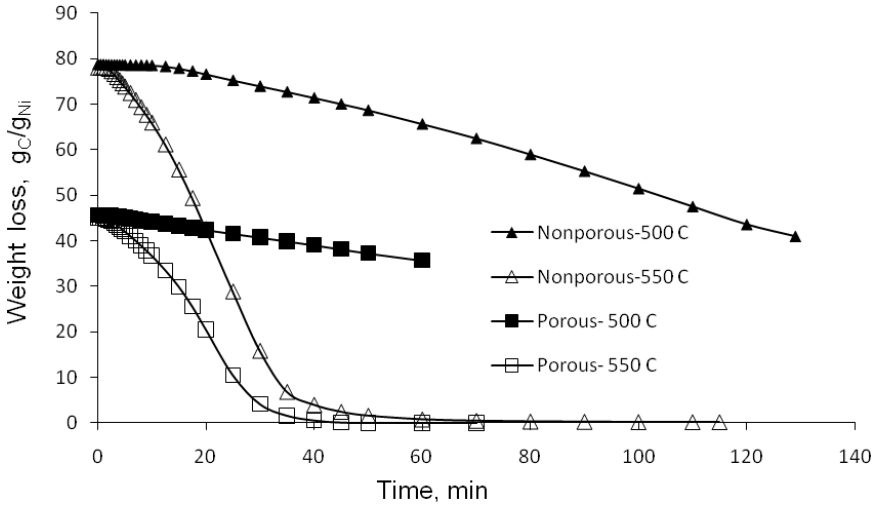

Figure 3.9 – Regeneration in air of porous and nonporous catalysts at 500°C and 550°C.

Results from Figures 3.10a for the porous catalyst show that the carbon capacity increased significantly in the second and third cycles compared to the first cycle. The carbon capacity was 45 g_C/g_{Ni} in the first cycle and increased to around 80 g_C/g_{Ni} in the third cycle. The increase in carbon capacity in the second cracking cycle is due to the fact that the regenerated catalyst is more reduced than the fresh reduced one, as seen from XRD pattern (see Figure 3.11). This figure shows that more metal nickel phase is present in the regenerated catalyst than in the fresh reduced catalyst, whereas it is the opposite for the nickel oxide phase. This is to be expected because the fresh catalyst was calcined at higher temperature (600°C) than the regeneration temperature (oxidation at 550°C). Another reason for faster build-up of carbon filament in the second cycle could be that it does not undergo the full nucleation stage due to the incomplete

burning of the deposited carbon during the previous regeneration [13, 17]. After the third cycle, the carbon capacity value stabilized around 80 g_C/g_{Ni}, and this until the 24th cycle. This shows that we did not observe any sign of rapid catalyst deterioration through 24 cycles. The main deterioration is the time to reach the carbon capacity that increases (moderately) over the cycles, as can be seen in Figure 3.10a. The stability of the carbon capacity indicates that the nickel surface area available for the reaction is nearly constant through the 24 cycles. During regeneration, encapsulating carbon and carbon filaments are oxidized and the nickel particle returns to the surface. The slow decrease in cracking rate however indicates that there may be a slow build-up in some carbon that resists oxidation, for example if the carbon filament does not fully oxidize, as was reported by Otsuka et al. [17] with Pd–Ni/SiO_2 and by Guo et al.[13] with 5% Ni/γAl_2O_3, where the nickel particle remains on the tip of the remaining part of the carbon filament as it is oxidized.

The results for the cracking/regeneration cycles for the non-porous catalyst are shown in Figures 3.10b. Unlike the porous catalyst, the carbon capacity for the non-porous catalyst decreased significantly from the first to the second cycle and continued to do so in subsequent cycles to reach almost no activity after the 6th cycle. The carbon capacity dropped from 80 g_C/g_{Ni} in the first cycle to 40 g_C/g_{Ni} in the second cycle. In the fourth cycle, the carbon capacity was 1/6th of its value at the end of the 1st cycle. In an attempt to regain activity, the catalyst was reduced in a 10/90 H_2/N_2 mixture at 550°C before the fifth cycle. As seen in Figure 3.10b, this did not help in regenerating the non-porous catalyst.

For the non-porous catalyst, the XRD results (Figure 3.11) show that a new phase, $NiAl_2O_4$, appeared after regeneration. The formation of $NiAl_2O_4$ reduced the total surface area of nickel available for the reaction leading to the rapid decrease in cracking performance for the non-porous support [4, 9, 25, 26]. This is consistent with the chemisorption results discussed later. One question remains for the non-porous catalyst: is the formation of $NiAl_2O_4$ on the non-porous catalyst the only reason for catalyst deterioration? To answer this question, nickel dispersion was measured to correlate sintering with catalyst activity and to distinguish it from $NiAl_2O_4$ formation. The nickel dispersion data are presented in Table 3.2. Nickel dispersion on the non-porous catalyst dropped by half, relative to the initial dispersion (from 6.3% to 3.0%), which coincides with the performance decrease observed. The drop in nickel dispersion may therefore be due to sintering, since most of the nickel is deposited on the external surface of the non-porous support. With the nickel loaded on a small surface area (as shown in Table 3.1),

nickel particles are more likely to merge, forming larger clusters, especially with the high localized temperature generated during regeneration [5, 20]. In conclusion, the two main reasons for rapid deactivation of the non-porous catalyst over a few cycles are 1) formation of inactive $NiAl_2O_4$ and 2) Ni sintering.

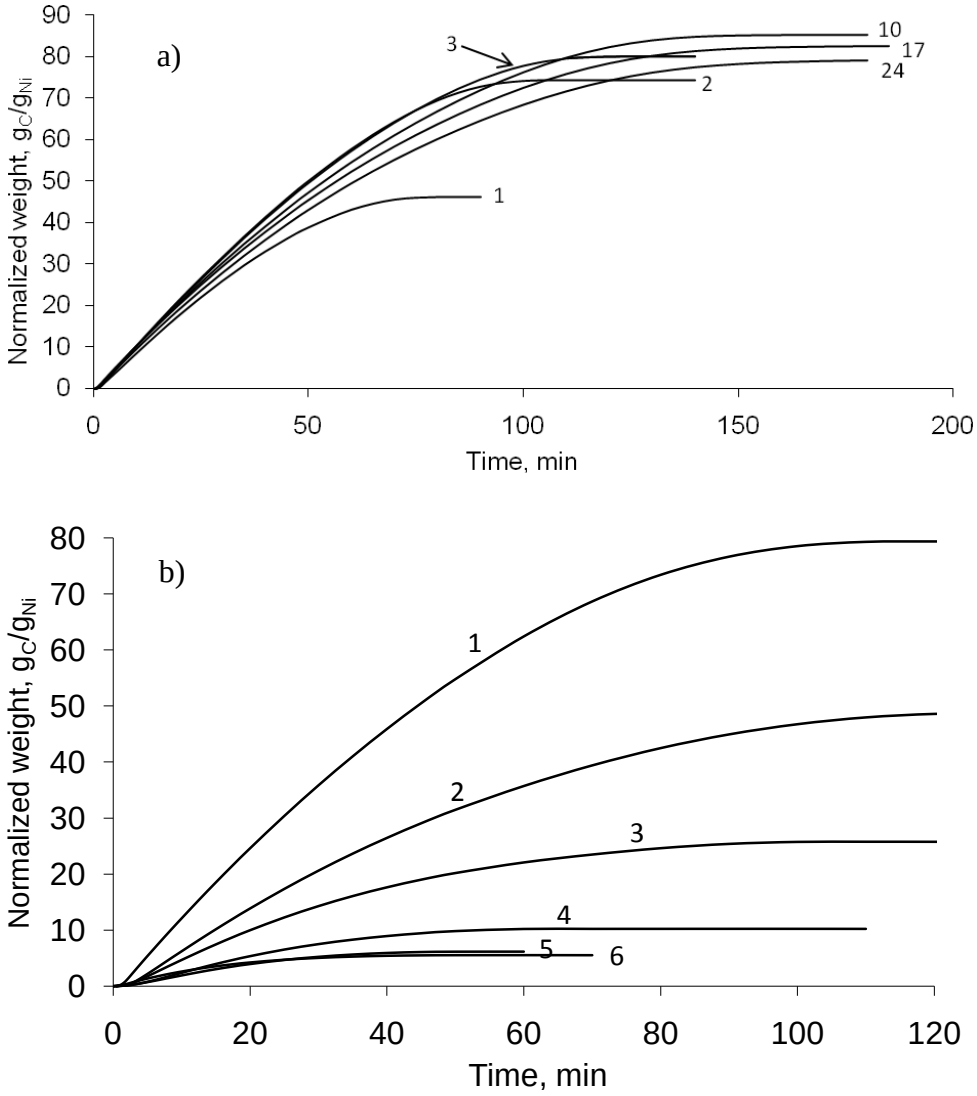

Figure 3.10 – Carbon deposition rate for different cracking/regeneration cycles for a) porous and b) nonporous catalysts. 100% methane for cracking step and air for regeneration.

The porous catalyst showed a smaller decrease in the nickel dispersion after the first regeneration. The drop in the porous catalyst dispersion is attributed to the formation of a new crystal phase, Ni metal (200) detected by XRD, which may affect the total surface area of the nickel subjected to the reaction. But the level of reduction in the dispersion of nickel on the porous catalyst did not affect the performance. In the SEM and the TEM graphs of deactivated

porous and non-porous catalysts after cracking in 100% CH_4 at 550°C, shown in Figures 3.12 and 3.13, respectively, it is apparent that the carbon deposited on the non-porous catalyst formed carbon agglomerates while the carbon deposited on the porous catalyst formed hollow carbon filaments.

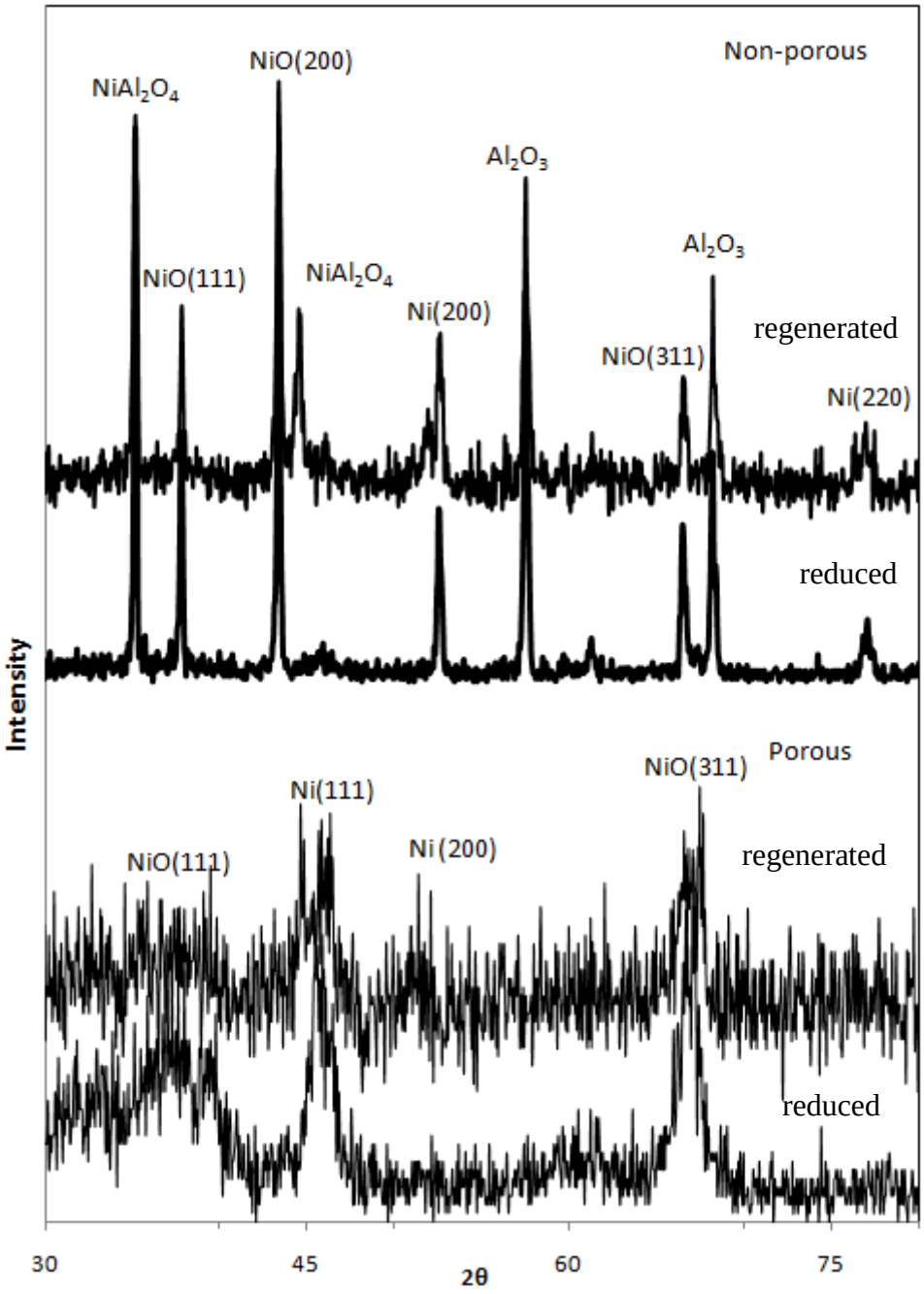

Figure 3.11– XRD pattern for the porous and non-porous catalysts: reduced fresh catalyst at the bottom and catalyst after first regeneration cycle at the top.

Due to the small surface area of the non-porous catalysts, larger Ni clusters formed from sintering prevent the formation of carbon filament, thus causing the formation of larger carbon agglomerates. On the porous catalyst, Ni is more dispersed and less prone to form large Ni cluster during the regeneration step, and thus carbon filament growth can take place. During gasification, the nickel particles stay on the tip of the filament, such that as the filament shrinks, the Ni particle ends up back on the surface without large displacement from its original position, which reduces the chance of sintering. From the SEM and TEM images, the outer diameter of the carbon filaments formed on the porous catalyst ranged between 20 and 40 nm, which suggests that the nickel particles size is in the same range. Using TEM for a similar catalyst as the one used in the present work, Li et al. [25] found that the nickel particles size was 30 nm.

Table 3.2 - Nickel dispersion for fresh and regenerated (after one regeneration using air at 550ºC) porous and non-porous catalysts. The cracking step was carried out at 550°C in 100% CH_4.

Catalyst	Nickel Dispersion %	
	Fresh	Regenerated
Porous	11	8.9
Nonporous	6.3	3.0

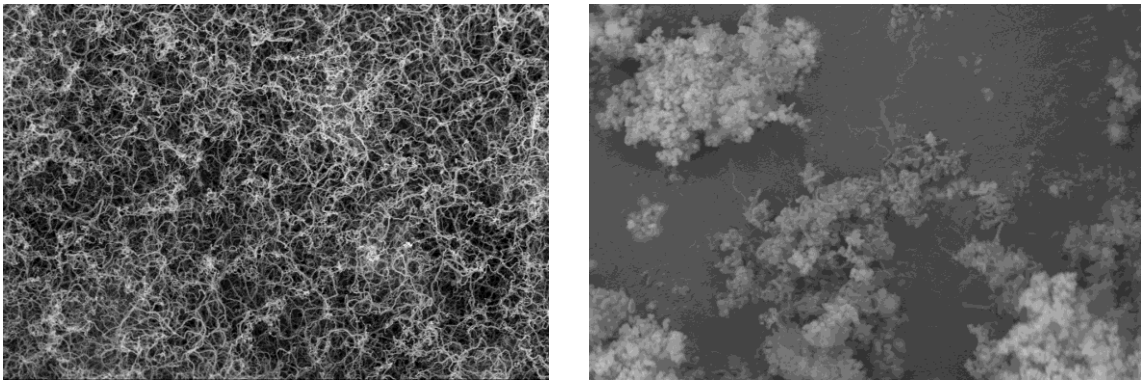

a) b)

200 nm

Figure 3.12 – SEM images for the deactivated catalysts for a) porous support and b) nonporous support. Cracking at 550°C in 100% methane.

The carbon deposited during the cracking/regeneration cycles experiments was oxidized using air at 550ºC in the TGA. The corresponding carbon gasification rate (CGR) curves for the porous and non-porous catalysts are shown in Figures 3.14a and 3.14b, respectively. The CGR

curves represent the carbon oxidation rate in g_C/g_{Ni}/min. The CGR curves, for the porous and non-porous catalysts pass through three stages, as indicated in Figure 3.14a. These three stages may indicate the presence of different types of carbon. Suelves et al. [9] differentiated between two types of carbon; carbon deposited as a filament and carbon deposited as a coating on nickel particles. Guo et al. [13] defined three different carbon species deposited on nickel during methane cracking: Cα, Cβ, and Cγ. Cα is the easiest to gasify, whereas Cγ is the hardest to gasify.

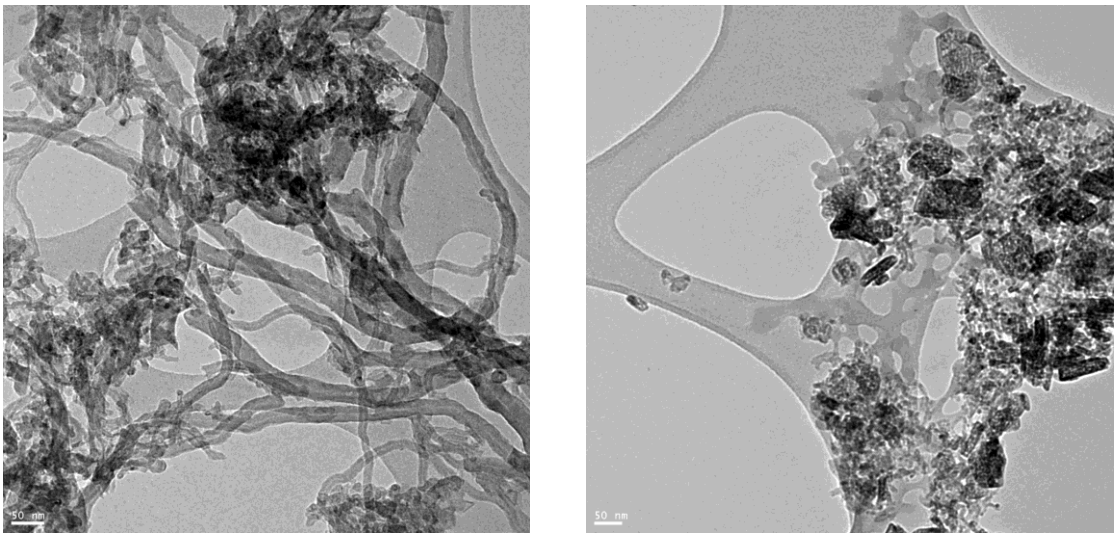

Figure 3.13 – TEM images for the deactivated catalysts for a) porous catalyst support and b) non-porous catalyst. Cracking at 550°C in 100% methane.

As seen in Figure 3.14, in the first stage of the CGR curve, the carbon gasification rate is high. This stage does not last more than three or four minutes, which indicates that the type of carbon oxidized during this first stage represents a minor portion of the total deposited carbon (~4%). This type of carbon may be mostly the encapsulating carbon. Also, a thermocouple located just under the sample holder shows a sharp temperature increase for approximately 3-4 minutes when switching to air, which corresponds to the duration of the first stage, after which the temperature stabilizes to its set value (usually 550°C).

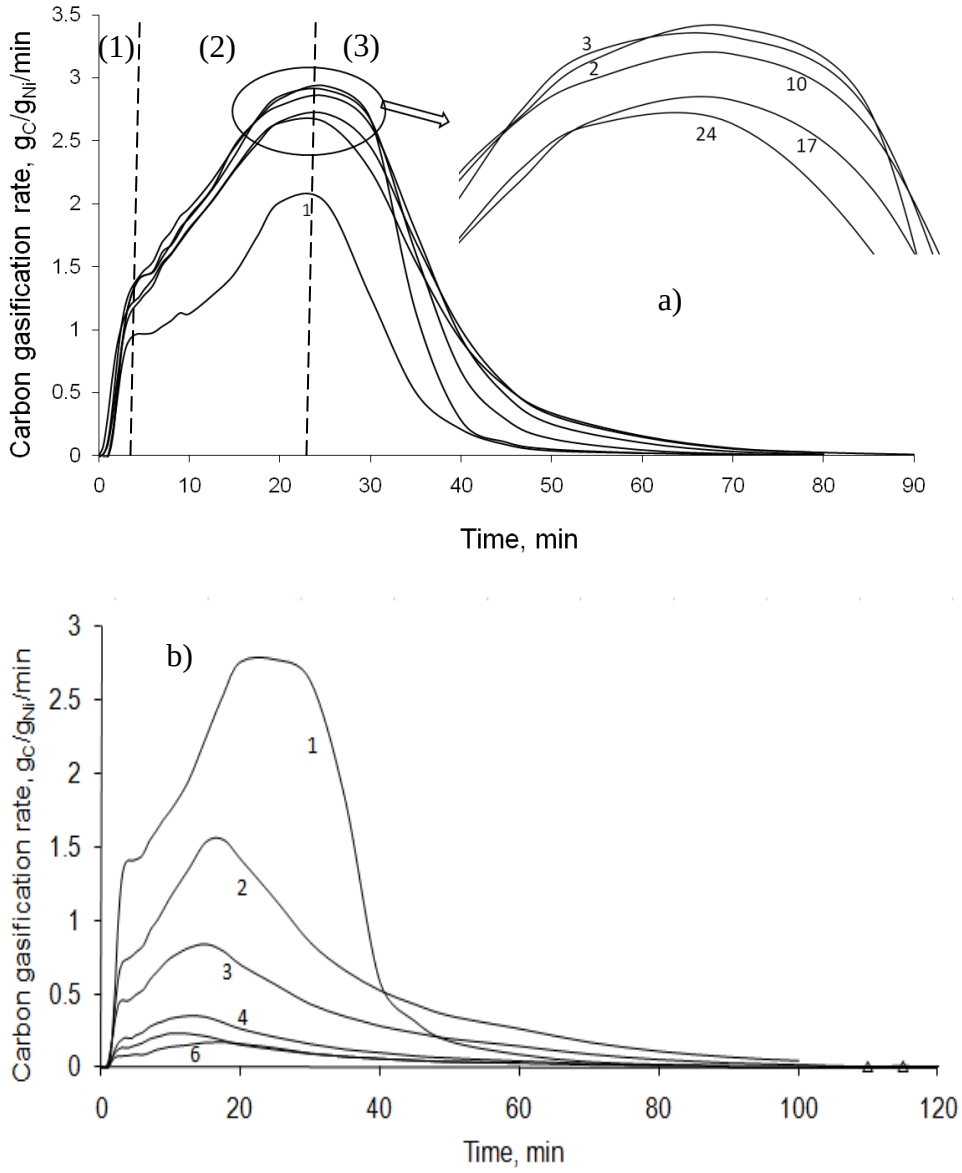

Figure 3.14– Carbon gasification rate for a) porous and b) non-porous catalysts, for different regeneration cycles. Cracking at 550°C in 100% methane. The three stages are shown on the top graph as (1), (2) and (3)

The rapid increase in oxidation during the first stage may thus be due to this effect of temperature. The carbon gasification rate then slows down, leading to a defined second stage. The rate still increases with time until it reaches a plateau after about 20 minutes from the beginning of the oxidation process. The carbon oxidized during the second stage represents about 82% of the total carbon. Since this represents the bulk of the carbon, in the case of the porous catalyst, it may represent the carbon filaments. For the non-porous catalyst, where almost no

carbon filament is present, we can just speculate that it is a different type of carbon than that oxidized during the first stage. Since the oxidation occurs at constant temperature after the first stage one could expect a constant carbon gasification rate. The fact that this rate actually increases suggest that more and more carbon is exposed to oxidation as the regeneration proceeds. In the third period, the carbon gasification rate decreases with time, which can be explained by less carbon to be gasified (e.g. shorter gasification filaments gasified by end of the second stage). The carbon oxidized during the third stage represents approximately 14% of the total carbon. One remarkable observation is that independently of the cycle number and of catalyst type, the fraction of carbon gasified in each stage remains nearly constant.

3.4 Conclusions

Nickel supported on porous (γ-Al_2O_3) and non-porous (α-Al_2O_3) alumina has been used as a catalyst for methane cracking. The results showed that the support type has an effect on the catalyst performance. The non-porous fresh catalyst showed higher carbon capacity than the porous catalyst.

At 550°C and below, the cracking reaction was not affected by the catalyst particle diameter (range 300 – 1000 μm), but above 550°C, deactivation was slower with the bigger particles. This was attributed to the increasing contribution of transport limitation as the particle growths.

Methane partial pressure below 1.0 atm has little effect on the carbon capacity at all temperatures considered. However, except for 550°C, the carbon capacity did increase more notably when increasing the methane partial pressure from 0.9 to 1.0 atm.

Increasing the hydrogen partial decreases the initial cracking rate at all temperatures. At temperatures below 550°C, increasing H_2 partial pressure did increase the carbon capacity (but the deactivation time is considerably increased). Nonetheless, for P_{H2} above 0.15 atm the catalyst was close to inactive at temperatures below 550°C. Above 550°C, the carbon capacity was not affected by P_{H2}.

During cracking/regeneration cycles, the non-porous catalyst showed rapid decrease in activity after the first cycle and onward. This was attributed to the formation of inactive $NiAl_2O_4$ phase and to nickel sintering during regeneration in air. On the other hand, the porous catalyst showed good stability in term cracking rate and carbon capacity over 24 cycles.

Another important difference between the porous and non-porous catalysts is that carbon filament growth took place on the porous catalyst, but not on the non-porous.

In summary, the non-porous Ni-αAl_2O_3 catalyst is not suitable for methane catalytic cracking, but the porous Ni-γAl_2O_3 catalyst appears as a promising candidate because of its good performance and stability over many cycles.

Chapter 4

Reaction and Deactivation Rates of Methane Catalytic Cracking over Nickel

---

Overview

Kinetic modeling of methane catalytic cracking for nickel supported on porous and nonporous alumina was performed to develop initial rate and activity decay equations using a separable kinetic approach. The model parameters were estimated using a set of experiments conducted in a thermo-balance. The experimental work covered the temperature range 500-650ºC, using pure methane, as well as different partial pressures of CH_4/N_2 and CH_4/H_2 mixtures at atmospheric pressure. The model results showed good match with the experimental data and the estimated kinetic parameters agreed well with those reported in literature. The morphology of the support affected the initial reaction rate and catalyst deactivation. The activation energy of methane cracking was estimated at 88 and 75 kJ/mol for the porous and non-porous catalysts, respectively. Alternatively, cracking/ regeneration cycles showed that the porous catalyst can be used for conducting continuous cracking/regeneration cycles of methane cracking. The activation energy for the encapsulating carbon formation is estimated at 147 and 149 kJ/mol for the porous and non-porous catalysts, respectively. The deactivation reaction was found to be half order reaction in surface carbon. The model was expanded to include the cracking/regeneration cycles. The model showed good agreement with the experimental data at different experimental conditions and over up to 39 cycles.

Key words: Methane, Hydrogen, Nickel, Model, Kinetic, Alumina

4.1 Introduction

Currently, CO-free hydrogen production is a major research interest. CO-free hydrogen has wide application in industry and fuel cell applications. Methane catalytic cracking (MCC) is a potential process for production of carbon monoxide-free hydrogen. MCC has the advantage over the conventional steam reforming process by sequestering the carbon, which eliminates any cross contamination of the products with CO_x and reduces the evolution of green house gases [1-5].

To conduct methane decomposition without a catalyst requires very high temperatures, higher than 1300ºC. An active catalyst is required to obtain high methane conversion at reasonable temperatures: 500-700ºC for nickel-based catalysts, 700-950ºC for iron-based catalysts, 850-950ºC for carbon-based catalysts, and 700-1000ºC Co, Pd, Pt, Cr, Ru, Mo, W catalysts [3, 6]. Besides its relatively low temperature range compared to other catalysts, nickel is known for its high activity for methane cracking and the highest carbon capacity among the iron group components [7]. The second element in the catalyst matrix is the support; the support material and its textural properties affect methane conversion. Minimal interaction between the catalyst and support is important to ensure high surface area of the active catalyst for the reaction [7, 8]. The textural properties of the support affect the reactant and product species diffusion to the active sites, which affects the methane catalytic cracking rate [9]. Takenaka et al. [9] reported that nickel supported on non-porous silica shows the highest activity among different surface area and textural structures silicas.

A major problem encountered with methane cracking is rapid catalyst deactivation. Also, catalyst deactivation is associated with the deposition of the carbon on the catalyst, with carbon being one of the reaction products [1, 6, 10]. Deposited carbon diffuses through nickel to form carbon filaments. Some of the carbon accumulates on the external surface of nickel sites, gradually blocking the nickel surface until completely encapsulating the nickel active sites causing complete deactivation [5]. According to the deactivation scenario mentioned above, the reaction rate starts with a maximum value then decreases gradually until it reaches zero. Competition is established between methane, hydrogen, and carbon over the nickel active sites as carbon deposits. The deposited carbon is therefore an indication of reaction extent, via carbon filament formation, but also a measure of deactivation as encapsulating carbon forms. The filamentous carbon formation does not affect the catalyst activity, since the carbon filament is formed by diffusion of carbon through nickel keeping the nickel on the tip of the filament and does not affect either the nickel surface area subjected to the reaction or the nickel activity. On the other hand, the

encapsulating carbon is formed as a layer on the catalyst surface preventing any contact between the catalyst and the reactants, thus encapsulating carbon is the main reason for catalyst deactivation, and it is expected that catalyst deactivation is a function of the encapsulating carbon concentration. Any change in reaction conditions that causes an increase in the reaction rate will lead to an increase in the deactivation rate and vice versa. To achieve maximum hydrogen production and to extend the catalyst lifetime, a balance should be achieved between reaction rate and deactivation rate. The optimum operating conditions can be explored using a well developed reaction rate model that takes into account the deactivation mechanism and the effect of the operating parameters.

Since the first methane catalytic cracking mechanism was proposed by Grabke [11, 12], different models have been proposed [11-17]. A study of catalyst deactivation was first performed by Demicheli et al. [15]. The deactivation behavior has been expressed in the form of a mathematically-fitted equation in different studies [13-17]. Chen et al. [18] proposed two reaction steps to explain the dependency of the catalyst activity on encapsulating carbon formation. Hazra et al. [4] used Chen's steps to develop a kinetic model for methane catalytic cracking using non-separable kinetics. In this model, deactivation was studied based on the reaction mechanism, providing a phenomenological quantification for the deactivation process in a separable kinetic form, which helped in providing a logical explanation for the deactivation phenomenon. The reaction equilibrium constant K_P value used in the model was calculated from thermodynamics and are within 30% of the values used by Zavkurin and Kuvshinov [14] as seen in Table 4.1.

Table 4.1 - Comparison of literature and thermodynamic values for K_P

Temperature, K	Thermodynamics	Zavkurin and Kuvshinov [14]
773	0.50	0.42
823	1.08	0.83
873	2.33	2.05
923	4.47	3.52

To conduct methane cracking in a continuous process, the catalyst is expected to go through several cracking/regeneration cycles. Modeling catalyst behavior during cyclic operation is critical in understanding/predicting the catalytic performance over long periods of operation. To develop such a model, two nickel catalysts, supported on porous γ-alumina (porous catalyst) and nonporous α-alumina

(non-porous catalyst), were prepared. An extensive study was conducted using an electro-balance, with effects of particle size, flow rate, temperature, and methane partial pressure with nitrogen as the inert gas or with different partial pressures of hydrogen, the main reaction. The experimental study was used to investigate the model parameters for each catalyst individually. The model parameters considered here are the pre-exponential factor and activation energy of the rate and adsorption constants when expressed in an Arrhenius form. The aim of the model is to predict the behavior of nickel supported on different forms of alumina for methane cracking for the fresh and regenerated catalyst.

4.2 Experimental work

The catalyst was prepared by wet impregnation of alumina using an aqueous solution of $Ni(NO_3)_2 \cdot 6H_2O$ (99.99%, Alfa Aesar). Two different supports were used: 1) a porous γ-alumina support [99.97% metal basis, 3 micron APS powder, Alfa Aesar] and 2) a non-porous α-alumina support [99.99% metal basis, 0.9-2.2 micron APS powder, Alfa Aesar]. The catalyst preparation method consisted in drying the support overnight at 150°C, preparing a solution of nickel nitrate hexa-hydrate in de-ionized water, then adding the alumina to the solution (the nickel and alumina amounts used were in a 10/100 ratio). The slurry was then stirred for 3 hrs at 80°C for the porous catalyst and in an oil bath at 100ºC for the non-porous catalyst.

The activity experiments were performed in a Cahn TG 151 electro balance, manufactured by Thermo Cahn. The electro-balance is composed of a quartz tube that can withstand high temperature and pressure applications (up to 1000°C at 60 bars). The sample holder is placed in the middle of a quartz tube hanging down from a wire attached to a balance that can record any change in the sample weight, with one microgram resolution. The temperature is controlled by a K–type thermocouple placed just below the sample holder. The catalysts were calcined in air at 600°C inside the thermal gravimetric analyzer (TGA) for 30 minutes. The reduction step was then also carried out in the TGA, at the reaction temperature, for 30 minutes using a 10 vol.% H_2 and 90 vol.% N_2 mixture [5]. The weight of the fresh catalyst was kept around 10 μg for each experiment to avoid spatial limitations. Also, a flat bottom sample holder was used to ensure that each catalyst particle behaved independently, as shown in Figure 4.1. All the gases used in the research were 99.99% purity supplied by Praxair. Except when studying the flow rate effect and particle diameter effect, 120 ml/min was used as a default flow rate and 725 μm was used as the default particle size. The activity experiments included experiments at different partial

pressures of CH_4/N_2 and CH_4/H_2 mixtures. The BET surface area measurements were conducted using a Micromeritics Gemini III 2375 surface area analyzer.

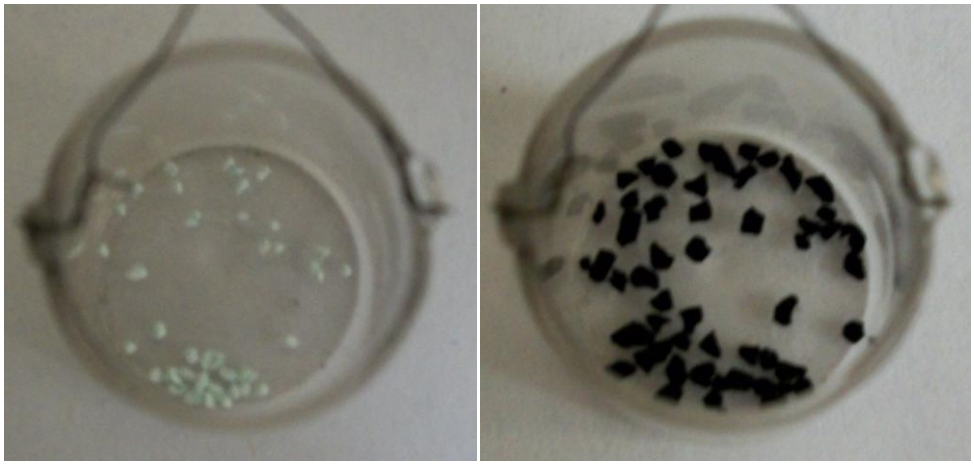

Figure 4.1 - A catalyst sample before reaction and after complete deactivation

4.3 Results and Discussion

4.3.1 Typical experimental result

Figure 4.2 shows the typical experimental results from the electro-balance, i.e. catalyst weight change, in grams of carbon per gram of nickel (g_C/g_{Ni}), as a function of time. By differentiating the catalyst weight change time, the rate of methane decomposition was calculated in terms of $mmol_{CH4}/g_{Ni}/min$. The maximum rate was used as the initial catalyst rate and the time was set at zero when the electro-balance control valve was switched from nitrogen (inert gas) to the reactant mixture. As seen in Figure 4.2, the maximum rate occurs after some period of time from switching the valve to the reactant mixture. The time to reach the maximum rate was further investigated by simulating the residence time distribution (RTD) of the gases inside the electro-balance and around the catalyst particles.

4.3.2 RTD

The RTD of the electro-balance reactor vessel was studied using COMSOL. Two built-in models, the Navier-Stokes and the Convection and Diffusion modes, were used to fully simulate momentum and mass transfer inside the reactor tube and around the catalyst particles. Figure 4.3 shows the simulation results for pure methane at 550ºC and 1 atm. at different flow rates. Figure 4.3 shows the change in methane concentration over time inside the gas bulk surrounding the catalyst particle. The results indicate

that the maximum rate occurs around the same time methane reaches its maximum concentration in the gas bulk around the catalyst particle. These RTD results show that attributing the maximum rate as the initial rate is acceptable.

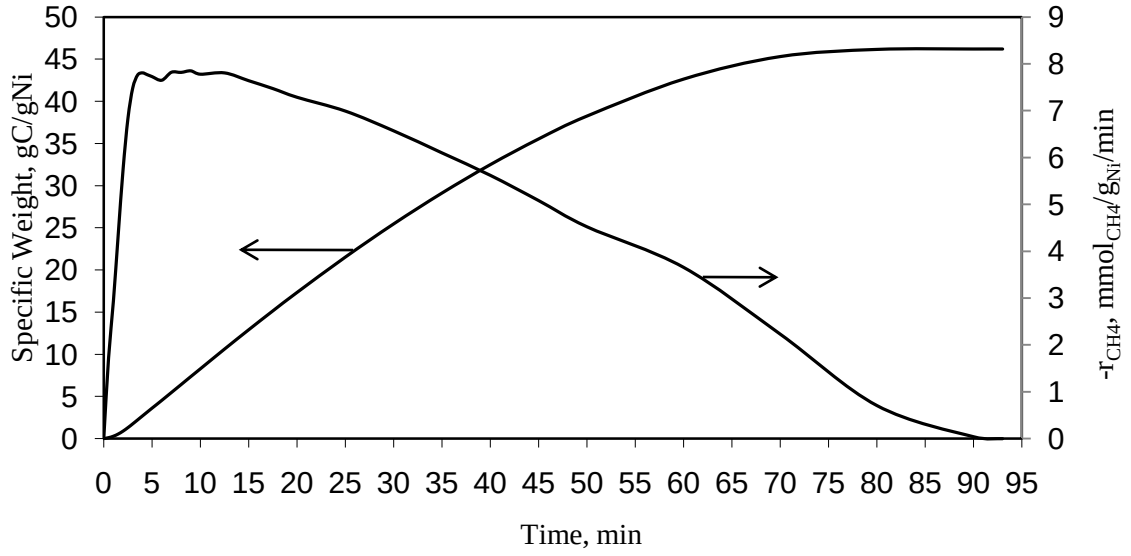

Figure 4.2 - Typical experimental results 550ºC and 1 atm. for 100% methane, 120 ml/min using $Ni/\gamma Al_2O_3$.

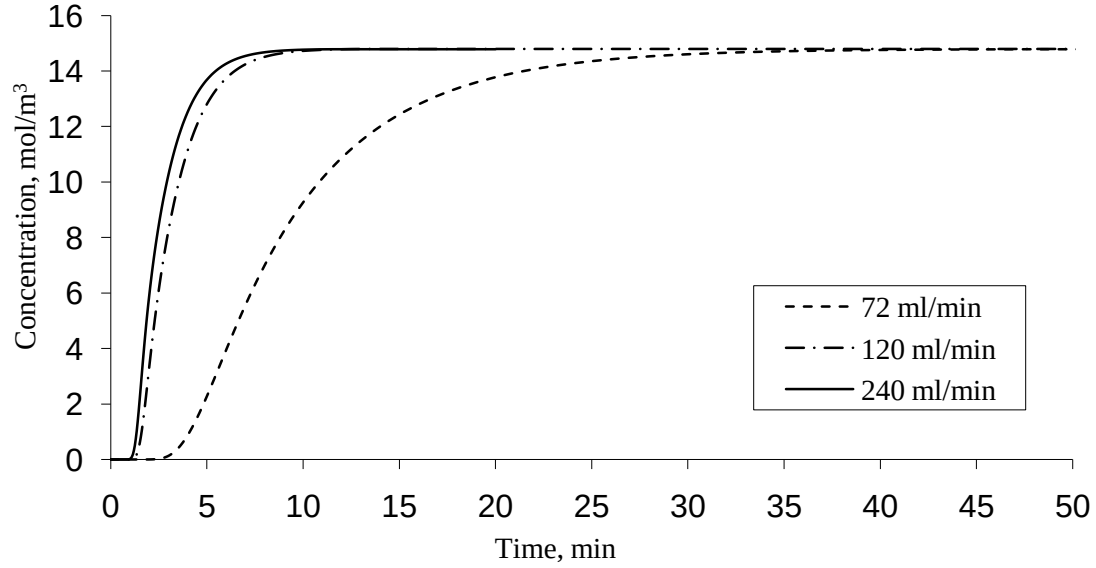

Figure 4.3 - Simulation of the RTD in the case of pure methane inside the electro-balance at different inlet flow rates at 550ºC and 1 atm. for 100% methane. The concentration corresponds to the methane concentration surrounding the catalyst particle.

4.3.3 Controlling regime

Before collecting kinetic data, the reaction was studied at different flow rates and with different particle diameters to examine the regime that controls the reaction, i.e. if the reaction is controlled by internal diffusion, external diffusion, or kinetics [19]. The particle diameter was varied between 300 and 1000 μm and the gas flow rate was varied between 72 and 240 ml/min. The BET surface area for each catalyst at different particle size is shown in Table 4.2. Figure 4.4 shows the reaction rate versus time for different particle diameters for the porous catalyst. This figure indicates that the initial rate (represented as the maximum rate) does not depend of the gas flow rate. Figure 4.4 also shows that there is no clear effect of particle size on the time required for full deactivation. The non-porous catalyst had a similar trend to that shown in Figure 4.4.

Table 4.2 - BET surface area for porous and non-porous reduced catalysts

Particle size, μm	Surface area, m^2/g	
	Porous	Nonporous
300	70.4	18.4
725	67	17.9
1000	59	15.9

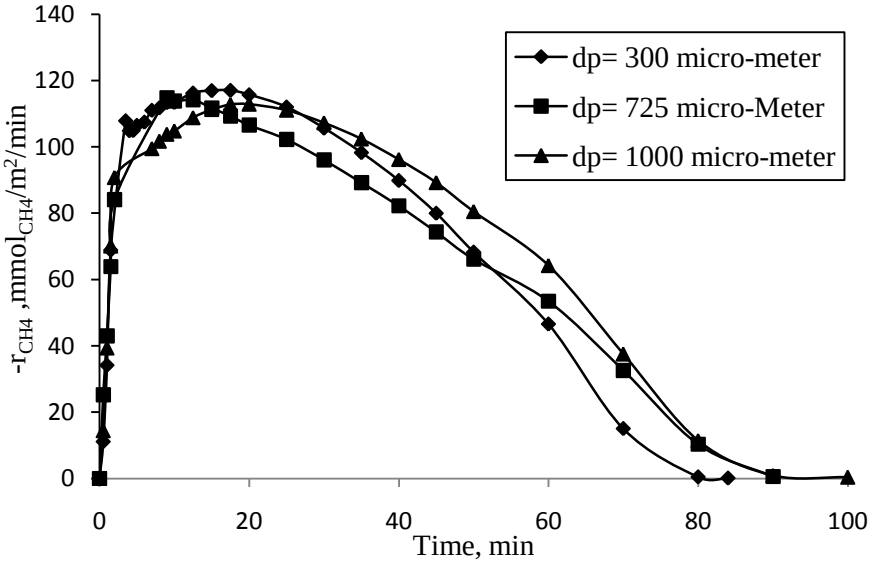

Figure 4.4 - Particle diameter effect on the reaction rate for the porous catalyst at 550ºC, 100% methane, 120 ml/min, and 1 atm.

The flow rate effect on the initial rate was studied at different temperatures and the results are illustrated for the porous and non-porous catalysts in Figures 4.5 and 4.6, respectively. The results indicate that the flow rate has no effect on the initial reaction rate at flow rates at or above 120 ml/min for both the porous and non-porous catalysts. Since the change in initial rate was insignificant above 120 mL/min, this was chosen for tests on initial rates. Because under the operating conditions used in the present study, the reaction rate is independent of particle diameter and gas flow rate (at least for flow rates above 120 ml/min), it is concluded that the reaction is kinetically controlled.

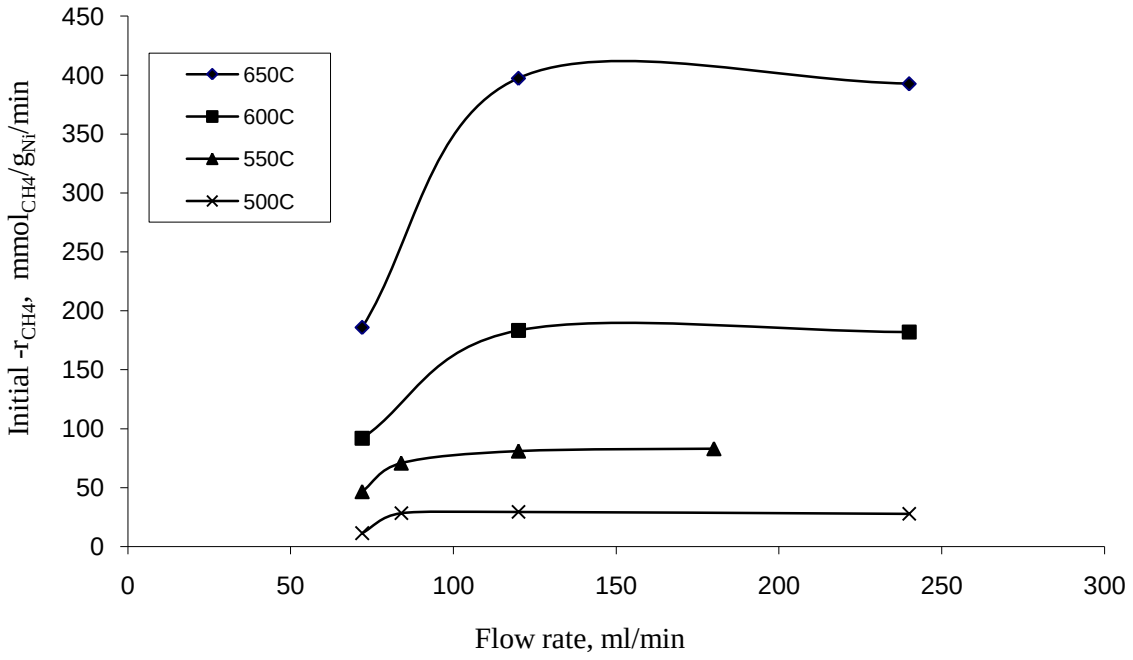

Figure 4.5 - Flow rate effect on the initial raeaction rate for the porous catalyst using 100% methane, 725 μm particles and 1 atm.

4.3.4 Reaction rate

The main problem for kinetic modeling of methane catalytic cracking is to take into account the rapid catalyst deactivation. Usually, the rate of a chemical reaction is a function of chemical species concentrations (or partial pressures) and temperature. Since the gaseous species involved in methane cracking are CH_4 and H_2, the initial rate can be expressed as:

$$\left[Initial\ \ reaction\ rate\right] = R_O = f_1\left(P_{CH4}, P_{H_2}, T\right) \tag{4.1}$$

Once the catalyst deactivation occurs, the instantaneous reaction rate is a function of species partial pressures, temperature and time, as indicated in Equation 1:

$$Instantaeous\ reaction\ rate = R_1 = f_2\left(P_{CH4}, P_{H_2}, T, t\right) \tag{4.2}$$

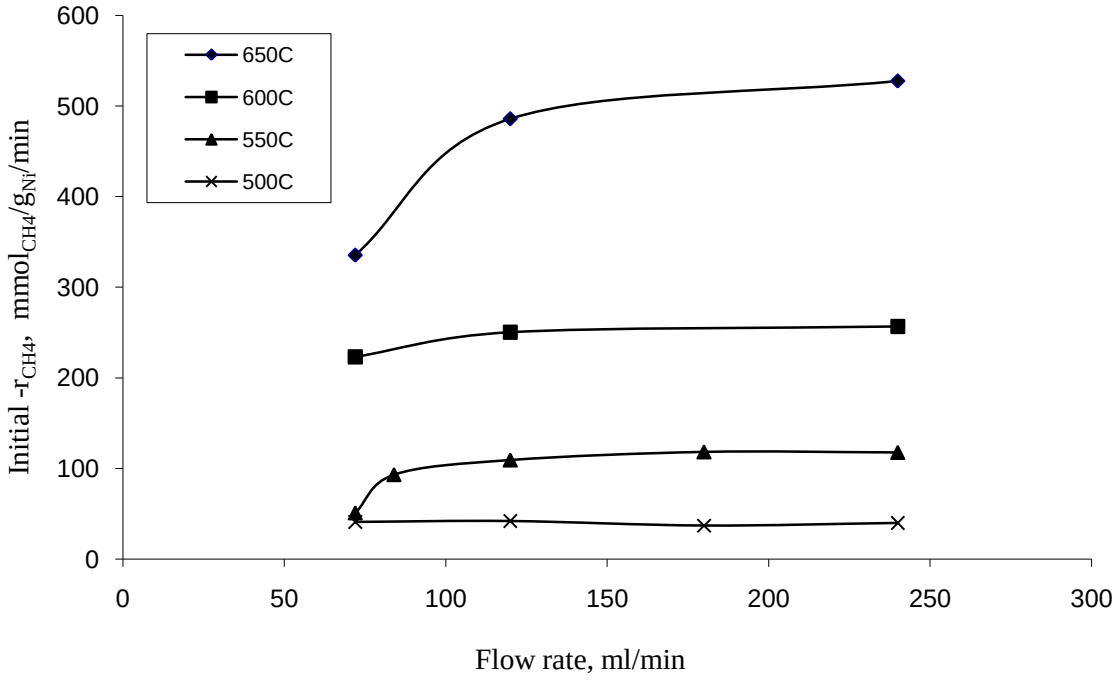

Figure 4.6 - Flow rate effect on the initial raeaction rate for the non-porous catalyst using 100% methane, 725 μm particles, and 1 atm.

It is conventional to define another variable called activity, which relates the rate at any time (t) to the initial rate R_O . The activity can be expressed by the following equation:

$$a = \frac{R_1(t)}{R_O} \tag{4.3}$$

The practical approach for studying deactivating reaction is to use the separable kinetic technique, which was implemented in the present study on methane cracking. In this method the reaction rate is separated into two terms: the first term accounts for reaction kinetics effect and is time independent, the second term accounts for the deactivation is time dependent. A complete description for the separable

kinetic approach is available in [20]. The detailed derivation for the reaction rate and the activity term is shown in Appendix B.

4.3.4.1 Reaction mechanism

Methane cracking occurs on the catalyst surface in a multi-step process. The reaction starts with the adsorption of methane, followed by a series of dehydrogenation reactions until it ends as adsorbed carbon on front of the nickel surface [15, 21]. A segregation/dissolution process for the adsorbed carbon takes place on the nickel surface based on the reacting mixture concentration and the active sites available for the reaction [16, 21]. The adsorbed carbon forms a solution with the nickel and diffuses through the nickel from the front to the rear where carbon is forming carbon filaments. The carbon diffusion process occurs simultaneously with encapsulating carbon formation. The encapsulating carbon is adsorbed carbon on the front nickel surface but remains and blocks the nickel site from the reaction and causes deactivation [4, 18, 21]. Based on this scheme, methane cracking can be divided into the following three processes:

Methane cracking process:

1. $CH_4 + I \Leftrightarrow CH_4 \cdot I$ K_1 (4.4)
2. $CH_4 \cdot I + I \Leftrightarrow CH_3 \cdot I + H.I$ rds/K_2 (4.5)
3. $CH_3 \cdot I + I \Leftrightarrow CH_2 \cdot I + H.I$ K_3 (4.6)
4. $CH_2 \cdot I + I \Leftrightarrow CH \cdot I + H.I$ K_4 (4.7)
5. $CH \cdot I + I \Leftrightarrow C \cdot I + H.I$ K_5 (4.8)
6. $2H.I \Leftrightarrow 2H_2 + 2I$ $1/K_H$ (4.9)
7. $C \cdot I \Leftrightarrow C_{Ni.f} + I$ $1/K_C$ (4.10)

Carbon diffusion process (carbon filament formation):

8. $C_{Ni.f} \rightarrow C_{Ni.r}$ $k_{dif.}$ (diffusion) (4.11)
9. $C_{Ni.r} \rightarrow C_{fil.}$ k_p (carbon filament formation) (4.12)

Deactivation (encapsulating carbon formation):

10. $$n\,C\cdot I \rightarrow n\,C_P.I \qquad k_d \qquad (4.13)$$

Where n is the deactivation order. I represent a vacant site and X.I represents adsorbed X species. $C_{Ni,f}$, $C_{Ni,r}$, and C_p.I are carbon adsorbed on the nickel front side, carbon adsorbed on the nickel rear side, and encapsulating carbon adsorbed on the nickel front side respectively.

4.3.4.2 Initial rate equation

The reaction step represented by Equation 4.5, the second step in the cracking sequence, is assumed to be the rate limiting step [21-23]. Therefore, it is assumed that all methane cracking reaction steps, Equations 4.4-4.10, are in equilibrium except step 2 (Equation 4.5), and that the catalyst is uniformly distributed over the support. Based on the previous assumptions, the following equation was developed to represent the methane cracking rate:

$$\frac{d\theta_{CH_3\cdot I}}{dt} = \mathrm{C}_0\, k_2\left[\theta_{CH_4\cdot I}\theta_I - \frac{\theta_{CH_3\cdot I}\theta_{H.I}}{K_2}\right] \qquad (4.14)$$

Where θ_j is the fraction of sites occupied by species j, and defined as:

$$\theta_j = \frac{C_j}{C_0} \qquad (4.15)$$

With C_0 the total site concentration (mol/cm^2) and C_j is the concentration of sites occupied by species j (mol/cm^2).

Replacing $\theta_{CH_4\cdot I}$, θ_I, $\theta_{CH_3\cdot I}$, and $\theta_{H.I}$ by their expressions from the reaction steps at equilibrium, it comes:

$$\frac{d\theta_{CH_3\cdot I}}{dt} = -r_{CH_4} = \frac{\mathrm{C}_0\, k_2 K_1 \theta_{C.I}^2}{k_C^2 C_{C_{Ni,f}}^2}\left[P_{CH_4} - \frac{K_H^2 K_C C_{CNi,f}}{K_1 K_2 K_3 K_4 K_5} P_{H_2}^2\right] \qquad (4.16)$$

Where r_{CH_4} is the overall methane cracking rate in $\mathrm{mmol}_{CH_4}/\mathrm{g}_{cat}/\mathrm{min}$ and it is equal to the rate of the rate limiting step ($d\theta_{CH3.I}/dt$).

Using the overall sites balance to replace $\theta_{C.I}$ in Equation 16:

$$\theta_I + \theta_{CH_4\cdot I} + \theta_{CH_3\cdot I} + \theta_{CH_2\cdot I} + \theta_{CH\cdot I} + \theta_{C.I} + \theta_{H.I} = 1 \qquad (4.17)$$

And by replacing the value of each θ_X from the individual reaction mechanism rate equations and by assuming that all methane cracking reaction steps, Equations 4.4-4.10, are in equilibrium except step 2 (Equation 4.5):

$$\theta_{C.I} = \frac{1}{\left(1+\frac{1}{K_C C_{C_{Ni,f}}}+\frac{K_{CH_4}P_{CH_4}}{K_C C_{C_{Ni,f}}}+\frac{K_{H_2}^{\frac{3}{2}}P_{H_2}^{\frac{3}{2}}}{K_3K_4K_5}+\frac{K_{H_2}P_{H_2}}{K_4K_5}+\frac{K_{H_2}^{\frac{1}{2}}P_{H_2}^{\frac{1}{2}}}{K_5}+\frac{K_{H_2}^{\frac{1}{2}}P_{H_2}^{\frac{1}{2}}}{K_C C_{C_{Ni,f}}}\right)} \quad (4.18)$$

If we consider the surface concentrations of $\theta_{CH_2.S}, \theta_{CH.S}, \theta_{H.S}$ are negligible then Equation 4.18 becomes:

$$\theta_{C.I} = \frac{1}{\left(1+\frac{1}{K_C C_{C_{Ni,f}}}+\frac{K_{CH_4}P_{CH_4}}{K_C C_{C_{Ni,f}}}+\frac{K_{H_2}^{\frac{3}{2}}P_{H_2}^{\frac{3}{2}}}{K_3K_4K_5}\right)} \quad (4.19)$$

Replacing $\theta_{C.I}$ in Equation 4.16 by its value from Equation 4.19:

$$\frac{d\theta_{CH_3\cdot I}}{dt} = \frac{C_0\, k_2 K_{CH_4}}{k_C^2 C_{C_{Ni,f}}^2\left(1+\frac{1}{K_C C_{C_{Ni,f}}}+\frac{K_{CH_4}P_{CH_4}}{K_C C_{C_{Ni,f}}}+\frac{K_{H_2}^{\frac{3}{2}}P_{H_2}^{\frac{3}{2}}}{K_3K_4K_5}\right)^2}\left[P_{CH_4}-\frac{K_{H_2}^2 K_C C_{C_{Ni,f}}}{K_{CH_4}K_2K_3K_4K_5}P_{H_2}^2\right] \quad (4.20)$$

The carbon concentration is found to be uniform over the nickel particle. Snoeck et al. [21] assumed as follows:

$$C_{C_{Ni,f}} \approx C_{C_{Ni,r}} \approx C_{C_{Ni,Sat}}$$

Then, $C_{CNi,f}$ can be replaced with $C_{CNi,sat}$ By dividing the denominator and numerator by $\left(1+\frac{1}{K_C C_{C_{Ni,sat}}}\right)^2$ and incorporating it into the other constants:

$$-r_{CH_4} = \frac{k(P_{CH_4}-\frac{P_{H_2}^2}{K_P})}{(1+K_{H_2}\cdot P_{H_2}^{3/2}+K_{CH_4}\cdot P_{CH_4})^2} \quad (4.21)$$

k is the specific reaction rate for methane cracking, in $\mathrm{mmol_{CH_4}/g_{cat}/min/atm}$.

$$k = \frac{C_0\, k_2 K_{CH_4}}{k_C^2 C_{C_{Ni,sat}}^2 \left(1 + \frac{1}{K_C C_{C_{Ni,sat}}}\right)^2}$$

K_{CH_4} and K_{H_2} are the overall adsorption constants for methane and hydrogen , in atm^{-1} and $atm^{-3/2}$ respectively.

$$K_{CH_4} = \frac{K_{CH_4}}{\left[K_C C_{C_{Ni,sat}} * \left(1 + \frac{1}{K_C C_{C_{Ni,sat}}}\right)\right]}$$

$$K_{H_2} = \frac{K_{H_2}^{\frac{3}{2}}}{\left[K_3 K_4 K_5 * \left(1 + \frac{1}{K_C C_{C_{Ni,sat}}}\right)\right]}$$

K_P is the equilibrium constant of the overall reaction with units of atm. and its values, from thermodynamic calculation, are listed in Table 4.1.

$$K_P = \frac{K_{H_2}^2 K_C C_{C_{Ni,sat}}}{K_{CH_4} K_2 K_3 K_4 K_5}$$

4.3.4.3 Model discrimination

The model parameters were evaluated statistically using a three steps method. In the first step, the kinetic and adsorption constants were estimated at four temperatures (500, 550, 600 and 650°C). In the second step, from the estimated values of the constants in step 1 at different temperatures, the pre-exponential and activation were determined (by plotting ln k vs. 1/T). In the third steps the estimated parameters in step 2 were used as initial values for an overall fitting that took into account all experimental results for a particular catalyst. The parameter estimation was achieved by minimizing the sum of the squares function [24, 25]:

$$f = \Sigma_{p=1}^{n} (r_{\mathrm{exp.}} - r_{calc.})^2 \qquad (4.22)$$

Where $r_{\exp.}$, $r_{calc.}$, and n are the reaction rate obtained experimentally, the rate calculated from the model, and the number of experiments, respectively. The results of the parameter estimation and analysis of variance are given in Tables 4.3 and 4.4 for the porous and non-porous catalysts, respectively. In the statistical analysis, three different tests were used; the Fischer (F) test was used to check the adequacy of the model to represent the data, the correlation coefficient was used to check if the model fits the data well, and finally the t-distribution test was used to examine if each term in the model contributes significantly to the model or not. The critical F tabulated value is 4.2 according to Montgomery and Runger [25]. If the calculated F test value is greater than 4.2, it implies that the model is adequate to represent the data, and the higher the F test value the better the model. From Table 4.3, the calculated F values are 2834 and 914 for the porous and non-porous catalysts, indicating that the model is adequate to represent the kinetic data for both catalysts. It also indicates that the model is more adequate for the porous catalyst data than the non-porous catalyst data. Nevertheless, the model has excellent adequacy for both catalysts. Also, the 0.995 and 0.984 correlation coefficient values for the porous and non-porous catalysts, respectively indicate good fit. As shown in the parity plot in Figures 4.7 and 4.8 for the porous and non-porous catalysts, respectively, most of the data points are distributed symmetrically around the line with the majority of the points falling on the diagonal. The parity plots represent the accuracy of the prediction of the model for the kinetic data which agree with the results of the F test and R^2 test.

Before conducting the t test (Student's t-test), the model coefficients have been examined to check that all are positive and that the rate constant increase with temperature and that the adsorption constants decrease with increasing temperature. For a 95% confidence interval, the t value must be greater than 4.3 in order to accept that the term contributes significantly to the model. The true mean of the parameters is estimated within an interval of 95% confidence. For the porous catalyst (see Table 4.3), all model parameters contribute significantly to the model. For the non-porous catalyst (see Table 4.4), except the methane adsorption parameters, all other parameters show significant contribution to the model. This can be explained by the poor fit of the methane adsorption constant to the Arrhenius equation. However, if the methane adsorption term is removed from the model for the non-porous catalyst, the F value becomes 220 and R^2 is reduced to 0.93, and the error sum of squares is increased by five folds which indicate the necessity of keeping the methane adsorption term.

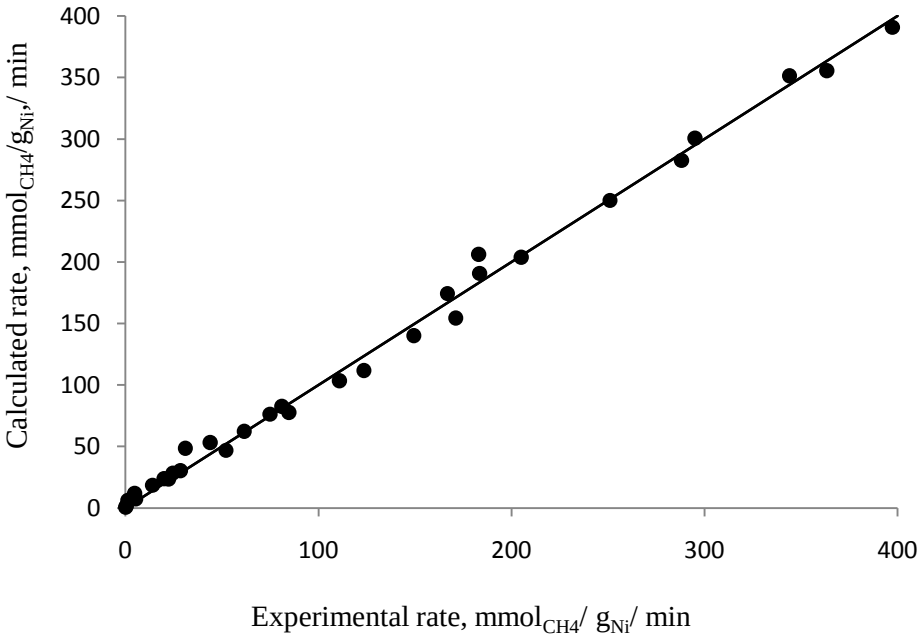

Figure 4.7 – The parity plot for the porous catalyst.

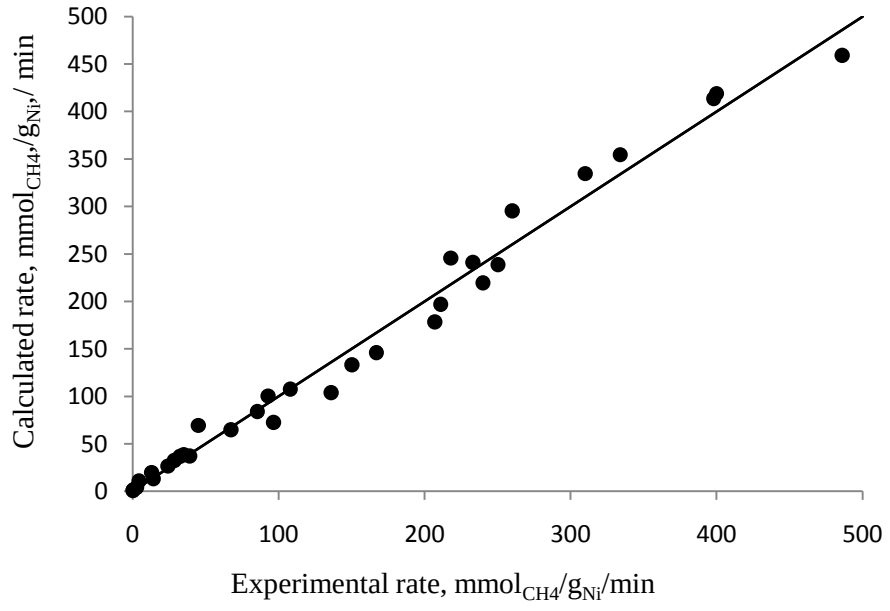

Figure 4.8 - The parity plot for the non-porous catalyst.

Table 4.3 - Parameter estimation for the porous catalyst.

Constant	Parameter	Estimate	t value
k	A($mmol_{CH4}/g_{Ni}$/min/atm)	4.64E7 ± 2.36E6	39
	E (kJ/mol)	88 ± 6	28
K_{H_2}	A_{H2} ($atm^{-3/2}$)	2E-8 ± 5 E-9	7.8
	ΔH_{H2} (kJ/mol)	144 ± 31	9.18
K_{CH_4}	A_{CH4} (atm^{-1})	3.75E-5 ± 4.68E-6	16
	ΔH_{CH4} (kJ/mol)	56 ± 8	13.5
F observed	2834		
Number of samples	30		
F Tabulated (0.05,2,28)	4.2	t critical (0.05/2,2)	4.3
R^2	0.995		

Table 4.4 - Parameter estimation for the non-porous catalyst.

Constant	Parameter	Estimate	t value
k	A($mmol_{CH4}/g_{Ni}$/min/atm)	1E7 ± 13E5	15
	E (kJ/mol)	75 ± 15	10
K_{H_2}	A_{H2} ($atm^{-3/2}$)	7.6E-8 ± 2.4E-8	6.3
	ΔH_{H2} (kJ/mol)	133 ± 36	7.3
K_{CH_4}	A_{CH4} (atm^{-1})	7.8E-6 ± 4.4E-5	0.36
	ΔH_{CH4} (kJ/mol)	69 ± 34	4
F observed	914		
Number of samples	31		
F Tabulated (0.05,2,29)	4.2	t critical (0.05/2,2)	4.3
R^2	0.984		

Where A, E, and ΔH are the pre-exponential factor for the Arrhenius equation, the activation energy in J/mol, and the heat of adsorption in J/mol respectively.

4.3.4.4 Comparison with literature data

The estimated parameters were compared to literature values. The measured activation energy is 88± 6 kJ/mol for the porous catalyst and 75±15 kJ/mol for the non-porous catalyst. The lower activation

energy can be related to the higher activity observed with the non-porous catalyst. In the literature, reported activation energies over a nickel catalyst are: 88 [15], 90 [16], 97 [17], 96 [26], and 75 kJ/mol [27]. An overlap of the activation energy range is observed if the standard error associated with the activation energy estimation for both catalysts is considered. 95% confidence range of the activation energy range is 81.7-94.3 and 60-90 KJ/mol for the porous and non-porous catalysts respectively.

The heat of hydrogen adsorption is estimated at 144± 31 and 133± 36 kJ/mol for the porous and non-porous catalysts, respectively. For nickel supported on alumina, Bartholomew [28] reported a value of 125 kJ/mol (wet-impregnation preparation method), and Germer and Macrae [29] reported 117 kJ/mol (using nickel rods). Bartholomew [28] mentioned that the heat of adsorption of hydrogen on nickel is affected by the catalyst preparation's method and the catalyst structure. The value in the literature was found to be in the same range but slightly lower that the estimated value in this work. The literature value is still in the 95% confidence range.

The heat of methane adsorption is estimated at 56± 8 and 69± 34 kJ/mol for the porous and non-porous catalysts, respectively. Beebe et al [30] found that the heat of adsorption of methane over the nickel surface (110), which is the most active surface for methane cracking, was 55.6 kJ/mol, very close to the estimated value for the porous catalyst. The higher value observed with the non-porous catalyst is attributed to the lower specific surface area available for the reaction, which increases competition over active sites.

4.3.5 Deactivation

Once the initial rate, as calculated from Equation 4.21, is achieved, deactivation starts and the rate decreases with time until the catalyst is completely deactivated. The actual rate at any time (t) can be expressed using the activity term defined in Equation 4.3. The initial rate is a function of methane and hydrogen partial pressures, and temperature, and the rate decreases due to encapsulation of the active sites by carbon. So, the activity term should be a function of the fraction of encapsulated sites. The overall site balance before deactivation is expressed by the following equation:

$$\theta_I + \theta_{CH_4 \cdot I} + \theta_{CH_3 \cdot I} + \theta_{CH_2 \cdot I} + \theta_{CH \cdot I} + \theta_{C.I} + \theta_{H.I} = 1 \qquad (4.23)$$

When taking into consideration encapsulated sites, whose fraction is expressed as $\theta_{C_P \cdot I}$, the overall site balance is expressed as follows:

$$\theta_I + \theta_{CH_4 \cdot I} + \theta_{CH_3 \cdot I} + \theta_{CH_2 \cdot I} + \theta_{CH \cdot I} + \theta_{C.I} + \theta_{H.I} + \theta_{C_P.I} = 1 \quad (4.24)$$

Replacing θ_I, $\theta_{CH_4 \cdot I}$, $\theta_{CH_3 \cdot I}$, $\theta_{CH_2 \cdot I}$, $\theta_{CH \cdot I}$, and $\theta_{H.I}$ in Equation 24 by their expression values from the reaction steps at equilibrium, the following relation between $\theta_{C.I}$ and $\theta_{C_P \cdot I}$ is obtained:

$$\theta_{C.I} = \frac{1 - \theta_{C_P \cdot I}}{k'} \quad (4.25)$$

Where:

$$k' = \left(1 + \frac{1}{K_C C_{C_{Ni,f}}} + \frac{K_{CH_4} P_{CH_4}}{K_C C_{C_{Ni,f}}} + \frac{K_{H_2}^{\frac{3}{2}} P_{H_2}^{\frac{3}{2}}}{K_3 K_4 K_5} + \frac{K_{H_2} P_{H_2}}{K_4 K_5} + \frac{K_{H_2}^{\frac{1}{2}} P_{H_2}^{\frac{1}{2}}}{K_5} + \frac{K_{H_2}^{\frac{1}{2}} P_{H_2}^{\frac{1}{2}}}{K_C C_{C_{Ni,f}}} \right) \quad (4.26)$$

By incorporating Equation 4.25 in Equation 4.21, it comes:

$$-r_{CH_4} = \frac{C_0 \, k_2 K_{CH_4}}{k_C^2 C_{C_{Ni,f}}^2} \left(\frac{1 - \theta_{C_P \cdot I}}{k'} \right)^2 \left[P_{CH_4} - \frac{K_{H_2}^2 K_C C_{C_{Ni,f}}}{K_{CH_4} K_2 K_3 K_4 K_5} P_{H_2}^2 \right] \quad (4.27)$$

A characteristic of the deactivation is the reduction in the total number of active sites. Therefore, it is important to estimate the total number of active sites at any time during the deactivation process. To do so, we introduce the fraction, α, of active sites not deactivated relative to the initial total number of active sites [20]:

$$\alpha = \frac{N_t}{N_0} \quad (4.28)$$

Where N_0 is the initial total number of active sites per mass of catalyst, and N_t is the total number of active sites per mass of catalyst at time t.

Because, $N_0 = N_t + N_{CP.I}$, it comes:

$$\alpha = (1 - \theta_{C_P \cdot I}) \quad (4.29)$$

Ultimately, the goal is to derive an expression of the activity as a function of time. The activity is related to the fraction α, and thus to $(1-\theta C_{P.I})$. From Equations 4.26 and 4.27, it can be seen that the cracking rate

is a complex function of temperature, P_{CH4}, P_{H2}, C_{CNif} and $\theta_{CP.I.}$ The variables C_{CNif} and $\theta_{CP.I}$ are related to each other, but are difficult to estimate. Because α is equal to $(1-\theta_{CP.I})$, it will be assumed that the cracking rate is proportional to $(1-\theta_{CP.I})^P$, where P is a fitting parameter:

$$\left(-r_{CH_4}\right)_t = \left(-r_{CH_4}\right)_{t=0}\left(1-\theta_{C_P\cdot I}\right)^P \tag{4.30}$$

Note that P is very likely different than 2, despite the dependence of the cracking rate on $(1-\theta_{CP.I})^2$ as seen in Equation 4.27. Indeed, $C_{CNi,f}$ is an intrinsic function $\theta_{CP.I}$.

Equation 4.30 satisfies the fact that at no deactivation, $\theta_{C_P\cdot I}$ is zero and the reaction rate is equal to the initial rate. After deactivation occurs, the reaction rate decreases as $\theta_{C_P\cdot I}$ increases until the rate reaches zero when all the active sites are encapsulated.

It should be clear that Equation 30 is equivalent to defining the activity, a, as:

$$a = \left(1-\theta_{C_P\cdot I}\right)^P \tag{4.31}$$

Therefore the relation between the ratio α and the activity a is simply:

$$a = \alpha^P \tag{4.32}$$

Differentiating Equation 29, we get

$$\frac{d\alpha}{dt} = -\frac{d\theta_{C_P\cdot I}}{dt} \tag{4.33}$$

From Step 10 in the reaction mechanism (Equation 4.13), we have:

$$\frac{d\theta_{C_P\cdot I}}{dt} = k_d\theta_{C.I}^n \tag{4.34}$$

Combining equations 4.25, 4.29, 4.33 and 4.34 we obtain a differential equation in α:

$$\frac{d\alpha}{dt} = -\frac{k_d}{k'^n}\alpha^n \tag{4.35}$$

By integration:

$$\alpha = \left(\frac{1}{1+(n-1)C_d t} \right)^{\frac{1}{n-1}} \tag{4.36}$$

Because C_d depends on k', the constant Cd is therefore a function T, P_{CH4}, P_{H2} and $C_{CNi,f}$. C_d is fitted to the following equation which is a simpler form of k', where the four terms that depend on P_{H2} are combined in one term for which the power of hydrogen partial pressure must range between 0.5-1:

$$C_d = k_d (kd_C + kd_{CH_4} * P_{CH_4} + kd_{H_2} * P_{H_2}^b) \tag{4.37}$$

From Equations 4.32 and 4.36 we finally have:

$$a = \left(\frac{1}{1+(n-1)C_d t} \right)^{\frac{P}{(n-1)}} \tag{4.38}$$

To calculate the activity as a function of time, three parameters need to be determined: C_d, n and P. Those three parameters are determined by fitting each experiment independently. Note that the parameters n and P must be the same for all experiments, but C_d is dependent.

Figures 4.9 and 4.10 show the fitting results for 100% methane at different temperatures for the porous and non-porous catalysts respectively. Figures 4.9 and 4.10 show the effect of the value of encapsulating order n on the modeling results. The best fits were obtained for the following values for P and n: P = 0.4 and n = 0.5. The order, n, is dependent on the carbon surface coverage.
Using n = 0.5 and P = 0.4, the equation for the deactivation becomes:

$$a = \left(\frac{1}{1-0.5\,k_d (kd_C + kd_{CH_4} * P_{CH_4} + kd_{H_2} * P_{H_2}^{0.83}) t} \right)^{-0.8} \tag{4.39}$$

The parameter estimation results for Equation 39 for both catalysts are listed in Table 4.5.

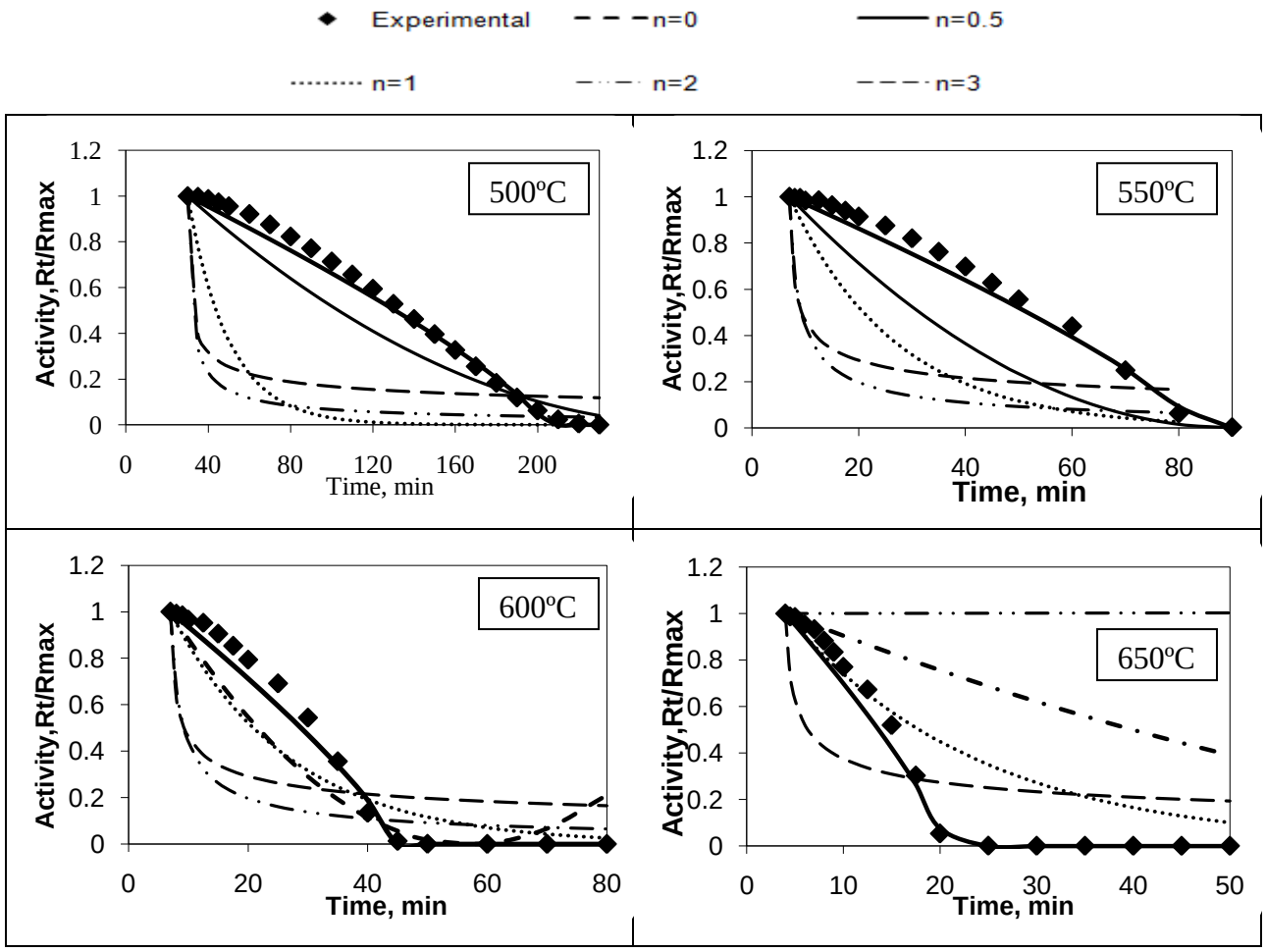

Figure 4.9- Deactivation order for the porous catalyst at different temperatures for 100% methane, 120 ml/min, 725 μm particles, and 1 atm, P = 0.4.

The calculated parameters listed in Table 4.5 demonstrate the adequacy of the model to represent the deactivation behavior data of both catalysts (F test) at reasonable correlation coefficient values. The true mean of the parameters is estimated within an interval of 95% confidence. The estimated values for the activation energy and adsorption heats are similar for porous and non-porous catalysts, which indicate that the deactivation mechanism is the same for both catalysts. The activation energy for encapsulating carbon formation is 147-149 kJ/mol, and values obtained from the literature range from 99 [17] to 135 kJ/mol [14], and to 178 kJ/mol [13].

Table 4.5 - Parameter estimation for the activity equation

Constant	Parameter	Porous	Non-porous
k_d	A_d	4904 ± 172	2214 ± 118
	E_d (kJ/mol)	147 ± 0.26	149 ± 0.41
kd_C	Ad	313 ± 6	531 ± 22
	ΔHd (kJ/mol)	26 ± 0.15	26 ± 0.33
kd_{CH_4}	Ad_{CH4} (atm^{-1})	-4082 ± 234	-1845 ± 830
	ΔHd_{CH4} (J/mol)	3.56 ± 0.43	3.33 ± 3.02
kd_{H_2}	Ad_{H2} (atm^{-b})	-0.34 ± 0.03	-0.39 ± 0.11
	ΔHd_{H2} (kJ/mol)	81 ± 1	81 ± 2
n		0.5	0.5
P		0.4	0.4
b		0.83 ± 0.05	0.83 ± 0.11
F observed		301	131
Number of Experiments		30	31
F Tabulated (0.05,2,29)		4.2	
R^2		0.98	0.96

The value of C_d decreased significantly when using CH_4/H_2 mixtures, compared to pure methane, at temperatures between 500-550ºC. The value of C_d is an indication of the deactivation rate, so a higher value of C_d leads to lower activity, as shown by Equation 38. Hydrogen adsorbs more on the active nickel sites at lower temperatures [28, 31], which decreases the availability or reactivity of the active sites, decreasing the reaction rate and the deactivation rate. But at higher temperatures, the rapid kinetics shifts the reaction to produce more carbon, which increases the fraction of active sites covered by carbon and increases the deactivation rate. The effect of adsorption on activity may explain Vilacampa et al. [32] conclusions that any factor that increases the rate of methane cracking also increases the rate of deactivation and vice versa. Increasing temperature leads to increasing the fraction of adsorbed carbon sites which in turn increases encapsulating carbon formation [31]. For hydrogen, increasing P_{H2} decreases the reaction rate, but also occupies a fraction of the active sites, which slows the formation of encapsulating carbon. And since hydrogen adsorption is reversible, the longer deactivation time observed with CH_4/H_2 mixtures is explained.

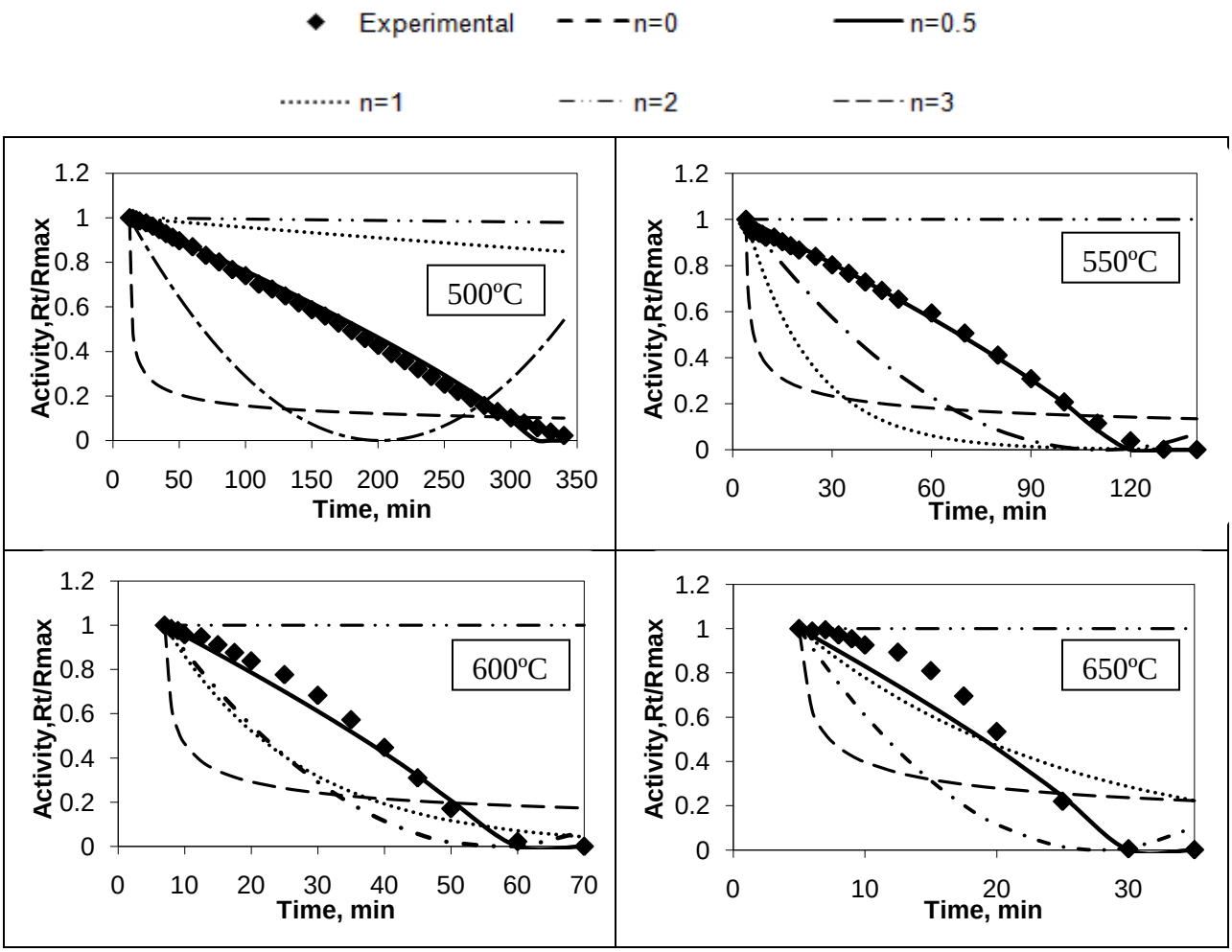

Figure 4.10 - Deactivation order for the non-porous catalyst at different temperatures for 100% methane, 120 ml/min, 725 μm particles, and 1 atm, P = 0.4

4.3.6 Cracking cycles

After studying deactivation of the fresh catalyst, this work was extended to study regenerated catalyst deactivation. A series of cracking/regeneration cycles were performed for porous and nonporous catalysts at 550ºC, 120 ml/min, 100% methane, using 725 μm particles, and at 1 atm. The regeneration was conducted at the same conditions but using 100% air. The porous catalyst sustained its activity for 24 cycles, at which point the experiment was ended, while the non-porous catalysts showed deterioration in performance in the second cycle and activity was almost exhausted after the fifth cycle.

The initial reaction rate varied with the cracking cycle, an equation has been developed for each catalyst to predict the initial rate for each catalyst. The initial reaction rate for the porous catalyst as a function of cycle number starting from the second cycle can be written as:

$$-r_{CH4}(cycle) = -r_{CH4}(cycle = 1) * 1.275 * Exp(-0.004 * cycle) \quad (4.40)$$

The initial reaction rate for the non-porous catalyst as a function of cycle number is calculated from the following equation:

$$-r_{CH4}(cycle) = -r_{CH4}(cycle = 1) * 1.5181 * Exp(-0.426 * cycle) \quad (4.41)$$

The activity changes with time for different cycles using the porous and non-porous catalysts are shown in Figures 4.11 and 4.12, respectively. The porous catalyst shows slower deactivation as the number of cycles increases, as shown in Figure 4.11, while the non-porous catalyst shows a remarkable increase in the deactivation rate as the number of cycles increases, as shown in Figure 4.12. The rapid decrease in activity for the non-porous catalyst implies that a change in the active site concentration or distribution leads to a change in the initial rate and deactivation due to sintering as indicated by the nickel chemisorption data in the previous chapter. Accordingly, catalyst activity deteriorated quickly. The porous catalyst showed excellent stability over 24 cycles, which indicates that the porous catalyst could be applicable in cyclic hydrogen production via methane cracking.

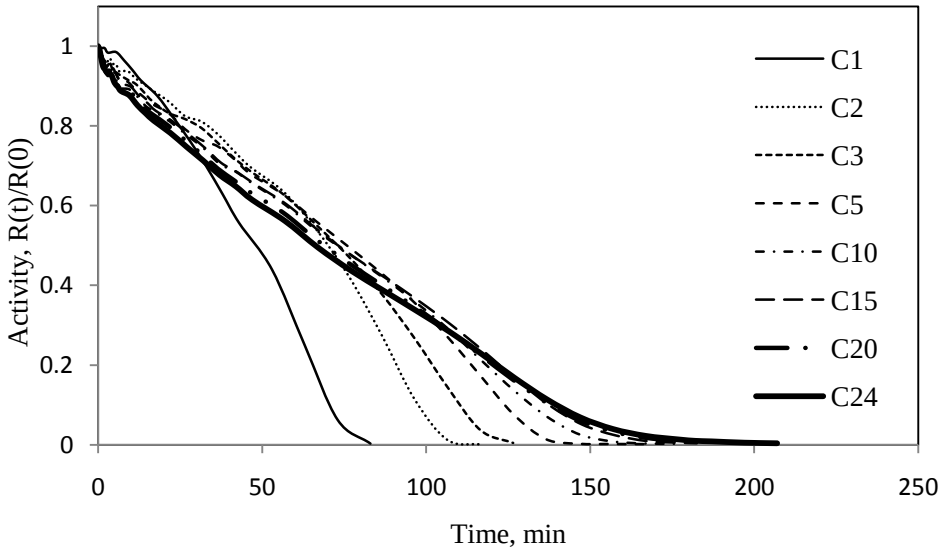

Figure 4.11 - Experimental data for Activity of different cracking cycles of the porous catalyst

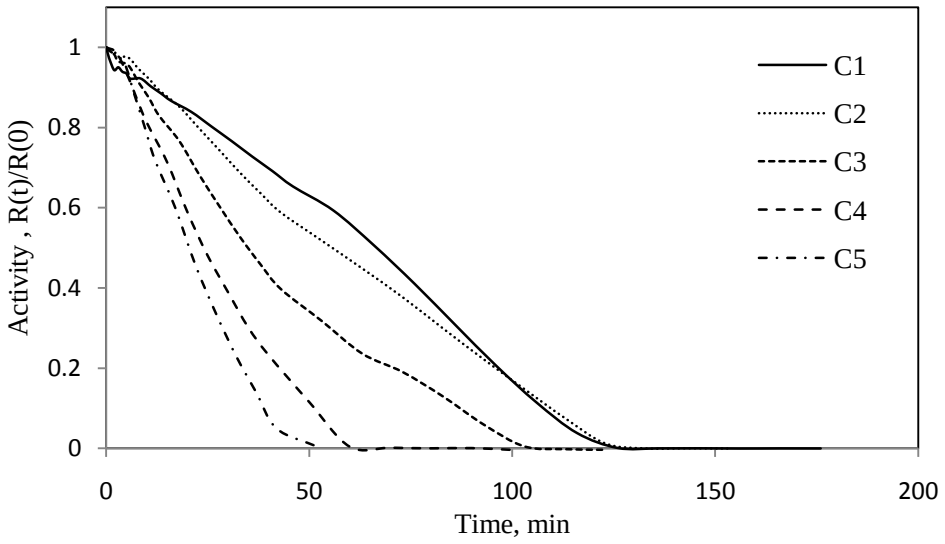

Figure 4.12 - Experimental data for activity of different cracking cycles of the non-porous catalyst

Equation 4.38 was applied for the different cracking cycles for the porous catalyst. The value of C_d was estimated based on the best fit of the data. Due to the slower deactivation observed with the second cycle for the porous catalyst, C_d decreased as the number of cycles increased. An equation similar to Equation 4.39 is developed to predict the activity at any cycle, but the value of C_d is corrected by multiplying it by a factor, f, to account for the change in deactivation rate over different cycles, as shown in the following equation:

$$a = \left(\frac{1}{1+(n-1)k_d f(kd_C + kd_{CH_4} * P_{CH_4} + kd_{H_2} * P_{H_2}^{0.83})t} \right)^{-0.8} \quad (4.42)$$

For the porous catalyst, the factor f is calculated from the following polynomial:

$$f = -7E-5(Cycle)^3 + 0.0036(Cycle)^2 - 0.0546(Cycle) + 0.7829 \quad (4.43)$$

Figures 4.13 compares the experimental data and model results for different cycles for the porous catalyst. The model results agree well with the experimental data. Figure 4.14 shows the model prediction for the initial rate of the porous catalyst as a function of the number of cycles. The model prediction shows a steady decrease in the initial rate as the number of cycles increases until the initial rate reaches around 50 $mmol_{CH4}/g_{Ni}/min$ after 170 cycles, which is equal to half of the initial cracking rate reported in

the second cycle. After 380 cycles, the initial rate dropped to 25 $mmol_{CH4}/g_{Ni}/min$. Equation 4.42 can be applied to predict the activity for any cycle between 1-39.

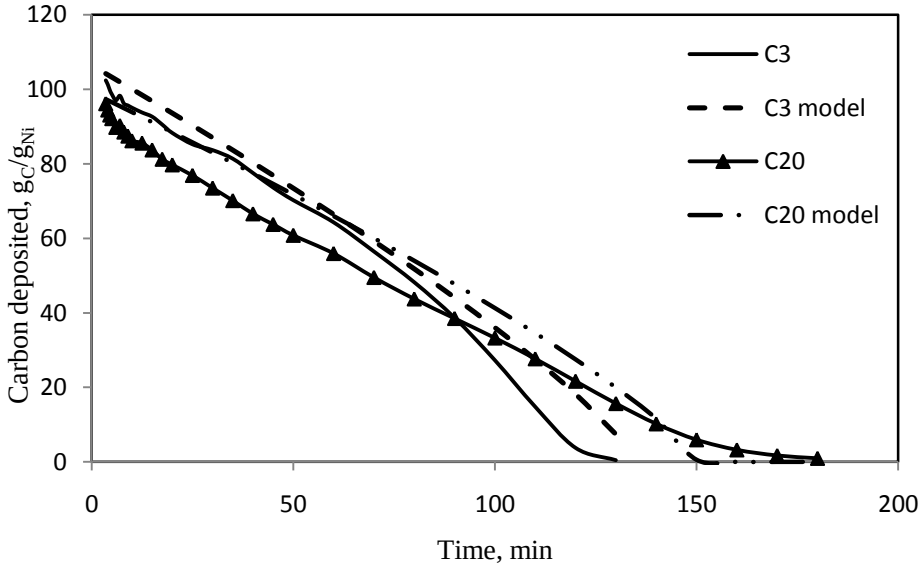

Figure 4.13 – Carbon deposited on the porous catalyst at 550ºC in different cycles

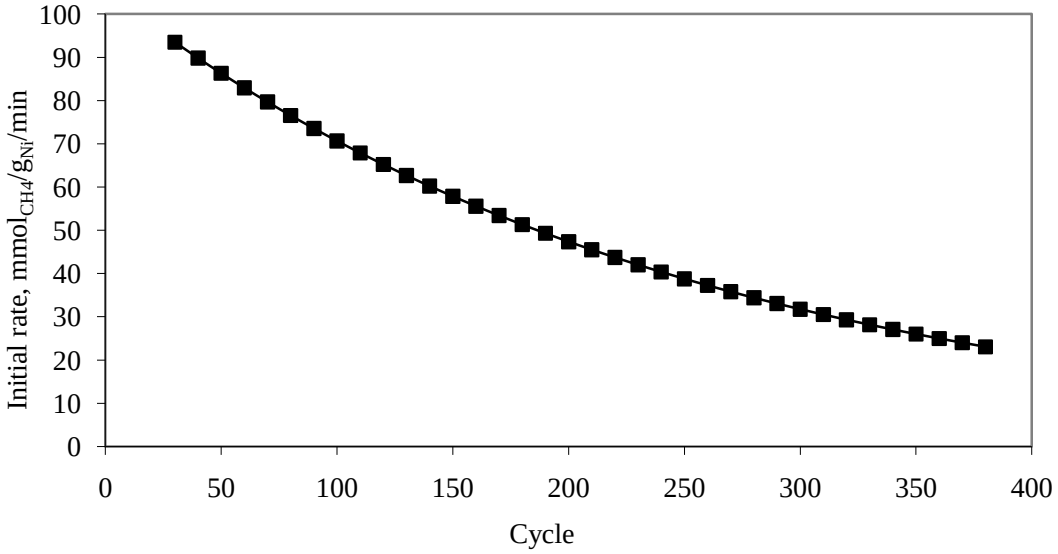

Figure 4.14 – The model prediction of initial reaction rate of the porous catalyst at 550ºC in different cycles

4.4 Conclusions

Methane cracking kinetics was investigated using nickel supported on porous and non-porous alumina. Models for predicting the initial reaction rate and activity decay were developed for the 500-650ºC temperature range, at atmospheric pressure. The reaction mechanism begins with molecular adsorption of methane, with the release of the first hydrogen atom as the rate limiting step. At constant temperature, the initial rate is a function of methane partial pressure and can be described by the Langmuir-Hinshelwood type equation that accounts for the competition between hydrogen and methane adsorption over the active sites. The activation energy for methane cracking is estimated at 88 and 75 kJ/mol for the porous and non-porous catalysts, respectively.

The activation energy for encapsulating carbon formation, which is responsible for deactivation, is 147 and 149 kJ/mol for the porous and non-porous catalysts, respectively. Catalyst deactivation depends on temperature, methane and hydrogen partial pressures, and the carbon surface coverage. The deactivation rate is a half order reaction in surface carbon. Deactivation during successive cracking cycles was studied. The change in the active site distribution and concentration from one cycle to another altered the deactivation behavior of the catalyst. The support type affected the activation energy of methane cracking. The presence of all the nickel on the outer surface of a low surface area support increased the sintering possibility in successive cracking/regeneration cycles. While the non-porous catalyst completely deactivated after 5 cycles, the porous catalyst kept its activity after 24 cycles.

The model predicts for the porous catalyst a steady decrease in the maximum initial rate: this rate reaches 25% of its initial rate after 350 cycles.

Chapter 5

Methane Cracking in a Fluidized Bed on Ni-Supported Catalysts

Overview

Nickel, supported on porous alumina (γAl_2O_3), non-porous alumina (αAl_2O_3), and porous silica, was used to catalyze methane cracking in a fluidized bed. An experimental design was developed to study the effect of temperature, P_{CH4}, and particle diameter and their interactions on methane conversion for each catalyst. It was found that for all catalysts temperature was the dominant parameter affecting the hydrogen production rate and that the particle diameter had the most effect on the total amount of carbon deposited. Then, an experimental parametric study showed variations in catalyst performance between the supports: maximum methane conversion observed followed this order: Ni/SiO_2> $Ni/\alpha Al_2O_3$> $Ni/\gamma Al_2O_3$. Nonetheless, better fluidization quality was obtained with $Ni/\gamma Al_2O_3$. Methane conversion was increased by increasing temperature and particle size from 108 to 275 μm. Increasing the flow rate and P_{CH4} caused a drop in methane conversion. Comparison between fluidized bed and fixed bed showed, at constant weight hourly space velocity (WHSV), higher conversion in the fixed bed, but at the same time faster deactivation. A critical problem with the fixed bed is the pressure build-up inside the reactor due to carbon accumulation. Finally, a series of cracking/regeneration cycle experiments were carried out in the fluidized bed. The regeneration was performed through carbon gasification in air. $Ni/\alpha Al_2O_3$ and $Ni/\gamma Al_2O_3$ saw their activity decreasing very rapidly after the first cycle, which was attributed to Ni sintering during regeneration in air. However, Ni/SiO_2 was thermally stable over at least three cracking/regeneration cycles, but mechanical attrition was observed.

Keywords: Methane cracking, Hydrogen production, Fluidized bed, Nickel catalyst, Alumina, Silica

5.1 Introduction

Increasing demands for CO-free hydrogen for automobile and industrial applications requires developing new technologies to replace the current traditional hydrogen production methods: steam reforming, and partial oxidation of hydrocarbons. These well developed methods produce hydrogen contaminated with COx, which requires further complicated separation process to achieve acceptable H_2 purity levels for PEM (polymer electrolyte membrane) fuel cells and other industrial applications. Currently, catalytic cracking of hydrocarbons has gained more interest as a CO-free hydrogen production method, with hydrocarbons remaining the main source of hydrogen in the near to medium future [1-3]. Methane, which has the highest percentage of hydrogen/carbon among hydrocarbons, is gaining even more interest due to the recent commercial application of carbon filaments, which is the only by-product of the cracking process. Although, carbon filaments are commercially viable, their production also helps to minimize the emissions of the greenhouse gases [4, 5].

The main problem observed with catalytic methane cracking is catalyst deactivation, since carbon is deposited on the catalyst. Carbon either diffuses through nickel to form carbon filaments or encapsulates the active sites and blocks methane access to them [1, 6-8]. Regeneration of the deactivated catalyst is necessary for reuse of the catalyst in a continuous process. To carry out methane cracking in a continuous mode of operation, continual addition of regenerated catalyst and removal of deactivated catalyst is needed [1, 5, 7]. A fluidized bed unit composed of a cracker and regenerator represents the default system for conducting continuous operation of methane cracking [5, 9, 10]. Lee et al. [11] conducted an experimental study in a fluidized bed using several kinds of activated carbon; they compared the performance of the fluidized bed to a fixed bed. They concluded that the performance of the fluidized bed was similar to the fixed bed in terms of reaction rate and deactivation rate but the plugging of the fixed bed was overcome by using the fluidized bed system. Fluidized bed systems provide different advantages for methane cracking when compared to a fixed bed: lower pressure drop, better mixing, and higher mass and heat transfer rates [5, 10, 11].

Different methane cracking studies have been conducted using fluidized beds to investigate the performance of different catalysts and/or to study the effect of the process parameters on methane conversion. In terms of the catalysts used for methane cracking in a fluidized bed, nickel has been the most widely used. Nickel, for such studies, has been supported on Al_2O_3 and SiO_2 [12], and La_2O_3 [13] or supported and promoted with another metals such as $Ni/Cu/Al_2O_3$ [14-16], $Ni/Ca/Al_2O_3$ [12], and

Ni/Rh/La_2O_3 [13]. Activated carbon has also been used as a catalyst [9, 11, 17], as well as carbon black [9, 17-20]. Cobalt has been tested as Co/Mo/Al_2O_3 [14], Co/Al_2O_3 [12], and Co/ Al_2O_3/SiO_2 [21]. Other metals, such as Cu and Fe have also been investigated [22, 23] [12, 24] [25].

Metallic catalysts are distinguished from carbon-based catalysts for their ability to sustain the cracking reaction for a longer period of time after carbon deposition begins due the diffusion of deposited carbon through the active metal site which then precipitates on the other side of the metal particle to form carbon filament. The carbon filament is formed via a mechanism that keeps the metallic active site on the tip of the carbon filament, so that it is still exposed to reacting gases, until deactivation by encapsulating carbon. Carbon-based catalysts are subjected to rapid deactivation due to the deposition of inactive carbon, which reduces the amount of active carbon surface [2, 4, 26]. For example, in their study of methane cracking, Lee et al. [11] reported that the activated carbon employed in the study showed good activity at the beginning but suffered from rapid deactivation. Also the temperature range where carbon-based catalysts are active is higher than in the case of nickel: 850-1000°C and 500-700°C, for carbon- and nickel-based catalysts, respectively [1, 2, 16].

For hydrocarbon cracking, nickel is known for its high catalytic activity, higher carbon loading, and reasonable cost [26-29]. Qian et al. [14] studied the effect of catalyst reduction on methane cracking in a fluidized bed using Ni/Cu/Al_2O_3 and Co/Mo/Al_2O_3. Their results showed that the nickel catalyst achieved higher conversion than the cobalt catalyst. Murata et al. [12] studied the activity of different catalysts supported on alumina for methane cracking in a fluidized bed. The order of the catalysts activity was: Ni/Ca/Al_2O_3>Ni/Al_2O_3> Co/Al_2O_3>Fe/Al_2O_3. Murata et al. [12] reported that Ni/SiO_2 has lower activity compared to all nickel catalysts supported on alumina.

The rate of methane cracking in a fluidized bed is affected by the residence time, temperature, methane partial pressure, P_{CH4}, and catalyst particle size. The residence time depends on gas flow rate and the amount of catalyst. The flow rate necessary to operate at minimum fluidizing velocity, U_{mf}, is used as a unit of flow rate multiplication [11, 16, 18, 30]. The published results show that reducing the residence time by increasing the velocity beyond U_{mf} or decreasing the catalyst amount decreases methane conversion due to the drop in contact time [11, 16, 18, 20, 30]. Also lower flow rates and/or larger catalyst amounts imply smaller output per reactor volume. The optimum flow rate is determined based on output hydrogen concentration and methane conversion [11]. Increasing the reaction temperature has a positive effect on methane conversion but it leads to faster deactivation, due to the increase in the

production of both carbon filaments and encapsulating carbon [11, 16, 18, 20, 30]. Ammendola et al. [30] studied the effect of P_{CH4} on methane conversion; they concluded that higher P_{CH4} reduced methane conversion due to the kinetic limitation imposed by the reaction and the catalyst. Optimum particle sizes reported in literature differs from one article to another e.g. 108 μm [11] and 150 μm [23]. Optimum particle size is different for different materials and can be determined based on the quality of fluidization, pressure drop, better contact efficiency, and the agglomeration and particle-particle interaction [11, 16, 23].

There is also clear evidence that the support affects catalyst performance and stability [13, 31]. Based on different studies in a fixed bed reactor, the factors that control methane conversion and type of carbon deposited on the catalyst are the catalyst material, the nature of the support, the catalyst textural properties, and the operating conditions [6, 13, 26, 32-34]. In this study, different supports were examined to study the effect of the support type and the catalyst textual properties on methane cracking rate in a fluidized bed. Porous and non-porous alumina and silica were used. An experimental design was developed for each support to study the effect of particle size, temperature, and P_{CH4} and their interactions on methane cracking. The effect of flow rate was also studied. Cracking/regeneration cycle experiments were conducted to check the durability for each catalyst for potential use in a continuous methane cracking process. Complete regeneration was achieved, by burning all the carbon on the catalyst in air oxidation.

5.2 Experimental work

10% nickel catalysts were prepared by wet impregnation of the support using an aqueous solution of $Ni(NO_3)_2 \cdot 6H_2O$ (99.99%, Alfa Aesar). The supports used in the study are: 1) porous γ-alumina [99.97% metal basis, 3 micron APS powder, S.A. 80-120 m^2/g, Alfa Aesar], 2) non-porous α-alumina [99.99% metal basis, 0.9-2.2 micron APS powder, S.A. 16-20 m^2/g, Alfa Aesar], and 3) porous silica [Aeroperl 300/30, 100% SiO_2, 30 micron white powder, S.A. 300 m^2/g, Degussa corporation]. The catalyst preparation method included drying the support overnight at 150°C, preparing a solution of $Ni(NO_3)_2 \cdot 6H_2O$ in de-ionized water, then adding the support to the solution (the nickel and support amounts used were in a 10/100 ratio). The slurry was then stirred for 3 hrs at 80°C and 95ºC for $Ni/\gamma Al_2O_3$ and Ni/SiO_2, respectively. For $Ni/\alpha Al_2O_3$, the slurry was stirred in oil bath at 100ºC. Then the catalyst was dried overnight at 120ºC. The catalyst was calcined in air at 600°C for 3 hrs. The reduction step

was carried out at the reaction temperature for 1 hr using a 10 vol. % H_2 and 90 vol. % N_2 mixture. The surface area of the reduced catalyst at each particle size is listed in the table below:

Table 5.1 - Surface area of the reduced catalyst in m^2/g

Particle size	108 μm	275 μm
	Surface area, m^2/g	
$Ni/\gamma Al_2O_3$	72.9	99.3
$Ni/\alpha Al_2O_3$	19	24.3
Ni/SiO_2	229	277

A lab-scale fluidized bed unit was built to conduct the experimental work. A quartz tube was used as the reactor and placed inside a vertical tube electrical furnace as shown in Figure 5.1. The quartz tube has two sections: the narrow diameter section (3.2 cm I.D, 75 cm long) where the fluidization occurs, and the wide diameter section (5 cm I.D, 15 cm long) at the tube outlet to reduce the gas velocity in order for the catalyst particles entrained with the outlet gases to settle and not being carried out with the outlet gases. The electrical furnace was controlled by an external temperature controller, which divides the furnace into three heating sections to enable better temperature control. A K-type thermocouple was placed just under the distributing plate to monitor the actual temperature inside the bed. In order to avoid direct contact between the thermocouple and fluidized bed materials, the thermocouple was inserted in a quartz tube so that the effect of catalytic activity of the metal thermocouple in the bed is eliminated. The thermocouple was connected to a data acquisition system, which also read pressure drop using a differential pressure transducer (from American Sensors) connected to both ends of the quartz tube. The outlet gas was analyzed using an Agilent 3000 micro GC, with a sample analysis time of 130 seconds. The regeneration experiments using air or air and nitrogen mixture were carried out in-situ.

A fixed bed unit was also used to compare the results of fixed and fluidized beds. The fixed bed reactor consisted of a quartz tube installed in a vertical tube furnace. The products together with unreacted reactants exit the reactor and are analyzed using a micro GC.

A factorial design was implemented to study the effect of temperature, P_{CH4}, and particle size and their interactions for each catalyst individually. The factor values were chosen based on literature data and the experimental setup limitation. The two levels for each factor

are given in Table 5.2. Detailed description of the experimental work is given in Appendix G. The effects of flow rate and cracking/regeneration cycles were evaluated to check the durability and ability to withstand attrition inside the fluidized bed. The SEM images were taken using a LEO FESEM 1550 manufactured by Carl Zeiss. BET experiments were conducted using a Micromeritics Gemini III 2375 surface area analyzer. The nickel dispersion was measured using a Hiden Catlab Microreactor with a QIC-20 mass spectrometer. A 5% H_2 in He mixture was used, with chemisorption measurements obtained at 25°C after the sample had been pre-treated at 550ºC using a 10% H_2 in N_2 mixture, then cooled in pure He to 25ºC.

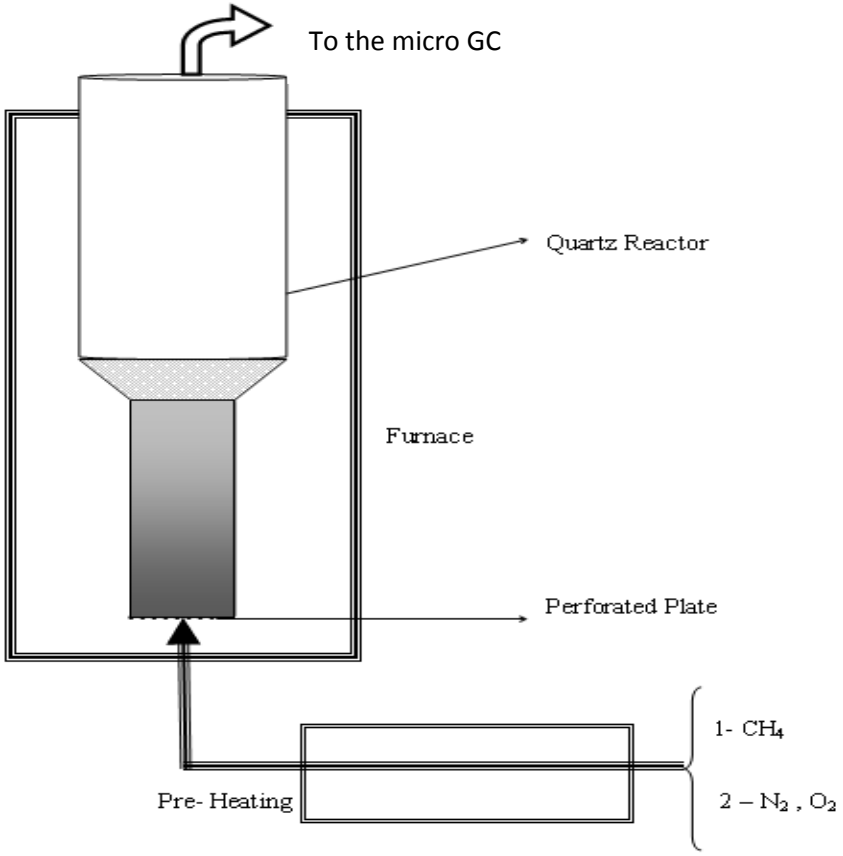

Figure 5.1 - Schematic diagram for the fluidized bed system

Table 5.2 – Higher and lower values of factors used in the factorial design

Temperature, T (°C)		mol%CH_4 / mol% N_2, P		Particle size, D (µm)	
-	+	-	+	-	+
550	650	50/50	80/20	108	275

5.3 Results and Discussion

5.3.1 Empty tube conversion

To check the reactivity of the empty reactor, methane conversion was studied using an empty tube. The results indicate that no conversion is observed up to 650ºC; but at 700ºC, which is outside the experimental range, around 0.08% of methane was converted, as shown in Figure5.2. This demonstrates that any methane conversion observed, up to 650°C, is attributed to the catalyst.

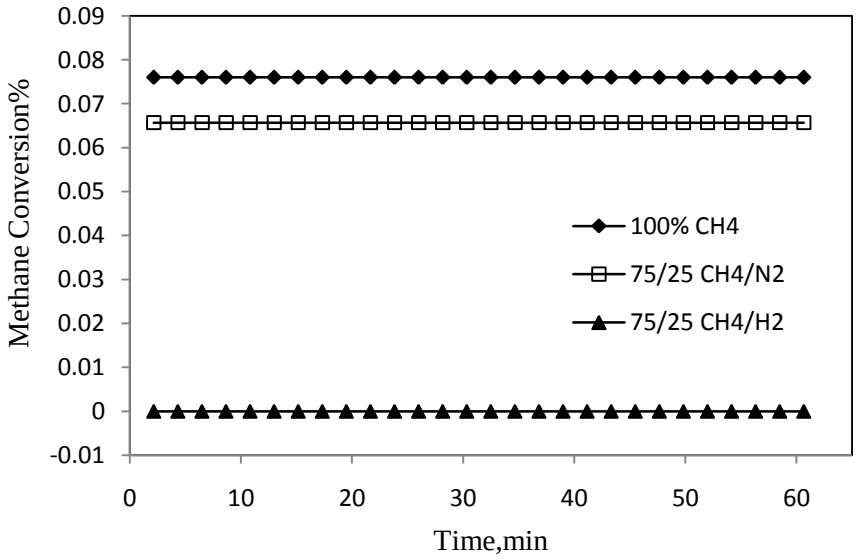

Figure 5.2 - Thermal conversion of methane at 700ºC in an empty tube

5.3.2 U_{mf} determination

The U_{mf} was determined experimentally using a technique developed by Pinilla et al. [15], which uses nitrogen gas at the reaction temperature. The U_{mf} was determined for each catalyst at different temperatures and for different particle sizes. Nitrogen was used to avoid changes in catalyst properties and agglomeration. 10 g of a mixture of fresh, partially deactivated, and completely deactivated catalyst were used and the pressure drop across the bed as a function of gas velocity inside the bed was measured. Results are shown in Figure 5.3, with the maximum pressure drop determining the minimum fluidizing velocity. An average value for the U_{mf} was calculated based on measuring the pressure drop by changing the gas velocity upward and downward, as shown in Figure 5.3; refer to Appendix F for more details

about the determination of U_{mf} and the results for each catalyst. Average values of U_{mf} determined experimentally for different temperatures and different particle sizes are shown in Table 5.3. The calculated U_{mf} using N_2 was corrected to CH_4 by multiplying it by 1.4 [15, 35]. Then the corrected U_{mf} was used as the minimum velocity to ensure complete fluidization.

The results, mentioned in Table 5.3 and appendix F, indicate that for the 275 μm particles the U_{mf} is independent of temperature (between 550 and 650°C) and catalyst type, and has a value of around 3.54 cm/s. For the smaller particle (108 μm) and for all catalyst types, U_{mf} decreases when increasing the temperature from 550 to 650°C.

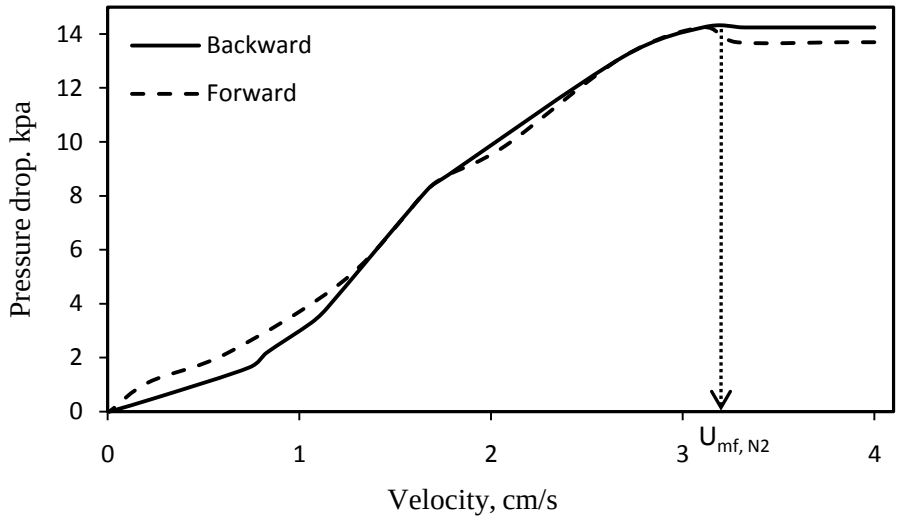

Figure 5.3 – U_{mf} for Ni/SiO_2 at 600ºC for particle size of 275 μm

Table 5.3 - U_{mf} for different catalysts in cm/s (for N_2 fluid)

Particle Diameter	108 μm		275 μm	
Temperature, ˚C	550	650	550	650
$Ni/\gamma Al_2O_3$	3.59±0.04	3.51±0.01	3.52±0.01	3.55±0.01
$Ni/\alpha Al_2O_3$	3.51±0.02	3.46±0.05	3.53±0.02	3.57±0.04
Ni/SiO_2	3.63±0.08	3.49±0.00	3.51±0.02	3.53±0.01

5.3.3 Typical experimental results:

The typical experimental result as reported from the micro GC is illustrated in Figure 5.4. The micro GC generates analysis report for the outlet gases each 130 s. From the analysis report, the hydrogen concentration in the outlet gases is calculated. By knowing the inlet flow rate and concentration of methane, the conversion X is calculated using the following equation:

$$X = \frac{C_{H2}}{2C_{CH4} - y_{CH4}C_{H2}} \quad (5.1)$$

The total carbon deposited during the run, C_{total} in g, is calculated using the following equation:

$$C_{total} = \frac{MW_C}{1000}\int_0^t F_{CH4i}(X_P)dt \quad (5.2)$$

Where, C_{H2} is the outlet concentration of hydrogen in mmol/l, C_{CH4} is the inlet concentration of methane in mmol/l, y_{CH4} is the mole fraction of methane in the inlet gases, MW_C is the carbon molecular weight (12 g/mol), F_{CH4i} is the inlet molar flow rate of methane in mmol/min, X_P is the conversion for one analysis period (lasts 130 s), and t is the total experiment time.

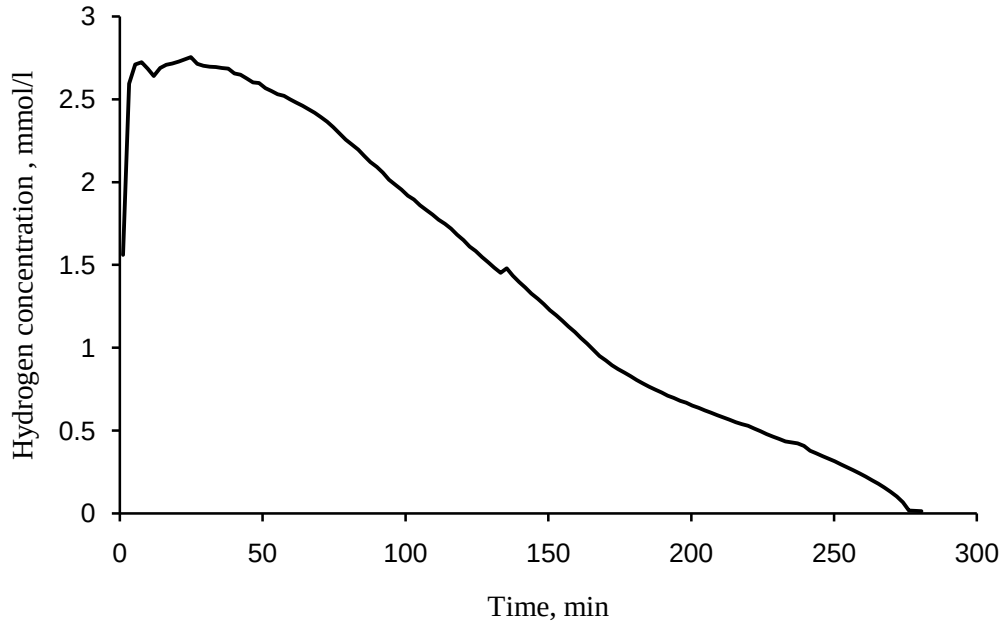

Figure 5.4 - Typical experimental results for Ni/γAl_2O_3 at 550ºC using 50/50 CH_4/N_2, 108 μm particles, and gas velocity (U_{mf} =3.59 cm/s)

5.3.4 Analysis of factorial design experiments

The results from the factorial design were analyzed to investigate the effects of temperature, P_{CH4}, and particle diameter, and their interactions, on the amount of carbon deposited and the overall hydrogen production rate. Because some experiments could be very long, requiring large amount of gas, the amount of carbon deposited here was defined as the amount of carbon deposited until the time where methane conversion reached 40% of its maximum value (t_{40}). The overall hydrogen production rate is defined here as the amount of hydrogen produced (mol) until the time t_{40} divided by the time t_{40}.

The results give the dominant effect for each catalyst and the significance for each effect. The dominant effect or interaction can be determined using the absolute value and the significance of the effect is determined using the Fisher test (F test) by comparing the criterion $F_{observed}$ for the effect or interaction. If $F_{observed}$ is greater than the tabulated F (18.5 for 95% confidence), then the effect or interaction is significant [36, 37]. A graphical example for the interaction between variables is given in Figure 5.5a for the case of an effective interaction between temperature and particle diameter on H_2 production rate (crossed lines). Figure 5.5b gives the example of an ineffective interaction between temperature and inlet P_{CH4} on total carbon deposited (parallel lines). The $F_{observed}$ for a parameter A was calculated using the equations for the ANOVA analysis shown in Table 5.4 [36, 37], note that all the factors in the present study has two levels and three replication of a centre point in the experimental region were carried out (600ºC, 108 μm, and 65% CH_4):

Table 5.4 - The ANOVA table used for calculating $F_{obseved}$

Factor	Sum of squares	DF	Mean square MS	$F_{observed}$
Temperature (T)	SS_T	1	$MS_T = SS_T/1$	MS_T/MS_E
P_{CH4}(P)	SS_P	1	$MS_P = SS_P/1$	MS_P/MS_E
Particle diameter (D)	SS_D	1	$MS_D = SS_D/1$	MS_D/MS_E
T*P	SS_{TP}	1	$MS_{TP} = SS_{TP}/1$	MS_{TP}/MS_E
T*D	SS_{TD}	1	$MS_{TD} = SS_{TD}/1$	MS_{TD}/MS_E
P*D	SS_{PD}	1	$MS_{PD} = SS_{PD}/1$	MS_{PD}/MS_E
T*P*D	SST_{PD}	1	$MS_{TPD} = SST_{PD}/1$	MS_{TPD}/MS_E
Error	SS_E	2	$MS_E = SS_E/2$	

Where:

The sum of squares of factor (SS) $= 2 * (Effect)^2$ (5.3)

And, the effect of factor= $average\ reponse\ at\ high\ value - average\ response\ at\ low\ value$

The results are shown in Tables 5.5 and 5.6 for overall hydrogen production rate and amount of carbon deposited, respectively. The effect of temperature, P_{CH4} and particle diameter on the hydrogen production rate is shown in Table 5.5. The results indicated that temperature is the dominating effect and the interaction of temperature and P_{CH4} is the dominating interaction for all catalysts. P_{CH4} and particle diameter have also significant effects on the hydrogen production rate of all catalysts, but to lesser degree than temperature. For the $Ni/\gamma Al_2O_3$ only the T-P interaction and to less extent the total interaction are dominating, whereas for the other two catalysts all interactions are dominant.

The effect of temperature, P_{CH4} and particle diameter on the total carbon deposited is shown in Table 5.6. Unlike the effect on the hydrogen production rate, the particle diameter main effect is the dominant effect on the total carbon deposited for all catalysts. The interaction between temperature and particle diameter is the dominant interaction on the total carbon deposited for Ni/SiO_2 and $Ni/\gamma Al_2O_3$. The interaction between temperature and P_{CH4} is the dominant interaction on the total carbon deposition for $Ni/\alpha Al_2O_3$.

Table 5.5 - Effect and interactions of temperature, P_{CH4}, and particle size for each catalyst on the hydrogen production rate

Source of Variation	Ni/Porous alumina		Ni/Non-Porous alumina		Ni/Silica	
	Effect	F observed	Effect	F observed	Effect	F observed
Main Effect						
Temperature (T)	13	48000	12	200000	21	2000
P_{CH4} (P)	2	1400	2.5	7700	8	280
Particle diameter (D)	3.5	3200	6	53000	-1	4
Interactions						
T*P	1.6	700	1.9	4500	7	250
T*D	0.04	0.6	1	1100	-5	126
P*D	0.1	3.6	-0.8	800	-4	103
T*P*D	-0.4	50	-0.7	700	-5	144

$f_{0.05,1,2}$=18.5

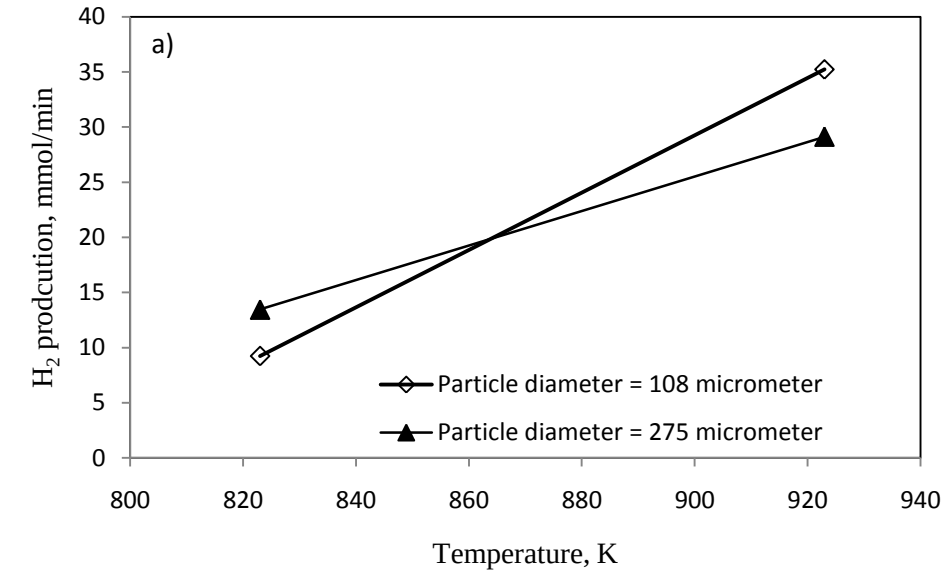

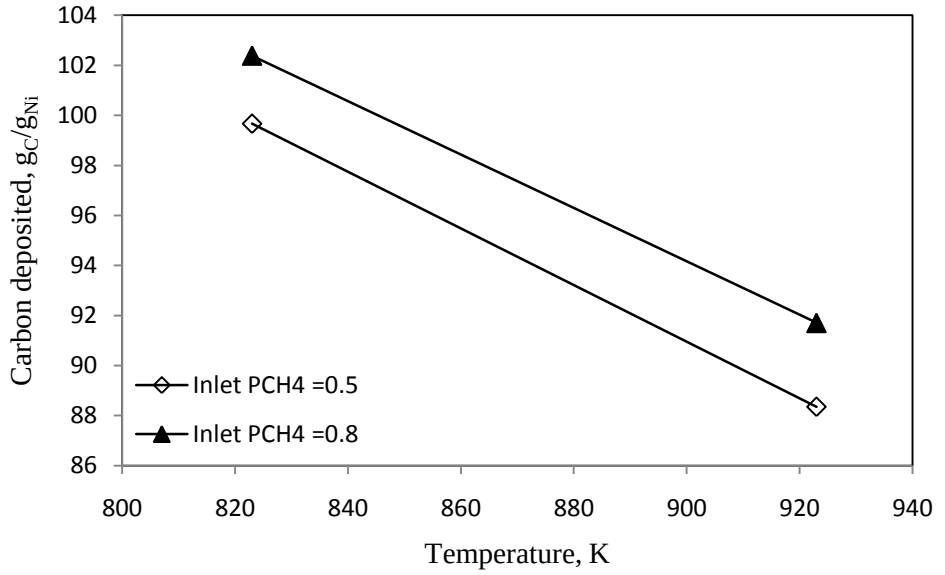

Figure 5.5 – Interactions for Ni/SiO_2 between a) temperature and particle diameter on the hydrogen production rate and b) temperature and P_{CH4} on carbon deposited on Ni/SiO_2

Table 5.6 - Effect and interactions of temperature, P_{CH4}, and particle size for each catalyst on the total carbon deposited

Source of Variation	Ni/Porous alumina		Ni/Non-Porous alumina		Ni/Silica	
	Effect	F observed	Effect	F observed	Effect	F observed
Main Effect						
Temperature (T)	1.4	80	14	2500	-11	146
P_{CH4} (P)	1.3	67	10	1100	3	11
Particle diameter (D)	12	5500	26	8100	32	1200
Interactions						
T*P	3	360	7.6	694	0.3	0.12
T*D	-11	4200	3.5	140	30	1100
P*D	-0.9	30	-5	280	2.8	9
T*P*D	-1	36	-7	550	-0.73	0.6

$f_{0.05,1,2}$=18.5

5.3.5 Comparison between fixed and fluidized beds

Keeping the same weight hourly space velocity (WHSV) in the fixed and fluidized beds, the performance of methane cracking with each catalyst was compared. The WHSV was 71.2, 71.7 and 71.4 L/hr/g_{Ni} for Ni/γAl_2O_3, Ni/αAl_2O_3, and Ni/SiO_2, respectively. From the results shown in Figure 5.6, the maximum methane conversion using Ni/SiO_2 is higher than the maximum conversion observed with both alumina-supported catalysts, in both the fixed and fluidized beds. However, the maximum conversions with Ni/SiO_2 and Ni/αAl_2O_3 are similar in the fluidized bed. The conversion over Ni/αAl_2O_3 was always higher than the conversion over Ni/γAl_2O_3. But the fluidization quality, which is determined based on observing the pressure drop during the experiment and the degree of "stickiness" of the deactivated bed, is in the following order: Ni/γAl_2O_3> Ni/SiO_2>Ni/αAl_2O_3. The degree of "stickiness" was evaluated here as the amount of materials that "sticks" on the reactor's wall when unloading the reactor. Here, for Ni/γAl_2O_3 almost no material remained attached on the wall, whereas for Ni/αAl_2O_3 most of the particles stayed on the reactor's wall.

Higher methane conversion was consistently observed, for all catalysts, in the fixed bed system compared to the fluidized bed. The lower conversion observed in the fluidized bed is because some

amounts of methane passes through the bed in form of the bubble phase, and this amount increases when increasing the flow rate [16]. As seen in Figure 5.6, for the two alumina supports, the catalyst deactivated faster in the fixed bed than in the fluidized bed. However, for the silica supported catalyst, the deactivation was similar in both reactors (curve close to be parallel). Lee et al. [11] also reported similar deactivation between fixed bed and fluidized bed, but using activated carbon. The results indicate that Ni/SiO_2 deactivation is not affected by the type of reactor.

The experiments in the fixed bed were not run until complete catalyst deactivation due to the high pressure drop that developed through the bed due to carbon formation in the reactor. Figure 5.7 shows the measured pressure drop through the fixed and the fluidized beds using $Ni/\alpha Al_2O_3$ at 550°C with 275 μm particles. As expected, in the fixed bed, the pressure drops is greater than in the fluidized bed and it builds up due to carbon deposition. It is also notable that the pressure drop in the fluidized bed remains constant throughout the experiment. For the other catalysts same pressure drops (~0.5 kPa) were observed for particles size of 275 μm. However, for smaller particle size (108 μm), the pressure dropped increased to 1-10 kPa.

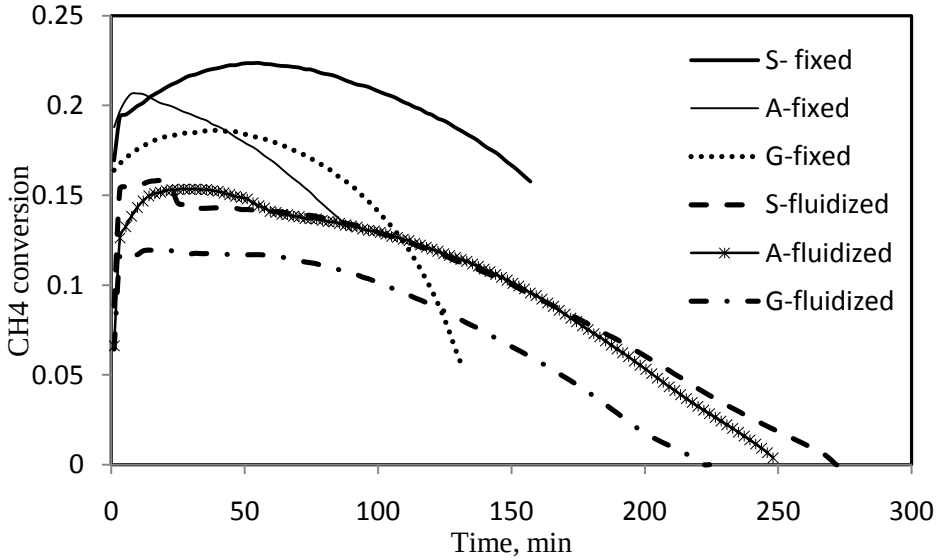

Figure 5.6 - Fixed and fluidized beds conversion at 550ºC using mixture of 50/50 CH_4/N_2 and 275 μm particle sizes. ($G=Ni/\gamma Al_2O_3$, $A=Ni/\alpha Al_2O_3$, $S= Ni/SiO_2$)

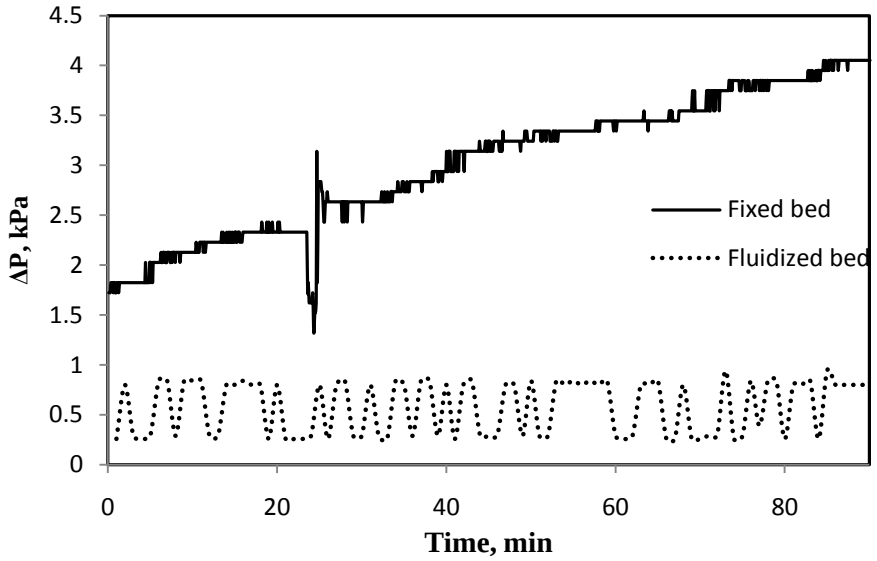

Figure 5.7 - Pressure drop across the fixed and fluidized during methane cracking using Ni/αAl_2O_3 at 550ºC and 275 μm particles.

5.3.6 Effect of P_{CH4}

The effect of P_{CH4} was studied by varying the P_{CH4} in a mixture of N_2/CH_4. Two CH_4/N_2 ratios were used, 50/50 and 80/20. Figure 5.8 shows the effect of P_{CH4} on methane conversion for Ni/γAl_2O_3 using different particle sizes at 550ºC. Similar trends were observed at 650ºC for the same catalyst and at 550 and 650ºC for Ni/αAl_2O_3 and Ni/SiO_2. Increasing P_{CH4} in the inlet mixture led to a decrease in methane conversion and increase in the time needed for complete deactivation. Lower conversion with higher methane concentration is attributed to kinetic limitations [30]. The longer deactivation time associated with the lower conversion is due to the decreased rate of carbon deposition [6].

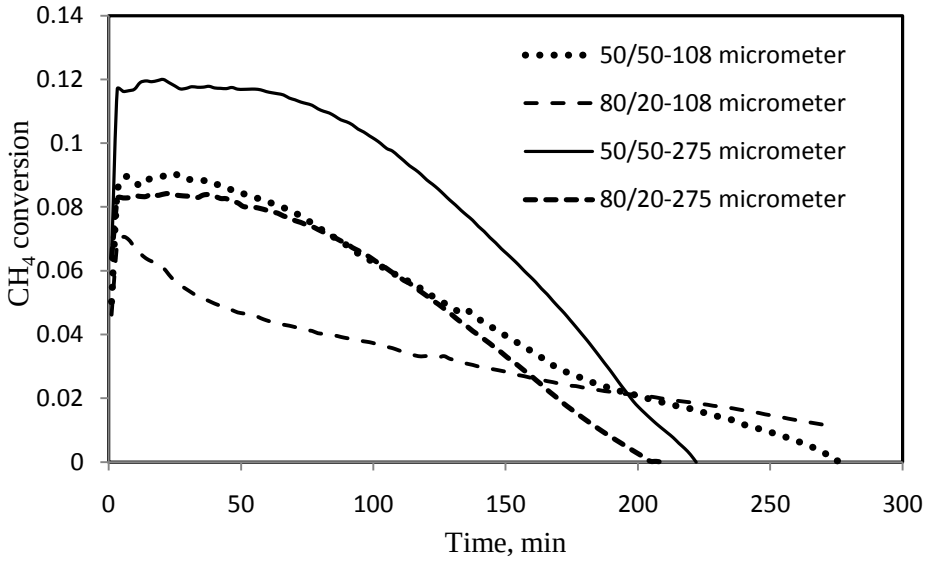

Figure 5.8 - Effect of P_{CH4}/N_2 ratio in the feed gas on conversion using $Ni/\gamma Al_2O_3$ at 550ºC

5.3.7 Effect of temperature and particle size

The effect of temperature on methane cracking was studied and the results are shown for Ni/SiO_2 in Figures 5.9a and 5.9b using CH_4/N_2 ratios of 50/50 and 80/20, respectively. Similar trends were observed for $Ni/\gamma Al_2O_3$ and $Ni/\alpha Al_2O_3$. The results indicate that as the temperature is increased higher methane conversion is achieved for all particle sizes and for all methane concentrations. Increasing the particle size from 108 to 275 μm also increased the conversion. Particle interaction and agglomeration were observed with 108 μm particles, while smooth fluidization was observed with 275 μm particles. The better quality of fluidization observed with 275 μm diameter particles compared to 108 μm diameter particles may explain why a higher surface area particle has lower conversion, since smooth fluidization means better contact efficiency [11, 16].

Comparing Figures 5.9a and 5.9b shows that at 550ºC, varying P_{CH4} did not affect the difference between the conversions observed with 275 μm and 108 μm particles at 80/20 and at 50/50 CH_4/N_2 ratios. At 650ºC and for 50/50 CH_4/N_2, the initial conversion is almost identical between the two particle sizes, but as the $\%CH_4$ increases to 80%, the conversion using the larger particle (275 μm) was 20% greater than using the smaller ones (108 μm). Except at the onset of 50/50 CH_4/N_2 at 650ºC experiment, the particle size shows a great influence on conversion and deactivation for all experimental conditions.

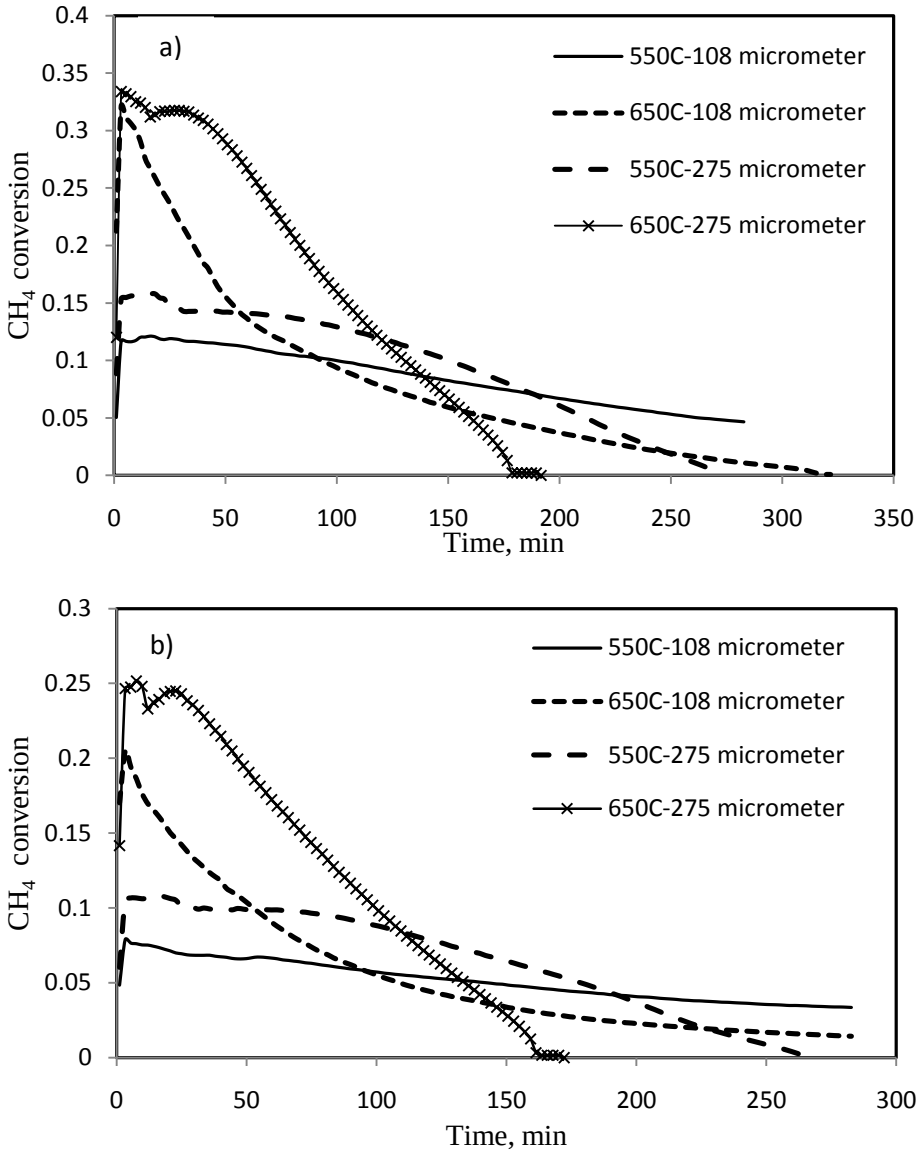

Figure 5.9 - Effect of temperature on methane cracking using Ni/SiO_2 and a mixture of a) 50/50 CH_4/N_2, and b) 80/20 CH_4/N_2

The deactivation pattern is similar for each combination of particle size and temperature independent of the ratio of CH_4/N_2. Faster deactivation is observed with higher maximum conversions and with the 275 μm particle size. At 108 μm, higher surface area is available, which increases the amount of encapsulating carbon required to block all sites, and with lower conversion attained with 108 μm particles, slow deactivation occurs.

5.3.8 Effect of flow rate

The effect of flow rate on methane conversion for the different catalysts is shown in Figures 5.10a for Ni/γAl_2O_3 and Ni/SiO_2 and 5.10b for Ni/αAl_2O_3. The flow rate was varied between 1 U_{mf} and 1.5 U_{mf}. For Ni/γAl_2O_3 and Ni/SiO_2, a lower conversion was observed with increasing the flow rate. By increasing the flow rate in the fluidized bed, the bubble sizes and the number of bubbles increase which decreases the contact efficiency between the methane and catalyst particles [11, 18]. However, after 3 hrs from the beginning of the reaction, deactivation for both flow rates showed a similar deactivation trend.

As shown in Figure 5.10b, increasing the flow rate has no effect on the percentage of methane conversion over Ni/αAl_2O_3; usually conversion decreases with increasing flow rate as observed with Ni/αAl_2O_3 and Ni/SiO_2. Quantitatively, more methane is converted using 1.5 U_{mf} which indicated that the reaction over Ni/αAl_2O_3 is controlled by diffusion and better mixing and mass transfer can be achieved by increasing the flow rate. Ni/αAl_2O_3 is a non-porous catalyst and nickel active sites are available at the external surface, if the reaction kinetics is fast then the rate will be dependent on the mass transfer step. As the most important parameter in fluidized bed performance; in literature, the optimum flow rate is determined based on the balance between contact efficiency and the volumetric throughput of the reactor [11, 16].

5.3.9 Comparison with thermo balance results

Figure 5.11show the normalized weight gain (carbon deposited) in the fluidized bed and thermo balance experiments using 50/50 CH_4/N_2 at 550°C for 10%Ni/γAl_2O_3 (Fig. 5.11a) and 10%Ni/αAl_2O_3 (Fig. 5.11b). The total carbon deposited on the catalyst after complete deactivation in 50/50 CH_4/N_2 at 550 and 650°C for 10%Ni/γAl_2O_3 and 10%Ni/αAl_2O_3, is given in Table 5.7. The results indicate that the total carbon deposited is always higher in the fluidized bed experiments than in TGA experiments. The increase in carbon capacity of the nickel catalyst in the fluidized bed is attributed to catalyst attrition which causes removal of encapsulating carbon off the nickel particles leading to longer activity time and higher carbon capacity.

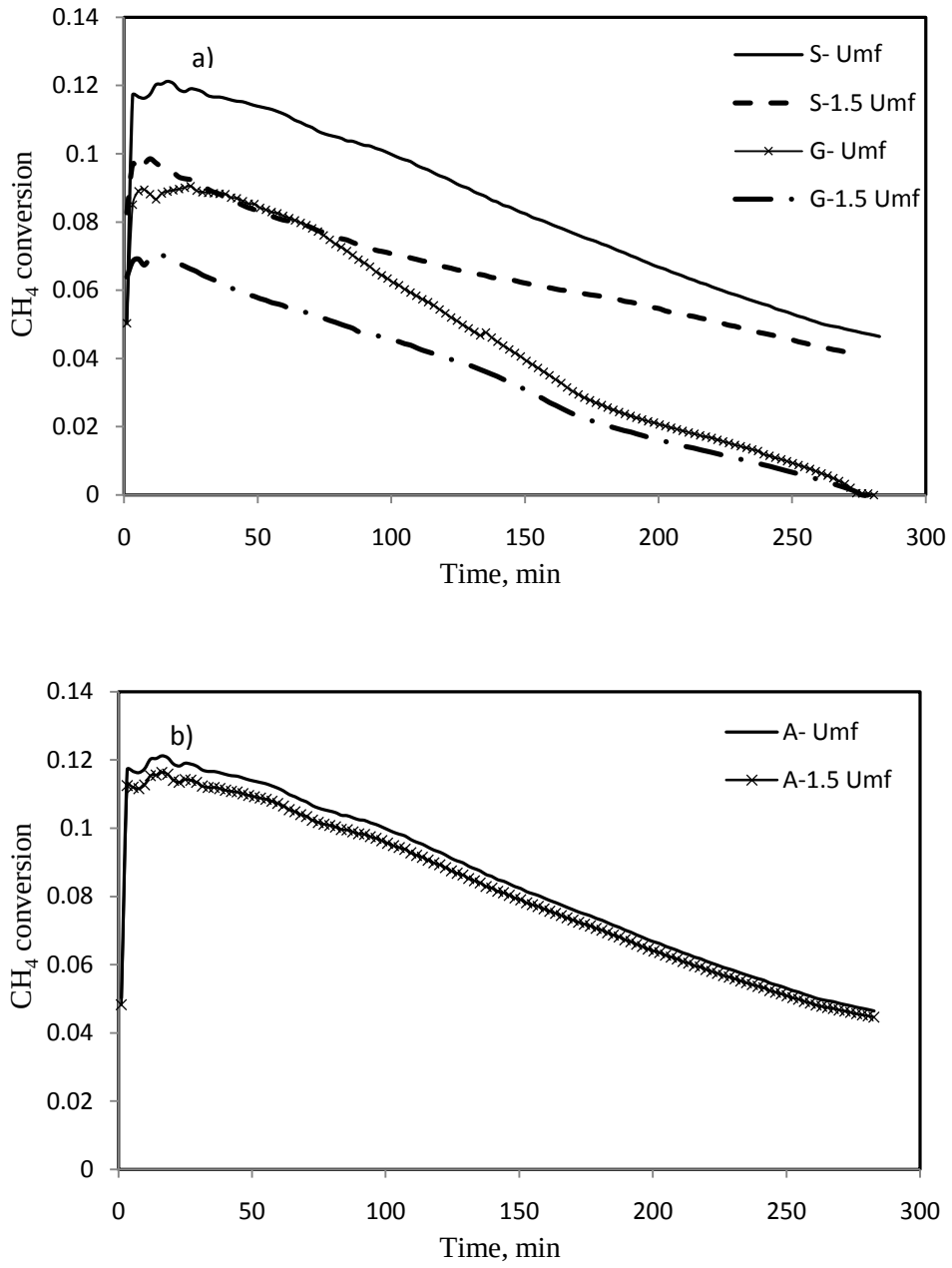

Figure 5.10 - Effect of flow rate on methane cracking at 550ºC, particle size of 108 μm, and CH_4/N_2 of 50/50 a) (G=Ni/γAl_2O_3, S= Ni/SiO_2), b) (A=Ni/αAl_2O_3)

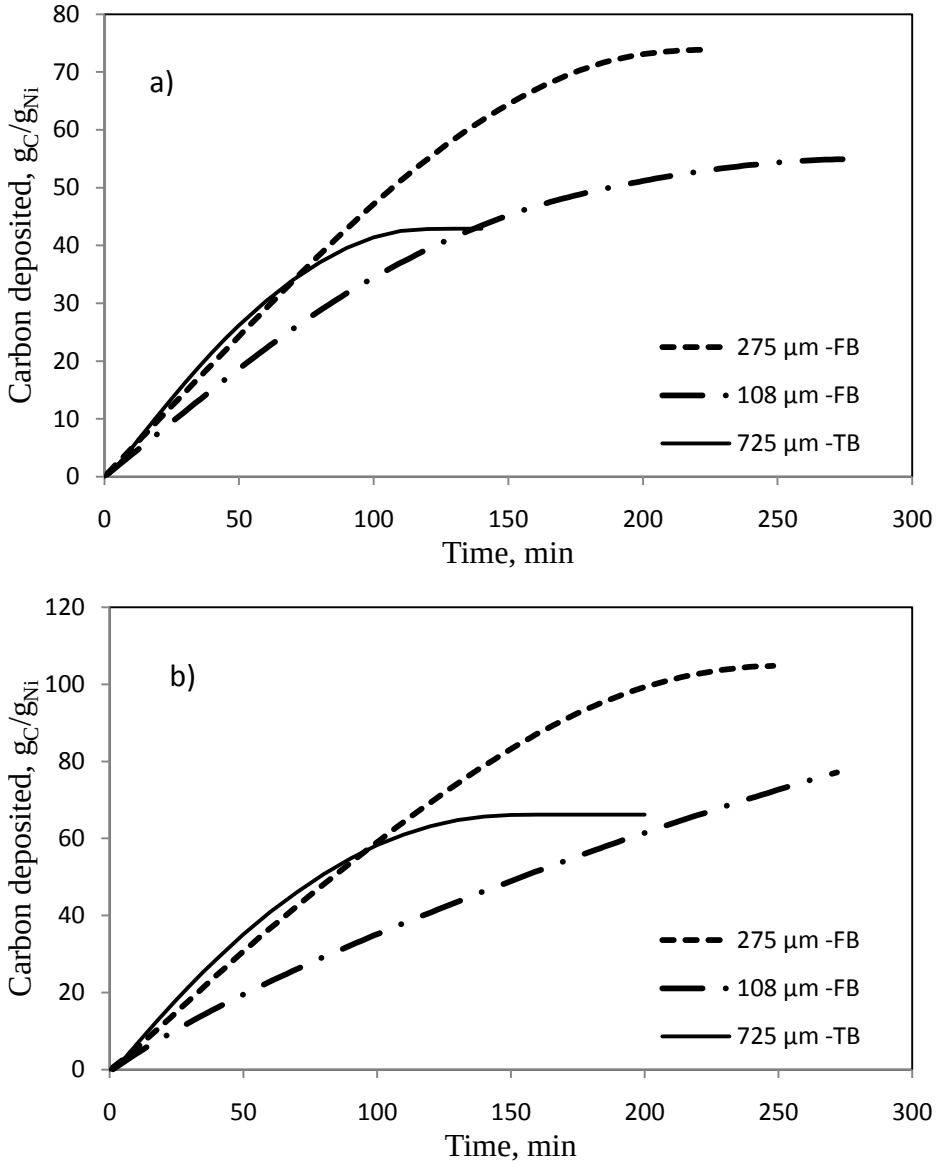

Figure 5.11 – Comparison of carbon deposition at different particle diameters in the fluidized bed (FB) and the thermo balance (TB) using 50/50 CH_4/N_2 at 550°C, a) 10%Ni/γAl_2O_3 and b) 10%Ni/αAl_2O_3

Table 5.7 - Total carbon deposited (g_C/g_{Ni}) in the fluidized bed (FB) and the thermo balance (TB) using 50/50 CH_4/N_2 at 550 and 650°C

Temperature, °C	10%Ni/γAl_2O_3			10%Ni/αAl_2O_3		
	Particle diameter μm/ reactor type					
	108/FB	275/FB	725/TB	108/FB	275/FB	725/TB
550	55	74	43	77[1]	104	70
650	59	66	30	116[1]	126	35

[1] experiments not completed (stopped after 5 hours), more carbon could still have been deposited

Figure 5.12 shows the SEM images for the deactivated 10%Ni/γAl_2O_3, 10%Ni/αAl_2O_3, and 10%Ni/SiO_2 in the fluidized bed at 550°C using 108 μm catalyst particles and 80/20 CH_4/N_2. The diameter of the carbon filaments formed on the Ni/γAl_2O_3 catalyst ranged between 20 and 50 nm which is slightly bigger than the diameter of the carbon filaments formed on the Ni/γAl_2O_3 catalyst in the thermo balance which ranged between 20 and 40 nm. Unlike in the thermo balance experiments where no carbon filaments were observed during cracking over Ni/αAl_2O_3, carbon filaments have been observed with Ni/αAl_2O_3 in the fluidized bed and the diameter ranged between 30 and 60 nm. For Ni/SiO_2, the range of the carbon filaments diameter was in the range 20-90nm.

5.3.10 Cracking/regeneration cycles

Cracking/regeneration cycling experiments were carried out for each catalyst to determine their durability and the stability in a fluidized bed. The cracking cycles were performed at 550ºC using 275 μm particles and 80/20 CH_4/N_2 mixture. Regeneration was carried out in-situ by fluidizing the deactivated particles in air at 550ºC. By fluidizing the particles during regeneration, the attrition of the particles during regeneration could also be evaluated. The results are shown in Figures 5.13, 5.14, and 5.15a for Ni/SiO_2, Ni/αAl_2O_3, and Ni/γAl_2O_3, respectively. The results show that Ni/SiO_2 is stable, with the conversion even increasing in the second cycle. In the third cycle, methane conversion decreased and the deactivation pattern was similar to that observed with 108 μm particles (Figure 5.9). By visual inspection after regeneration, it was apparent that attrition led to smaller particle sizes. Reduction of the particle size resulted in the deactivation pattern becoming similar to that associated with 108 μm particles, as shown in Figure 5.9a. Catalyst attrition during fluidization led to lower fluidization quality.

a)

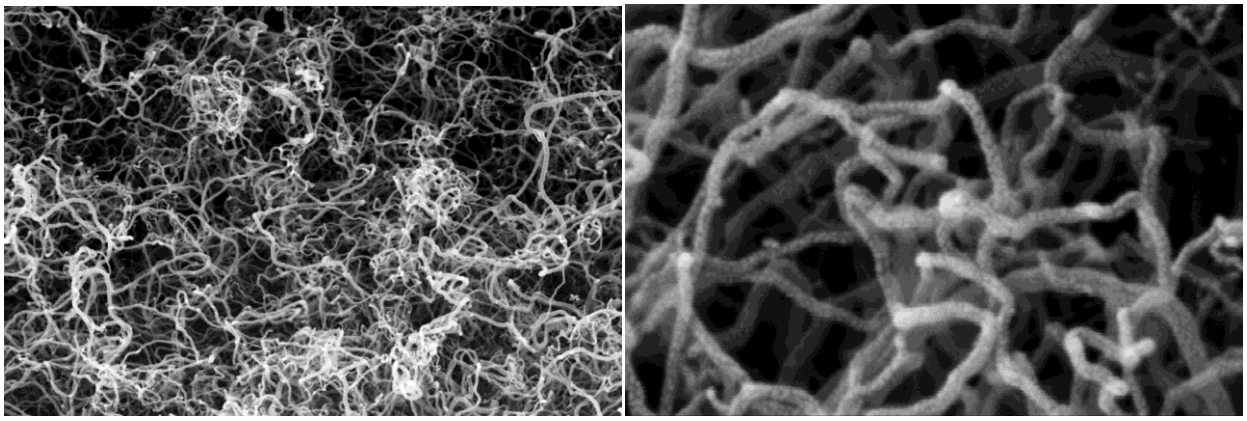

b)

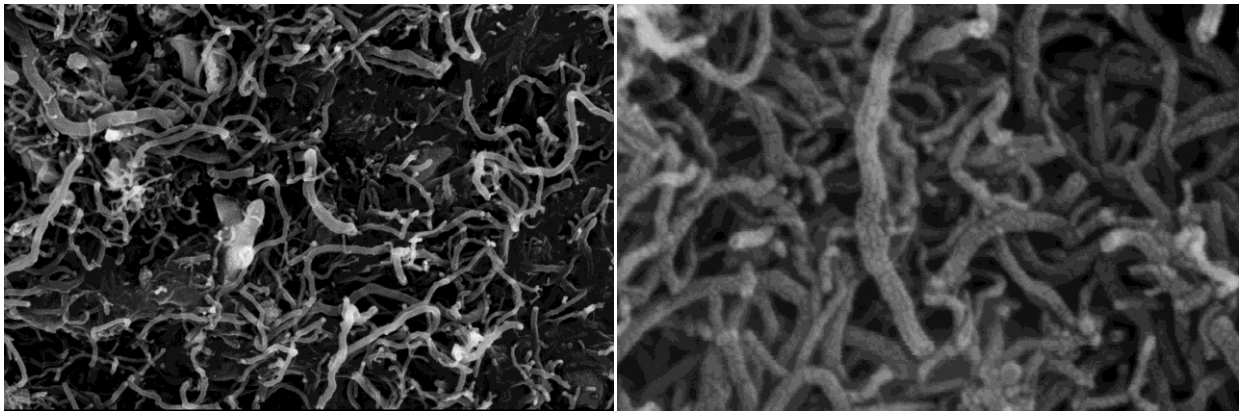

c)

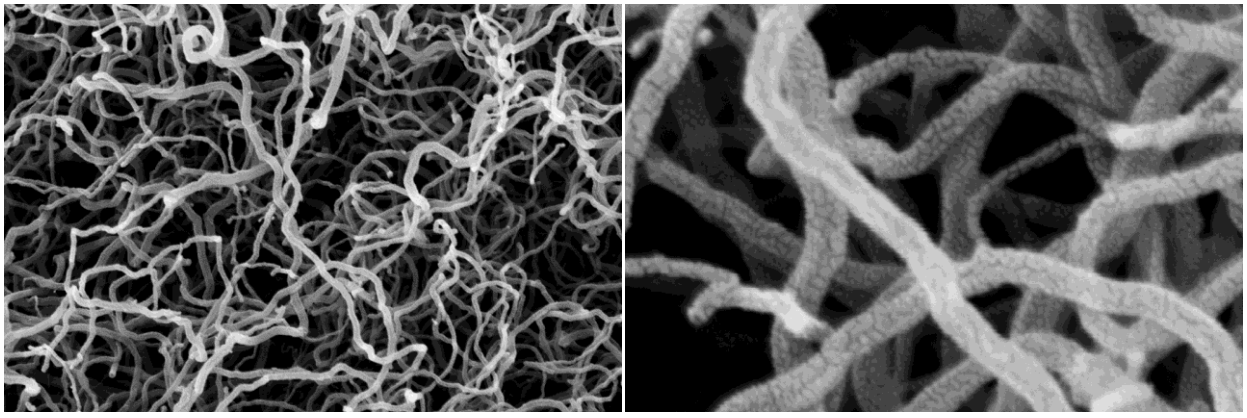

200 nm 100 nm

Figure 5.12 - SEM pictures for a) Ni/γAl_2O_3, b)Ni/αAl_2O_3, and c) Ni/SiO_2 using 80/20 CH_4/N_2 at 550°C and 108 μm catalyst particles.

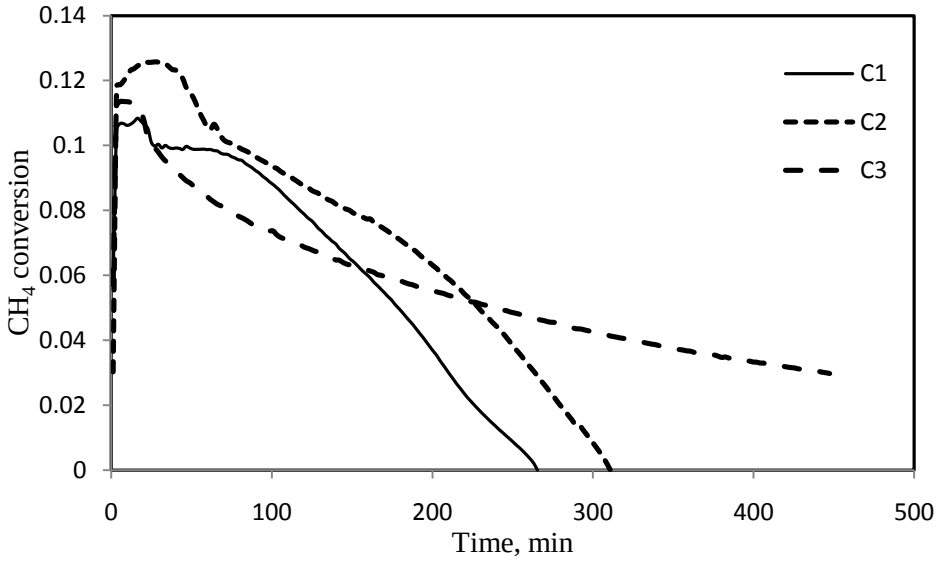

Figure 5.13 – Cracking cycles for Ni/SiO_2, at 550ºC, 275 μm, CH_4/N_2 = 80/20

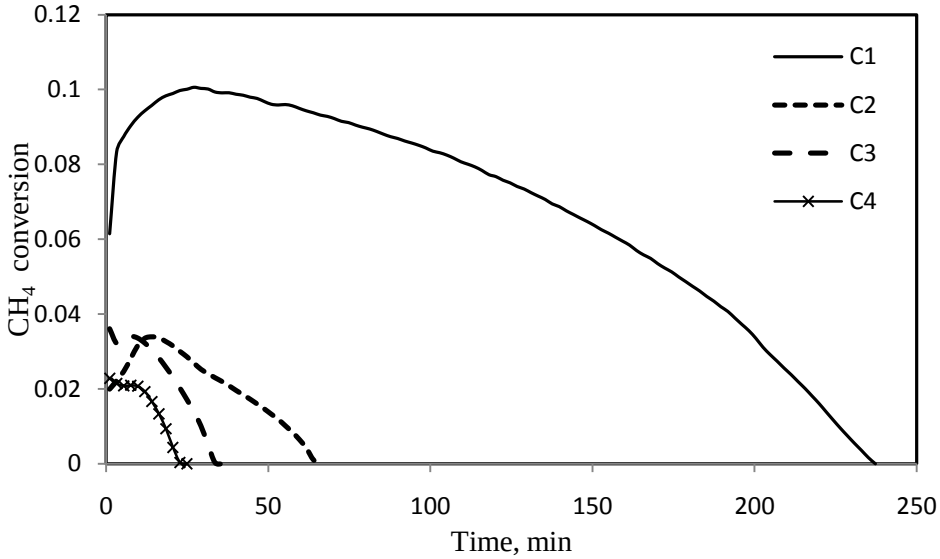

Figure 5.14 – Cracking cycles for $Ni/\alpha Al_2O_3$, at 550ºC, 275 μm, CH_4/N_2 = 80/20

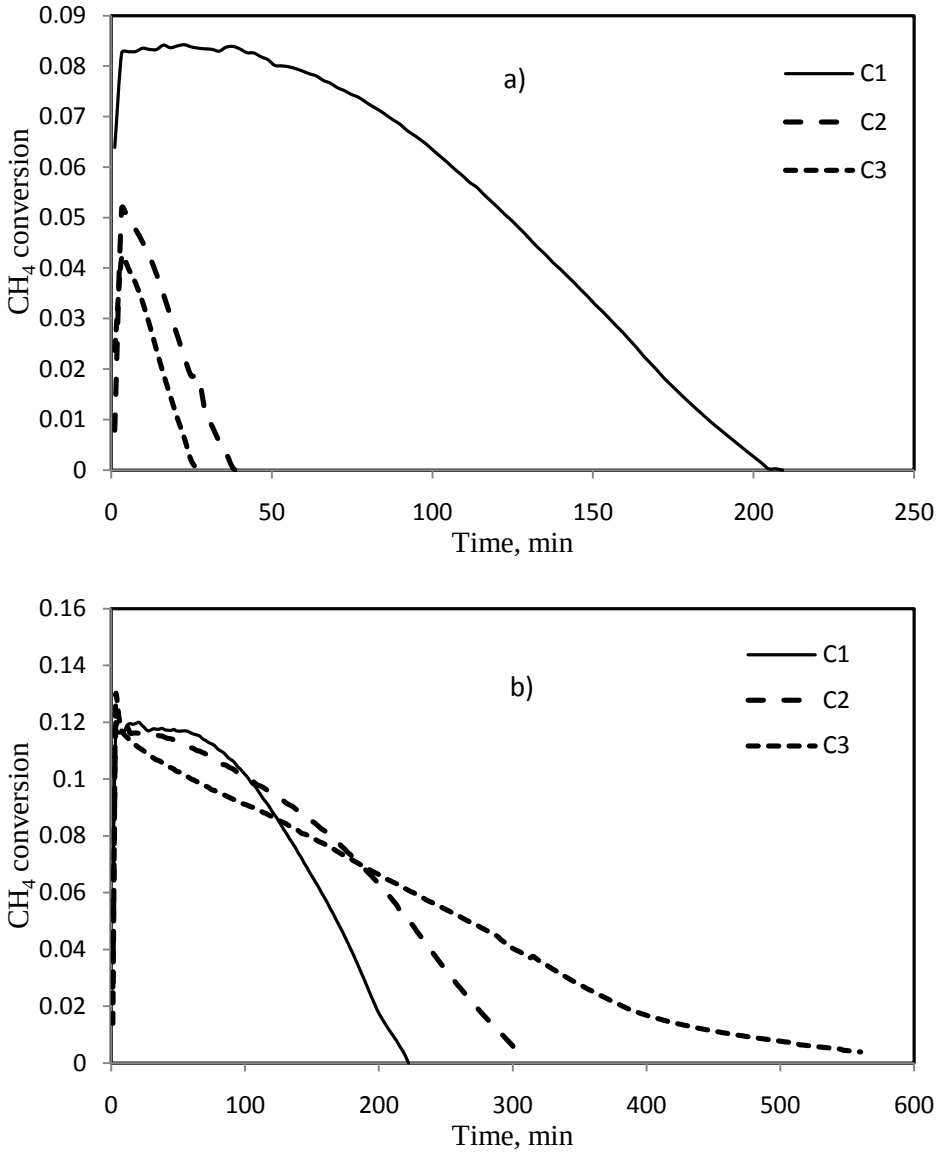

Figure 5.15– Cracking cycles for Ni/γAl_2O_3, at 550ºC, 275 μm, a) CH_4/N_2 = 80/20, regenerated with air, b) CH_4/N_2 = 50/50, regenerated using 1% O_2/N_2 mixture

As shown in Figure 5.14, Ni/αAl_2O_3 showed quick deterioration in activity, which was expected from the results in Chapter 3. The presence of nickel active sites over a low surface area led to quick sintering of the active sites (based on nickel chemisorption study mentioned in Chapter 3). However, the quick activity drop over cycle using Ni/γAl_2O_3 (Figure 5.15a) was unexpected in light of the results in Chapter 3 which showed excellent stability over at least 24 cycles in the TGA. In the fluidized bed, Ni/γAl_2O_3 undergoes a similar deterioration as that observed with Ni/αAl_2O_3. Note that a thermocouple located just beneath the distributing plate recorded increases in temperature in the order of 100°C during

the first 10 minutes of regeneration in air. The local increase in temperature on the catalyst is certainly much higher. This excess temperature may have caused more sintering in the Ni/γAl_2O_3 catalyst, leading to fast deactivation over the cycles. To investigate the reason of Ni/γAl_2O_3 instability, another cracking/regeneration cycling experiment was performed. The cracking step was carried out at 550ºC using 275 μm particles and 50/50 CH_4/N_2 ratio and the regeneration step was done at 550°C in 1% O_2 mixed with O_2 to control the heat generated from burning the deposited carbon. The results are shown in Figure 5.15b. These results show considerable improvement in catalyst stability over cycles, which support the conclusion that sintering is the reason for quick Ni/γAl_2O_3 performance deterioration when regenerated in air. Hydrogen chemisoprtion results for Ni/γAl_2O_3 regenerated in air showed a reduction in nickel dispersion from 34% for the fresh catalyst to 22% for the regenerated catalyst, which indicate that sintering is the reason for quick Ni/γAl_2O_3 deterioration. Another issue observed with Ni/γAl_2O_3 is that the catalyst particles disintegrated due to attrition during fluidization. In the third cycle, more particle attrition was observed and the catalyst needed around 10 hours to deactivate. As the particle size was reduced lower fluidization quality was experienced and catalyst particle interaction and agglomeration increased.

5.4 Conclusions

The results demonstrate that the type of support significantly influences the methane cracking catalyst performance in a fluidized bed. Ni/SiO_2 achieved the highest conversion but Ni/γAl_2O_3 showed the best fluidization quality.

An experimental design showed that temperature was the dominant factor influencing the hydrogen production rate for all catalysts. However, the particle diameter affected the most the total carbon deposited and this for all catalysts (the bigger the particle, the more the total carbon deposited).

Increasing temperature and particle diameter from 108 to 275 μm positively affected methane conversion. Smooth fluidization was observed with 275 μm particles. Increasing the flow rate and P_{CH4} had a negative effect on methane conversion since increasing flow rate and P_{CH4} led to lower contact efficiency. Higher methane conversion was observed in a fixed bed than in a fluidized bed due to better contact efficiency. An important problem with the fixed bed is agglomeration and particle interactions that increased the pressure drop across the bed until the flow of the gases through the bed was completely

blocked. The pressure drop through the fluidized bed remains small (0.5 kPa with 275 μm particles) even after complete deactivation.

Cracking/regeneration cycles in a fluidized were carried out for each catalyst. Both Ni/αAl_2O_3 and Ni/γAl_2O_3 lost most of their activity after the first regeneration step in air. The main reason is attributed to Ni sintering due to elevated temperature occurring during regeneration in air as indicated by hydrogen chemisorption. On the other hand, the Ni/SiO_2 showed good thermal stability over several cycles, but the catalyst particles decreased due to attrition which affected the quality of fluidization. The final conclusion is that neither Ni/αAl_2O_3 nor Ni/γAl_2O_3 is suitable for practical operation, but Ni/SiO_2 remains a suitable catalyst for catalytic methane cracking.

Chapter 6
Model for Methane Catalytic Cracking in Bubbling Fluidized Bed

---

Overview

A three phase bubbling fluidized bed model has been developed to simulate the performance of methane catalytic cracking in a fluidized bed when using a nickel/alumina catalyst. The objective of the model is to predict the performance of a methane catalytic cracking fluidized bed reactor under relevant conditions, by including the chemistry and hydrodynamics occurring within the fluidized bed reactor. The model has the ability to estimate the impact of different process parameters including reactor dimensions and process conditions e.g. temperature and catalyst circulation rate. Methane cracking kinetics developed in a previous work using a thermo balance has been implemented in this model. Only two parameters needed to be adjusted: the ratio of cloud-wake phase to the bubble phase, and one parameter in the activity term to take into consideration longer deactivation time in the fluidized bed than in the thermobalance. Good fit between experimental data and model results were obtain under a wide range of reaction conditions, such as different temperatures, methane partial pressure, particle size, catalysts. The model was used to investigate the fluidized bed behaviour. The results calculated from the model showed that, the conversion is decreasing with increasing the superficial velocity and maximum conversion occurs at the minimum fluidizing velocity.

Keywords: Methane cracking, Hydrogen production, Fluidized bed, Nickel, Alumina, Model

6.1 Introduction

There is currently a growing interest in methane catalytic cracking (MCC) as a promising process for producing CO-free hydrogen from natural gas [1-4]. Steam reforming is the conventional method for hydrogen production from methane, but the produced hydrogen needs a complicated downstream purification process to reduce carbon monoxide concentrations to suitable levels for PEM fuel cell and other industrial applications [4-6]. Methane catalytic cracking presents an alternate solution for producing CO-free hydrogen. Methane cracking converts methane (CH_4) into hydrogen (H_2) and carbon (C). Because of the absence of an oxidant, no carbon oxides are produced. In addition, a significant amount of carbon is produced, which could be burned to provide heat to the cracking process and/or be used in different applications as a high value product [2, 3, 7].

Supported nickel is widely used in research as a catalyst for the MCC process. In the reaction sequence, carbon is deposited on the catalyst leading to carbon filament growth (desired path) or to encapsulating carbon (undesired path leading to deactivation) [8]. Cyclic operation is needed to regenerate the deactivated catalyst [9]. A fluidized bed reactor would permit cyclic operation between a cracker and a regenerator allowing continuous methane cracking operation. In addition, fine catalyst particles can be used in a fluidized bed, which improves catalyst effectiveness [10]. A fluidized bed reactor also overcomes fixed bed plugging problems due to catalyst agglomeration and massive amount of carbon formed. Therefore, a fluidized bed reactor could provide many advantages over a fixed bed reactor, but such a process needs to be optimized for MCC [11]. A fluidized bed process for MCC, known as the "HYPRO" process, was patented back in 1966 [12]. The "HYPRO" process was the first process conducted at an industrial scale for catalytic cracking of methane and light hydrocarbons in a fluidized bed at temperatures up to 980°C and at atmospheric pressure [7, 12, 13]. The carbon produced during the cracking step was burned to supply the process heat demand and to regenerate the catalyst activity in a fluidized bed burner (regenerator). The catalyst particles were transferred between the cracker and the regenerator using a circulation loop [7]. The "HYPRO" process could convert a dry gas mixture of methane and light hydrocarbons to 90% hydrogen with 10% remaining methane, using a 7% nickel supported on alumina catalyst.

The "HYPRO" process was suitable for producing a concentrated stream of hydrogen with a capital cost lower than the steam reforming process [7, 12, 13]. However, the cost of maintaining the pressure drop across the fluidized bed system to ensure fluidization and to transfer the catalyst particles back and forth between the cracker and regenerator, in addition to the high maintenance cost for the fluidized bed

increased the operating cost of the "HYPRO" process. The increase in the operating cost made the "HYPRO" process uncompetitive for hydrogen production [7, 13]. However, many improvements can be made by optimizing the catalyst and the overall operating conditions [7]. A critical step to study the feasibility of the process is developing a useful model of the overall process. The model would help in predicting the effect of various parameters (e.g. methane flow rate, concentration, pressure, residence time, reaction kinetics, hydrodynamics) on the overall performance [14].

The model developed here describes the basic phenomena occurring in a bubbling fluidized bed, including contact between methane and the catalyst, kinetics and hydrodynamics. The purpose of this model is to calculate methane conversion under the proposed conditions, and the deactivation rate for the catalyst using the data extracted from the kinetic study presented in Chapter 4. The model can be used to optimize reactor dimensions (designing and scaling up the fluidized bed reactor) and operating conditions. The model was implemented in MATLAB. The key outputs of this model are:

- Methane and hydrogen concentration as a function of the distance above the distributor
- Methane conversion as a function of the distance above the distributor
- Methane concentration in the effluent
- Bubble properties as a function of the distance above the distributor

This chapter includes a description for the three-phase model, its basic assumptions and the equations used to build the model. This chapter is extended to include comparison of the model predictions with experiments found in the literature. Finally, the model prediction for methane cracking is compared with experimental data that were presented in Chapter 5. The proposed model simulates the behaviour of the solid catalyzed reaction in a bubbling bed regime using the kinetic parameters developed in Chapter 4. The model assumes the presence of three different phases in the fluidized bed; the bubble phase, the cloud-wake phase, and the emulsion phase.

6.2 Model assumptions

The following points summarize the basic assumptions of the model:

- A fluidized bed can be divided into a number of stages in series. The height of each stage is equal to the bubble diameter at the middle of the bed; a schematic of the three phase model is shown in Figure 6.1, whose nomenclature is as follows: C_o is the inlet gas concentration, C_x is the gas concentration in stage x (b, cw, or e stands for bubbling, cloud-wake phase, and emulsion phase respectively), and C_n is the outlet gas concentration.
- Each stage consists of three phases, the bubble phase, the cloud-wake phase, and the emulsion phase as shown in Figure 6.2.
- Methane and hydrogen concentrations in the bubble phase, the cloud-wake phase, and the emulsion (dense) phase are functions of the distance above the gas distributor.
- Gas diffusion occurs from the bubble phase to the cloud-wake (C-W) phase and from the C-W phase to the emulsion phase, and vice-versa.
- Voids in the C-W and emulsion phases are equal to the voids at the minimum fluidizing condition.
- Catalyst particles are distributed between the emulsion and cloud-wake phases.
- The bubble diameter is a function of the height above the gas distributor.

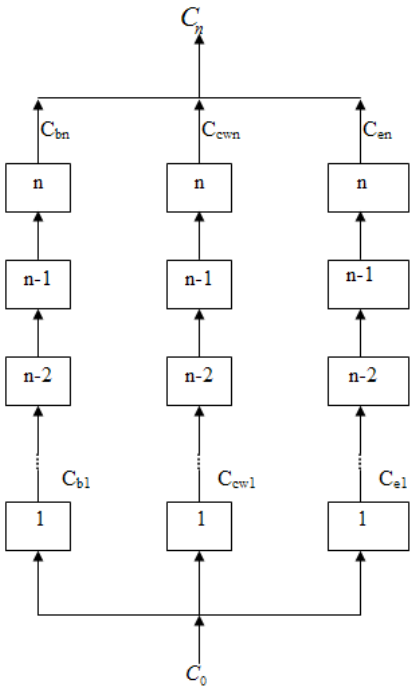

Figure 6.1- Multistage three-phase model (Reprinted from [15], with permission from Elsevier)

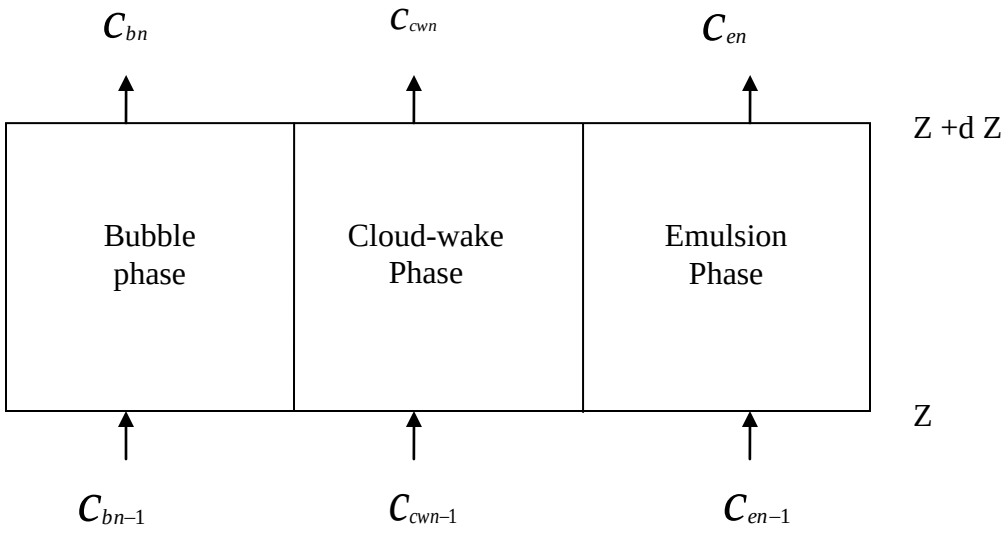

Figure 6.2 - Schematic representation of a stage

6.3 Estimation of bed properties

6.3.1 Hydrodynamic properties

Minimum fluidizing velocity

The minimum fluidizing velocity, U_{mf}, is an important parameter for fluidized bed design. The minimum fluidizing velocity is the minimum velocity required to fully support the catalyst bed. It can be defined as the gas superficial velocity at the minimum fluidizing condition [16, 17]. A large number of correlations are available in the literature for predicting U_{mf}, for example Equations 6.1 and 6.2 [18]:

For particles larger than 100 μm:

$$U_{mf} = \frac{\mu}{\rho_g d_P}\left[(1135.7 + 0.0408 * Ar)^{1/2} - 33.7\right] \quad (6.1)$$

and for particles smaller than 100 μm:

$$U_{mf} = \frac{d_p^{1.8}\left(\rho_s - \rho_g\right)^{0.934} g^{0.934}}{1111\mu^{0.87}\rho_g^{0.066}} \quad (6.2)$$

Where:

P_g is the gas density in kg/m^3,

μ is the gas viscosity in kg/m.s,

d_P is the particle diameter in m.

P_s is the catalyst density in kg/m^3,

g is the Acceleration of gravity= 9.8 m^2/s, and

Ar is the Archimedes number, and is defined as:

$$Ar = \frac{d_p^{3}\rho_g\left(\rho_s - \rho_g\right)g}{\mu^2} \quad (6.3)$$

Despite the large number of correlations available in the literature for calculating U_{mf}, the minimum fluidizing velocity is better determined experimentally for the particles being used. In this study, U_{mf} was determined experimentally by increasing the gas inlet velocity and recording the increase in the pressure drop until a velocity was reached where the pressure drop through the bed became constant and did not change with further velocity increase. A detailed description of the method is given in the experimental part of Chapter 5.

Terminal velocity of particles

Usually the superficial inlet gas velocity is kept between the minimum fluidizing velocity and the terminal velocity of particles to reduce the carryover of particles. By keeping the superficial velocity below terminal falling velocity, fewer particles are entrained with the exit gases. If a cyclone is used to return the entrained solids, higher gas velocities can be used. The free falling velocity, u_t, of a particle through a fluid is given by [16]:

$$u_t = u^* \left[\frac{\mu(\rho_s - \rho_g)g}{\rho_g^{\,2}} \right]^{1/3} \tag{6.4}$$

Where:

u^* is calculated from the following equation:

$$u^* = \left[\frac{18}{(d_p^*)^2} + \frac{2.335 - 1.744\phi_s}{(d_p^*)^{0.5}} \right]^{-1} \qquad \text{For} \qquad 0.5 < \phi_s < 1 \tag{6.5}$$

ϕs is the Sphericity of catalyst particles, and

$$d_p^* = (Ar)^{1/3} \tag{6.6}$$

Minimum bubbling velocity

Fine powders (Geldart A and C) have the ability to fluidize at velocities beyond U_{mf} without bubble formation. The minimum bubbling velocity represents the minimum velocity that can be used to ensure that the fluidized bed is in the bubbling regime. With increasing the velocity beyond the minimum fluidizing velocity, the bed is expanded smoothly and homogenously until a velocity is reached at which small bubbles appear at the surface. If the gas velocity is reduced, a velocity is reached at which the last bubble disappears; the average of the velocities at which bubbles appear or disappear is the minimum bubbling velocity [16].

The minimum bubbling velocity, u_{mb}, can be calculated using Equation 6.7 [19] or Equation 6.8 [20]:

$$u_{mb} = 2\sqrt{u_t} \tag{6.7}$$

$$u_{mb} = 0.5231 \left(\frac{d_p}{D_B} \right)^{1.13} \left(\frac{D_B}{l_m} \right)^{-0.0384} \left(\frac{\rho_s}{\rho_g} \right)^{0.74} \tag{6.8}$$

Where:

D_B is the bed diameter in m, and
l_m is the height of the bed at the fixed bed conditions in m

Incipient turbulent velocity

The minimum (incipient) turbulent velocity, U_c, where turbulent flow begins, is given by the following equation [21]:

$$U_c = \frac{0.7 * \mu}{\rho_g d_p} (Ar)^{0.485} \quad (6.9)$$

The superficial velocity should be less than the incipient turbulent velocity to avoid operating the fluidized bed in the turbulent regime.

Diameter of a bubble just detached from the distributing plate

The diameter of the bubble just detached from the distributing plate is an initial value for the bubble size under the working conditions; later on, it will be used for calculating the bubble diameter at any height. Two common types of distributor are commonly used in industry: porous and perforated plates.

For a porous plate

The bubble diameter of a bubble that just detached from a porous plate may be expressed as follows [16]:

$$d_{b0} = \frac{2.78}{g} (U_0 - U_{mf})^2 \quad (6.10)$$

Where U_0 is the superficial gas velocity in m/s

For a perforated plate

For a perforated plate, the distributor plate is drilled or punched with a regular array of orifices or slots, more suitable for fine powder, and the bubble diameter of a bubble that is just detached from a perforated plate can be calculated as follows [16]:

For a low gas flow rate:

$$d_{b0} = \frac{1.3}{g^{0.2}}\left[\frac{U_0 - U_{mf}}{n_d}\right]^{0.4} \qquad d_{or} \le l_{or} \tag{6.11}$$

Where n_d is calculated from the following equations:

For a square array of holes

$$n_d = \frac{1}{l_{or}^2} \tag{6.12}$$

For an equilateral triangle array of holes

$$n_d = \frac{2}{\sqrt{3} l_{or}^2} \tag{6.13}$$

Where,

n_d is the number of orifices per unit area

l_{or} is the spacing between the adjacent holes

For a high gas flow rate:

$$d_{b0} = \frac{2.78}{g}(U_0 - U_{mf})^2 \qquad d_{or} \ge l_{or} \tag{6.14}$$

6.3.2 Bubble properties

Rise velocity of single bubble

Gas in excess of that needed to ensure minimum fluidization condition passes through the bed as bubbles but the voidage of the bed, without accounting for that associated with the bubbles, stays at the same value of the minimum fluidizing conditions (for emulsion and cloud-wake phases). Mass transfer occurs between the bubbles and the other phases present. The bubbles have different rising velocities in the bed; the bubble rising velocity is proportional to its size, the larger the bubble diameter the faster the bubble rising velocity. Controlling the bubble rising velocity is essential to improve the mass transfer in the bed. The rising velocity of a single bubble is related to the bubble size by the following equation [16]:

$$u_{br} = 0.711(g\,d_b)^{1/2} \qquad \text{For} \qquad \frac{d_b}{D_B} < 0.125 \tag{6.15}$$

$$u_{br} = \left[0.711(g\,d_b)^{1/2}\right] 1.2\exp\left(-1.49\frac{d_b}{D_B}\right) \qquad \text{For} \qquad 0.125 < \frac{d_b}{D_B} < 0.6 \tag{6.16}$$

Bubble size

In the real world, the bubbles are not spherical but irregular. Therefore, a mean diameter of a sphere, which has the same volume as the bubble, is used as bubble diameter. Bubble diameters increase as they rise through the bed but this increase is highly dependent on the catalyst particles sizes. For example, in a bed of Geldart A particles, bubbles increase in size to a certain maximum, due to a balance between coalescence and splitting of the bubbles. d_b follows the following relationship [16]:

$$\frac{d_{bm} - d_b}{d_{bm} - d_{b0}} = e^{-0.3z/D_B} \tag{6.17}$$

Where d_{bm} is the limiting size of the bubble expected in a very deep bed, expressed as [16]:

$$d_{bm} = 0.65\left[\frac{\pi}{4}D_B^2(U_0 - U_{mf})\right]^{0.4} \tag{6.18}$$

Where d_{b0} is the initial bubble size formed near the bottom of the bed (see Equations 6.10 to 6.14).

Bubble rising velocity

The bubble rising velocity is dependent on catalyst particle size; the general equations for the bubble rising velocity that cover the whole range of particle sizes is [16]:

For Geldart A particles with $D_B \leq 1m$

$$u_b = 1.55\left[\left(U_0 - U_{mf}\right) + 14.1\left(d_b + 0.005\right)\right]D_B^{0.32} + u_{br} \quad (6.19)$$

For Geldart B particles with $D_B \leq 1m$

$$u_b = 1.6\left[\left(U_0 - U_{mf}\right) + 1.13\left(d_b^{0.5}\right)\right]D_B^{1.35} + u_{br} \quad (6.20)$$

6.3.3 Bed specifications

Height of bed

The following equation gives the bed height at fixed bed l_m, at minimum fluidization conditions l_{mf}, at minimum bubbling bed l_{mb}, and at bubbling bed l_b [16]:

$$l_m\left(1-\varepsilon_m\right) = l_{mf}\left(1-\varepsilon_{mf}\right) = l_{mb}\left(1-\varepsilon_{mb}\right) = l_b\left(1-\varepsilon_b\right) \quad (6.21)$$

Where ε_m, ε_{mf}, ε_{mb}, and ε_b are the bed voidage at the fixed bed, the minimum fluidization, the minimum bubbling, and the bubbling conditions, respectively. ε_{mf} can be calculated from the following equation [22]:

$$\varepsilon_{mf} = 0.568\phi^{-0.7}\left[\frac{\mu^2}{\rho_g g(\rho_s - \rho_g)d_p^3}\right]^{0.029} * \left[\frac{\rho_g}{\rho_s}\right]^{0.021} \quad (6.22)$$

Rising velocity of emulsion gas through the bed

The rising velocity of gas in the emulsion phase is calculated by the following equation [16]:

$$u_e = \frac{U_{mf}}{\varepsilon_{mf}} - u_{s,down} \tag{6.23}$$

Where $U_{s,down}$ is the down flow velocity of emulsion catalyst particles, and is equal to [16]:

$$u_{s,down} = \frac{f_w \varepsilon_b u_b}{1 - \varepsilon_b - f_w \varepsilon_b} \tag{6.24}$$

Where f_W is the ratio of the wake phase to the bubble phase

Bubble fraction of the bed

The bubble fraction of the bed may be expressed as [16]:

For slow bubbles $u_b < u_e$

$$\varepsilon_b = \frac{U_0 - U_{mf}}{u_b + 2U_{mf}} \tag{6.25}$$

For intermediate velocity bubbles with thick clouds $U_{mf} / \varepsilon_{mf} < u_b < 5U_{mf} / \varepsilon_{mf}$

$$\varepsilon_b = \frac{U_0 - U_{mf}}{u_b + U_{mf}} \qquad u_b \cong U_{mf} / \varepsilon_{mf} \tag{6.26}$$

$$\varepsilon_b = \frac{U_0 - U_{mf}}{u_b} \qquad u_b \cong 5U_{mf} / \varepsilon_{mf} \tag{6.27}$$

For fast bubbles $u_b > 5U_{mf} / \varepsilon_{mf}$

$$\varepsilon_b = \frac{U_0 - U_{mf}}{u_b - U_{mf}} \tag{6.28}$$

In vigorously bubbling beds $u_b >> U_{mf}$

$$\varepsilon_b = \frac{U_0}{u_b} \tag{6.29}$$

Ratio of the cloud-wake phase to the bubble phase

The cloud can be simply defined as the gaseous region that is surrounding the bubble. The wake is the region just below the bubble [16, 19]. The ratio of cloud-wake phase to the bubble phase f_{CW} is adjusted to fit the experimental conditions.

Fraction of bed in emulsion

The volumetric percent of bed present as an emulsion is defined as [16]:

$$f_e = 1 - \varepsilon_b \ (1 + f_{Cw}) \tag{6.30}$$

Catalyst particle percent in each phase

Kunii et al. [16]defined the fraction of catalyst in the cloud-wake, and emulsion phases as follows:
Fraction of solids in wake and bubble:

$$\gamma_c = (1 - \varepsilon_{mf}) f_{CW} \tag{6.31}$$

Fraction of solids in emulsion [16]:

$$\gamma_e = \frac{(1 - \varepsilon_{mf})(1 - \varepsilon_b)}{\varepsilon_b} - \gamma_c \tag{6.32}$$

Number of stages

The bed is divided into equal height stages based on the bubble diameter at the centre of the bed. The height of the bed (l_b) is calculated from Equation 6.21 and the bubble diameter at the middle of the bed (d_b) is calculated from Equation 6.17 to give the number of stages as follows:

n (Number of stages) = l_b/d_b (rounded to the nearest integer) (6.33)

6.3.4 Gas interchange coefficient

The gas transfer between different phases in a fluidized bed requires calculating the interchange coefficients between different phases. Mass transfer occurs in two stages: the first stage between the bubble and cloud-wake phases, and the second stage between the cloud-wake and the emulsion phases. The interchange coefficients between the different phases may be expressed as [16]:

The interchange coefficient between bubble and cloud-wake phase:

$$k_{bc} = 4.5\left(\frac{U_{mf}}{d_b}\right) + 5.85\left(\frac{D^{1/2} g^{1/4}}{d_b^{5/4}}\right) \quad (6.34)$$

The interchange coefficient between cloud-wake and emulsion phases:

$$k_{ce} = 6.77\left(\frac{D * \varepsilon_{mf} * u_b}{d_b^3}\right)^{1/2} \quad (6.35)$$

6.3.5 Gas properties

Diffusivity

The Chapman-Enskog equation for the diffusion coefficient is used to calculate the gas diffusion coefficients as follows [23]:

$$D_{AB} = D_{BA} = 1.8583 * 10^{-27} \frac{\left[T^3\left[(1/M_A) + (1/M_B)\right]\right]^{1/2}}{P_{atm}\sigma_{AB}^2 \Omega_D} \quad (6.36)$$

Where:

D_{AB} is the diffusion coefficient in m^2/s^{-1}

P is the pressure in atm

T is the temperature in K

M_A & M_B are the molecular weights for gases A & B

(Note: $M_A=M_B$ in self diffusion problems)

Ω_D is the diffusion collision integral

σ_{AB} is the collision diameter in meters

See appendix C for Ω_D and σ_{AB} values

Viscosity

To calculate the viscosity of the gases, the Chapman-Enskog equation of viscosity is used [23]:

$$\mu = 2.6693*10^{-26}\left(\frac{(MT)^{1/2}}{\sigma^2\Omega_\mu}\right) \tag{6.37}$$

where

μ is the gas viscosity in kg/m.s. or Pa.s

T: Temperature in K

M: The molecular weight of gas

Ω_μ : The viscosity collision integral

σ : Collision diameter in meter

See appendix D for parameters Ω_μ and σ values

6.3.6 Kinetic data

The reaction rate of methane cracking and the activity of the catalyst used in the model are developed in Chapter 4. The activity term is modified to adjust the catalyst performance in the fluidized bed since the deactivation is slower in the fluidized bed than in the thermo balance. As shown in Chapter 4, the activity term developed in the kinetic study is:

$$a = \left(\frac{1}{1+(n-1)k_d (kd_C + kd_{CH_4} * P_{CH_4} + kd_{H_2} * P_{H_2}^{0.83})t} \right)^{-0.8} \quad (6.38)$$

The previous term has been corrected for the catalyst deactivation regime in the fluidized bed by adding the factor h in the denominator, as follows:

$$a = \left(\frac{1}{1+(n-1)k_d * h(kd_C + kd_{CH_4} * P_{CH_4} + kd_{H_2} * P_{H_2}^{0.83})t} \right)^{-0.8} \quad (6.39)$$

Where h is calculated from the following equations:

For 10% Ni/γAl_2O_3

$$h = 4.7 \times 10^{-6} * Exp(6.7 \times 10^4 / 8.314 / T) * (P_{CH4}^{0.45}) * (d_p^{-0.18}) \quad (6.40)$$

For 10% Ni/αAl_2O_3

$$h = 5 \times 10^{-6} * Exp(6.7 \times 10^4 / 8.314 / T) * (P_{CH4}^{0.38}) * (d_p^{-0.18}) \quad (6.41)$$

6.4 Model equations (see appendix H for the MATLAB code)

Mass balance equations

- Bubble phase

$$u_b C_{bn-1} \varepsilon_b - u_b C_{bn} \varepsilon_b - (k_{bc}) \varepsilon_b \int_{Zn-1}^{Zn} (C_{bn} - C_{cwn}) dz = 0 \quad (6.42)$$

- Cloud-wake phase

$$u_b (C_{cwn-1} - C_{cwn}) \varepsilon_b f_{cw} \varepsilon_{mf} + (k_{bc}) \varepsilon_b \int_{Zn-1}^{Zn} (C_{bn} - C_{cwn}) dz - \varepsilon_b \gamma_C f_{cw} r_A dz - k_{ce} (C_{cwn} - C_{en}) \varepsilon_b = 0 \quad (6.43)$$

- Emulsion phase

$$U_{mf} (C_{en-1} - C_{en}) + k_{ce} (C_{cwn} - C_{en}) dz - r_A \gamma_e \, dz = 0 \quad (6.44)$$

- Overall balance

$$u_o = u_b \varepsilon_b + u_b \varepsilon_b \varepsilon_{mf} f_{cw} + U_{mf} \quad (6.45)$$

6.5 Model validation

6.5.1 Comparison of model prediction with experimental results from literature

Figures 6.3 and 6.4 show a comparison of the data predicted by the model and the experimental results in the case of ozone decomposition using air as the fluidizing gas. Useful fluidized bed data for methane cracking were not available and thus the ozone decomposition reaction was chosen to validate the model because of the availability of fluidized bed experimental data in the literature for that particular reaction. Obviously, the reaction rate has been changed to represent the ozone decomposition reaction. The difference between Figures 6.3 and 6.4 is the catalyst used, which translates into different rate constants. These results show good agreement between model prediction and experimental results for both reaction rate constants and for a wide range of inlet superficial gas velocities.

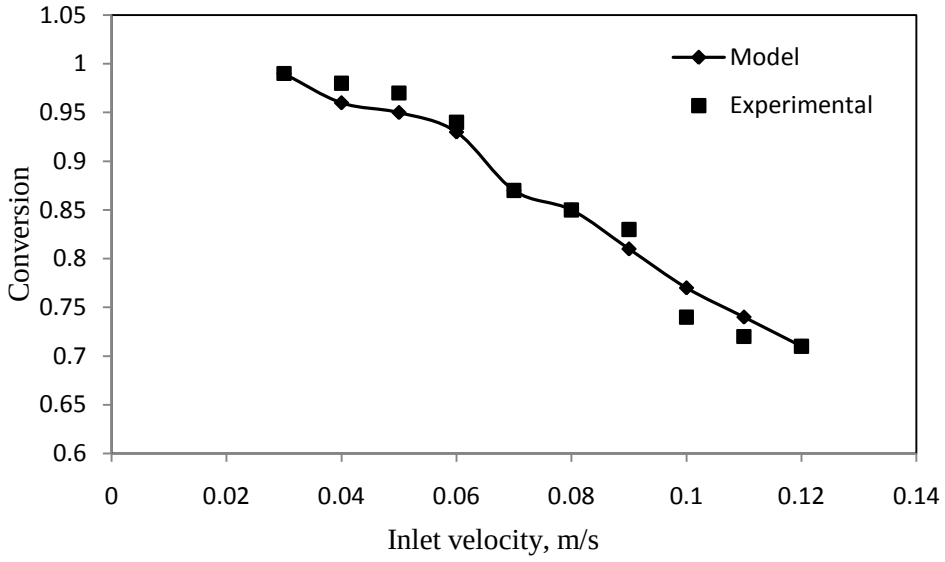

Figure 6.3 - Comparison of conversion between model and experimental data [24]

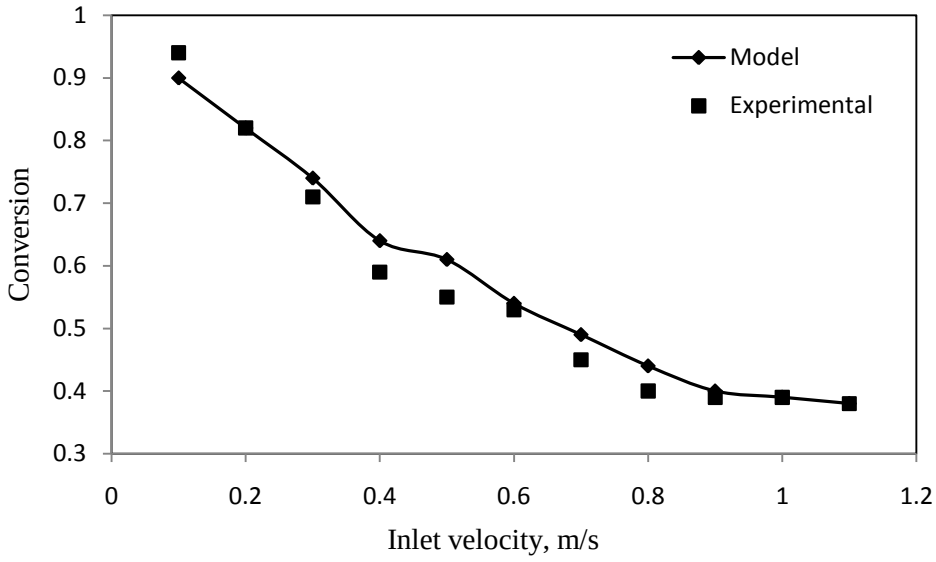

Figure 6.4 - Comparison of model conversion with experimental data [25]

6.5.2 Comparison of model prediction with methane cracking in a fluidized bed

The model was modified by adding the reaction rate and activity equations developed in Chapter 4, to simulate methane cracking in a fluidized bed. The conversion calculated from the model is compared with the conversion achieved with 10% Ni/γAl_2O_3 and 10% Ni/αAl_2O_3 catalysts. Figures 6.5 to 6.7 compare the model prediction with the experimental results for different conditions of temperature, catalysts, particle size and methane partial pressure. The results show that the model can effectively predict the conversion of methane using both catalysts under study at different reaction conditions.

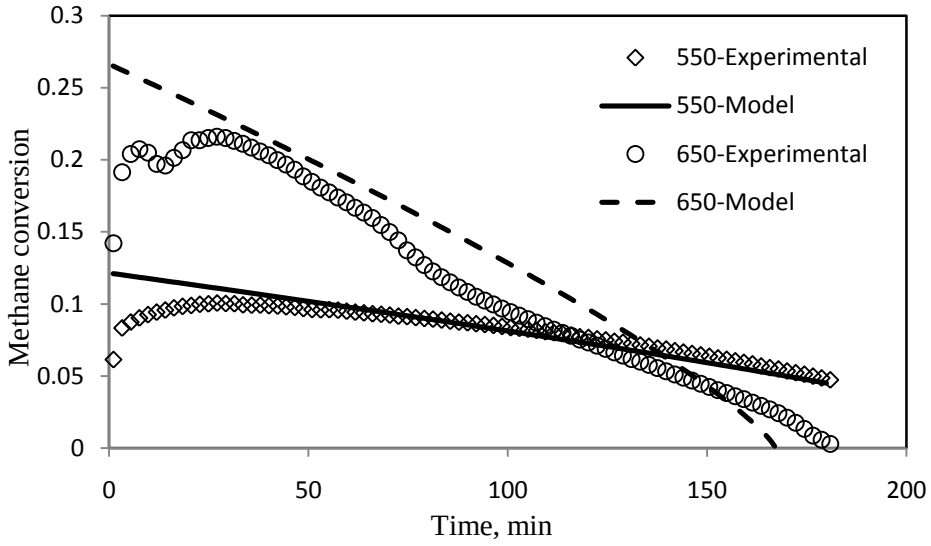

Figure 6.5 - Model and experimental conversions using 10% $Ni/\alpha Al_2O_3$, 275 μm, and 80/20 CH_4/N_2

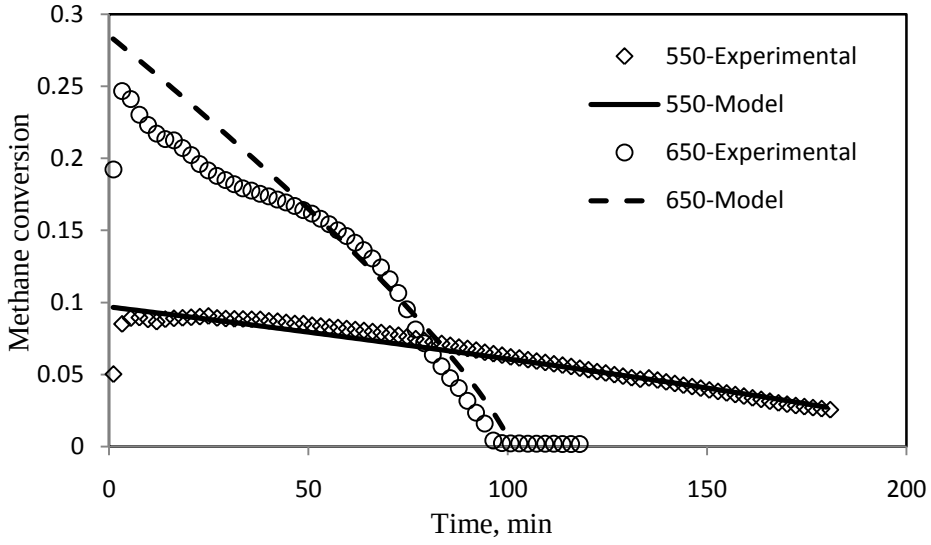

Figure 6.6 - Model and experimental conversions using 10% $Ni/\gamma Al_2O_3$, 108 μm, and 50/50 CH_4/N_2

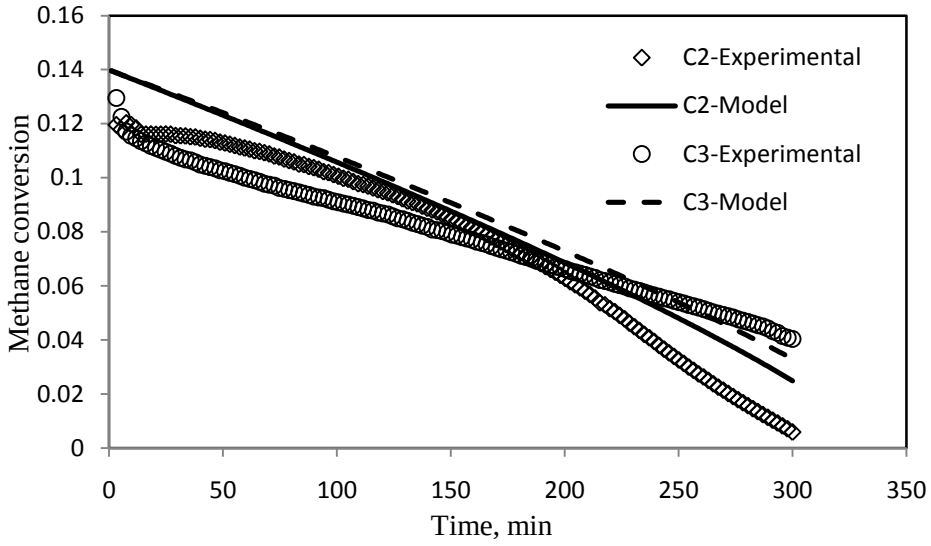

Figure 6.7 - Model and experimental conversions for different cycles using 10% $Ni/\gamma Al_2O_3$, 275 μm, and 80/20 CH_4/N_2

6.6 Model output and application

The developed model and its implementation in MATLAB were evaluated for methane cracking using the following simplifying assumptions:

- Isothermal conditions
- Constant particle size and density
- No catalyst recirculation (no output of solids)

The developed model can be used to predict the effect of different process parameters:

- Particle diameter
- Particle density
- Wake fraction
- Voidage at fixed bed conditions
- Bed height at fixed bed conditions
- Bed diameter
- Reactor temperature
- Inlet velocity

- Distributor type

The developed model outputs include:

- velocity of different phases
- concentration of reactant and product
- conversion
- bubble diameter
- overall conversion

6.6.1 Concentration of reactant and products along the reactor length

Figure 6.8 shows the concentrations of methane and hydrogen along the reactor height at different temperatures. The figure shows that the bed height is not affected by temperature but higher hydrogen concentration is calculated at higher temperatures.

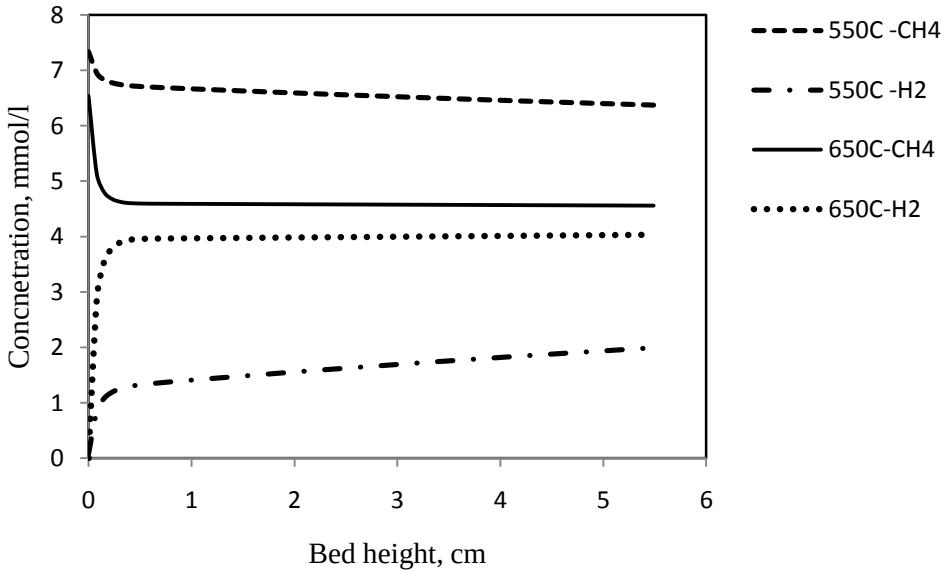

Figure 6.8 - Methane and hydrogen concentration variations with bed height for 10% $Ni/\gamma Al_2O_3$ at 550, and 650ºC using 275 μm particles and 50/50 CH_4/N_2

6.6.2 Conversion and inlet velocity

Figure 6.9 shows total methane conversion at the exit of the fluidized bed as a function of inlet velocity at different reaction times (the time is a measure for catalyst deactivation). The figure

indicates the importance of the inlet velocity as a major factor affecting the reaction rate. The conversion increases as the superficial velocity decreases, and the maximum conversion is reported for a velocity near the minimum fluidizing velocity due to increasing contact time [15, 25].

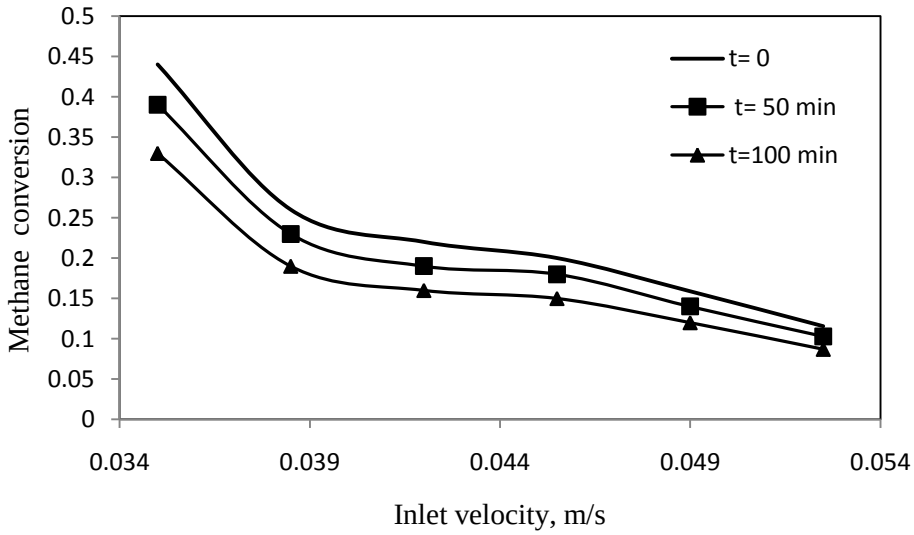

Figure 6.9 - Methane conversion as a function of the inlet velocity at different reaction times for 10% $Ni/\alpha Al_2O_3$ at 550ºC using 275 μm particles and 80/20 CH_4/N_2

6.6.3 Bubble diameter at different bed heights

Figure 6.10 shows the bubble diameter variation as the bubbles rise up through the bed. The bubble size increases with the height above the distributor, which is a common behaviour of the bubble in case of Geldart A catalyst particles [16].

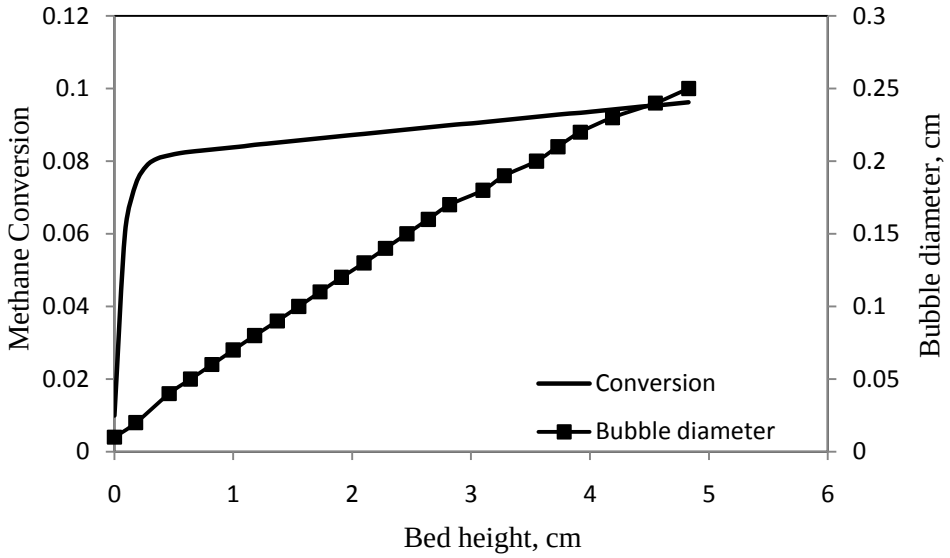

Figure 6.10 - Bubble diameter and conversion as a function of bed height for an inlet velocity of 0.03 m/s for 10% Ni/γAl_2O_3 at 550ºC using 108 μm particles and 50/50 CH_4/N_2

6.7 Conclusions

A three phase (bubble, cloud-wake, and emulsion phases) model was developed to simulate methane cracking in a fluidized bed for producing CO-free hydrogen using 10% Ni/γAl_2O_3 and 10% Ni/αAl_2O_3. The model was adopted for the bubbling regime fluidized beds. The model captures most of the chemistry and physics within the bubbling fluidized bed. The kinetic behaviour of the catalyst was developed based on a kinetic study in a thermo balance (Chapter 4). The activity term was modified to be compatible with the longer deactivation time observed for the catalysts compared that in the thermo balance experiments. The developed model was validated and calibrated using experimental data. A good fit was obtained between the model and experimental results for a wide range of reaction conditions (temperature, methane partial pressure, catalyst particle size, catalyst type).

The model was used to predict methane cracking behaviour in a fluidized bed using different catalysts, temperatures, methane concentrations, and flow rates. The model can be used to study the effect of temperature, methane concentration, particle size, bed diameter, and flow rate on methane cracking in a fluidized bed. The simulation results show that increasing the flow rate decreasing the conversion and the bubble size increase as the gases rising through the bed. Lower methane partial pressure and low flow rate are necessary to achieve higher conversion rates.

Chapter 7

Conclusions and Recommendations

7.1 Conclusions

The focus of this research was to provide a methodical and comprehensive understanding of methane catalytic cracking for hydrogen production. An extensive study was performed for methane catalytic cracking using different supports (porous alumina, nonporous alumina) with 10% nickel in a thermo balance. The temperature range was 500-650ºC at atmospheric pressure, using different flow rates (72, 120, 180, and 240 ml/min), particle sizes (300, 725, and 1000 μm), different mole fractions of methane and nitrogen (in terms of CH_4/N_2; 90/10, 70/30 and 50/50), and different mole fractions of methane and hydrogen (in terms of CH_4/H_2; 95/5, 90/10, 85/15 and 80/20). In the first cracking cycle for the fresh catalyst, the nonporous catalyst showed better performance than the porous catalyst in terms of carbon deposition rate, and longer deactivation time. Full regeneration of the catalysts using air oxidation was achieved at 550°C, while carbon oxidation was very slow at 500°C. After regeneration, the performance of the porous catalyst became better than the nonporous. The porous catalyst kept its activity for 24 cracking/regeneration cycles, while the non-porous catalyst lost half of its activity by the second cracking cycle and almost all of its activity after six cycles. Formation of $NiAl_2O_4$ and sintering caused the nonporous catalyst activity loss. The carbon deposited on the catalyst was found in the form of carbon filaments with a diameter of 20-40 nm on the porous catalyst and chunks of carbon on the nonporous catalyst. The TEM images showed hollow carbon filaments on the porous catalyst.

A kinetic model was developed to express methane catalytic cracking on $Ni/\alpha Al_2O_3$ and $Ni/\gamma Al_2O_3$. The model agrees well with the experimental data and the model parameters agree with the literature values. The model was developed based on the experimental work in the thermo balance using the separable kinetic approach, by using a reaction rate term for the initial rate and activity term for predicting the deactivation behavior of the catalyst. The rate is the product of multiplying the initial rate by the activity term. The residence time distribution inside the thermo balance was simulated and the results indicated that methane reaches the maximum concentration around the catalyst particles at a time that matches the maximum rate. The activation energy for methane cracking was estimated at 88 and 75 kJ/mol for $Ni/\gamma Al_2O_3$ and $Ni/\alpha Al_2O_3$, respectively. Cracking/regeneration cycles showed that the $Ni/\gamma Al_2O_3$ can be used for conducting continuous cracking/regeneration cycles of methane cracking. The

activation energy for the encapsulating carbon formation, which is responsible for catalyst deactivation, is estimated at 147 and 149 kJ/mol for the $Ni/\gamma Al_2O_3$ and $Ni/\alpha Al_2O_3$ catalysts, respectively. The deactivation reaction is half order in surface carbon. The experimental results of cracking/regeneration cycles were used to develop the kinetic model to predict the catalyst performance in different cracking cycles. The model showed good agreement with the experimental data at different experiment conditions and as a function of cracking cycles.

To investigate the behavior of methane cracking in a fluidized bed and to validate the fluidized bed model, an extensive study was performed for methane catalytic cracking using different supports (porous alumina, nonporous alumina, and silica) with 10% nickel in a fluidized bed and a fixed bed. The temperature used was between 550-650ºC; using different flow rates, particle sizes, and different mole fractions of methane and hydrogen. The results showed variation in catalyst performance between the different supports, and the methane conversion observed for each catalyst was in the following order: $Ni/SiO_2 > Ni/\alpha Al_2O_3 > Ni/\gamma Al_2O_3$. Ni/SiO_2 achieved the highest conversion and $Ni/\gamma Al_2O_3$ showed the best fluidization quality. Increasing the temperature and the particle size from 108 to 275 μm had a positive effect on methane conversion for all catalysts. Increasing the flow rate and P_{CH4} caused a drop in methane conversion. A higher conversion and faster deactivation with methane were observed in the fixed bed. The pressure build up inside the fixed bed stopped the reaction. During cracking/regeneration cycles in the fluidized bed, Ni/SiO_2 was thermally stable but the mechanical attrition in the fluidized bed crushed the catalyst into smaller particles, although the catalyst maintained its activity. $Ni/\alpha Al_2O_3$ and $Ni/\gamma Al_2O_3$ were thermally unstable due to sintering of the active sites after the first cycle, leading to decreased methane conversion. Using moderate conditions during the regeneration step for $Ni/\gamma Al_2O_3$, the catalyst kept its activity for three cracking cycles. SEM pictures were taken and the carbon filament diameter was:30-50, 30-60, and 29-90 nm for $Ni/\gamma Al_2O_3$, $Ni/\alpha Al_2O_3$, and Ni/SiO_2, respectively.

Finally, a three-phase bubbling fluidized bed model was developed. The model fully simulates the performance of methane cracking in a fluidized bed cracking unit using 10% $Ni/\gamma Al_2O_3$ and 10% $Ni/\alpha Al_2O_3$. The model was developed using the kinetic parameters developed in the kinetic study in the thermo balance. The model predicts the effect of various parameters (e.g. methane flow rate, concentration, pressure, reaction kinetics, hydrodynamics) on the overall system performance. The model agrees well with the data from the experimental study conducted in the fluidized bed. The model can be used to study methane conversion in a fluidized bed and optimize the operating conditions for maximum conversion.

7.2 Recommendations

The ultimate goal of this research was to develop a clear understanding of methane catalytic cracking and to develop a kinetics model that take into account deactivation, as well as a fluidized bed model to predict the performance of methane catalytic cracking in a fluidized bed and the effect of the different process parameters on methane conversion. However, there are still to be answered in order to advance the commercialization of methane catalytic cracking for hydrogen production. The following are recommendations for future research:

- Develop methods for separating carbon filaments from the catalyst for further use (other than burning it) will further improve the economics of the process. In that regards, improving the quality of the carbon deposited during methane cracking needs to be improved as well.
- A durable catalyst for fluidized bed applications needs to be developed. Different characteristics are required. The catalyst needs to:
    - provide high conversion;
    - have excellent thermal and chemical stability;
    - have high carbon capacity;
    - last a long time (until complete deactivation);
    - withstand attrition; and
    - be light weight.

  Because of its activity and cost, nickel is likely to be the active metal of choice. However, more work must be done to maximize nickel dispersion and control the nickel particulate size. As well, stronger support must be developed for fluidized bed applications. As a starting point, nickel supported on silica used in the fluidized bed experimental work can be used after improving the catalyst by adding a binder to increase its mechanical resistance.

- A model of the entire process must be developed. This model will include the cracking reactor, the regeneration reactor and solids circulation between the two reactors. A catalyst circulation loop is indeed essential to carry out the process continuously. Catalyst circulation rate (related to residence time in both reactors) can be determined by reactor energy requirements since the regenerated catalyst is the heat source for the endothermic cracking process.

References:

References (Chapter 1):

1. Rahman, M., E. Croiset, and R. Hudgins, *Catalytic Decomposition of Methane for Hydrogen Production.* Topics in Catalysis, 2006. **37**(2): p. 137-145.
2. Abbas, H.F. and W.M.A. Wan Daud, *Hydrogen production by methane decomposition: A review.* International Journal of Hydrogen Energy, 2010. **35**(3): p. 1160-1190.
3. Amin, A.M., E. Croiset, and W. Epling, *Review of methane catalytic cracking for hydrogen production.* International Journal of Hydrogen Energy, 2011. **36**(4): p. 2904-2935.
4. Chen, Z. and S.S.E.H. Elnashaie, *Steady-state modeling and bifurcation behavior of circulating fluidized bed membrane reformer-regenerator for the production of hydrogen for fuel cells from heptane.* Chemical Engineering Science, 2004. **59**(18): p. 3965-3979.
5. Muradov, N.Z. and T.N. Veziroglu, *"Green" path from fossil-based to hydrogen economy: An overview of carbon-neutral technologies.* International Journal of Hydrogen Energy, 2008. **33**(23): p. 6804-6839.
6. Otsuka, K., S. Takenaka, and H. Ohtsuki, *Production of pure hydrogen by cyclic decomposition of methane and oxidative elimination of carbon nanofibers on supported-Ni-based catalysts.* Applied Catalysis A: General, 2004. **273**(1-2): p. 113-124.
7. Muradov, N.Z., *How to produce hydrogen from fossil fuels without CO2 emission.* International Journal of Hydrogen Energy, 1993. **18**(3): p. 211-215.
8. Muradov, N. *Thermo-catalytic CO_2-free production of hydrogen from hydrocarbon fuels*. in *DOE hydrogen program review*. 2001. The National Renewable Energy Laboratory for the U.S. Department of Energy, Baltimore, Maryland, USA.
9. Suelves, I., et al., *Hydrogen production by thermo catalytic decomposition of methane on Ni-based catalysts: influence of operating conditions on catalyst deactivation and carbon characteristics.* International Journal of Hydrogen Energy, 2005. **30**(15): p. 1555-1567.
10. Avdeeva, L.B., D.I. Kochubey, and S.K. Shaikhutdinov, *Cobalt catalysts of methane decomposition: accumulation of the filamentous carbon.* Applied Catalysis A: General, 1999. **177**(1): p. 43-51.
11. Muradov, N.Z. and T.N. Veziroglu, *From hydrocarbon to hydrogen-carbon to hydrogen economy.* International Journal of Hydrogen Energy, 2005. **30**(3): p. 225-237.
12. Ermakova, M.A., D.Y. Ermakov, and G.G. Kuvshinov, *Effective catalysts for direct cracking of methane to produce hydrogen and filamentous carbon: Part I. Nickel catalysts.* Applied Catalysis A: General, 2000. **201**(1): p. 61-70.
13. Takenaka, S., et al., *Decomposition of methane over supported-Ni catalysts: effects of the supports on the catalytic lifetime.* Applied Catalysis A: General, 2001. **217**(1-2): p. 101-110.
14. Hazra, M., et al., *Experimental investigation of the catalytic cracking of methane over a supported Ni catalyst.* The Canadian Journal of Chemical Engineering, 2009. **87**(1): p. 99-105.
15. Snoeck, J.W., G.F. Froment, and M. Fowles, *Kinetic Study of the Carbon Filament Formation by Methane Cracking on a Nickel Catalyst.* Journal of Catalysis, 1997. **169**(1): p. 250-262.
16. Aiello, R., et al., *Hydrogen production via the direct cracking of methane over Ni/SiO2: catalyst deactivation and regeneration.* Applied Catalysis A: General, 2000. **192**(2): p. 227-234.
17. Lee, K.K., et al., *Thermocatalytic hydrogen production from the methane in a fluidized bed with activated carbon catalyst.* Catalysis Today, 2004. **93-95**: p. 81-86.
18. Pohlenz, J.B., Scott, Norman H., *Method for hydrogen production by catalytic decomposition of a gaseous hydrocarbon stream*. 1966, UNIVERSAL OIL PROD CO: United States.

References (Chapter 2):

1. Malaika A., Krzyzynska B., Kozlowski M. Catalytic decomposition of methane in the presence of in situ obtained ethylene as a method of hydrogen production. Int. J. Hydrogen Energy 2010; 35: 7470-7475.
2. Muradov N.Z. How to produce hydrogen from fossil fuels without CO_2 emission. Int. J. Hydrogen Energy 1993; 18: 211-215.
3. Abbas H.F., Daud W.M.A.W. Hydrogen production by thermocatalytic decomposition of methane using a fixed bed activated carbon in a pilot scale unit: Apparent kinetic, deactivation and diffusional limitation studies. Int. J. Hydrogen Energy 2010; 35: 12268-12276.
4. Luengnaruemitchai A., Osuwan S., Gulari E. Comparative studies of low-temperature water-gas shift reaction over Pt/CeO_2, Au/CeO_2, and Au/Fe_2O_3 catalysts. Catal. Commun. 2003; 4: 215-221.
5. Otsuka K., Takenaka S., Ohtsuki H. Production of pure hydrogen by cyclic decomposition of methane and oxidative elimination of carbon nanofibers on supported-Ni-based catalysts. Appl. Catal., A 2004; 273: 113-124.
6. Poirier M.G., Sapundzhiev C. Catalytic decomposition of natural gas to hydrogen for fuel cell applications. Int. J. Hydrogen Energy 1997; 22: 429-433.
7. Muradov N. Thermo-catalytic CO_2-free production of hydrogen from hydrocarbon fuels. 2001 DOE hydrogen program review. The National Renewable Energy Laboratory for the U.S. Department of Energy, Baltimore, Maryland, USA, 271-296.
8. ABS-energy-research. The hydrogen economy Hydrogen and fuel cells Ed1. 2006.
9. Ermakova M.A., Ermakov D.Y. Ni/SiO_2 and Fe/SiO_2 catalysts for production of hydrogen and filamentous carbon via methane decomposition. Catal. Today 2002; 77: 225-235.
10. Catón N., Villacampa J.I., Royo C., Romeo E., Monzón A. Hydrogen production by catalytic cracking of methane using $Ni-Al_2O_3$ catalysts. Influence of the operating conditions, in: (Ed. Spivey J.J, Roberts G.W, Davis B.H) Stud. Surf. Sci. Catal.: Elsevier; 2001. 391-398.
11. Bartholomew C.H., Robert J.F. Fundamentals of Industrial Catalytic Processes. 2ed. New Jersey: Wiley-AIChE; 2005.
12. Rodat S., Abanades S., Sans J.-L., Flamant G. A pilot-scale solar reactor for the production of hydrogen and carbon black from methane splitting. Int. J. Hydrogen Energy 2010; 35: 7748-7758.
13. Villacampa J.I., Royo C., Romeo E., Montoya J.A., Del Angel P., Monzón A. Catalytic decomposition of methane over $Ni-Al_2O_3$ coprecipitated catalysts: Reaction and regeneration studies. Appl. Catal., A 2003; 252: 363-383.
14. Takenaka S., Ogihara H., Yamanaka I., Otsuka K. Characterization of silica-supported Ni catalysts effective for methane decomposition by Ni K-edge XAFS. Synchrotron Rad. 2001; 8: 587-589.
15. Dunker A.M., Kumar S., Mulawa P.A. Production of hydrogen by thermal decomposition of methane in a fluidized-bed reactor-Effects of catalyst, temperature, and residence time. Int. J. Hydrogen Energy 2006; 31: 473-484.
16. Muradov N. Hydrogen via methane decomposition: an application for decarbonization of fossil fuels. Int. J. Hydrogen Energy 2001; 26: 1165-1175.
17. Abbas H.F., Wan Daud W.M.A. Hydrogen production by methane decomposition: A review. Int. J. Hydrogen Energy 2010; 35: 1160-1190.
18. Avdeeva L.B., Kochubey D.I., Shaikhutdinov S.K. Cobalt catalysts of methane decomposition: accumulation of the filamentous carbon. Appl. Catal., A 1999; 177: 43-51.
19. Ermakova M.A., Ermakov D.Y., Kuvshinov G.G. Effective catalysts for direct cracking of methane to produce hydrogen and filamentous carbon: Part I. Nickel catalysts. Appl. Catal., A 2000; 201: 61-70.
20. Echegoyen Y., Suelves I., Lázaro M.J., Moliner R., Palacios J.M. Hydrogen production by thermocatalytic decomposition of methane over Ni-Al and Ni-Cu-Al catalysts: Effect of calcination temperature. J. Power Sources 2007; 169: 150-157.

21. Pohlenz J., Scott N. Method for hydrogen production by catalytic decomposition of a gaseous hydrocarbon stream. in: (Ed. Universal Oil Prod), U.S. Patent No 3,284,161 (UOP); 1966.
22. Kermode R.I. Hydrogen: its technology and implications: Vol. 1, Production Technology. (Ed. Cox K.E., Williamson K.D), Chap.3, 61-115. Cleveland: CRC Press; 1977.
23. Chin S.Y., Chin Y.-H., Amiridis M.D. Hydrogen production via the catalytic cracking of ethane over Ni/SiO_2 catalysts. Appl. Catal., A 2006; 300: 8-13.
24. Rahman M., Croiset E., Hudgins R. Catalytic Decomposition of Methane for Hydrogen Production. Top. Catal. 2006; 37: 137-145.
25. Snoeck J.W., Froment G.F., Fowles M. Kinetic Study of the Carbon Filament Formation by Methane Cracking on a Nickel Catalyst. J. Catal. 1997; 169: 250-262.
26. Figueiredo J.L., Órfão J.J.M., Cunha A.F. Hydrogen production via methane decomposition on Raney-type catalysts. Int. J. Hydrogen Energy 2010, 35: 9795-9800.
27. Lee K.K., Han G.Y., Yoon K.J., Lee B.K. Thermocatalytic hydrogen production from the methane in a fluidized bed with activated carbon catalyst. Catal. Today 2004; 93-95: 81-86.
28. Rostrup-Nielsen J.R. Equilibria of decomposition reactions of carbon monoxide and methane over nickel catalysts. J. Catal. 1972; 27: 343-356.
29. Alstrup I. A new model explaining carbon filament growth on nickel, iron, and Ni-Cu alloy catalysts. J. Catal. 1988; 109: 241-251.
30. Fukada S., Nakamura N., Monden J., Nishikawa M. Experimental study of cracking methane by Ni/SiO_2 catalyst. J. Nucl. Mater. 2004; 329-333: 1365-1369.
31. Rostrup-Nielsen J., Trimm D.L. Mechanisms of carbon formation on nickel-containing catalysts. J. Catal. 1977; 48: 155-165.
32. Yang R.T., Chen J.P. Mechanism of carbon filament growth on metal catalysts. J. Catal. 1989; 115: 52-64.
33. Snoeck J.W., Froment G.F., Fowles M. Filamentous Carbon Formation and Gasification: Thermodynamics, Driving Force, Nucleation, and Steady-State Growth. J. Catal. 1997; 169: 240-249.
34. Ginsburg J.M., Pina J., El Solh T., de Lasa H.I. Coke Formation over a Nickel Catalyst under Methane Dry Reforming Conditions: Thermodynamic and Kinetic Models. Ind. Eng. Chem. Res. 2005; 44: 4846-4854.
35. De Bokx P.K., Kock A.J.H.M., Boellaard E., Klop W., Geus J.W. The formation of filamentous carbon on iron and nickel catalysts: I. Thermodynamics. J. Catal. 1985; 96: 454-467.
36. Zhang Y., Smith K.J. Carbon Formation Thresholds and Catalyst Deactivation During CH_4 Decomposition on Supported Co and Ni Catalysts. Catal. Lett. 2004; 95: 7-12.
37. Zhang T., Amiridis M.D. Hydrogen production via the direct cracking of methane over silica-supported nickel catalysts. Appl. Catal., A 1998; 167: 161-172.
38. Avdeeva L.B., Reshetenko T.V., Ismagilov Z.R., Likholobov V.A. Iron-containing catalysts of methane decomposition: accumulation of filamentous carbon. Appl. Catal., A 2002; 228: 53-63.
39. Zhang Y., Smith K.J. CH_4 decomposition on Co catalysts: effect of temperature, dispersion, and the presence of H_2 or CO in the feed. Catal. Today 2002; 77: 257-268.
40. Gac W., Denis A., Borowiecki T., Kepinski L. Methane decomposition over $Ni\text{-}MgO\text{-}Al_2O_3$ catalysts. Appl. Catal., A 2009; 357: 236-243.
41. Venugopal A., Naveen Kumar S., Ashok J., Hari Prasad D., Durga Kumari V., Prasad K.B.S., Subrahmanyam M. Hydrogen production by catalytic decomposition of methane over Ni/SiO_2. Int. J. Hydrogen Energy 2007; 32: 1782-1788.
42. Chesnokov V.V., Chichkan A.S. Production of hydrogen by methane catalytic decomposition over $Ni\text{-}Cu\text{-}Fe/Al_2O_3$ catalyst. Int. J. Hydrogen Energy 2009; 34: 2979-2985.
43. Jang H.T., Cha W.S. Hydrogen production by the thermocatalytic decomposition of methane in a fluidized bed reactor. Korean J. Chem. Eng. 2007; 24: 374-377.
44. Ammendola P., Chirone R., Ruoppolo G., Russo G. Production of hydrogen from thermo-catalytic decomposition of methane in a fluidized bed reactor. Chem. Eng. J. 2009; 154: 287-294.

45. Suelves I., Lázaro M.J., Moliner R., Pinilla J.L., Cubero H. Hydrogen production by methane decarbonization: Carbonaceous catalysts. Int. J. Hydrogen Energy 2007; 32: 3320-3326.
46. Li G., Hu L., Hill J.M. Comparison of reducibility and stability of alumina-supported Ni catalysts prepared by impregnation and co-precipitation. Appl. Catal., A 2006; 301: 16-24.
47. Takenaka S., Ogihara H., Yamanaka I., Otsuka K. Decomposition of methane over supported-Ni catalysts: effects of the supports on the catalytic lifetime. Appl. Catal., A 2001; 217: 101-110.
48. Li Y., Zhang B., Tang X., Xu Y., Shen W. Hydrogen production from methane decomposition over Ni/CeO_2 catalysts. Catal. Commun. 2006; 7: 380-386.
49. Guo J., Lou H., Zheng X. The deposition of coke from methane on a $Ni/MgAl_2O_4$ catalyst. Carbon 2007; 45: 1314-1321.
50. McCarty J.G., Hou P Y., Sheridan D., Wise H. Reactivity of Surface Carbon on Nickel Catalysts: Temperature-Programmed Surface Reaction with Hydrogen and Water: 1982, Ch.13. in: Albright, L.F., Baker, R.T.K. (Eds.), Coke Formation on Metal Surfaces: 202. American chemical society, Washington, pp. 253-282.
51. Baker R.T.K., Barber M.A., Harris P.S., Feates F.S., Waite R.J. Nucleation and growth of carbon deposits from the nickel catalyzed decomposition of acetylene. J. Catal. 1972; 26: 51-62.
52. Kock A.J.H.M., de Bokx P.K., Boellaard E., Klop W., Geus J.W. The formation of filamentous carbon on iron and nickel catalysts: II. Mechanism. J. Catal. 1985; 96: 468-480.
53. Boellaard E., de Bokx P.K., Kock A.J.H.M., Geus J.W. The formation of filamentous carbon on iron and nickel catalysts: III. Morphology. J. Catal. 1985; 96: 481-490.
54. Tracz E., Scholz R., Borowiecki T. High-resolution electron microscopy study of the carbon deposit morphology on nickel catalysts. Appl. Catal., A 1990; 66: 133-147.
55. Sacco A., Thacker P., Chang T.N., Chiang A.T.S. The initiation and growth of filamentous carbon from [alpha]-iron in H_2, CH_4, H_2O, CO_2, and CO gas mixtures. J. Catal. 1984; 85: 224-236.
56. Schouten F.C., Kaleveld E.W., Bootsma G.A. AES-LEED-ellipsometry study of the kinetics of the interaction of methane with Ni(110). Surf. Sci. 1977; 63: 460-474.
57. Aiello R., Fiscus J.E., zur Loye H.-C., Amiridis M.D. Hydrogen production via the direct cracking of methane over Ni/SiO2: catalyst deactivation and regeneration. Appl. Catal., A 2000; 192: 227-234.
58. Shah N., Panjala D., Huffman G.P. Hydrogen Production by Catalytic Decomposition of Methane. Energy Fuels 2001; 15: 1528-1534.
59. Toebes M.L., Bitter J.H., van Dillen A.J., de Jong K.P. Impact of the structure and reactivity of nickel particles on the catalytic growth of carbon nanofibers. Catal. Today 2002; 76: 33-42.
60. Trimm D.L. Catalysts for the control of coking during steam reforming. Catal. Today 1999; 49: 3-10.
61. Fogler H.S. Elements of Chemical Reaction Engineering. 3ed. New Jersey: Prentice-Hall 1999.
62. Abbas H.F., Daud W.M.A.W. An experimental investigation into the CO_2 gasification of deactivated activated-carbon catalyst used for methane decomposition to produce hydrogen. Int. J. Hydrogen Energy 2010; 35: 141-150.
63. Bartholomew C.H. Mechanisms of catalyst deactivation. Appl. Catal., A 2001; 212: 17-60.
64. Ishihara T., Miyashita Y., Iseda H., Taketa Y. Decomposition of methane over Ni/SiO_2 catalysts with membrane reactor for the production of hydrogen. Chem. Lett. 1995; 24: 93-94.
65. Suelves I., Lázaro M.J., Moliner R., Corbella B.M., Palacios J.M. Hydrogen production by thermo catalytic decomposition of methane on Ni-based catalysts: influence of operating conditions on catalyst deactivation and carbon characteristics. Int. J. Hydrogen Energy 2005; 30: 1555-1567.
66. Muradov N., Chen Z., Smith F. Fossil hydrogen with reduced CO_2 emission: Modeling thermocatalytic decomposition of methane in a fluidized bed of carbon particles. Int. J. Hydrogen Energy 2005; 30: 1149-1158.
67. Rahman M.S. Catalytic Decomposition of Methane for Hydrogen Production: 2004. Master thesis, University of Waterloo.
68. Koc R., Alper E., Croiset E., Elkamel A. Partial Regeneration of Ni-Based Catalysts for Hydrogen Production via Methane Cracking. Turk. J. Chem. 2008; 32: 157-168.

69. Beebe T.P., Goodman D.W., Kay B.D. Kinetics of the activated dissociative adsorption of methane on the low index planes of nickel single crystal surfaces. J. Chem. Phys. 1987; 87: 2305-2315.
70. Choudhary V.R., Banerjee S., Rajput A.M. Continuous Production of H_2 at Low Temperature from Methane Decomposition over Ni-Containing Catalyst Followed by Gasification by Steam of the Carbon on the Catalyst in Two Parallel Reactors Operated in Cyclic Manner. J. Catal. 2001; 198: 136-141.
71. Pinilla J.L., Suelves I., Utrilla R., Gálvez M.E., Lázaro M.J., Moliner R. Hydrogen production by thermo-catalytic decomposition of methane: Regeneration of active carbons using CO_2. J. Power Sources 2007; 169: 103-109.
72. Takenaka S., Tomikubo Y., Kato E., Otsuka K. Sequential production of H_2 and CO over supported Ni catalysts. Fuel 2004; 83: 47-57.
73. Abbas H.F., Daud W.M.A.W. Thermocatalytic decomposition of methane for hydrogen production using activated carbon catalyst: Regeneration and characterization studies. Int. J. Hydrogen Energy 2009; 34: 8034-8045.
74. Grabke H.J. The kinetics of decarburization and carburization of gamma.-iron in methane-hydrogen mixtures. Physik. Chem 1965; 69: 409-414.
75. Grabke H. Evidence on the surface concentration of carbon on gamma iron from the kinetics of the carburization in CH_4−H_2. Metall. Mater. Trans. B 1970; 1: 2972-2975.
76. Demicheli M.C., Ponzi E.N., Ferretti O.A., Yeramian A.A. Kinetics of carbon formation from CH_4-H_2 mixtures on nickel-alumina catalyst. Chem. Eng. J. 1991; 46: 129-136.
77. Kuvshinov G.G., Mogilnykh Y.I., Kuvshinov D.G. Kinetics of carbon formation from CH_4-H_2 mixtures over a nickel containing catalyst. Catal. Today 1998; 42: 357-360.
78. Zavarukhin S.G., Kuvshinov G.G. The kinetic model of formation of nanofibrous carbon from CH_4-H_2 mixture over a high-loaded nickel catalyst with consideration for the catalyst deactivation. Appl. Catal., A 2004; 272: 219-227.
79. Alstrup I., Tavares T.M. The kinetics of carbon formation from CH_4 + H_2 on a silica-supported nickel catalyst. J. Catal. 1992; 135: 147-155.
80. Hazra M., Croiset E., Hudgins R.R., Silveston P.L., Elkamel A. Experimental investigation of the catalytic cracking of methane over a supported Ni catalyst. Can. J. Chem. Eng. 2009; 87: 99-105.
81. Chen D., Lødeng R., Anundskås A., Olsvik O., Holmen A. Deactivation during carbon dioxide reforming of methane over Ni catalyst: microkinetic analysis. Chem. Eng. Sci. 2001; 56: 1371-1379.
82. Bernardo C.A., Alstrup I., Rostrup-Nielsen J.R. Carbon deposition and methane steam reforming on silica-supported Ni-Cu catalysts. J. Catal. 1985; 96: 517-534.
83. Borghei M., Karimzadeh R., Rashidi A., Izadi N. Kinetics of methane decomposition to COx-free hydrogen and carbon nanofiber over Ni-Cu/MgO catalyst. Int. J. Hydrogen Energy 2010; 35: 9479-9488.
84. Chen Z., Elnashaie S.S.E.H. Steady-state modeling and bifurcation behavior of circulating fluidized bed membrane reformer-regenerator for the production of hydrogen for fuel cells from heptane. Chem. Eng. Sci. 2004; 59: 3965-3979.
85. Steinberg M., Cheng H.C. Modern and prospective technologies for hydrogen production from fossil fuels. Int. J. Hydrogen Energy 1989; 14: 797-820.
86. Weizhong Q., Tang L., Zhanwen W., Fei W., Zhifei L., Guohua L., Yongdan L. Production of hydrogen and carbon nanotubes from methane decomposition in a two-stage fluidized bed reactor. Appl. Catal., A 2004; 260: 223-228.
87. Shah N., Ma S., Wang Y., Huffman G.P. Semi-continuous hydrogen production from catalytic methane decomposition using a fluidized-bed reactor. Int. J. Hydrogen Energy 2007; 32: 3315-3319.
88. Pinilla J.L., Suelves I., Lázaro M.J., Moliner R., Palacios J.M. Parametric study of the decomposition of methane using a $NiCu/Al_2O_3$ catalyst in a fluidized bed reactor. Int. J. Hydrogen Energy 2010; 35: 9801-9809.
89. Geldart D. Gas Fluidization Technology. In: (Ed. Geldart D), Chap. 2, 11-32. New York: John Wiley; 1986.

90. Fluidization. Othmer D., editor. New York: Reinhold Publ., 1956.
91. Richardson JE. Incipient fluidization and particulate systems. In: (Ed. Davidson JF, Harrison D). Fluidization. London: Academic Press; 1971. p. 25–64.
92. Yang W.C. Fluidization, Solids Handling, and Processing - Industrial Applications. New Jersey: William Andrew Publishing/Noyes; 1998.
93. Sangeetha V., Swathy R., Narayanamurthy N., Lakshmanan C.M., Miranda L.R. Minimum Fluidization Velocity At High Temperatures Based on Geldart Powder Classification. Chem. Eng. Technol. 2000; 23: 713-719.
94. Pinilla J.L., Moliner R., Suelves I., Lázaro M.J., Echegoyen Y., Palacios J.M. Production of hydrogen and carbon nanofibers by thermal decomposition of methane using metal catalysts in a fluidized bed reactor. Int. J. Hydrogen Energy 2007; 32: 4821-4829.
95. Cheremisinoff N.P., Cheremisionoff P.N. Hydrodynamics of gas-solid fluidization. Houston: Gulf publishing; 1984.
96. Kunii D., Levenspiel O. Fluidization engineering. 2ed. Boston: Butterworth-Heinemann; 1991.
97. Pattipati R.R., Wen C.Y. Minimum fluidization velocity at high temperatures. Industrial & Engineering Chemistry Process Design and Development 1981; 20: 705-707.
98. Gibilaro L.G., Di Felice R., Waldram S.P., Foscolo P.U. Generalized friction factor and drag coefficient correlations for fluid-particle interactions. Chem. Eng. Sci. 1985; 40: 1817-1823.
99. El-Halwagi M.M., El-Rifai M.A. Mathematical modeling of catalytic fluidized-bed reactors--I. The multistage three-phase model. Chem. Eng. Sci. 1988; 43: 2477-2486.
100. Jafari R., Sotudeh-Gharebagh R., Mostoufi N. Modular Simulation of Fluidized Bed Reactors. Chem. Eng. Technol. 2004; 27: 123-129.
101. Grace J.R. Contacting modes and behaviour classification of gas-solid and other two-phase suspensions. Can. J. Chem. Eng. 1986; 64: 353-363.
102. Gungor A., Eskin N. Hydrodynamic modeling of a circulating fluidized bed. Powder Technol. 2007; 172: 1-13.
103. Amin, A.M., E. Croiset, and W. Epling, Review of methane catalytic cracking for hydrogen production. International Journal of Hydrogen Energy, 2011. 36(4): p. 2904-2935.

References (Chapter 3):

1. ABS-energy-research, The hydrogen economy and fuel cells Ed1. 2006.
2. Amin, A.M., E. Croiset, and W. Epling, Review of methane catalytic cracking for hydrogen production. International Journal of Hydrogen Energy, 2011. 36(4): p. 2904-2935.
3. Abbas, H.F. and W.M.A. Wan Daud, Hydrogen production by methane decomposition: A review. International Journal of Hydrogen Energy, 2010. 35(3): p. 1160-1190.
4. Echegoyen, Y., I. Suelves, M.J. Lázaro, R. Moliner, and J.M. Palacios, Hydrogen production by thermocatalytic decomposition of methane over Ni-Al and Ni-Cu-Al catalysts: Effect of calcination temperature. Journal of Power Sources, 2007. 169(1): p. 150-157.
5. Aiello, R., J.E. Fiscus, H.-C. zur Loye, and M.D. Amiridis, Hydrogen production via the direct cracking of methane over Ni/SiO2: catalyst deactivation and regeneration. Applied Catalysis A: General, 2000. 192(2): p. 227-234.
6. Takenaka, S., H. Ogihara, I. Yamanaka, and K. Otsuka, Decomposition of methane over supported-Ni catalysts: effects of the supports on the catalytic lifetime. Applied Catalysis A: General, 2001. 217(1-2): p. 101-110.
7. Hazra, M., E. Croiset, R.R. Hudgins, P.L. Silveston, and A. Elkamel, Experimental investigation of the catalytic cracking of methane over a supported Ni catalyst. The Canadian Journal of Chemical Engineering, 2009. 87(1): p. 99-105.
8. Kermode, R.I., Chapter 3, in Hydrogen: its technology and implications: Vol. 1, Production Technology, W.K.D. Cox K.E., Editor. 1977, CRC Press: Cleveland. p. 61-115.
9. Suelves, I., M.J. Lázaro, R. Moliner, B.M. Corbella, and J.M. Palacios, Hydrogen production by thermo catalytic decomposition of methane on Ni-based catalysts: influence of operating conditions on catalyst deactivation and carbon characteristics. International Journal of Hydrogen Energy, 2005. 30(15): p. 1555-1567.
10. González, I., J.C. De Jesus, C.U. de Navarro, and M. García, Effect of Cu on Ni nanoparticles used for the generation of carbon nanotubes by catalytic cracking of methane. Catalysis Today, 2010. 149(3-4): p. 352-357.
11. De Jesus, J.C., I. Gonzalez, M. Garcia, and C. Urbina, Preparation of nickel nanoparticles and their catalytic activity in the cracking of methane. Journal of Vacuum Science & Technology A: Vacuum, Surfaces, and Films, 2008. 26(4): p. 913-918.
12. Venugopal, A., et al., Hydrogen production by catalytic decomposition of methane over Ni/SiO2. International Journal of Hydrogen Energy, 2007. 32(12): p. 1782-1788.
13. Guo, J., H. Lou, and X. Zheng, The deposition of coke from methane on a Ni/MgAl2O4 catalyst. Carbon, 2007. 45(6): p. 1314-1321.
14. Ermakova, M.A., D.Y. Ermakov, and G.G. Kuvshinov, Effective catalysts for direct cracking of methane to produce hydrogen and filamentous carbon: Part I. Nickel catalysts. Applied Catalysis A: General, 2000. 201(1): p. 61-70.
15. Ermakova, M.A. and D.Y. Ermakov, Ni/SiO2 and Fe/SiO2 catalysts for production of hydrogen and filamentous carbon via methane decomposition. Catalysis Today, 2002. 77(3): p. 225-235.
16. Takenaka, S., Y. Tomikubo, E. Kato, and K. Otsuka, Sequential production of H2 and CO over supported Ni catalysts. Fuel, 2004. 83(1): p. 47-57.

17. Otsuka, K., S. Takenaka, and H. Ohtsuki, Production of pure hydrogen by cyclic decomposition of methane and oxidative elimination of carbon nanofibers on supported-Ni-based catalysts. Applied Catalysis A: General, 2004. 273(1-2): p. 113-124.
18. Koc R., Alper E., Croiset E., and Elkamel A., Partial Regeneration of Ni-Based Catalysts for Hydrogen Production via Methane Cracking. Turkish Journal of Chemistry, 2008. 32: p. 157-168.
19. Rahman, M., E. Croiset, and R. Hudgins, Catalytic Decomposition of Methane for Hydrogen Production. Topics in Catalysis, 2006. 37(2): p. 137-145.
20. Villacampa, J.I., et al., Catalytic decomposition of methane over Ni-Al2O3 coprecipitated catalysts: Reaction and regeneration studies. Applied Catalysis A: General, 2003. 252(2): p. 363-383.
21. Muradov, N.Z. and T.N. Veziroglu, From hydrocarbon to hydrogen-carbon to hydrogen economy. International Journal of Hydrogen Energy, 2005. 30(3): p. 225-237.
22. Pinilla, J.L., et al., Production of hydrogen and carbon nanofibers by thermal decomposition of methane using metal catalysts in a fluidized bed reactor. International Journal of Hydrogen Energy, 2007. 32(18): p. 4821-4829.
23. Hardiman, K.M., C.-H. Hsu, T.T. Ying, and A.A. Adesina, The influence of impregnating pH on the postnatal and steam reforming characteristics of a Co-Ni/Al2O3 catalyst. Journal of Molecular Catalysis A: Chemical, 2005. 239(1-2): p. 41-48.
24. Zhang, T. and M.D. Amiridis, Hydrogen production via the direct cracking of methane over silica-supported nickel catalysts. Applied Catalysis A: General, 1998. 167(2): p. 161-172.
25. Li, Y., et al., Novel Ni catalysts for methane decomposition to hydrogen and carbon nanofibers. Journal of Catalysis, 2006. 238(2): p. 412-424.
26. Guevara, J.C., et al., Ni/Ce-MCM-41 mesostructured catalysts for simultaneous production of hydrogen and nanocarbon via methane decomposition. International Journal of Hydrogen Energy, 2010. 35(8): p. 3509-3521.

References (Chapter 4):

1. Abbas, H.F. and W.M.A.W. Daud, Hydrogen production by thermocatalytic decomposition of methane using a fixed bed activated carbon in a pilot scale unit: Apparent kinetic, deactivation and diffusional limitation studies. International Journal of Hydrogen Energy, 2010. **35**(22): p. 12268-12276.
2. Muradov, N. Thermo-catalytic CO_2-free production of hydrogen from hydrocarbon fuels. in DOE hydrogen program review. 2001. The National Renewable Energy Laboratory for the U.S. Department of Energy, Baltimore, Maryland, USA.
3. Pinilla, J.L., I. Suelves, M.J. Lázaro, R. Moliner, and J.M. Palacios, Parametric study of the decomposition of methane using a NiCu/Al2O3 catalyst in a fluidized bed reactor. International Journal of Hydrogen Energy, 2010. **35**(18): p. 9801-9809.
4. Hazra, M., E. Croiset, R.R. Hudgins, P.L. Silveston, and A. Elkamel, Experimental investigation of the catalytic cracking of methane over a supported Ni catalyst. The Canadian Journal of Chemical Engineering, 2009. **87**(1): p. 99-105.
5. Rahman, M., E. Croiset, and R. Hudgins, Catalytic Decomposition of Methane for Hydrogen Production. Topics in Catalysis, 2006. **37**(2): p. 137-145.
6. Muradov, N.Z. and T.N. Veziroglu, From hydrocarbon to hydrogen-carbon to hydrogen economy. International Journal of Hydrogen Energy, 2005. **30**(3): p. 225-237.
7. Ermakova, M.A., D.Y. Ermakov, and G.G. Kuvshinov, Effective catalysts for direct cracking of methane to produce hydrogen and filamentous carbon: Part I. Nickel catalysts. Applied Catalysis A: General, 2000. **201**(1): p. 61-70.
8. Ermakova, M.A. and D.Y. Ermakov, Ni/SiO2 and Fe/SiO2 catalysts for production of hydrogen and filamentous carbon via methane decomposition. Catalysis Today, 2002. **77**(3): p. 225-235.
9. Takenaka, S., H. Ogihara, I. Yamanaka, and K. Otsuka, Decomposition of methane over supported-Ni catalysts: effects of the supports on the catalytic lifetime. Applied Catalysis A: General, 2001. **217**(1-2): p. 101-110.
10. Guo, J., H. Lou, and X. Zheng, The deposition of coke from methane on a Ni/MgAl2O4 catalyst. Carbon, 2007. **45**(6): p. 1314-1321.
11. Grabke, H., Evidence on the surface concentration of carbon on gamma iron from the kinetics of the carburization in CH₄−H<sub>2</sub&gt. Metallurgical and Materials Transactions B, 1970. **1**(10): p. 2972-2975.
12. Grabke, H., The kinetics of decarburization and carburization of gamma-iron in methane-hydrogen mixtures. Physik. Chim., 1965. **69**(5): p. 14.
13. Borghei, M., R. Karimzadeh, A. Rashidi, and N. Izadi, Kinetics of methane decomposition to COx-free hydrogen and carbon nanofiber over Ni-Cu/MgO catalyst. International Journal of Hydrogen Energy, 2010. **35**(17): p. 9479-9488.
14. Zavarukhin, S.G. and G.G. Kuvshinov, The kinetic model of formation of nanofibrous carbon from CH4-H2 mixture over a high-loaded nickel catalyst with consideration for the catalyst deactivation. Applied Catalysis A: General, 2004. **272**(1-2): p. 219-227.
15. Demicheli, M.C., E.N. Ponzi, O.A. Ferretti, and A.A. Yeramian, Kinetics of carbon formation from CH4-H2 mixtures on nickel-alumina catalyst. The Chemical Engineering Journal, 1991. **46**(3): p. 129-136.
16. Alstrup, I. and M.T. Tavares, Kinetics of Carbon Formation from CH4 + H2 on Silica-Supported Nickel and Ni-Cu Catalysts. Journal of Catalysis, 1993. **139**(2): p. 513-524.
17. Kuvshinov, G.G., Y.I. Mogilnykh, and D.G. Kuvshinov, Kinetics of carbon formation from CH4-H2 mixtures over a nickel containing catalyst. Catalysis Today, 1998. **42**(3): p. 357-360.
18. Chen, D., R. Lødeng, A. Anundskås, O. Olsvik, and A. Holmen, Deactivation during carbon dioxide reforming of methane over Ni catalyst: microkinetic analysis. Chemical Engineering Science, 2001. **56**(4): p. 1371-1379.

19. Fogler, H.S., Elements of Chemical Reaction Engineering. Third ed. 2002, New Jersey: Prentice Hall International Series.
20. Butt, J.B. and E.E. Petersen, Activation, Deactivation, and poisoning of Catalysts. 1988, San Diego: Academic Press.
21. Snoeck, J.W., G.F. Froment, and M. Fowles, Kinetic Study of the Carbon Filament Formation by Methane Cracking on a Nickel Catalyst. Journal of Catalysis, 1997. **169**(1): p. 250-262.
22. Lee, M.B., Q.Y. Yang, S.L. Tang, and S.T. Ceyer, Activated dissociative chemisorption of CH[sub 4] on Ni(111): Observation of a methyl radical and implication for the pressure gap in catalysis. The Journal of Chemical Physics, 1986. **85**(3): p. 1693-1694.
23. Hamza, A.V. and R.J. Madix, The activation of alkanes on Ni(100). Surface Science, 1987. **179**(1): p. 25-46.
24. Englezos, P. and N. Kalogerakis, Applied Parameter Estimation For Chemical Engineers. 2001, New York: Marcel Dekker.
25. Montgomery, D.C. and G.C. Runger, Applied Statistics and Probability for Engineers. 3rd ed. 2003, New York: John Wiley & Sons.
26. Gilliland, E.R. and P. Harriott, Reactivity of Deposited Carbon. Industrial & Engineering Chemistry, 1954. **46**(10): p. 2195-2202.
27. Chesnokov, V.V., V.I. Zaikovskii, R.A. Buyanov, V.V. Molchanov, and L.M. Plyasova, Formation of Carbon Morphological Structures from Hydrocarbons over Nickel Containing Catalysts. Kinet. & Catal., 1994. **35**(1): p. 6.
28. Bartholomew, C.H., Hydrogen adsorption on supported cobalt, iron, and nickel. Catalysis Letters, 1990. **7**(1): p. 27-51.
29. Germer, L.H. and A.U. MacRae, Adsorption of Hydrogen on a (110) Nickel Surface. The Journal of Chemical Physics, 1962. **37**(7): p. 1382-1386.
30. Beebe, J.T.P., D.W. Goodman, B.D. Kay, and J.J.T. Yates, Kinetics of the activated dissociative adsorption of methane on the low index planes of nickel single crystal surfaces. The Journal of Chemical Physics, 1987. **87**(4): p. 2305-2315.
31. Schouten, F.C., E.W. Kaleveld, and G.A. Bootsma, AES-LEED-ellipsometry study of the kinetics of the interaction of methane with Ni(110). Surface Science, 1977. **63**: p. 460-474.
32. Villacampa, J.I., et al., Catalytic decomposition of methane over Ni-Al2O3 coprecipitated catalysts: Reaction and regeneration studies. Applied Catalysis A: General, 2003. **252**(2): p. 363-383.

References (Chapter 5):

1. Abbas, H.F. and W.M.A. Wan Daud, Hydrogen production by methane decomposition: A review. International Journal of Hydrogen Energy, 2010. **35**(3): p. 1160-1190.
2. Muradov, N.Z. and T.N. Veziroglu, From hydrocarbon to hydrogen-carbon to hydrogen economy. International Journal of Hydrogen Energy, 2005. **30**(3): p. 225-237.
3. Muradov, N.Z. and T.N. Veziroglu, "Green" path from fossil-based to hydrogen economy: An overview of carbon-neutral technologies. International Journal of Hydrogen Energy, 2008. **33**(23): p. 6804-6839.
4. Suelves, I., M.J. Lázaro, R. Moliner, B.M. Corbella, and J.M. Palacios, Hydrogen production by thermo catalytic decomposition of methane on Ni-based catalysts: influence of operating conditions on catalyst deactivation and carbon characteristics. International Journal of Hydrogen Energy, 2005. **30**(15): p. 1555-1567.
5. Muradov, N.Z., How to produce hydrogen from fossil fuels without CO2 emission. International Journal of Hydrogen Energy, 1993. **18**(3): p. 211-215.
6. Villacampa, J.I., et al., Catalytic decomposition of methane over Ni-Al2O3 coprecipitated catalysts: Reaction and regeneration studies. Applied Catalysis A: General, 2003. **252**(2): p. 363-383.
7. Rahman, M., E. Croiset, and R. Hudgins, Catalytic Decomposition of Methane for Hydrogen Production. Topics in Catalysis, 2006. **37**(2): p. 137-145.
8. Guo, J., H. Lou, and X. Zheng, The deposition of coke from methane on a Ni/MgAl2O4 catalyst. Carbon, 2007. **45**(6): p. 1314-1321.
9. Muradov, N., Z. Chen, and F. Smith, Fossil hydrogen with reduced CO2 emission: Modeling thermocatalytic decomposition of methane in a fluidized bed of carbon particles. International Journal of Hydrogen Energy, 2005. **30**(10): p. 1149-1158.
10. Muradov, N. Thermo-catalytic CO_2-free production of hydrogen from hydrocarbon fuels. in DOE hydrogen program review. 2001. The National Renewable Energy Laboratory for the U.S. Department of Energy, Baltimore, Maryland, USA.
11. Lee, K.K., G.Y. Han, K.J. Yoon, and B.K. Lee, Thermocatalytic hydrogen production from the methane in a fluidized bed with activated carbon catalyst. Catalysis Today, 2004. **93-95**: p. 81-86.
12. Murata, K., M. Inaba, M. Miki, and T. Yamaguchi, Formation of filamentous carbon and hydrogen by methane decomposition over supported Ni catalysts. Reaction Kinetics and Catalysis Letters, 2005. **85**(1): p. 21-28.
13. Rivas, M.E., C.E. Hori, J.L.G. Fierro, M.R. Goldwasser, and A. Griboval-Constant, H2 production from CH4 decomposition: Regeneration capability and performance of nickel and rhodium oxide catalysts. Journal of Power Sources, 2008. **184**(1): p. 265-275.
14. Qian, W., T. Liu, F. Wei, Z. Wang, and Y. Li, Enhanced production of carbon nanotubes: combination of catalyst reduction and methane decomposition. Applied Catalysis A: General, 2004. **258**(1): p. 121-124.
15. Pinilla, J.L., et al., Production of hydrogen and carbon nanofibers by thermal decomposition of methane using metal catalysts in a fluidized bed reactor. International Journal of Hydrogen Energy, 2007. **32**(18): p. 4821-4829.
16. Pinilla, J.L., I. Suelves, M.J. Lázaro, R. Moliner, and J.M. Palacios, Parametric study of the decomposition of methane using a NiCu/Al2O3 catalyst in a fluidized bed reactor. International Journal of Hydrogen Energy, 2010. **35**(18): p. 9801-9809.
17. Sarada Prasad, J., Dhand V., and H. Y.A., Methane cracking over commercial carbons for hydogen production. International Journal of Energy and Environment, 2010. **1**(4): p. 607-616.
18. Dunker, A.M., S. Kumar, and P.A. Mulawa, Production of hydrogen by thermal decomposition of methane in a fluidized-bed reactor--Effects of catalyst, temperature, and residence time. International Journal of Hydrogen Energy, 2006. **31**(4): p. 473-484.

19. Chen, J., M. He, G. Wang, Y. Li, and Z.J. Zhu, Production of hydrogen from methane decomposition using nanosized carbon black as catalyst in a fluidized-bed reactor. International Journal of Hydrogen Energy, 2009. **34**(24): p. 9730-9736.
20. Lazaro, M.J., et al., H_2 - CH4 Mixtures Produced by Carbon-Catalyzed Methane Decomposition as a Fuel for Internal Combustion Enginesâ€ Energy & Fuels, 2010. **24**(6): p. 3340-3345.
21. Italiano, G., A. Delia, C. Espro, G. Bonura, and F. Frusteri, Methane decomposition over Co thin layer supported catalysts to produce hydrogen for fuel cell. International Journal of Hydrogen Energy, 2010. **35**(20): p. 11568-11575.
22. Ammendola, P., R. Chirone, G. Ruoppolo, and G. Russo. Regenration of Deactivated Catalysts for TCD Process by Carbon Oxidation in a Fludized bed Reactor. in Third European Combustion meeting ECM 2007. 2007. Mediterranean Agronomic Institute of Chania, Crete, Greece.
23. Ammendola, P., R. Chirone, G. Ruoppolo, and G. Russo. Zero emissions hyrogen production by fludiized bed catalytic decomposition of methane. in The 20th International Conference on Fludized Bed Combustion. 2010. Tsinghua University, Beijing: Springer and Tsinghua Unniversity.
24. Jang, H.T. and W.S. Cha, Hydrogen production by the thermocatalytic decomposition of methane in a fluidized bed reactor. Korean Journal of Chemical Engineering, 2007. **24**(2): p. 374-377.
25. Shah, N., S. Ma, Y. Wang, and G.P. Huffman, Semi-continuous hydrogen production from catalytic methane decomposition using a fluidized-bed reactor. International Journal of Hydrogen Energy, 2007. **32**(15): p. 3315-3319.
26. Bonura, G., O. Di Blasi, L. Spadaro, F. Arena, and F. Frusteri, A basic assessment of the reactivity of Ni catalysts in the decomposition of methane for the production of "COx-free" hydrogen for fuel cells application. Catalysis Today, 2006. **116**(3): p. 298-303.
27. Borghei, M., R. Karimzadeh, A. Rashidi, and N. Izadi, Kinetics of methane decomposition to COx-free hydrogen and carbon nanofiber over Ni-Cu/MgO catalyst. International Journal of Hydrogen Energy, 2010. **35**(17): p. 9479-9488.
28. Ermakova, M.A., D.Y. Ermakov, and G.G. Kuvshinov, Effective catalysts for direct cracking of methane to produce hydrogen and filamentous carbon: Part I. Nickel catalysts. Applied Catalysis A: General, 2000. **201**(1): p. 61-70.
29. Ermakova, M.A. and D.Y. Ermakov, Ni/SiO2 and Fe/SiO2 catalysts for production of hydrogen and filamentous carbon via methane decomposition. Catalysis Today, 2002. **77**(3): p. 225-235.
30. Ammendola, P., R. Chirone, G. Ruoppolo, and G. Russo, Production of hydrogen from thermo-catalytic decomposition of methane in a fluidized bed reactor. Chemical Engineering Journal, 2009. **154**(1-3): p. 287-294.
31. Takenaka, S., H. Ogihara, I. Yamanaka, and K. Otsuka, Decomposition of methane over supported-Ni catalysts: effects of the supports on the catalytic lifetime. Applied Catalysis A: General, 2001. **217**(1-2): p. 101-110.
32. Spiess, F.-J., S.L. Suib, K. Irie, Y. Hayashi, and H. Matsumoto, Metal effect and flow rate effect in the hydrogen production from methane. Catalysis Today, 2004. **89**(1-2): p. 35-45.
33. Li, Y., et al., Novel Ni catalysts for methane decomposition to hydrogen and carbon nanofibers. Journal of Catalysis, 2006. **238**(2): p. 412-424.
34. Ashok, J., S. Naveen Kumar, A. Venugopal, V. Durga Kumari, and M. Subrahmanyam, COX-free H2 production via catalytic decomposition of CH4 over Ni supported on zeolite catalysts. Journal of Power Sources, 2007. **164**(2): p. 809-814.
35. Wen, C.Y. and Y.H. Yu, A generalized method for predicting the minimum fluidization velocity. AIChE Journal, 1966. **12**(3): p. 610-612.
36. Montgomery, D.C. and G.C. Runger, Applied Statistics and Probability for Engineers. 3rd ed. 2003, New York: John Wiley & Sons.
37. Box, G.E.P., J.S. Hunter, and W.G. Hunter, Statistics for Experimenters Design, Innovation, and Discovery. 2nd ed. 2005, New Jersey: John Wiley & Sons.

References (Chapter 6):

1. Muradov, N.Z. and T.N. Veziroglu, "Green" path from fossil-based to hydrogen economy: An overview of carbon-neutral technologies. International Journal of Hydrogen Energy, 2008. **33**(23): p. 6804-6839.
2. Amin, A.M., E. Croiset, and W. Epling, Review of methane catalytic cracking for hydrogen production. International Journal of Hydrogen Energy, 2011. **36**(4): p. 2904-2935.
3. Abbas, H.F. and W.M.A. Wan Daud, Hydrogen production by methane decomposition: A review. International Journal of Hydrogen Energy, 2010. **35**(3): p. 1160-1190.
4. ABS-energy-research, The hydrogen economy and fuel cells Ed1. 2006.
5. Otsuka, K., S. Takenaka, and H. Ohtsuki, Production of pure hydrogen by cyclic decomposition of methane and oxidative elimination of carbon nanofibers on supported-Ni-based catalysts. Applied Catalysis A: General, 2004. **273**(1-2): p. 113-124.
6. Muradov, N. Thermo-catalytic CO_2-free production of hydrogen from hydrocarbon fuels. in DOE hydrogen program review. 2001. The National Renewable Energy Laboratory for the U.S. Department of Energy, Baltimore, Maryland, USA.
7. Muradov, N.Z., How to produce hydrogen from fossil fuels without CO2 emission. International Journal of Hydrogen Energy, 1993. **18**(3): p. 211-215.
8. Snoeck, J.W., G.F. Froment, and M. Fowles, Kinetic Study of the Carbon Filament Formation by Methane Cracking on a Nickel Catalyst. Journal of Catalysis, 1997. **169**(1): p. 250-262.
9. Muradov, N., Z. Chen, and F. Smith, Fossil hydrogen with reduced CO2 emission: Modeling thermocatalytic decomposition of methane in a fluidized bed of carbon particles. International Journal of Hydrogen Energy, 2005. **30**(10): p. 1149-1158.
10. Aiello, R., et al., Hydrogen production via the direct cracking of methane over Ni/SiO2: catalyst deactivation and regeneration. Applied Catalysis A: General, 2000. **192**(2): p. 227-234.
11. Lee, M.B., et al., Activated dissociative chemisorption of CH4 on Ni(111): Observation of a methyl radical and implication for the pressure gap in catalysis. The Journal of Chemical Physics, 1986. **85**(3): p. 1693-1694.
12. Pohlenz, J.B., Scott, Norman H., Method for hydrogen production by catalytic decomposition of a gaseous hydrocarbon stream. 1966, UNIVERSAL OIL PROD CO: United States.
13. Kermode, R.I., Chapter 3, in Hydrogen: its technology and implications: Vol. 1, Production Technology, W.K.D. Cox K.E., Editor. 1977, CRC Press: Cleveland. p. 61-115.
14. Gungor, A. and N. Eskin, Hydrodynamic modeling of a circulating fluidized bed. Powder Technology, 2007. **172**(1): p. 1-13.
15. El-Halwagi, M.M. and M.A. El-Rifai, Mathematical modeling of catalytic fluidized-bed reactors--I. The multistage three-phase model. Chemical Engineering Science, 1988. **43**(9): p. 2477-2486.
16. Kunii, D. and O. Levenspiel, Fluidization engineering. 2 ed. 1991, Boston: Butterworth.
17. Cheremisinoff, N.P. and P.N. Cheremisionoff, Hydrodynamic of gas-solid fluidization. 1984, Houston: Gulf puplishing.
18. Geldart, D., Gas Fluidization Technology. 1986, New York: John Wiley.
19. Doraiswamy, L.K. and M.M. Sharma, Heterogeneous Reactions: Analysis, Examples, and Reactor Design. Vol. 1. 1984, New York: John Wiley and Sons.

20. Singh, R.K. and G.K. Roy, Prediction of minimum bubbling velocity, fluidization index and range of particulate fluidization for gas-solid fluidization in cylindrical and non-cylindrical beds. Powder Technology, 2005. **159**(3): p. 168-172.
21. Lee, G.S. and S.D. Kim, Bed expansion characteristics and transition velocity in turbulent fluidized beds. Powder Technology, 1990. **62**(3): p. 207-215.
22. Fogler, H.S., Elements of Chemical Reaction Engineering. Third ed. 2002, New Jersey: Prentice Hall International Series.
23. Brodkey, R.S. and H.C. Hershey, Transport phenomena A unified apparoach. 1988, New York: McGraw-Hill.
24. Fryer, C. and O.E. Potter, Experimental investigation of models for fluidized bed catalytic reactors. AIChE Journal, 1976. **22**(1): p. 38-47.
25. Jafari, R., R. Sotudeh-Gharebagh, and N. Mostoufi, Modular Simulation of Fluidized Bed Reactors. Chemical Engineering & Technology, 2004. **27**(2): p. 123-129.

Appendix A: Propagation of Uncertainty

In this experimental work, different measurements have been conducted to evaluate the catalyst performance for methane cracking. To verify the experimental finding, the uncertainty associated with the work is studied to estimate the effect of measurements uncertainty on the actual experimental results. In this appendix, a detailed uncertainty analysis is performed.

The rules for estimating the standard deviation and the error are

The standard deviation: $s = \sqrt{\frac{\sum_{i=1}^{n}(x_i - \bar{x})^2}{n-1}}$

Where x_i is the result of the ith measurement and $\bar{x}$ is is the arithmetic mean of an experiment repeated n times.

Or $\sigma = \sqrt{\frac{\sum_{i=1}^{n}(x_i - \bar{x})^2}{N-1}}$

When measured for a pool of different experiments repeated N times.

The variance: $v = s^2$

The standard error or uncertainty: $u = \frac{s}{\sqrt{n}}$

The rules used for estimating the uncertainty are

Summation and subtraction:

$$u(A+B) = u(A-B) = \sqrt{u(A)^2 + u(B)^2}$$

Multiplication:

$$u(A.B) = \sqrt{(B)^2.u(A)^2 + (A)^2.u(B)^2}$$

Division:

$$u(A/B) = \sqrt{(A/B^2)^2.u(B)^2 + (1/B)^2.u(A)^2}$$

Fractional uncertainty:

$$u(A.B) = \sqrt{(u(B)/B)^2 + (u(A)/A)^2}$$

Where A and B are the measured values while $u(A)$ and $u(B)$ are the uncertainties in measurements.

For the experimental work in the thermo balance

Uncertainty in the bench balance

The typical weight for the catalyst is 10 mg. the balance response using standard 10 mg weight is given in Table A.1:

Table A.1: Balance measurement

Weight, mg	Deviation, mg
10.2	0.2
9.9	0.1
10.1	0.1

The balance weight is measured with the following uncertainty:

10±0.1 mg

Uncertainty in the mass flow controller

The typical feed for the thermo balance was 120 ml/min of methane, the uncertainty associated with the measurement is calculated below:

Table A.2: Flow rate

Flow rate, ml/min	Deviation, ml/min
122	1
118	2
117	1

The mass flow controller effect on the uncertainty is:1 ml/min

And the inlet flow rate is:

120 ±1.68 ml/min

Uncertainty in the nickel loading

The catalyst used throughout this study is: 10%Ni/αAl_2O_3 and 10%Ni/γAl_2O_3. ICP check for the catalyst is performed and the result of the nickel loading is given in Table A.3:

A.3: Nickel loading

Catalyst	Nickel loading
10%Ni/γAl_2O_3	10±0.04
10%Ni/αAl_2O_3	10±0.2

Uncertainty in the thermo balance measurement

Repeated experiments were conducted to check the uncertainty in the thermo balance measurements, the amount of carbon formation rate is used as indication for the error as shown in Table A.4. The condition of the experiment is the typical experimental condition: 550ºC, 725 µm, and 120 ml/min.

A.4: Carbon formation rate

Catalyst	Carbon formation rate gC/gNi/min
10%Ni/γAl_2O_3	0.52±0.01
10%Ni/αAl_2O_3	0.62±0.01

Using the fractional uncertainty rule, the total uncertainty can be calculated:

$$u(Overall) = \sqrt{\left(\frac{u(Weight)}{Weight}\right)^2 + \left(\frac{u(Flow)}{Flow}\right)^2 + \left(\frac{u(Ni)}{Ni}\right)^2 + \left(\frac{u(TB)}{TB}\right)^2}$$

For 10%Ni/γAl_2O_3:

The total uncertainty is: 2.8%

For 10%Ni/αAl_2O_3:

The total uncertainty is: 3.2%

Representing the total uncertainty in the thermo balance results

The following Figures were selected to represent the effect of the uncertainty range of the thermo balance results, the dashed lines represent the uncertainty range:

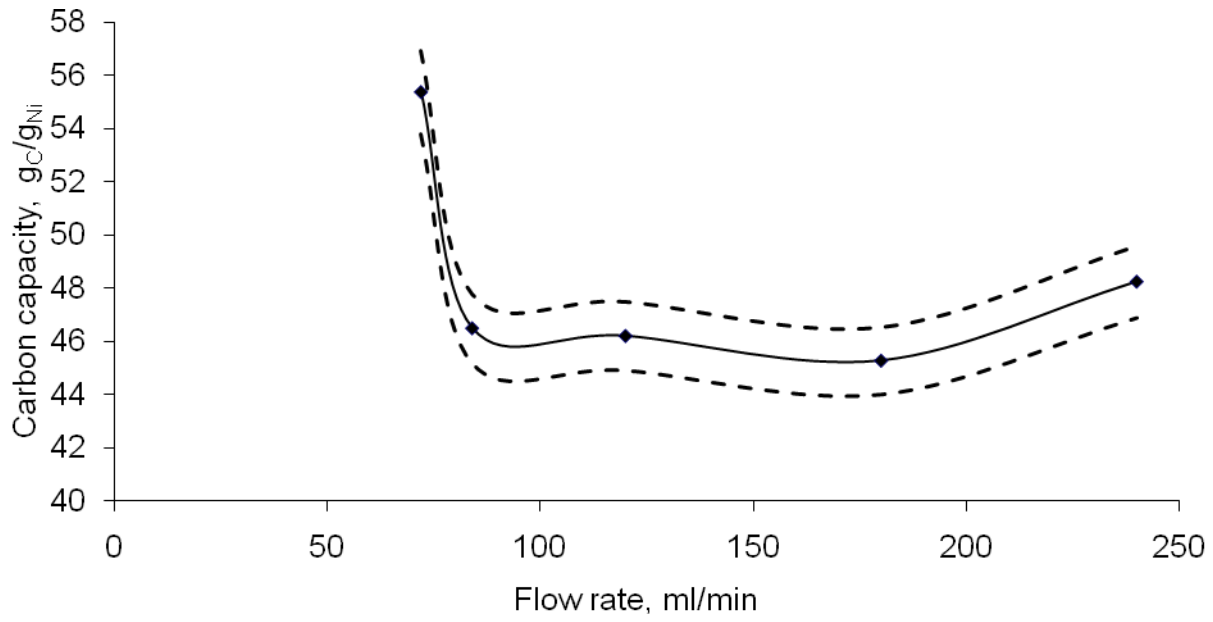

Figure A1: Effect of flow rate on the carbon capacity of $Ni/\gamma Al_2O_3$, at 550ºC, 120 ml/min, and 100% methane

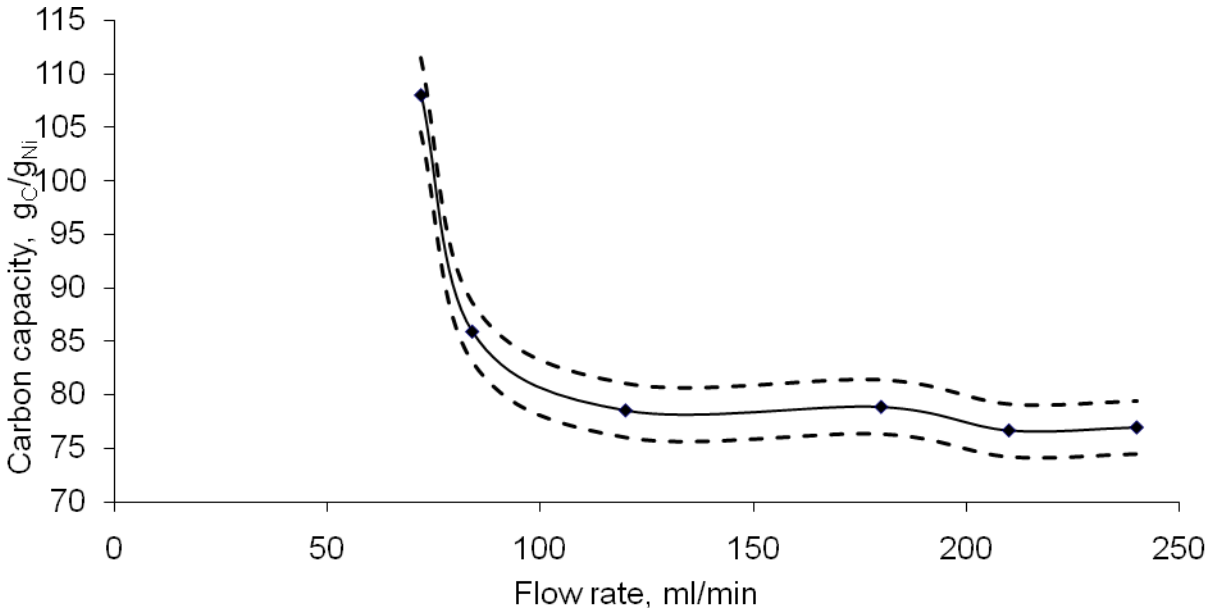

Figure A2: Effect of flow rate on the carbon capacity of $Ni/\alpha Al_2O_3$, at 550ºC, 120 ml/min, and 100% methane

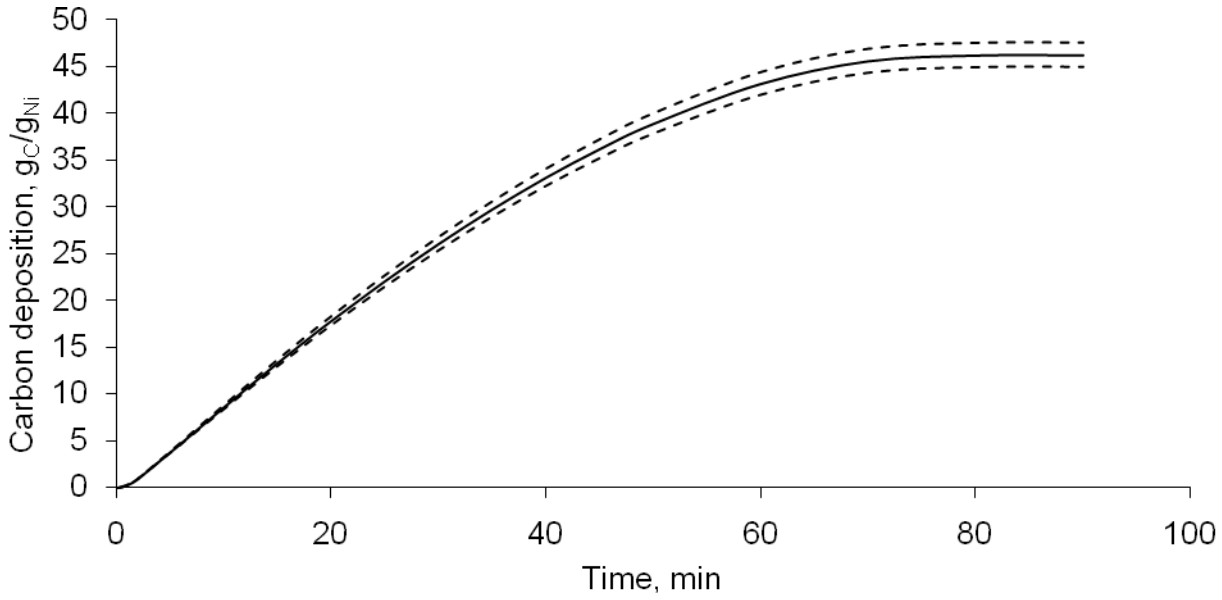

Figure A3: Carbon deposition of Ni/γAl_2O_3, at 550ºC, 120 ml/min, and 100% methane

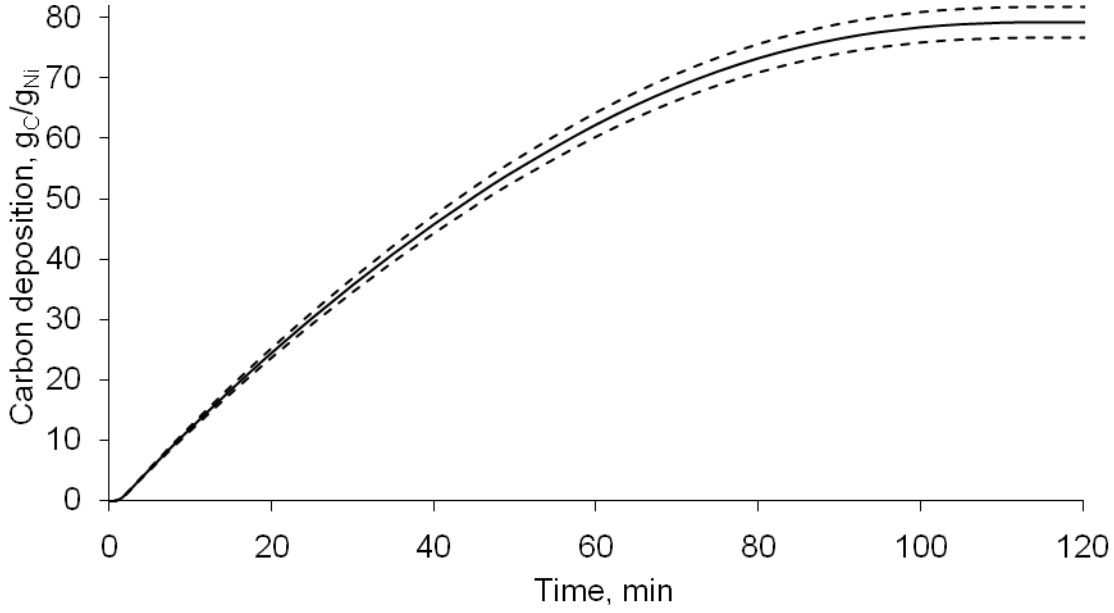

Figure A4: Carbon deposition of Ni/αAl_2O_3, at 550ºC, 120 ml/min, and 100% methane

The uncertainty of the initial rate determination

To determine an initial rate for any experiment, the raw data from the thermo balance need to be smoothed. The raw data was very noisy and even a trend can't be concluded from the data in its original form. An example of the raw data before and after smoothing is illustrated in Figure 5A for Ni/αAl_2O_3, at 550ºC, 120 ml/min, and 100% methane. The raw data is smoothed using the software – WinTga Cahn TG systems. The uncertainty in the initial rate after smoothing is shown in Table A.5

A.5: Uncertainty associated with the initial rate

Catalyst	Carbon formation rate gC/gNi/min
10%Ni/γAl_2O_3	2.1%
10%Ni/αAl_2O_3	1.3%

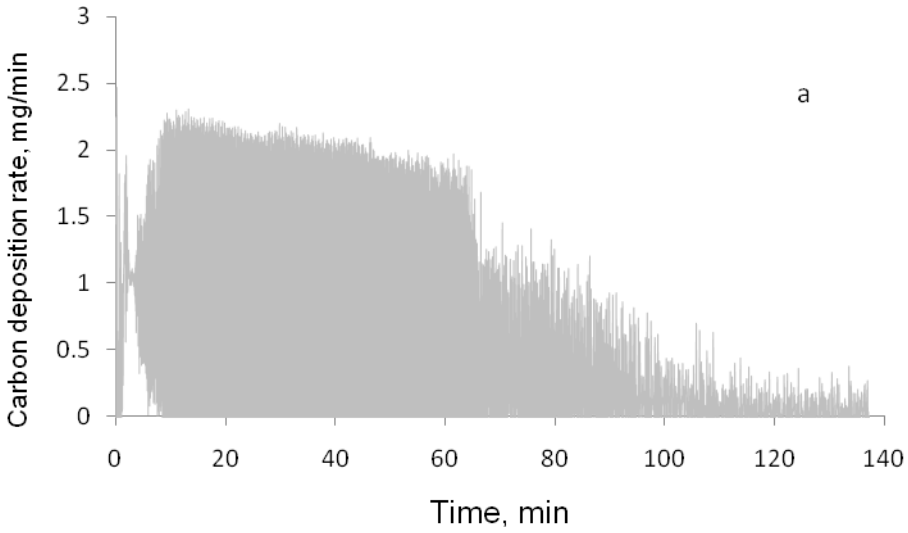

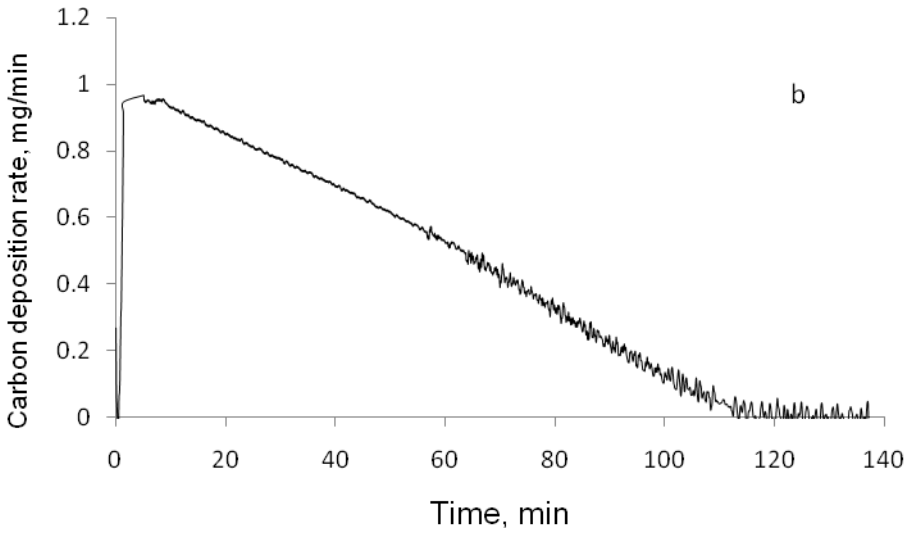

Figure A5: Carbon deposition rate in mg/min for Ni/αAl_2O_3, at 550ºC, 120 ml/min, and 100% methane, a: before smoothing, b: after smoothing

Using the fractional uncertainty rule, the total uncertainty can be calculated:

$$u(Overall) = \sqrt{\left(\frac{u(Weight)}{Weight}\right)^2 + \left(\frac{u(Flow)}{Flow}\right)^2 + \left(\frac{u(Ni)}{Ni}\right)^2 + \left(\frac{u(TB)}{TB}\right)^2}$$

For 10%Ni/γAl_2O_3:

The total uncertainty is: 3.3%

For 10%Ni/αAl_2O_3:

The total uncertainty is: 3.3%

<u>Representing the total uncertainty in initial rate</u>

The following Figures were selected to represent the effect of the uncertainty range of the initial rate:

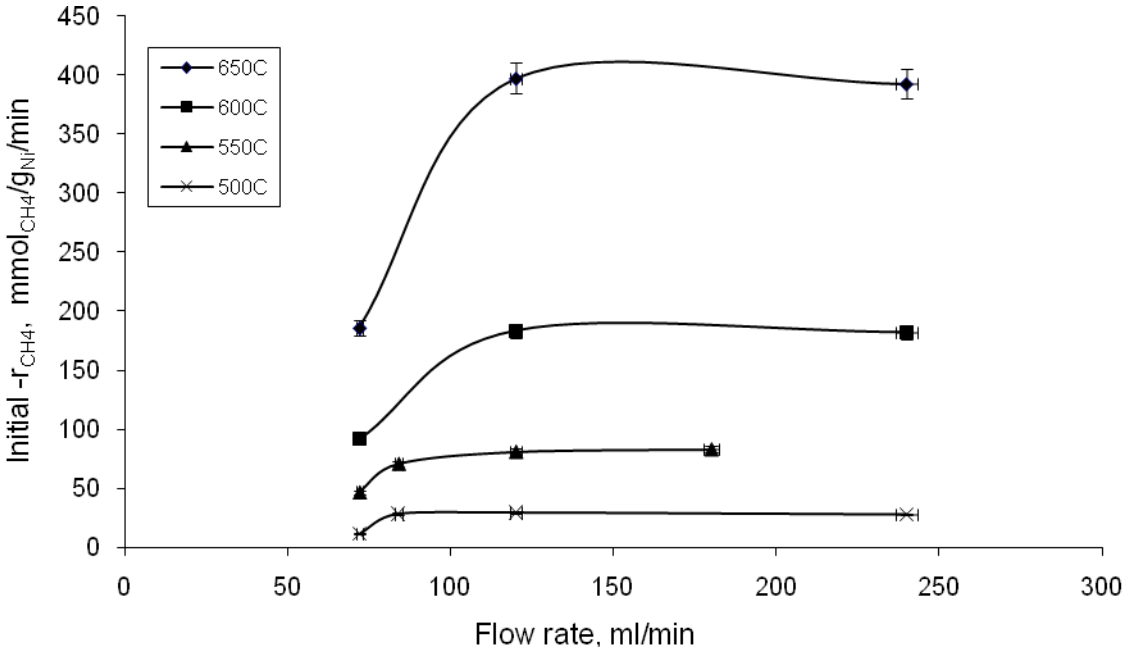

Figure A6: Flow rate effect on the initial raeaction rate for Ni/γAl_2O_3 using 100% methane, 120 ml/min, and 1 atm.

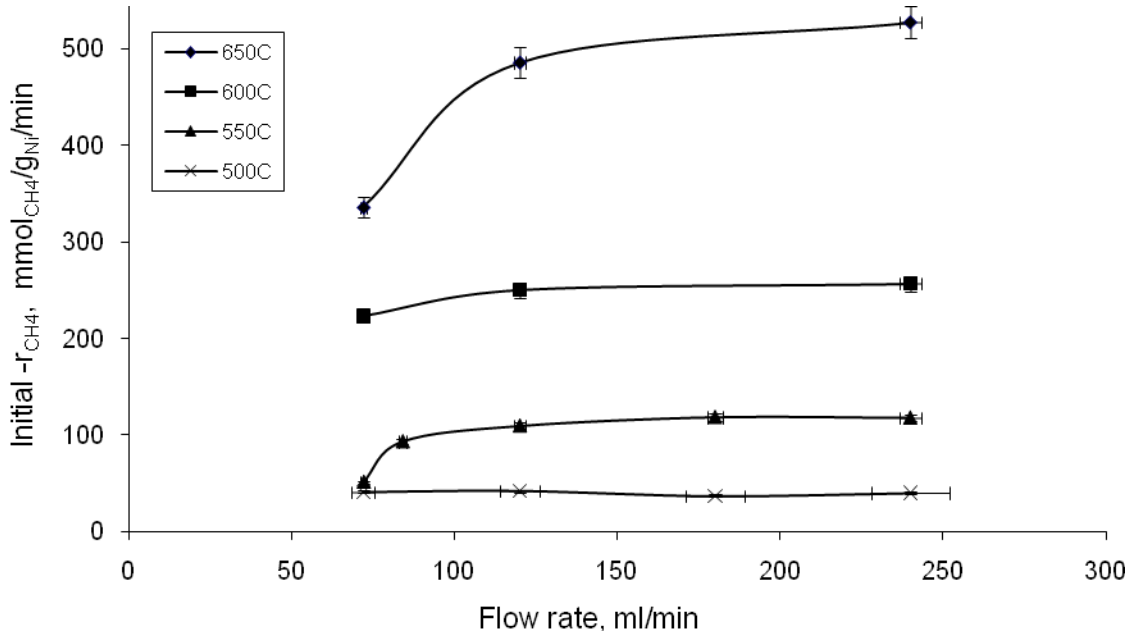

Figure A7: Flow rate effect on the initial raeaction rate for Ni/αAl_2O_3 using 100% methane, 120 ml/min, and 1 atm.

For fluidized bed experimental work

Uncertainty in the bench balance

The typical weight for the catalyst load is 2 gm. the performance of the balance using standard weight of 1 gm is given in Table A.6:

Table A.6: Balance error

Weight, gm	Error, gm
1.04	0.04
1. 04	0.04
1.03	0.03

The balance weight is measured with the following uncertainty:

1±0.026 mg

Uncertainty in the mass flow controller

The typical feed for the fluidized bed is 2.4 l/min of 80/20 methane/nitrogen feed, the uncertainty associated with the measurement is calculated below:

Table A.7: Flow rate error

Gas	Flow rate, ml/min
Methane	1960±50
Nitrogen	480±12

The uncertainty associated with the inlet flow rate is calculated using the summation rule as follows:

$$u(CH_4 + N_2) = \sqrt{u(CH_4)^2 + u(N_2)^2}$$

And the inlet flow rate uncertainty is:

2400 ±50 ml/min

Uncertainty in the nickel loading

The catalyst used throughout this study is: 10%Ni/αAl_2O_3, 10%Ni/γAl_2O_3, and 10%Ni/SiO_2. ICP check for the catalyst is performed and the result of the nickel loading is given in Table A.8:

A.8: Nickel loading

Catalyst	Nickel loading
10%Ni/γAl_2O_3	10±0.04
10%Ni/αAl_2O_3	10±0.2
10%Ni/SiO_2	10±0.2

Uncertainty associated with the replicated experiments

Repeated experiments are conducted to check the uncertainty in the fluidized bed measurements. Hydrogen produced in mmol/min used to check the uncertainty associated with the fluidized bed setup. The uncertainty for each catalyst is given in table A.9:

A.9: Hydrogen produced

Catalyst	Hydrogen produced mmol /min
10%Ni/γAl_2O_3	9.8±0.04
10%Ni/αAl_2O_3	11±0.043
10%Ni/SiO_2	8.8±0.08

Using the fractional uncertainty rule, the total uncertainty can be calculated:

$$u(Overall) = \sqrt{\left(\frac{u(Weight)}{Weight}\right)^2 + \left(\frac{u(Flow)}{Flow}\right)^2 + \left(\frac{u(Ni)}{Ni}\right)^2 + \left(\frac{u(FB)}{FB}\right)^2}$$

For 10%Ni/γAl_2O_3:

The total uncertainty is: 3.4%

For 10%Ni/αAl_2O_3:

The total uncertainty is: 4%

For 10%Ni/SiO_2:

The total uncertainty is: 4%

Representing the total uncertainty in the thermo balance results

The following Figures were selected to represent the effect of the uncertainty range of the fluidized bed results, the dashed lines represent the uncertainty range:

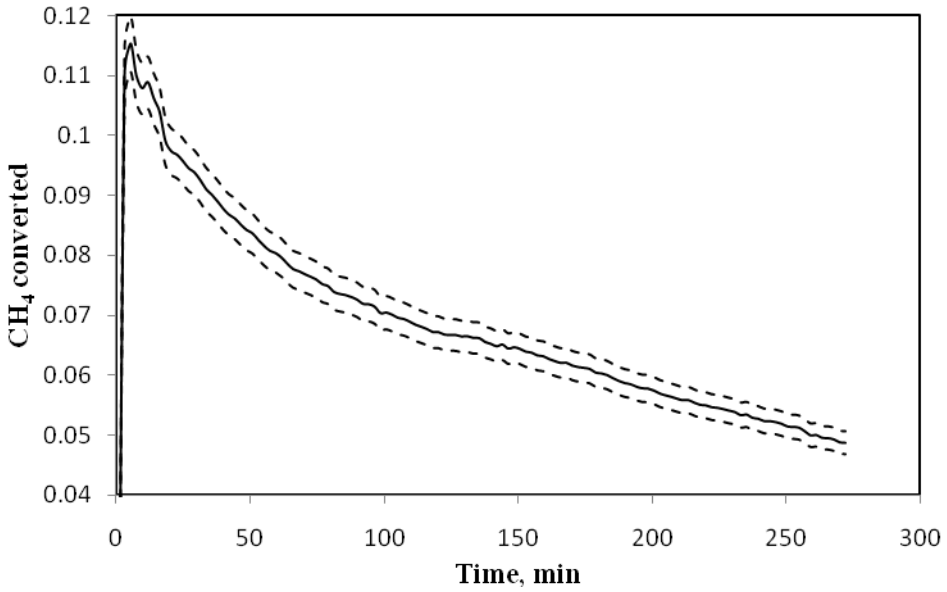

Figure A8: Methane conversion in a fluidized bed of Ni/αAl_2O_3, at 550ºC, 108μm, and 50/50 CH_4/N_2

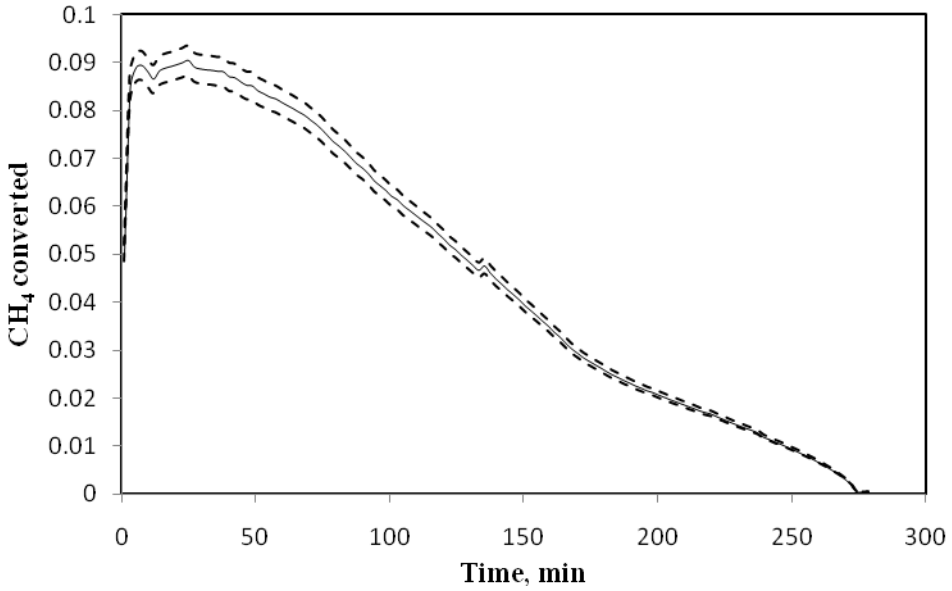

Figure A9: Methane conversion in a fluidized bed of $Ni/\gamma Al_2O_3$, at 550ºC, 108µm, and 50/50 CH_4/N_2

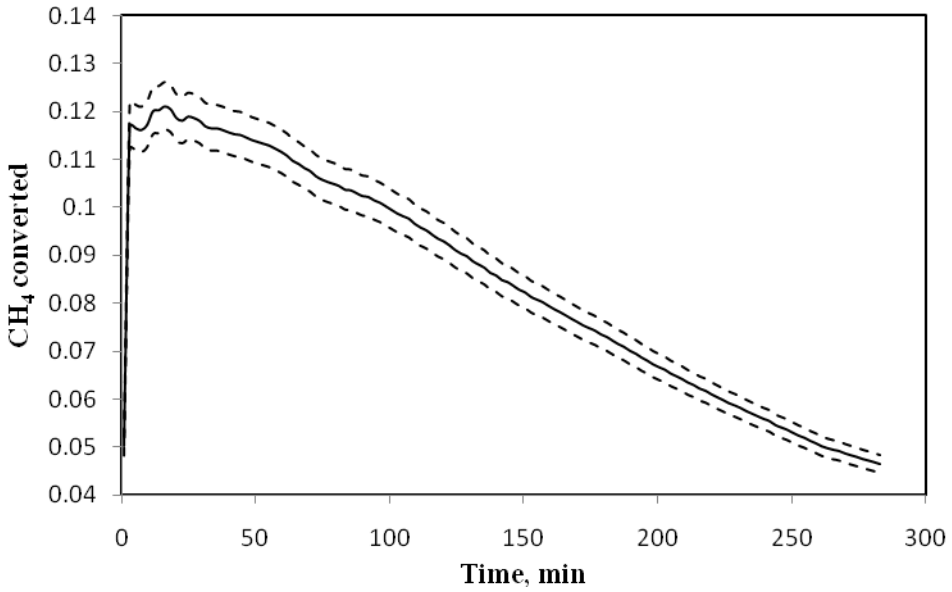

Figure A10: Methane conversion in a fluidized bed of Ni/SiO_2, at 550ºC, 108µm, and 50/50 CH_4/N_2

Appendix B: Reaction rate and catalyst deactivation during a methane catalyst cracking

During thermal-catalytic cracking of methane, methane is dissociatively adsorbed on the catalyst surface forming two hydrogen molecules and an adsorbed carbon atom; usually supported nickel is used as a catalyst. The hydrogen is released in the product gas phase while carbon adsorbs to the active sites either to diffuse through the active sites a filamentous carbon or to form an encapsulating carbon. During the reaction, the catalyst activity decreases from a full activity to no activity due to the buildup of the encapsulating carbon on the catalyst surface. The filamentous carbon formation does not affect the catalyst activity, since the carbon filament is formed by diffusion of carbon through nickel keeping the nickel on the tip of the filament and does not affect either the nickel surface area subjected to the reaction or the nickel activity. On the other hand, the encapsulating carbon is formed as a layer on the catalyst surface preventing any contact between the catalyst and the reactants, the encapsulating carbon is the main reason for catalyst deactivation, and we expect that the catalyst deactivation is a function of the encapsulating carbon concentration and time of the catalyst on the stream.

To study the reaction rate and the deactivation we need to know how the reaction occurs. The elementary reaction for methane catalytic cracking is shown in Equation B1.

$$CH_4 \xrightarrow[cat]{\Delta} C + 2H_2 \qquad \text{(B1)}$$

Unfortunately the reaction does not occur on one step; the actual process is successive reactions of hydrogen release from methane, the actual reaction mechanism can be written as:

Reaction mechanism

Methane cracking process

1.	$CH_4 + I \Leftrightarrow CH_4 \cdot I$	K_{CH_4}	(B2)
2.	$CH_4 \cdot I + I \Leftrightarrow CH_3 \cdot I + H.I$	rds/K_2	(B3)
3.	$CH_3 \cdot I + I \Leftrightarrow CH_2 \cdot I + H.I$	K_3	(B4)
4.	$CH_2 \cdot I + I \Leftrightarrow CH \cdot I + H.I$	K_4	(B5)
5.	$CH \cdot I + I \Leftrightarrow C \cdot I + H.I$	K_5	(B6)
6.	$2H.I \Leftrightarrow 2H_2 + 2I$	$\frac{1}{K_{H_2}}$	(B7)
7.	$C \cdot I \Leftrightarrow C_{\text{Ni.f}} + I$	$\frac{1}{K_C}$	(B8)

The process described above is the methane cracking process, but at the same time, we have two processes taking place with methane cracking namely carbon diffusion to form carbon filaments and deactivation. The rate of carbon diffusion through nickel depends on the competition between carbon segregation and gas adsorption; but the rate of deactivation is a function of reaction conditions, For example, if nitrogen is present in the reacting mixture, the active sites present for carbon segregation decrease, which reduce the chance of encapsulating carbon formation since the reaction step 7 will shift more toward producing more $C_{C_{Ni.f}}$. If hydrogen presents, in addition to the competition about the active sites found in nitrogen case, the carbon formation affinity of the reacting mixture decreases since the amount of carbon available for carbon filaments growth is lower at the same diffusion rate which will reduce the deactivation rate. We can describe the diffusion and the encapsulating carbon formation as follows:

The Diffusion Process

8. $C_{Ni.f} \rightarrow C_{Ni.r}$ $k_{dif.}$ (Diffusion) (B9)

9. $C_{Ni.r} \rightarrow C_{fil.}$ k_p (Precipitation) (B10)

The Encapsulating Carbon Formation

10. $nC \cdot I \rightarrow nC_{P.I}$ k_d (B11)

During the formation of a carbon filament, it passes through two periods of formation, the nucleation and the growth periods. During the nucleation period of the carbon filament, the reaction conditions have affinity for carbon formation, since all carbon formed is quickly diffuse through nickel to initiate the carbon filamentous, which means there is no chance for carbon deposition on the catalyst, in other words, no encapsulating carbon exists during the nucleation period. Once the growth period started, the rate of carbon diffusion formation in nickel decreases since carbon concentration required for filament growth is less than the super saturation required for nucleation period which increases the possibility of carbon deposition on the catalyst surface. Hence encapsulating carbon is formed. Figure 1 shows the different steps for methane catalytic cracking including filaments formation and encapsulating carbon.

The specific rate of a chemical reaction can be expressed as:

Rate of reactions $f(C_1, C_2, ..., C_i; T)$ (B12)

If a catalyst deactivation is involved, then the rate of the fully regenerated catalyst will be:

$$\left[reaction\ rate\ of\ catalyst\ initially\right] = R_O = f_1(C_1, C_2, ..., C_i; T) \quad \text{(B13)}$$

After catalyst deactivation occurred:

$$\left[reaction\ rate\ of\ catalyst\ after\ deactivation\right] = R_1 = f_2(C_1, C_2, ..., C_i; T) \quad \text{(B14)}$$

So we can define the activity as:

$$a = \frac{R_1}{R_O} \quad \text{(B15)}$$

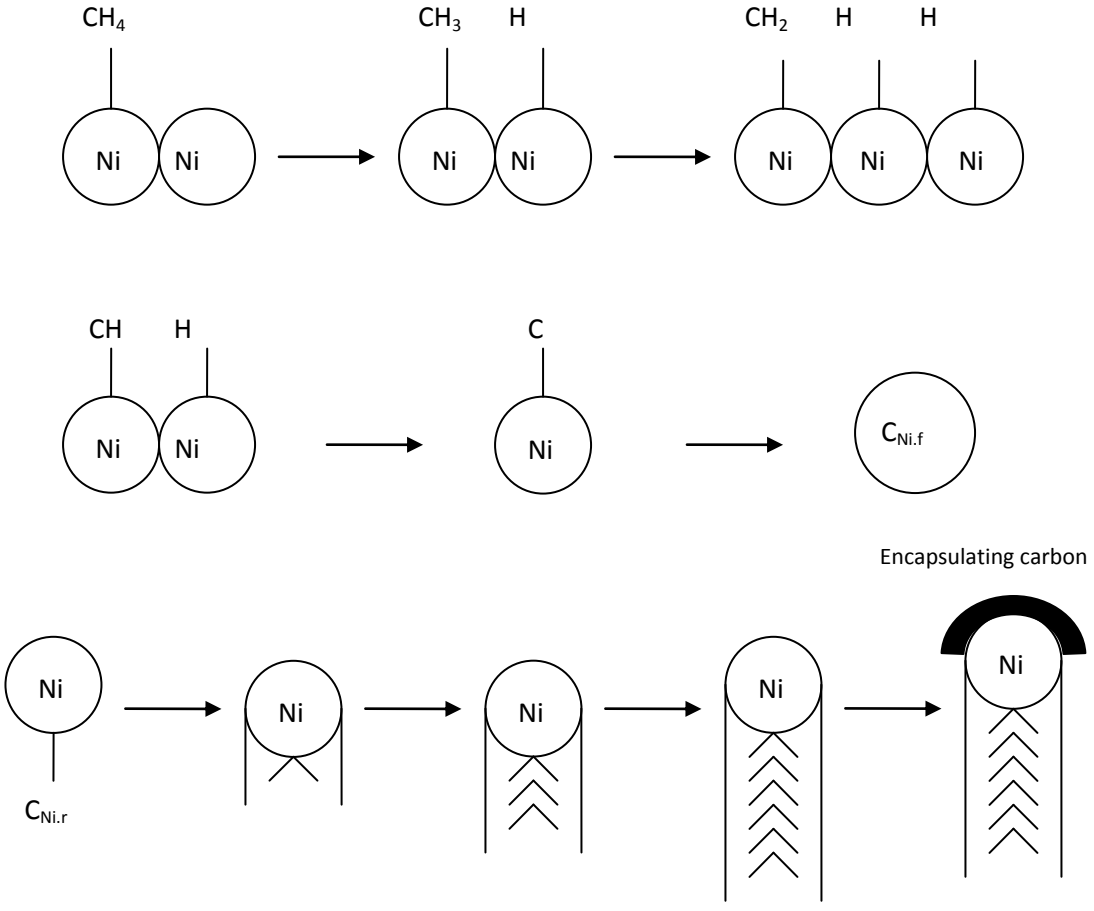

Figure B1: Carbon filament and encapsulating carbon formation

Catalyst deactivation includes active sites fouling or poisoning, so we can define a ratio called α , which is the fraction of the active sites or the ratio of un-deactivated sites as:

$$\alpha = \frac{N_t}{N_0} \qquad \text{(B16)}$$

Where

N_t : The number of active sites at any stage of deactivation per unit mass of catalyst.

N_0 : The number of the active sties of a fully activated catalyst per unit mass of catalyst.

The rate of the reaction may be separated into two terms:

1. The first one accounts for reaction kinetics effect and is a time independent.
2. The second term accounts for deactivation.

The specific rate for each step:

1. $$r_1 = k_1 P_{CH_4}\theta_I - k_{-1}\theta_{CH_4} = k_1\left[P_{CH_4}\theta_I - \frac{k_{-1}}{k_1}\theta\right] = k_1\left[P_{CH_4}\theta_I - \frac{\theta_{CH_4\cdot I}}{K_{CH_4}}\right]$$

   $$\frac{r_1}{k_1} \approx 0 \Rightarrow \theta_{CH_4} = K_{CH_4} P_{CH_4}\theta_I \qquad \text{(B17)}$$

2. $$r_2 = \frac{dC_{CH_3\cdot I}}{dt} = k_2 C_{CH_4\cdot I} C_I - k_{-2} C_{CH_3\cdot I} C_{H.I} = k_2\left[C_{CH_4\cdot I} C_I - \frac{k_{-2}}{k_2} C_{CH_3\cdot I} C_{H.I}\right]$$

   $$= k_2\left[C_{CH_4\cdot I} C_I - \frac{C_{CH_3\cdot I} C_{H.I}}{K_2}\right]$$

   $$r_2^{'} = \frac{\mathrm{r}_2}{\mathrm{C}_0} = \frac{d\theta_{CH_3\cdot I}}{dt} \qquad \text{with} \qquad \theta_{CH_3\cdot I} = \frac{C_{CH_3\cdot I}}{C_0}$$

   C_0 is the total number of sites (including encapsulated sites)

   So,

$$\frac{d\theta_{CH_3\cdot I}}{dt} = \mathrm{C}_0\, k_2\left[\theta_{CH_4\cdot I}\theta_I - \frac{\theta_{CH_3\cdot I}\theta_{H.I}}{K_2}\right] \quad \text{(B18)}$$

3. $r_3 = k_3\left[\theta_{CH_3\cdot I}\theta_I - \frac{\theta_{CH_2\cdot I}\theta_{H.I}}{K_3}\right]$

$$\frac{r_3}{k_3} \approx 0 \Rightarrow \theta_{CH_3\cdot I}\theta_I = \frac{\theta_{CH_2\cdot I}\theta_{H.I}}{K_3} \quad \text{(B19)}$$

4. $r_4 = k_4\left[\theta_{CH_2\cdot I}\theta_I - \frac{\theta_{CH\cdot I}\theta_{H.I}}{K_4}\right]$

$$\frac{r_4}{k_4} \approx 0 \Rightarrow \theta_{CH\cdot I}\theta_{H.I} = K_4\theta_{CH_2\cdot I}\theta_I \quad \text{(B20)}$$

5. $r_5 = k_5\left[\theta_{CH\cdot I}\theta_I - \frac{\theta_{C\cdot I}\theta_{H.I}}{K_5}\right]$

$$\frac{r_5}{k_5} \approx 0 \Rightarrow \theta_{C\cdot I}\theta_{H.I} = K_5\theta_{CH\cdot I}\theta_I \quad \text{(B21)}$$

6. $r_6 = k_6\left[\theta_I{}^2 - K_{H_2}P_{H_2}\theta_I{}^2\right]$

$$\frac{r_6}{k_6} \approx 0 \Rightarrow \theta_{H.I} = \left(\sqrt{K_{H_2}P_{H_2}}\right)\theta_I \quad \text{(B22)}$$

7. Equilibrium between C.I and carbon in front

$r_7 = k_7\left[\theta_{C.I} - K_C C_{C_{Ni,f}}\theta_I\right]$

$$\frac{r_7}{k_7} \approx 0 \Rightarrow \theta_{C.I} = K_C C_{C_{Ni,f}}\theta_I \quad \text{(B23)}$$

8.

The rate of carbon diffusion through the nickel can be written in Fick's law:

$$r_{C,Diff} = \frac{D_{C_{Ni}}}{l}.(C_{C_{Ni,f}} - C_{C_{Ni,R}}).A_{Ni} \quad \text{(B24)}$$

Where

l : The average path length

$D_{C_{Ni}}$: Diffusivity of carbon in nickel

$C_{C_{Ni,f}}$: The concentration of carbon dissolved in nickel at the front of the nickel

$C_{C_{Ni,R}}$: The concentration of carbon dissolved in nickel at the rear of the nickel particle

A_{Ni} : Specific surface area of nickel

9. $r_9 = \frac{dC_{P.I}}{dt} = k_d C_{C\cdot I}$

Dividing by C_0, it comes:

$$\frac{d\theta_{P.I}}{dt} = k_d \theta_{C\cdot I}^{n} \quad \text{(B25)}$$

Overall site balance:

$$\theta_I + \theta_{CH_4\cdot I} + \theta_{CH_3\cdot I} + \theta_{CH_2\cdot I} + \theta_{CH\cdot I} + \theta_{C.I} + \theta_{H.I} + \theta_{C_P\cdot I} = 1 \quad \text{(B26)}$$

From Equation B17: $\theta_{CH_4.I} = K_{CH_4} P_{CH_4} \theta_I$

From Equation 18:

$$\frac{d\theta_{CH_3\cdot I}}{dt} = \mathrm{C}_0\, k_2 \left[\theta_{CH_4\cdot I}\theta_I - \frac{\theta_{CH_3\cdot I}\theta_{H.I}}{K_2} \right]$$
$$= \mathrm{C}_0\, K_{CH_4} k_2 \left[P_{CH_4} - \frac{K_C K_{H_2}^2}{K_{CH_4} K_2 K_3 K_4 K_5} C_{C_{Ni,f}} P_{H_2}^2 \right] {\theta_I}^2 \quad \text{(B27)}$$

From Equation 19: $\theta_{CH_3\cdot I} = \frac{\theta_{CH_2\cdot I}\theta_{H.I}}{\theta_I K_3} = \frac{K_C K_{H_2} P_{H_2} \left(\sqrt{K_{H_2} P_{H_2}}\right) C_{C_{Ni,f}}}{K_3 K_4 K_5} \theta_I$ (B28)

From Equation 20: $\theta_{CH_2\cdot I} = \frac{\theta_{CH\cdot I}\theta_{H.I}}{K_4 \theta_I} = \frac{K_C K_{H_2} P_{H_2} C_{C_{Ni,f}}}{K_4 K_5} \theta_I$ (B29)

From Equation 21: $\theta_{CH\cdot I} = \frac{\theta_{C\cdot I}\theta_{H.I}}{K_5 \theta_I} = \frac{K_C C_{C_{Ni,f}} \left(\sqrt{K_{H_2} P_{H_2}}\right)}{K_5} \theta_I$ (B30)

From Equation 22: $\theta_{HI.} = \left(\sqrt{K_{H_2} P_{H_2}}\right) \theta_I$ (B31)

From Equation 23: $\theta_{C.I} = K_C C_{C_{Ni,f}} \theta_I$ (B32)

The initial rate derivation

Let's start from the specific rate for the rate limiting step:

$$\frac{d\theta_{CH_3 \cdot I}}{dt} = \mathrm{C}_0\, k_2 \left[\theta_{CH_4 \cdot I} \theta_I - \frac{\theta_{CH_3 \cdot I} \theta_{H.I}}{K_2} \right]$$
$$= \mathrm{C}_0\, K_{CH_4} k_2 \left[P_{CH_4} - \frac{K_C K_{H_2}^2}{K_{CH_4} K_2 K_3 K_4 K_5} C_{C_{Ni,f}} P_{H_2}^2 \right] \theta_I{}^2 \quad \text{(B27)}$$

$$\frac{d\theta_{CH_3 \cdot I}}{dt} = \mathrm{C}_0\, k_2 \left[\theta_{CH_4 \cdot I} \theta_I - \frac{\theta_{CH_3 \cdot I} \theta_{H.I}}{K_2} \right]$$

$$\frac{d\theta_{CH_3 \cdot I}}{dt} = \mathrm{C}_0\, k_2 \left[\theta_{CH_4 \cdot I} \theta_I - \frac{\theta_{CH_2 \cdot I} \theta_{H.I}^2}{K_2 K_3 \theta_I} \right]$$

$$\frac{d\theta_{CH_3 \cdot I}}{dt} = \mathrm{C}_0\, k_2 \left[\theta_{CH_4 \cdot I} \theta_I - \frac{\theta_{H.I}^2}{K_2 K_3 \theta_I} . \frac{\theta_{CH \cdot I} \theta_{H.I}}{K_4 \theta_I} \right]$$

$$= \mathrm{C}_0\, k_2 \left[P_{CH_4} K_{CH_4} \theta_I \theta_I - \frac{\theta_{H.I}^2}{K_2 K_3 \theta_I} . \frac{\theta_{CH \cdot I} \theta_{H.I}}{K_4 \theta_I} \right]$$

$$= \mathrm{C}_0\, k_2 \left[P_{CH_4} K_{CH_4} \theta_I^2 - \frac{\theta_{CH \cdot I} \theta_{H.I}^3}{K_2 K_3 K_4 \theta_I^2} \right]$$

$$= \mathrm{C}_0\, k_2 \left[P_{CH_4} K_{CH_4} \frac{\theta_{CI}^2}{k_C^2 C_{C_{Ni,f}}^2} - \frac{\theta_{CI} \theta_{H.I}^4}{K_2 K_3 K_4 K_5 \theta_I^3} \right]$$

$$= \mathrm{C}_0\, k_2 \left[P_{CH_4} K_{CH_4} \frac{\theta_{CI}^2}{k_C^2 C_{C_{Nif}}^2} - \frac{\theta_{CI} K_{H_2}^2 P_{H_2}^2 \theta_I}{K_2 K_3 K_4 K_5} \right]$$

$$= \mathrm{C}_0\ k_2 \left[P_{CH_4} K_{CH_4} \frac{\theta_{CI}^2}{k_C^2 C_{C_{Ni,f}}^2} - \frac{\theta_{CI} K_{H_2}^2 P_{H_2}^2 \theta_I}{K_2 K_3 K_4 K_5} \right]$$

$$= \mathrm{C}_0\ k_2 K_{CH_4} \left[P_{CH_4} \frac{\theta_{CI}^2}{k_C^2 C_{C_{Ni,f}}^2} - \frac{\theta_{CI} K_{H_2}^2 P_{H_2}^2 \theta_I}{K_{CH_4} K_2 K_3 K_4 K_5} \right]$$

$$= \mathrm{C}_0\ k_2 K_{CH_4} \left[P_{CH_4} \frac{\theta_{CI}^2}{k_C^2 C_{C_{Ni,f}}^2} - \frac{\theta_{CI} K_{H_2}^2 P_{H_2}^2 \theta_{CI}}{K_{CH_4} K_2 K_3 K_4 K_5 K_C C_{C_{Ni,f}}} \right]$$

$$= \mathrm{C}_0\ k_2 K_{CH_4} \left[P_{CH_4} \frac{\theta_{CI}^2}{k_C^2 C_{C_{Ni,f}}^2} - \frac{\theta_{CI}^2 K_{H_2}^2 P_{H_2}^2}{K_{CH_4} K_2 K_3 K_4 K_5 K_C C_{C_{Ni,f}}} \right]$$

$$= \frac{\mathrm{C}_0\ k_2 K_{CH_4} \theta_{CI}^2}{k_C^2 C_{C_{Ni,f}}^2} \left[P_{CH_4} - \frac{K_{H_2}^2 K_C C_{C_{Ni,f}}}{K_{CH_4} K_2 K_3 K_4 K_5} P_{H_2}^2 \right]$$

$$\frac{d\theta_{CH_3 \cdot I}}{dt} = \mathrm{C}_0\ K_{CH_4} k_2 \left[P_{CH_4} - \frac{K_C K_{H_2}^2}{K_{CH_4} K_2 K_3 K_4 K_5} C_{C_{Ni,f}} P_{H_2}^2 \right] {\theta_I}^2$$

$$\frac{d\theta_{CH_3 \cdot I}}{dt} = \frac{\mathrm{C}_0\ k_2 K_{CH_4} \theta_{CI}^2}{k_C^2 C_{C_{Ni,f}}^2} \left[P_{CH_4} - \frac{K_{H_2}^2 K_C C_{C_{Ni,f}}}{K_{CH_4} K_2 K_3 K_4 K_5} P_{H_2}^2 \right] \qquad \text{(B33)}$$

Equation B33 shows the rate in terms of partial pressure of methane and hydrogen. θ_{CI} can be replaced from the overall site balance, Equation B26:

At no deactivation condition, Equation B26 becomes:

$$\theta_I + \theta_{CH_4 \cdot I} + \theta_{CH_3 \cdot I} + \theta_{CH_2 \cdot I} + \theta_{CH \cdot I} + \theta_{C.I} + \theta_{H.I} = 1 \qquad \text{(B34)}$$

By replacing a fractional coverage for each species in Equation B34 by its value from Equations B17, and B27-B32:

$$1=\left(\theta_I+\theta_{CH_4\cdot I}+\frac{\theta_{CH_2\cdot I}\cdot\theta_{H.I}}{K_3\theta_I}+\frac{\theta_{CH\cdot I}\cdot\theta_{H.I}}{K_4\theta_I}+\frac{\theta_{C.I}\cdot\theta_{H.I}}{K_5\theta_I}+K_{H_2}^{\frac{1}{2}}P_{H_2}^{\frac{1}{2}}\theta_I+K_C C_{C_{Ni,f}}\theta_I\right)$$

$$1=\left(\theta_I+K_{CH_4}P_{CH_4}\theta_I+\frac{\theta_{CH\cdot I}\cdot\theta_{HI}^2}{K_3K_4\theta_I^2}+\frac{\theta_{C\cdot I}\cdot\theta_{HI}^2}{K_4K_5\theta_I^2}+\frac{\theta_{C.I}\cdot\theta_{HI}}{K_5\theta_I}+K_{H_2}^{\frac{1}{2}}P_{H_2}^{\frac{1}{2}}\theta_I+K_C C_{C_{Ni,f}}\theta_I\right)$$

$$1=\left(\theta_I+K_{CH_4}P_{CH_4}\theta_I+\frac{\theta_{C\cdot I}\cdot\theta_{H.I}^3}{K_3K_4K_5\theta_I^3}+\frac{\theta_{C\cdot I}\cdot\theta_{H.I}^2}{K_4K_5\theta_I^2}+\frac{\theta_{C.I}\cdot\theta_{H.I}}{K_5\theta_I}+K_{H_2}^{\frac{1}{2}}P_{H_2}^{\frac{1}{2}}\theta_I+K_C C_{C_{Ni,f}}\theta_I\right)$$

$$1=\left(\frac{\theta_{C.I}}{K_C C_{C_{Ni,f}}}+\theta_{C.I}\frac{K_{CH_4}P_{CH_4}}{K_C C_{C_{Ni,f}}}+\theta_{C.I}\frac{K_{H_2}^{\frac{3}{2}}P_{H_2}^{\frac{3}{2}}}{K_3K_4K_5}+\theta_{C.I}\frac{K_{H_2}P_{H_2}}{K_4K_5}+\theta_{C.I}\frac{K_{H_2}^{\frac{1}{2}}P_{H_2}^{\frac{1}{2}}}{K_5}+\theta_{C.I}\frac{K_{H_2}^{\frac{1}{2}}P_{H_2}^{\frac{1}{2}}}{K_C C_{C_{Ni,f}}}+\theta_{C.I}\right)$$

$$1=\theta_{C.I}\left(1+\frac{1}{K_C C_{C_{Ni.f}}}+\frac{K_{CH_4}P_{CH_4}}{K_C C_{C_{Ni,f}}}+\frac{K_{H_2}^{\frac{3}{2}}P_{H_2}^{\frac{3}{2}}}{K_3K_4K_5}+\frac{K_{H_2}P_{H_2}}{K_4K_5}+\frac{K_{H_2}^{\frac{1}{2}}P_{H_2}^{\frac{1}{2}}}{K_5}+\frac{K_{H_2}^{\frac{1}{2}}P_{H_2}^{\frac{1}{2}}}{K_C C_{C_{Ni,f}}}\right)$$

$$\theta_{C.I}=\frac{1}{\left(1+\frac{1}{K_C C_{C_{Ni,f}}}+\frac{K_{CH_4}P_{CH_4}}{K_C C_{C_{Ni,f}}}+\frac{K_{H_2}^{\frac{3}{2}}P_{H_2}^{\frac{3}{2}}}{K_3K_4K_5}+\frac{K_{H_2}P_{H_2}}{K_4K_5}+\frac{K_{H_2}^{\frac{1}{2}}P_{H_2}^{\frac{1}{2}}}{K_5}+\frac{K_{H_2}^{\frac{1}{2}}P_{H_2}^{\frac{1}{2}}}{K_C C_{C_{Ni,f}}}\right)} \quad \text{(B35)}$$

If we consider the surface concentrations of $\theta_{CH_2.S},\theta_{CH.S},\theta_{H.S}$ are negligible then Equation B35 becomes:

$$\theta_{C.I}=\frac{1}{\left(1+\frac{1}{K_C C_{C_{Ni,f}}}+\frac{K_{CH_4}P_{CH_4}}{K_C C_{C_{Ni,f}}}+\frac{K_{H_2}^{\frac{3}{2}}P_{H_2}^{\frac{3}{2}}}{K_3K_4K_5}\right)} \quad \text{(B36)}$$

By replacing the value of θ_{CI} from Equation B36 into Equation B33:

$$\frac{d\theta_{CH_3\cdot I}}{dt}=\frac{\mathrm{C}_0\,k_2K_{CH_4}}{k_C^2C_{C_{Ni,f}}^2\left(1+\frac{1}{K_C C_{C_{Ni,f}}}+\frac{K_{CH_4}P_{CH_4}}{K_C C_{C_{Ni,f}}}+\frac{K_{H_2}^{\frac{3}{2}}P_{H_2}^{\frac{3}{2}}}{K_3K_4K_5}\right)^2}\left[P_{CH_4}-\frac{K_{H_2}^2K_C C_{C_{Ni,f}}}{K_{CH_4}K_2K_3K_4K_5}P_{H_2}^2\right]$$

(B37)

A cretin degree of super-saturation is required of carbon in nickel $C_{C_{Ni,Sat}}$ for carbon filaments formation. The carbon concentration is found to be uniform over the nickel particle. Snoeck et al. (1997) et al. assumed as follows:

$$C_{C_{Ni,f}} \approx C_{C_{Ni,r}} \approx C_{C_{Ni,Sat}}$$

$$\frac{d\theta_{CH_3 \cdot I}}{dt} = \frac{\mathrm{C}_0\, k_2 K_{CH_4}\left[P_{CH_4} - \frac{K_{H_2}^2 K_C C_{C_{Ni,sat}}}{K_{CH_4} K_2 K_3 K_4 K_5} P_{H_2}^2\right]}{k_C^2 C_{C_{Ni,sat}}^2 \left(1 + \frac{1}{K_C C_{C_{Ni,sat}}} + \frac{K_{CH_4} P_{CH_4}}{K_C C_{C_{Ni,sat}}} + \frac{K_{H_2}^{\frac{3}{2}} P_{H_2}^{\frac{3}{2}}}{K_3 K_4 K_5}\right)^2}$$

By dividing the denominator and numerator by $\left(1 + \frac{1}{K_C C_{C_{Ni,sat}}}\right)^2$ and incorporating it into the other constants:

$$\frac{d\theta_{CH_3 \cdot I}}{dt} = \frac{\mathrm{C}_0\, k_2 K_{CH_4}\left[P_{CH_4} - \frac{K_{H_2}^2 K_C C_{C_{Ni,sat}}}{K_{CH_4} K_2 K_3 K_4 K_5} P_{H_2}^2\right]}{k_C^2 C_{C_{Ni,sat}}^2 \left(1 + \frac{1}{K_C C_{C_{Ni,sat}}}\right)^2 \left(1 + K_{CH_4} P_{CH_4} + K_{H_2}^{\frac{3}{2}} P_{H_2}^{\frac{3}{2}}\right)^2}$$

$$\frac{d\theta_{CH_3 \cdot I}}{dt} = \frac{k\left[P_{CH_4} - \frac{K_{H_2}^2 K_C C_{C_{Ni,sat}}}{K_{CH_4} K_2 K_3 K_4 K_5} P_{H_2}^2\right]}{\left(1 + K_{CH_4} P_{CH_4} + K_{H_2}^{\frac{3}{2}} P_{H_2}^{\frac{3}{2}}\right)^2} \quad \text{(B38)}$$

Equilibrium pressure constant

$$K_P = \frac{P_{H_2}^2}{P_{CH_4}} \quad \text{(B39)}$$

From Equation B17 and B22:

$$P_{CH_4} = \frac{\theta_{CH_4}}{\theta_I \cdot K_{CH_4}}$$

$$P_{H_2} = \frac{\theta_{H.I}^2}{K_H \cdot \theta_I^2}$$

$$K_P = \frac{P_{H_2}^2}{P_{CH_4}} = \frac{K_{CH_4} \cdot \theta_{H \cdot I}^4}{K_H^2 \cdot \theta_I^3 \cdot \theta_{CH_4 \cdot I}} \quad \text{(B40)}$$

From Equations B19- B22:

$$\theta_I = \frac{\theta_{CH_2 \cdot I} \cdot \theta_{H \cdot I}}{K_3 \cdot \theta_{CH_3 \cdot I}}$$

$$\theta_I = \frac{\theta_{CH \cdot I} \cdot \theta_{H \cdot I}}{K_4 \cdot \theta_{CH_2 \cdot I}}$$

$$\theta_I = \frac{\theta_{C \cdot I} \cdot \theta_{H \cdot I}}{K_5 \cdot \theta_{CH \cdot I}}$$

$$\theta_I^3 = \frac{\theta_{CH_2 \cdot I} \cdot \theta_{H \cdot I}}{K_3 \cdot \theta_{CH_3 \cdot I}} \cdot \frac{\theta_{CH \cdot I} \cdot \theta_{H \cdot I}}{K_4 \cdot \theta_{CH_2 \cdot I}} \cdot \frac{\theta_{C \cdot I} \cdot \theta_{H \cdot I}}{K_5 \cdot \theta_{CH \cdot I}}$$

$$\theta_I^3 = \frac{\theta_{H \cdot I}^3 \cdot \theta_{C \cdot I}}{K_3 \cdot K_4 \cdot K_5 \cdot \theta_{CH_3 \cdot I}} \quad \text{(B41)}$$

Replacing θ_I^3 from Equation 41 into Equation 40:

$$K_p = \frac{P_{H_2}^2}{P_{CH_4}} = \frac{K_{CH_4} \cdot K_3 \cdot K_4 \cdot K_5 \cdot \theta_{CH_3 \cdot I} \cdot \theta_{H \cdot I}}{K_H^2 \cdot \theta_{C \cdot I} \cdot \theta_{CH_4 \cdot I}}$$

At equilibrium, the reaction rate is zero, From Equation B18:

$$\frac{\theta_{H \cdot I} \cdot \theta_{CH_3 \cdot I}}{\theta_{CH_4 \cdot I}} = \theta_I \cdot K_2$$

$$\Rightarrow K_p = \frac{K_{CH_4} \cdot K_3 \cdot K_4 \cdot K_5 \cdot \theta_I \cdot K_2}{K_H^2 \cdot \theta_{C \cdot I}}$$

From Equation B32:

$$\frac{\theta_I}{\theta_{C \cdot I}} = \frac{1}{K_C \cdot C_{C_{Ni,f}}}$$

$$K_P = \frac{K_{CH_4} \cdot K_2 \cdot K_3 \cdot K_4 \cdot K_5 \cdot \frac{1}{K_{H_2}^2} \cdot \frac{1}{K_C}}{C_{C_{Ni,f}}}$$

Since $C_{C_{Ni,f}} \approx C_{C_{Ni,R}} \approx C_{C_{Ni,Sat}}$

$$K_P = \frac{K_{CH_4} \cdot K_2 \cdot K_3 \cdot K_4 \cdot K_5 \cdot \frac{1}{K_{H_2}^2} \cdot \frac{1}{K_C}}{C_{C_{Ni,sa}t}} \qquad \text{(B42)}$$

By replacing the right hand in Equation B42 into Equation 38:

$$\frac{d\theta_{CH_3 \cdot I}}{dt} = \frac{k\left[P_{CH_4} - \frac{P_{H_2}^2}{K_P}\right]}{\left(1 + K_{CH_4} P_{CH_4} + K_{H_2}^{\frac{3}{2}} P_{H_2}^{\frac{3}{2}}\right)^2} \qquad \text{(B43)}$$

Where:

k is the specific reaction rate for methane cracking, in $\text{mmol}_{\text{CH}_4}/\text{g}_{\text{cat}}/\text{min/atm}$.

K_{CH_4} and K_{H_2} are the adsorption constants for methane and hydrogen in atm^{-1} and $\text{atm}^{-3/2}$ respectively.

K_P is the equilibrium constant with units of atm. and its values is calculated from thermodynamic.

Activity term:

The overall sites balance in Equation B26 can be written as follows:

$$\theta_{C_P \cdot I} = 1 - \left(\theta_I + \theta_{CH_4 \cdot I} + \theta_{CH_3 \cdot I} + \theta_{CH_2 \cdot I} + \theta_{CH \cdot I} + \theta_{C.I} + \theta_{H.I}\right) \qquad \text{(B44)}$$

$C_{CH_4.S}, C_{CH_3.S}$, $C_{H.S}$ and C_v are replaced by their values from Equation B17, and B27-B32:

$$\theta_{C_P \cdot I} = 1 - \left(\theta_I + \theta_{CH_4 \cdot I} + \frac{\theta_{CH_2 \cdot I} \cdot \theta_{H.I}}{K_3 \theta_I} + \frac{\theta_{CH \cdot I} \cdot \theta_{H.I}}{K_4 \theta_I} + \frac{\theta_{C.I} \cdot \theta_{H.I}}{K_5 \theta_I} + K_{H_2}^{\frac{1}{2}} P_{H_2}^{\frac{1}{2}} \theta_I + K_C C_{C_{Ni,f}} \theta_I\right)$$

$$\theta_{C_P \cdot I} = 1 - \left(\theta_I + K_{CH_4} P_{CH_4} \theta_I + \frac{\theta_{CH \cdot I} \cdot \theta_{H.I}^2}{K_3 K_4 \theta_I^2} + \frac{\theta_{C \cdot I} \cdot \theta_{H.I}^2}{K_4 K_5 \theta_I^2} + \frac{\theta_{C.I} \cdot \theta_{H.I}}{K_5 \theta_I} + K_{H_2}^{\frac{1}{2}} P_{H_2}^{\frac{1}{2}} \theta_I + K_C C_{C_{Ni,f}} \theta_I\right)$$

$$\theta_{C_P \cdot I} = 1 - \left(\theta_I + K_{CH_4} P_{CH_4} \theta_I + \frac{\theta_{C \cdot I} \cdot \theta_{H.I}^3}{K_3 K_4 K_5 \theta_I^3} + \frac{\theta_{C \cdot I} \cdot \theta_{H.I}^2}{K_4 K_5 \theta_I^2} + \frac{\theta_{C.I} \cdot \theta_{H.I}}{K_5 \theta_I} + K_{H_2}^{\frac{1}{2}} P_{H_2}^{\frac{1}{2}} \theta_I + K_C C_{C_{Ni,f}} \theta_I\right)$$

$$\theta_{C_P\cdot I} = 1-\left(\frac{\theta_{C.I}}{K_C C_{C_{Ni,f}}} + \theta_{C.I}\frac{K_{CH_4}P_{CH_4}}{K_C C_{C_{Ni,f}}} + \theta_{C.I}\frac{K_{H_2}^{\frac{3}{2}}P_{H_2}^{\frac{3}{2}}}{K_3K_4K_5} + \theta_{C.I}\frac{K_{H_2}P_{H_2}}{K_4K_5} + \theta_{C.I}\frac{K_{H_2}^{\frac{1}{2}}P_{H_2}^{\frac{1}{2}}}{K_5} + \theta_{C.I}\frac{K_{H_2}^{\frac{1}{2}}P_{H_2}^{\frac{1}{2}}}{K_C C_{C_{Ni,f}}} + \theta_{C.I} \right)$$

$$\theta_{C_P\cdot I} = 1-\theta_{C.I}\left(1+\frac{1}{K_C C_{C_{Ni,f}}} + \frac{K_{CH_4}P_{CH_4}}{K_C C_{C_{Ni,f}}} + \frac{K_{H_2}^{\frac{3}{2}}P_{H_2}^{\frac{3}{2}}}{K_3K_4K_5} + \frac{K_{H_2}P_{H_2}}{K_4K_5} + \frac{K_{H_2}^{\frac{1}{2}}P_{H_2}^{\frac{1}{2}}}{K_5} + \frac{K_{H_2}^{\frac{1}{2}}P_{H_2}^{\frac{1}{2}}}{K_C C_{C_{Ni,f}}} \right)$$

$$\theta_{C_P\cdot I} = 1-\theta_{C.I}k' \qquad \text{(B45)}$$

Where

$$k' = \left(1+\frac{1}{K_C C_{C_{Ni,f}}} + \frac{K_{CH_4}P_{CH_4}}{K_C C_{C_{Ni,f}}} + \frac{K_{H_2}^{\frac{3}{2}}P_{H_2}^{\frac{3}{2}}}{K_3K_4K_5} + \frac{K_{H_2}P_{H_2}}{K_4K_5} + \frac{K_{H_2}^{\frac{1}{2}}P_{H_2}^{\frac{1}{2}}}{K_5} + \frac{K_{H_2}^{\frac{1}{2}}P_{H_2}^{\frac{1}{2}}}{K_C C_{C_{Ni,f}}} \right)$$

We can rewrite Equation B45, as follows:

$$\boxed{\therefore \theta_{C.I} = \frac{1-\theta_{C_P\cdot I}}{k'}} \qquad \text{(B46)}$$

By replacing $\theta_{C.I}$ from Equation B46 into equation B33:

$$\frac{d\theta_{CH_3\cdot I}}{dt} = \frac{C_0\, k_2 K_{CH_4}}{k_C^2 C_{C_{Ni,f}}^2}\frac{\left(1-\theta_{C_P\cdot I}\right)^2}{(k')^2}\left[P_{CH_4} - \frac{K_{H_2}^2 K_C C_{C_{Ni,f}}}{K_{CH_4}K_2K_3K_4K_5}P_{H_2}^2 \right] \qquad \text{(B47)}$$

The proportionality between the reaction rate and the ratio of encapsulated sites is:

$$\text{rate } \alpha\left(1-\theta_{C_P\cdot I}\right)^2 \qquad \text{(B48)}$$

But k' in Equation B47 is a function of $C_{C_{Ni,f}}$, but $C_{C_{Ni,f}}$ is also present in the denominator. And $C_{C_{Ni,f}}$ is related to $\theta_{C.I}$ as shown by reaction step 7 (Equation B23), so Equation B48 can be written as:

$$\text{rate } \alpha\left(1-\theta_{C_P\cdot I}\right)^P \qquad \text{(B49)}$$

From Equations B15, B16, and B49:

$$\alpha = 1 - \theta_{C_P \cdot I}$$

$$a = \frac{R_t}{R_0} = \frac{\left(1 - \theta_{C_P \cdot I}\right)^P}{1^2} = \left(1 - \theta_{C_P \cdot I}\right)^P$$

$$a = \alpha^P \tag{B50}$$

$$\alpha = 1 - \theta_{C_P \cdot I}$$

$$\frac{d\alpha}{dt} = -\frac{d\theta_{C_P \cdot I}}{dt} \tag{B51}$$

From equation B25:

$$\frac{d\theta_{C_P \cdot I}}{dt} = k_d \theta^n_{C \cdot I}$$

$$\frac{\mathrm{d}\alpha}{\mathrm{dt}} = -\mathrm{k_d}\theta^{\mathrm{n}}_{\mathrm{C \cdot I}} \tag{B52}$$

From equation B46:

$$\theta_{C.I} = \frac{1 - \theta_{C_P \cdot I}}{k'}$$

Then B52 is written as follows:

$$\frac{d\alpha}{dt} = -\frac{k_d}{k'^n}\left(1 - \theta_{C_P \cdot I}\right)^n$$

$$\frac{d\alpha}{dt} = -\frac{k_d}{k'^n}\alpha^n$$

$$\frac{d\alpha}{\alpha^n} = -\frac{k_d}{k'^n}dt$$

By integration:

$$^{n \neq 1}\left[\frac{-1}{n-1}\frac{1}{\alpha^{n-1}}\right]_1^{\alpha} = -\frac{k_d}{k'^n}t$$

$$\frac{-1}{n-1}\left[\frac{1}{\alpha^{n-1}}-1\right]=-\frac{k_d}{k'^n}t$$

$$\left[\frac{1}{\alpha^{n-1}}\right]=1+(n-1)\frac{k_d}{k'^n}t$$

$$\alpha^{n-1}=\frac{1}{1+(n-1)\frac{k_d}{k'^n}t}$$

$$\alpha=\left(\frac{1}{1+(n-1)\frac{k_d}{k'^n}t}\right)^{\frac{1}{n-1}} \qquad \text{(B53)}$$

From B50:

$$a=\alpha^P$$

Equation B53 will be:

$$a=\left(\frac{1}{1+(n-1)C*t}\right)^{\frac{P}{(n-1)}} \qquad \text{(B54)}$$

References:

- Butt J.B., Petersen E.E., Activation, Deactivation, and poisoning of Catalysts, Academic Press, San Diego, 1988.
- Fogler H.S. Elements of Chemical Reaction Engineering. 3ed. New Jersey: Prentice-Hall 1999.
- Snoeck J.W., Froment G.F., Fowles M. Filamentous Carbon Formation and Gasification: Thermodynamics, Driving Force, Nucleation, and Steady-State Growth. J. Catal. 1997; 169: 250-262.

Appendix C: Diffusion equation parameters (Equation 6.36)

Ω_D & σ_{AB}

The diffusion collision integral for non-polar gas molecule is (Brodkey et al., 1988):

$$\Omega_{D,nonploar} = \frac{A}{\left(T^*\right)^B} + \frac{C}{\exp\left(DT^*\right)} + \frac{E}{\exp\left(FT^*\right)} + \frac{G}{\exp\left(HT^*\right)}$$

The constants of the law are given in the following table:

Table C1: Diffusion equation parameters

A	B	C	D	E	F	G	H
1.06036	0.15610	0.19300	0.47635	1.03587	1.52996	1.76474	3.89411

Where T^* is the dimensionless (reduced) temperature for mixtures; and can be calculated as follows:

$$T^* = \frac{T}{\varepsilon_{AB} / k_B}$$

Where

$$\sigma_{AB} = \frac{1}{2}\left(\sigma_A + \sigma_B\right)$$

$$\varepsilon_{AB} = \left(\varepsilon_A \varepsilon_B\right)^{1/2}$$

Value of σ & ε / k are provided in the following table:

Table C2: Value of σ & ε / k for calculating viscosity and diffusion

Compound name	Collision diameter σ *10^{10},m	Energy ratio ε / k , k
Methane	3.758	148.6
Hydrogen	2.827	59.7
Nitrogen	3.798	71.4
Helium	2.551	10.22
Air	3.771	78.6

Diffusivity (cm^2/s) of methane and hydrogen at 0ºC is found in Perry and green (1999):

0.625 While the formula at 0ºC showed a diffusivity of 0.606

Reference:

Brodkey R.S., Hershey H.C., 'Transport phenomena A unified approach', McGraw-Hill, New York, 1988

Perry R.H., Green D.W., ' Perry's chemical engineering handbook', 7th edition, McGraw-Hill, New York, 1999

Appendix D: Viscosity equation parameters (Equation 6.37)

Ω_μ & σ

The viscosity collision integral for non-polar gas molecule is (Brodkey et al., 1988):

$$\Omega_{\mu,nonploar} = \frac{A}{\left(T^*\right)^B} + \frac{C}{\exp\left(DT^*\right)} + \frac{E}{\exp\left(FT^*\right)}$$

The constants of the law are given in the following table:

Table D1: Viscosity equation parameters

A	B	C	D	E	F
1.16145	0.14874	0.52487	0.77320	2.16178	2.43787

Where T^* is the dimensionless (reduced) temperature for mixtures; and can be calculated as follows:

$$T^* = \frac{T}{\varepsilon / k}$$

Value of σ & ε / k are provided in table C2 (Appendix C)

Viscosity (Pa.s) of methane is found in Perry and green (1999):

500 K:	0.17E-4	from the formula	0.167E-4
600K:	0.195E-4		0.191E-4

Reference

Brodkey R.S., Hershey H.C., 'Transport phenomena A unified approach', McGraw-Hill, New York, 1988

Perry R.H., Green D.W., ' Perry's chemical engineering handbook', 7th edition, McGraw-Hill, New York, 1999

Appendix E: Experimental conditions for thermo balance Experiments

Two different catalysts were used in the thermo balance experimental work; namely; 10%Ni/αAl_2O_3 and 10%Ni/γAl_2O_3. All the experiments were conducted under atmospheric pressure in a temperature range of 500-650ºC.Methane, methane and nitrogen, and methane and hydrogen mixtures were used as inlet gas. Cracking/regeneration cycles were conducted to assess the catalyst performance for methane cracking cyclic unit. The following experimental conditions are shown for one catalyst only and similar plans were conducted for the other catalyst. The average particle size used throughout the experimental work is 725 μm unless otherwise stated.

The experiments listed in the following table were conducted at each temperature (500, 550, 600, 650ºC):

Table E1: Experimental work repeated at each temperature level

Experiment Number	Volumetric percentage of each gas			Inlet flow rate ml/min
	Methane	Nitrogen	Hydrogen	
1	100	0	0	72
2	100	0	0	120
3	100	0	0	180
4	100	0	0	240
5	90	10	0	120
6	70	30	0	120
7	50	50	0	120
8	95	0	5	120
9	90	0	10	120
10	85	0	15	120
11	80	0	20	120

The following experiments were conducted only at 550ºC at 100% methane

- Different particle size:

Table E2: Particle size effect experiments

Experiment Number	Particle size, μm	Flow rate, ml/min
12	500	120
13	1000	120

- Cracking/regeneration cycles

Table E3: Cracking/regeneration cycles experiments

Catalyst	No. of cycles	Oxidation gas
10%Ni/αAl_2O_3	5	Air, 120 ml/min
10%Ni/γAl_2O_3	24	Air, 120 ml/min

Appendix F: Determination of minimum fluidizing velocity

The minimum fluidizing velocity term is introduced to distinguish clearly between the inception of fluidization and the onset of the complete fluidization. The minimum fluidizing velocity can be determined from empirical equations or experimentally. In methane cracking, the catalyst is subjected to carbon deposition which affects the catalyst fluidodynamic properties. The experimental determination for U_{mf} is preferred. In the experimental approach, the pressure drop across a fixed bed is plotted against the gas velocity; by increasing the gas velocity, the pressure drop across the bed increases until it reaches a point where it keeps a constant value with further increase of gas velocity. The minimum gas velocity at which the pressure drop reaches the maximum value is the minimum fluidizing velocity (Cheremisinoff and Cheremisionoff, 1984).

Experimental investigation of U_{mf} at high temperature

Pinilla et al. (2007) developed an approach for measuring U_{mf} for the catalyst used for methane cracking. In this approach, the minimum fluidizing velocity is determined at the reaction conditions using inert gas like nitrogen, by plotting the pressure drop across a bed of partially deactivated catalyst particles against fluidizing gas velocity, as shown in Figure F1. Then, the velocity calculated experimentally for nitrogen is multiplied by 1.4 to account for using methane.

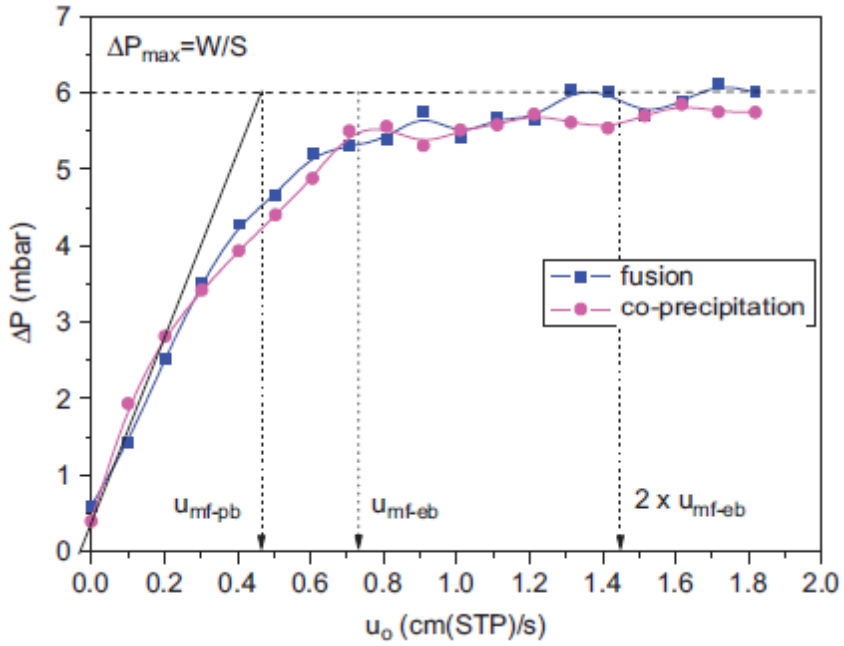

Figure F1- U_{mf} and pressure drop, using nitrogen at 700 °C (Pinilla et al., 2007)

U_{mf-pb} : The minimum fluidizing velocity at the onset of fluidization calculated for the particle.

U_{mf-eb} : The minimum fluidizing velocity at the complete fluidization calculated for the bed.

The figures below are examples of the experimental measurement of U_{mf} for different catalysts at different particle size and temperatures using nitrogen.

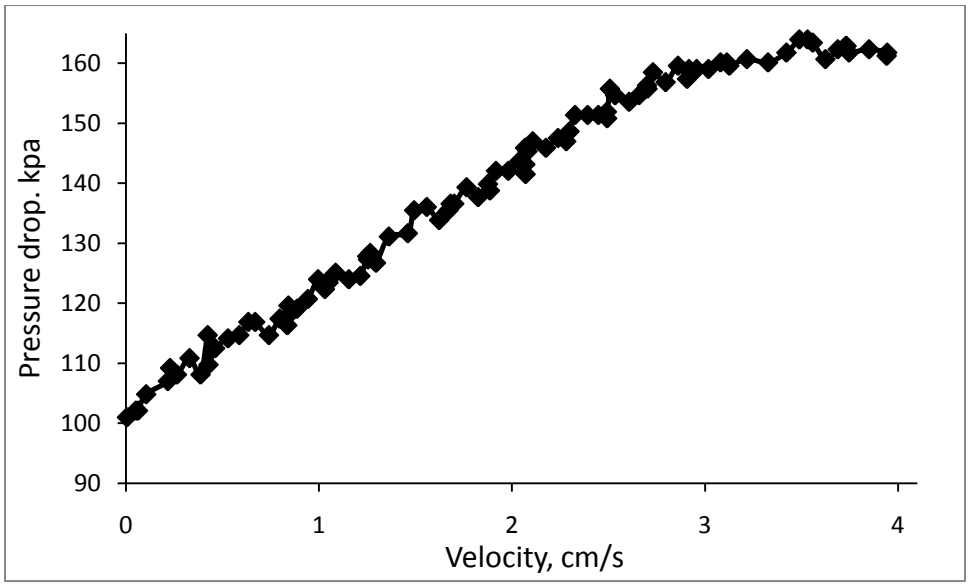

Figure F2: U_{mf} for 108 μm 10%Ni/αAl_2O_3 at 600ºC using N_2 as fluidizing gas

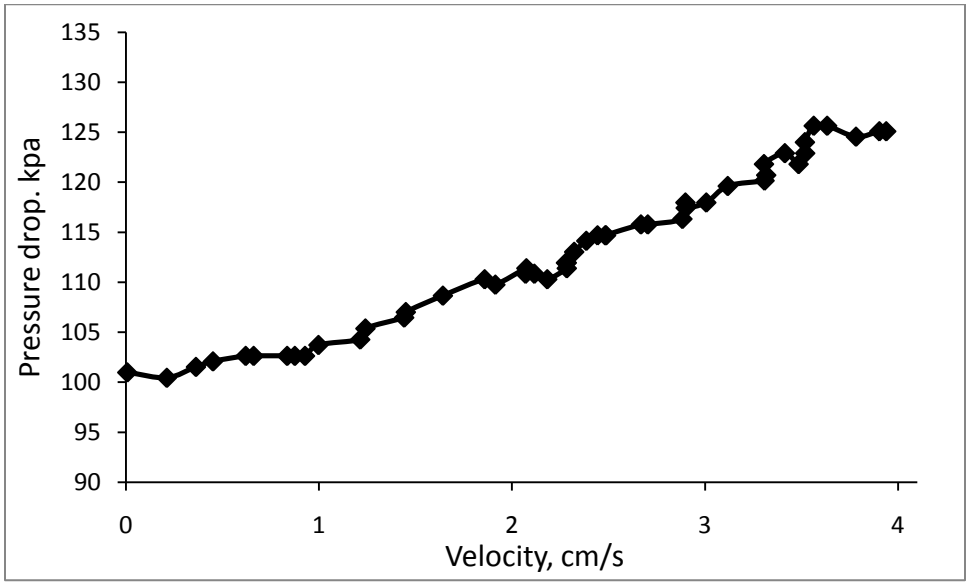

Figure F3: U_{mf} for 108 μm 10%Ni/γAl_2O_3 at 600ºC using N_2 as fluidizing gas

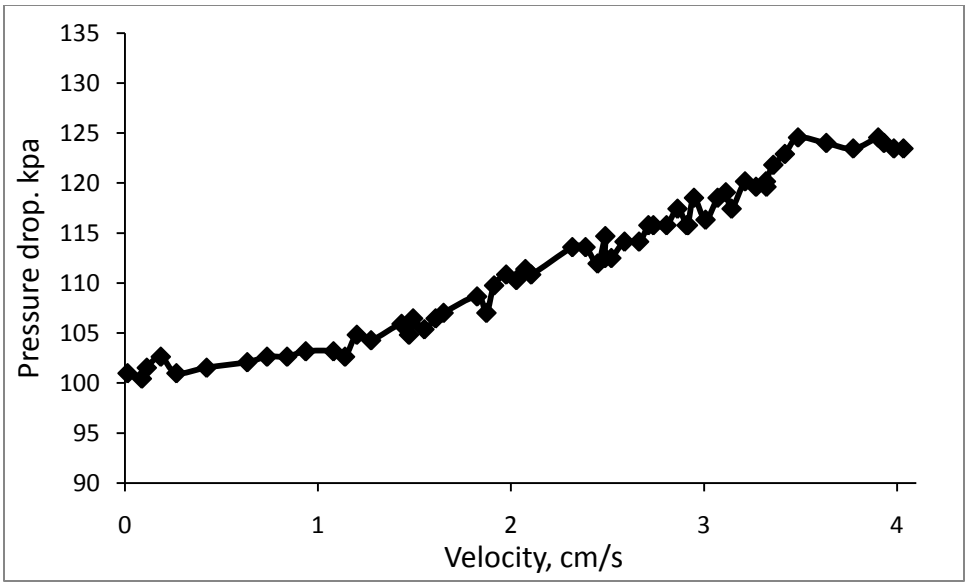

Figure F4: U_{mf} for 108 μm 10%Ni/SiO_2 at 600ºC using N_2 as fluidizing gas

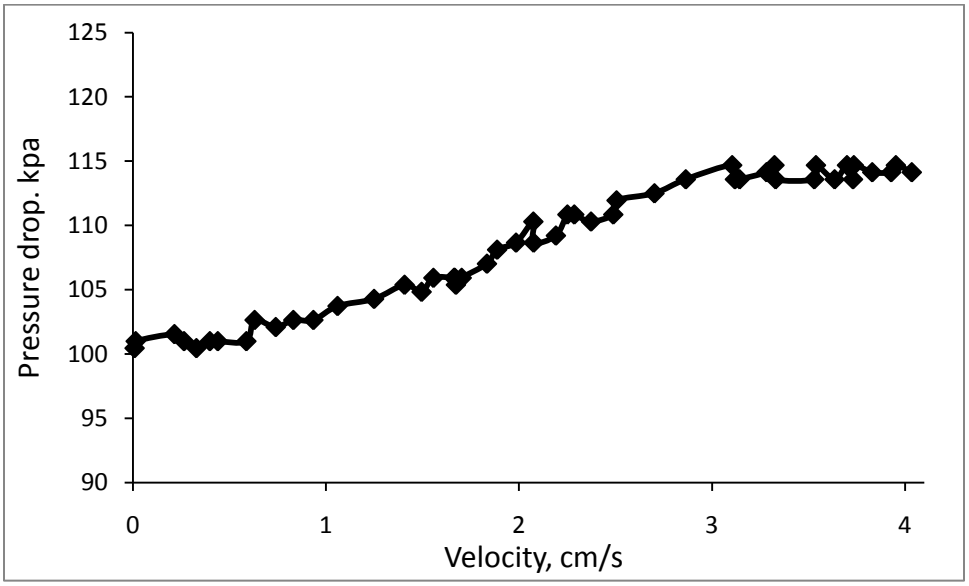

Figure F5: U_{mf} for 275 μm 10%Ni/αAl_2O_3 at 650ºC using N_2 as fluidizing gas

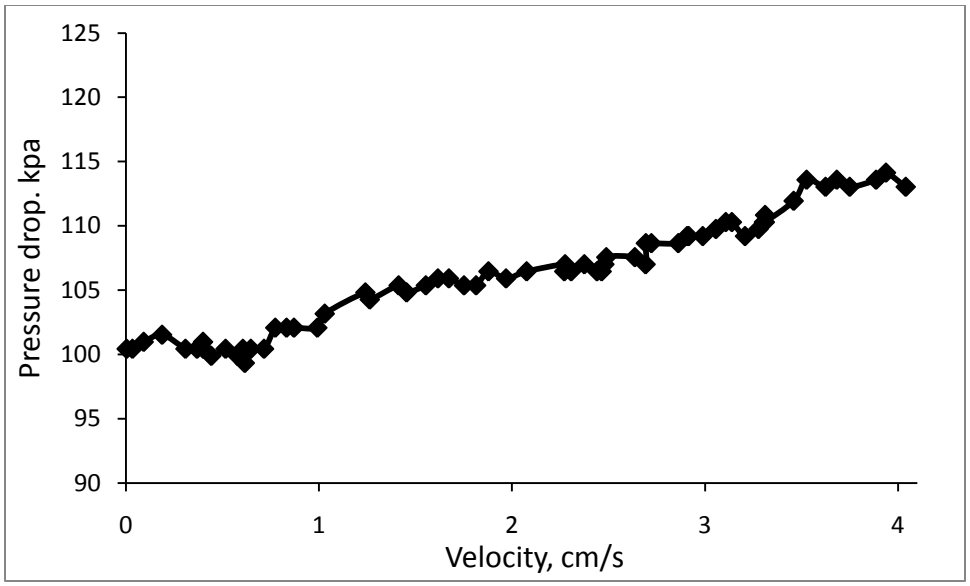

Figure F6: U_{mf} for 275 μm 10%Ni/γAl_2O_3 at 650ºC using N_2 as fluidizing gas

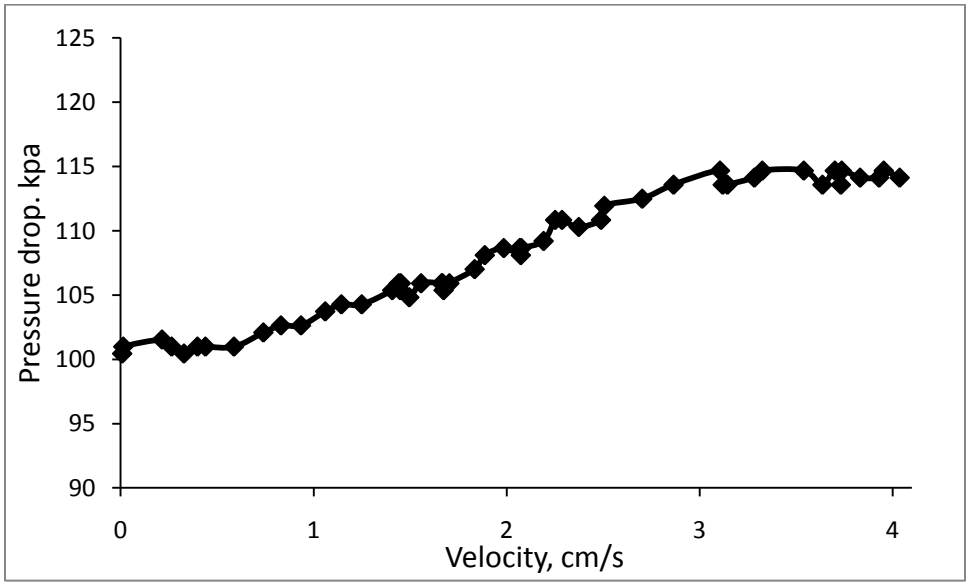

Figure F7: U_{mf} for 275 μm 10%Ni/SiO_2 at 650ºC using N_2 as fluidizing gas

References

Cheremisinoff N.P., Cheremisionoff P.N., 'Hydrodynamics of gas-solid fluidization', Gulf publishing, Houston, 1984

Pinilla J.L., Moliner R., Suelves I., L´azaro M.J., Echegoyen Y.,Palacios J.M. 'Production of hydrogen and carbon nanofibers by thermal decomposition of methane using metal catalysts in a fluidized bed reactor', International journal of hydrogen energy 32 (2007) 4821–4829

Appendix G: Experimental conditions for fluidized bed experiments

The experimental work in the fluidized bed was conducted using %Ni/αAl_2O_3, 10%Ni/SiO_2, and 10%Ni/γAl_2O_3. A factorial experimental design was used at two levels of temperature, methane concentration, particle size. Also, different experiments were conducted to study the effect of flow rate and to assess the catalyst durability to be used in cracking/regeneration cycles. The following presentation is a brief description of the experimental conditions for one catalyst, and a similar experimental design is used for the other two catalysts:

A 2^3 Factorial design for the fluidized bed experiments

Table G1: Factors and levels for fluidized bed factorial design

Factors and levels

Temperature, T (°C)		Methane percentage in inlet gases R (As methane/Nitrogen partial pressure ratio)		Particle size, P (μm)	
-	+	-	+	-	+
550	650	50(1/1)	80(4/1)	108	275

Coded units of Factors

T	R	P	TR	TP	RP	TRP
-	-	-	+	+	+	-
+	-	-	-	-	+	+
-	+	-	-	+	-	+
+	+	-	+	-	-	-
-	-	+	+	-	-	+
+	-	+	-	+	-	-
-	+	+	-	-	+	-
+	+	+	+	+	+	+

Table G2: Operational levels of factors

Experiment Number	T (°C)	R (P_{CH4}/P_{N2})	P
1	550	50 (1/1)	108
2	650	50 (1/1)	108
3	550	80 (4/1)	108
4	650	80 (4/1)	108
5	550	50 (1/1)	275
6	650	50 (1/1)	275
7	550	80 (4/1)	275
8	650	80 (4/1)	275

Table G3: Replicated experiments in factorial design

Experiment Number	T (°C)	R (P_{CH4}/P_{N2})	P
9	600	65 (6.5/3.5)	108
10	600	65 (6.5/3.5)	108
11	600	65 (6.5/3.5)	108

Additional Experiments

Cracking/Regeneration

Table G4: Cracking/regeneration cycles experiments

Experiment Number	T (°C)	R (P_{CH4}/P_{N2})	P
12	550	80 (4/1)	275

Fixed bed experiment

An experiment was conducted in a fixed bed to compare its performance with the fluidized bed by keeping the same weight hourly space velocity (WHSV):

Table G5: Fixed bed experiment

Experiment Number	T (°C)	R (P_{CH4}/P_{N2})	P
13	550	80 (4/1)	275

Flow rate effect

This set of experiments was conducted at 1.5 U_{mf}

Table G6: Flow rate effect experiment

Experiment Number	T (°C)	R (P_{CH4}/P_{N2})	P
14	550	50 (1/1)	108

Appendix H: Fluidized bed model for methane cracking at different cycles of Ni/γAl_2O_3

```
%This model considers the conversion of methane using a fluidized bed catalyst
% This model studies the conversion based on the internal properties on the bed
% Inlet data include working temperature of the reactor and catalyst properties
% The model is a three phase type model
fprintf('Welcome to the CRE group model for methane cracking in a fluidized bed\n');
fprintf('Please enter the following data:\n');
fprintf('                                        \n');
dmin= input('Enter minimum particle diameter in meter:');
dmax= input('Enter maximum particle diameter in meter:');
t= input('Enter reactor temperature in ºC:');
Em= input('Enter voidage at fixed bed conditions:');
lm= input('Enter height at fixed bed conditions:');
d= input('Enter bed diameter in meter:');
rhos= input('Enter catalyst particle average density in Kg/m3:');global k KH KM kd kdc kdm kdh R1 R2
R3 R4 R5 R6 R7 tm C0 T d1
dp=(dmin+dmax)/2;
T=t1+273.15;
C0=1/(T*0.082);
Ccwn1=rat*0.99*C0;
Cbn1=rat*0.99*C0;
Cen1=rat*0.99*C0;
Ccwnh1=rat*0.01*C0;
Cbnh1=rat*0.01*C0;
Cenh1=rat*0.01*C0;
rho=((28)*((1-rat)*C0))+((16)*(rat*C0));
```

```
T1=T/103;

T2=298/103;

C01=2/(298*0.082);

rho1=((28)*((1-rat)*C01))+((16)*(rat*C01));

Mwt=(rat*16)+((1-rat)*28);

om=(1.16145/((T1)^(0.14874)))+(0.52487/(exp(0.7732*T1)))+(2.16178/(exp(2.43787*T1)));

mu=(1.89e-7)*(((Mwt*T)^(1/2))/om);

om1=(1.16145/((T2)^(0.14874)))+(0.52487/(exp(0.7732*T2)))+(2.16178/(exp(2.43787*T2)));

mu1=(1.89e-7)*(((Mwt*298)^(1/2))/om);

omd=(1.06036/((T1)^(0.1561)))+(0.193/(exp(0.47635*T1)))+(1.03587/(exp(1.52996*T1)))+(1.76474/(exp(3.89411*T1)));

DMH=(1.3158e-8)*((((T^3)*0.125)^(0.5))/omd);

k=4.64E4*(exp(-88837.109/8.314/T));

KH=1.96E-8*(exp(144262/8.314/T));

KM=3.75E-5*(exp(56154/8.314/T));

kd=4904*(exp(-147470/8.314/T));

kdc=313.53*(exp(26367/8.314/T));

kdm=-4082*(exp(3.56/8.314/T));

kdh=-0.34*(exp(81324/8.314/T));

Ar=(9.8*((dp)^3)*rho*(rhos-rho))/(mu);

if dp <= 0.0001

  umf=(((9.8)^(0.934))*((dp)^(1.8))*((rhos-rho)^(0.934)))/(1111*((mu)^(0.87))*((rho)^(0.066)));

else

 umf=((mu/(rho*dp))*(((1135.7+0.0408*Ar)^(0.5))-33.7));

end

umf= 0.035;

Abed=(pi/4)*((d)^2);
```

```
fprintf('Please enter the particle shape:1 for sphere \n');
fprintf('Please enter the particle shape: 2 for other shapes\n');
shape=input('Enter the particle shape value:');
if shape>1
      sp=input('Enter the sphercity value:');
    Emf=(0.586*((sp)^(-0.7)))*(((mu^2)/(rho*(9.8)*(rhos-rho)*(dp^3)))^(0.029))*((rho/rhos)^(0.021));
else
  sp=1;
Emf=(0.586*((sp)^(-0.7)))*(((mu^2)/(rho*(9.8)*(rhos-rho)*(dp^3)))^(0.029))*((rho/rhos)^(0.021));
end
lmf=((1-Em)*lm)/(1-Emf);
n= input('Enter 1 for a perforated plate or 2 for porous plate:');
if n > 1
   db0=((0.283)*((umf)^2));
else
  ior= input('The spacing between adjacent holes:');
  dor= input('The hole diameter:');
  type=input('Enter 1 for equilateral triangle array or 2 for square array')
  if type>1
     nd=1/((ior)^2);
  else
     nd=2/((3^(0.5))*((ior)^2));
  end
  if dor>ior
   db0=((0.283)*((umf)^2));
  else
```

```
    db0=(0.347*(((Abed*(umf))/nd)^(0.4)));
   end
end
dbm=(0.65*((Abed*(umf))^(0.4)));
if dbm>d
    dbm=d;
else
end
db=dbm-((dbm-db0)*(exp(-0.3*(lmf/(2*d)))));
cebm=mu/(((rhos-rho)*rhos*9.8*((dp)^(3)))^(0.5));
f=@(x)-(cebm)+(0.149*((1-x)^(0.5))*(x^(3.8)));
Ebm=fzero(f,0.5);
ub=(0.711*((9.8*db)^(1/2)))*((1-Emf)/((rhos/(rhos-rho))-Emf));
switch ub
    case ub<(umf/Emf);
U=umf+(Ebm*(ub+2*umf));
    case ub>=(umf/Emf)&ub<=(3*(umf/Emf));
  U =umf+(Ebm*(ub+umf));
    case ub>(3*(umf/Emf))&ub<=(6*(umf/Emf));
     U=umf+(Ebm*ub);
    case  ub>(6*(umf/Emf))&ub<=(10*(umf/Emf));
    U =umf+(Ebm*(ub-umf));
    otherwise
        U =Ebm*ub;
end
Ar=(((dp)^3)*rho1*(rhos-rho1)*9.8)/((mu1)^2);
```

```
Uc=((0.7*mu1)/(rho1*dp))*((Ar)^(0.485));

fprintf('\n The minimum bubbling velocity is :%3.5f m/s\n The Incepient turblent velocity is:%3.5f m/s\n',U,Uc);

fprintf(' Enter 1 to study the effect of inlet velocity on the different bed properties\n');

fprintf('Enter 2 to study the conversion rate change with height at definite inlet velocity\n');

study= input('1 or 2:');

if study >1

fprintf('Enter the inlet velocity \n');

U0= input('The inlet velocity in m/s:');

fw= input('The wake fraction:');

if n > 1

else

  ior= input('The spacing between adjacent holes:');

  dor= input('The hole diameter:');

  type=input('Enter 1 for equilateral triangle array or 2 for square array');

end

if n > 1

   db0=((0.283)*((U0-umf)^2));

else

  if type>1

     nd=1/((ior)^2);

  else

     nd=2/((3^(0.5))*((ior)^2));

  end

  if dor>ior

   db0=((0.283)*((U0-umf)^2));

  else
```

```
    db0=(0.347*(((Abed*(U0-umf))/nd)^(0.4)));
   end
end
dbm=(0.65*((Abed*(U0-umf))^(0.4)));
if dbm>d
    dbm=d;
else
end
db=dbm-((dbm-db0)*(exp(-0.3*(lmf/(d)))));
ubr=0.711*((9.8*db)^(1/2));
if dp<0.0001
ub=(1.55*((U0-umf)+(14.1*(db+0.005)))*(d^(0.32)))+ubr;
else
  ub=(1.6*((U0-umf)+(1.13*(db^(0.5))))*(d^(1.35)))+ubr;
end
switch ub
    case ub<(umf/Emf)
Eb=(U0-umf)/(ub+2*umf);
    case ub>=(umf/Emf)&ub<=(3*(umf/Emf));
   Eb=(U0-umf)/(ub+umf);
    case ub>(3*(umf/Emf))&ub<=(6*(umf/Emf));
        Eb=(U0-umf)/(ub);
    case  ub>(6*(umf/Emf))&ub<=(10*(umf/Emf));
       Eb=(U0-umf)/(ub-umf);
    otherwise
         Eb=(U0)/(ub);
```

```
end
lb=lmf/(1-Eb);
N=round(lb/db);
NS=lb/N;
z=0;
rho=((28)*((1-rat)*C0))+((16)*(rat*C0));
Ar=(9.8*((dp)^3)*rho*(rhos-rho))/(mu);
Emf=(0.586*((sp)^(-0.7)))*(((mu^2)/(rho*(9.8)*(rhos-rho)*(dp^3)))^(0.029))*((rho/rhos)^(0.021));
dbm=(0.65*((Abed*(U0-umf))^(0.4)));
db=(dbm-((dbm-db0)*(exp(-0.3*(lb/d)))));
ubr=0.711*((9.8*db)^(1/2));
if dp<0.0001
ub=(1.55*((U0-umf)+(14.1*(db+0.005)))*(d^(0.32)))+ubr;
else
  ub=(1.6*((U0-umf)+(1.13*(db^(0.5))))*(d^(1.35)))+ubr;
end
switch ub
    case ub<(umf/Emf)
Eb=(U0-umf)/(ub+2*umf);
    case ub>=(umf/Emf)&ub<=(3*(umf/Emf));
   Eb=(U0-umf)/(ub+umf);
    case ub>(3*(umf/Emf))&ub<=(6*(umf/Emf));
        Eb=(U0-umf)/(ub);
    case  ub>(6*(umf/Emf))&ub<=(10*(umf/Emf));
       Eb=(U0-umf)/(ub-umf);
    otherwise
```

```
        Eb=(U0)/(ub);
end
fc=3/(((ubr*Emf)/umf)-1);
fcw=1.41;
yc=(1-Emf)*(fcw);
ye=(((1-Emf)*(1-Eb))/Eb)-yc;
kbc=(4.5*(umf/db))+(5.85*((((DMH)^(1/2))*((9.8)^(1/4)))/(db^(5/4))));
kce=6.77*(((DMH*Emf*ub)/((db)^3))^(1/2));
usdown=(fw*Eb*ub)/(1-Eb-fw*Eb);
ue=(umf/Emf)+usdown;
R1=(kbc/ub);
R3=(kbc/(fcw*ub*Emf));
R4=0.077*((3200*yc)/(Emf*ub*60));
R5=(kce/(fcw*Emf*ub));
R6=(kce*((1-Eb*(1+fcw))))/(umf);
R7=0.077*ye*3200*((1-Eb*(1+fcw)))/(umf*60);
    [p,Y] = ode23s(@methane,[0:NS:lb],[Cbn1; Ccwn1; Cen1; Cbnh1; Ccwnh1; Cenh1]);
  tm= input('Time in min:');
for i=1:N
    Htot(i)=z;
    z3=(z+NS/2);
bdia(i)=(dbm-((dbm-db0)*(exp(-0.3*(z3/d)))));
Cbns=Y(i,1);
Ccwns=Y(i,2);
Cens=Y(i,3);
Cbnhs=Y(i,4);
```

```
Ccwnhs=Y(i,5);
Cenhs=Y(i,6);
q=(Ccwns*Eb*fcw)+(Eb*Cbns)+((1-Eb*(1+fcw))*Cens);
m=(Ccwnhs*Eb*fcw)+(Eb*Cbnhs)+((1-Eb*(1+fcw))*Cenhs);
  d1=((1/(1-0.33*0.5*tm*kd*(kdc+kdm*(0.082*T*rat*C0)+kdh*((0.01*0.082*T*rat*C0)^0.83))))^-0.8);
con=(1-(q/(rat*C0)))*d1;
metcon(i)=con;
mconv(i)=q;
hconv(i)=m;
z=z+NS;
end
fprintf('Enter the suitable value to get the required curve\n');
fprintf('Enter 1 to get a chart of height and concentration\n');
fprintf('Enter 4 to get a chart of height and bubble diametr\n');
fprintf('Enter 7 to get a chart of height and conversion\n');
draw=input('The chart required is:');
if draw<2
plot(Htot,mconv,'-r*','linewidth',2,'markersize',4);
xlabel('Reactor height(m)');ylabel('concentration(Kmol/m3)');
hold on
plot(Htot,hconv,'-b*','linewidth',2,'markersize',4);
elseif draw>6
plot(Htot,metcon,'-r*','linewidth',2,'markersize',4);
xlabel('Reactor height(m)');ylabel('conversion');
else
   plot(Htot,bdia,'-r*','linewidth',2,'markersize',4);
```

```
xlabel('Reactor height(m)');ylabel('bubble diameter(m3)');
end
else
fprintf('Enter the inlet velocity \n');
U0= input('The inlet velocity in m/s:');
%0.049;
fw= input('The wake fraction:');
if n > 1
else
   ior= input('The spacing between adjacent holes:');
   dor= input('The hole diameter:');
   type=input('Enter 1 for equilateral triangle array or 2 for square array');
end
 time=zeros(180,1);
 totconv=zeros(180,1);
if n > 1
    db0=((0.283)*((U0-umf)^2));
else
   if type>1
      nd=1/((ior)^2);
   else
      nd=2/((3^(0.5))*((ior)^2));
   end
   if dor>ior
    db0=((0.283)*((U0-umf)^2));
   else
```

```
    db0=(0.347*(((Abed*(U0-umf))/nd)^(0.4)));
   end
end
dbm=(0.65*((Abed*(U0-umf))^(0.4)));
if dbm>d
    dbm=d;
else
end
db=dbm-((dbm-db0)*(exp(-0.3*(lmf/(d)))));
ubr=0.711*((9.8*db)^(1/2));
if dp<0.0001
ub=(1.55*((U0-umf)+(14.1*(db+0.005)))*(d^(0.32)))+ubr;
else
  ub=(1.6*((U0-umf)+(1.13*(db^(0.5))))*(d^(1.35)))+ubr;
end
switch ub
    case ub<(umf/Emf)
Eb=(U0-umf)/(ub+2*umf);
    case ub>=(umf/Emf)&ub<=(3*(umf/Emf));
   Eb=(U0-umf)/(ub+umf);
    case ub>(3*(umf/Emf))&ub<=(6*(umf/Emf));
        Eb=(U0-umf)/(ub);
    case  ub>(6*(umf/Emf))&ub<=(10*(umf/Emf));
       Eb=(U0-umf)/(ub-umf);
    otherwise
         Eb=(U0)/(ub);
```

```
end
lb=lmf/(1-Eb);
N=round(lb/db);
NS=lb/N;
z=0;
rho=((28)*((1-rat)*C0))+((16)*(rat*C0));
Ar=(9.8*((dp)^3)*rho*(rhos-rho))/(mu);
Emf=(0.586*((sp)^(-0.7)))*(((mu^2)/(rho*(9.8)*(rhos-rho)*(dp^3)))^(0.029))*((rho/rhos)^(0.021));
dbm=(0.65*((Abed*(U0-umf))^(0.4)));
db=(dbm-((dbm-db0)*(exp(-0.3*(lb/d)))));
ubr=0.711*((9.8*db)^(1/2));
if dp<0.0001
ub=(1.55*((U0-umf)+(14.1*(db+0.005)))*(d^(0.32)))+ubr;
else
  ub=(1.6*((U0-umf)+(1.13*(db^(0.5))))*(d^(1.35)))+ubr;
end
switch ub
    case ub<(umf/Emf)
Eb=(U0-umf)/(ub+2*umf);
    case ub>=(umf/Emf)&ub<=(3*(umf/Emf));
   Eb=(U0-umf)/(ub+umf);
    case ub>(3*(umf/Emf))&ub<=(6*(umf/Emf));
        Eb=(U0-umf)/(ub);
    case  ub>(6*(umf/Emf))&ub<=(10*(umf/Emf));
       Eb=(U0-umf)/(ub-umf);
    otherwise
```

```
        Eb=(U0)/(ub);
end
fc=3/(((ubr*Emf)/umf)-1);
fcw=1.41;
yc=(1-Emf)*(fcw);
ye=(((1-Emf)*(1-Eb))/Eb)-yc;
kbc=(4.5*(umf/db))+(5.85*((((DMH)^(1/2))*((9.8)^(1/4)))/(db^(5/4))));
kce=6.77*(((DMH*Emf*ub)/((db)^3))^(1/2));
usdown=(fw*Eb*ub)/(1-Eb-fw*Eb);
ue=(umf/Emf)+usdown;
R1=(kbc/ub);
R3=(kbc/(fcw*ub*Emf));
R4=0.077*((3200*yc)/(Emf*ub*60));
R5=(kce/(fcw*Emf*ub));
R6=(kce*((1-Eb*(1+fcw))))/(umf);
R7=0.077*ye*3200*((1-Eb*(1+fcw)))/(umf*60);
Htot=lb;
tm=0;
for t=1:300
   [p,Y] = ode23s(@methane,[0:NS:lb],[Cbn1; Ccwn1; Cen1; Cbnh1; Ccwnh1; Cenh1]);
Cbns=Y(N,1);
Ccwns=Y(N,2);
Cens=Y(N,3);
Cbnhs=Y(N,4);
Ccwnhs=Y(N,5);
Cenhs=Y(N,6);
```

```
%q=((Ccwns*Eb*fcw*Emf*ub)+(Eb*ub*Cbns)+(1-Eb*(1+fcw))*umf*Cens)/U0;

%bal=((rat*C0*Eb*fcw*Emf*ub)+(Eb*ub*rat*C0)+(1-Eb*(1+fcw))*umf*rat*C0)/U0;

q=((Ccwns*Eb*fcw)+(Eb*Cbns)+((1-Eb*(1+fcw))*Cens));

m=(Ccwnhs*Eb*fcw)+(Eb*Cbnhs)+((1-Eb*(1+fcw))*Cenhs);

c= input('Enter number of cycle:');

f1=-7e-5*(c^3)+0.0036*(c^2)-0.0546*c+0.783;

  d1=((1/(1-f1*0.33*0.5*tm*kd*(kdc+kdm*(0.082*T*rat*C0)+kdh*((0.01*0.082*T*rat*C0)^0.83))))^-
0.8);

convm=(1-(q/(C0*rat)))*d1;

time(t)=t;

%convm=(1-(q/(bal)));

totconv(t)=convm;

tm=tm+1;

end

plot(time,totconv,'-r*','linewidth',2,'markersize',4);

xlabel('Time, min');ylabel('conversion');

end
```